The analysis and interpretation of microseismicity induced by a collapsing solution mining cavity: A contribution for progress in hazard assessment of underground cavities

Jannes Lennart Kinscher

UNIVERSITÉ DE LORRAINE

Ecole Nationale Supérieure des Mines de Nancy

Laboratoire GeoRessources

ÉCOLE DOCTORALE : RP2E

THÈSE

présentée en vue de l'obtention du grade de :

DOCTEUR DE L'UNIVERSITÉ DE LORRAINE

en Mécanique - Génie Civil

par :

Jannes Lennart Kinscher

The analysis and interpretation of microseismicity induced by a collapsing solution mining cavity

A contribution for progress in hazard assessment of underground cavities

---

Soutenu publiquement le 30 Janvier 2015 devant le jury composé de:

Judith SAUSSE	Professeur, Ecole des Mines de Nancy	Président du jury
Aldo ZOLLO	Professeur, Université de Naples	Rapporteur
Thorsten DAHM	Professeur, Université de Potsdam	Rapporteur
Herve CUCHE	Ingénieur, SOLVAY	Examinateur
Pascal DOMINIQUE	Ingénieur, BRGM	Examinateur
Jack-Pierre PIGUET	Professeur,Université de Lorraine	Directeur de thèse
Isabelle CONTRUCCI	Ingénieur, INERIS	Co-Directeur de thèse
Pascal BERNARD	Professeur, IPGP Paris	Co-Directeur de thèse
Anne MANGENEY	Professeur, IPGP Paris	Co-Directeur de thèse

Für B. und E.

"Primary causes are unknown to us; but are subject to simple and constant laws, which may be discovered by observation, the study of them being the object of natural philosophy."

Jean Baptiste Joseph Fourier (21 March 1768 – 16 May 1830)

The Analytical Theory of Heat, 1878

Acknowledgments

La réalisation de cette thèse n'aurait jamais été possible sans le grand soutien, le conseil, et la patience de Jack-Pierre Piguet, Isabelle Contrucci, Pascal Bernard et Anne Mangeney. Merci Jack-Pierre : tu m'as permis de conserver un œil objectif sur les travaux de thèse ! Merci Isabelle : je n'oublierai pas ton intérêt, tes suggestions, et ta motivation et tous tes efforts pour m'intégrer dans la vie française et dans le monde d'une entreprise ! Merci Pascal : si tu n'as rien compris, demande à Pascal ! Tu m'as appris beaucoup! Anne : merci de m'avoir aidé à garder les pieds sur terre et de m'avoir appris la peinture.

My special thanks go to Thorsten Dahm and Aldo Zollo for their interest and review of this thesis. Mes remerciements vont également à Judith Sausse, à Pascal Dominique et à Herve Cuche pour leur intérêt et leur participation dans le jury de cette thèse. Je souhaiterais exprimer ma gratitude à Pascal Bigarré, Christophe Didier et Xavier Daupley pour leurs participations et conseils dans plusieurs COPIL de thèse. Je tiens à remercier l'INERIS pour le financement de cette thèse. Je remercie également le GISOS et SOLVAY pour la mise en place de ce projet extraordinaire qui m'a plu énormément. Egalement un grand merci à toute l'équipe et les thésards de l'INERIS, l'école des mines, GEORESSOURCE et plus particulièrement Virginie qui m'a soutenu beaucoup dans une situation compliquée. Je remercie sincèrement Alain Thoraval, Marwan Al Heib, Armand Lizeur et Moutaka Souley pour leur soutien, leur intérêt et leurs renseignements. Merci à Phillipe Jousset pour la révision du Chapitre 2. I owe much gratitude to Simone Cesca for discussing, reading and reviewing Chapter 3 of this thesis. For many processing and imaging steps, the KIWI tools (Heimann et al., 2014) and the OBSPY tools (Beyreuther et al., 2010) were used. You guys did really an incredible good job!

Meine lieben Eltern, ich hoffe ihr wisst, dass diese Arbeit ausschließlich euer Werk ist. Danke auch an den Rest der Familie, und diejenigen, die mir von oben herab Glück gewünscht haben. Danke meine lieben Freunde für die vielen Besuche in Nancy: Henry, Otti, Hagen, Fabse, Hannes, Till, Malte, Suse, und alle weiteren die zur Hochzeit kamen. Merci beaucoup à mes amis nancéiens: Babel, Olivier, Romain, Julien, Bastian, Guillaume, Brice, Nadia et toutes les personnes que j'aurais obliées. Al final, agradezco mucho a mi esposa Pilar por

su amor, apoyo y por haber cargado mi cabezoncito que me hizo sentir mucho más ligero. Gracias, abrazos y besos también a mi familia en el otro lado del atlántico.

Summary

Ground failures, caving processes and collapses of large natural or man-made underground cavities can produce significant socio-economic damages and represent a serious risk envisaged by the stakeholders and municipalities. In order to improve our understanding of the mechanisms governing such a geohazard and to test the potential of geophysical methods to prevent them, the development and collapse of a salt solution mining cavity was monitored. This experiment was conducted by the research "Groupement d'Intérêt Scientifique sur l'impact et la Sécurité des Ouvrages Souterrains" (GISOS), at the SOLVAY exploitation site of Cerville-Buissoncourt (Lorraine basin, France). The potential to create large- scale, shallow cavity structure at the study site is suggested from the presence of a stiff Dolomite layer, acting as a beam that keeps the overburden stable, and thus retards its collapse. During the experiment, an important catalogue ($\sim 50,000$ event files) was recorded by a local high frequency microseismic network, installed by INERIS, which provides a unique opportunity to study in detail the microseismic response of a caving and collapsing underground cavity. However, $\sim 80\%$ of the data comprised unusual swarming sequences with complex clusters of superimposed microseismic events. These waveforms could not be processed through automatic standard, body wave phase based detection, location and source analysis routines. Further problems in signal processing arise from the limited network station coverage, short hypocentral recording distances and propagation and near-field effects. This thesis presents a detailed analysis and interpretation of this unique microseismic data base, using and adapting innovative methods proposed from tectonic, volcanic and mining seismic swarm studies.

In the first part of this thesis, a probabilistic, automatic detection location design has been developed, able to resolve the spatio-temporal characteristics of microseismic swarms in a first order. In this approach, mainly signal polarization attributes were used to identify P wave phases. Event locations were then obtained by using the information of the corresponding polarization angles, as well as signal amplitudes, enabled by a detailed study of the attenuation characteristics, describing the amplitude decay with distance. Moreover, seismic source mechanisms and standard source parameters were investigated by comparing observed and synthetic wave forms, amplitude spectra and peak-to-peak amplitude ratios, assuming different standard source models. Within this source study, it was possible to assess the common

source mechanisms of many swarming events at once, using the observation from only one single three component station.

The second part of this thesis summarizes and discusses the results obtained by the developed methods, as well as by detailed statistical analysis of the spatio-temporal and energetic microseismic attributes. The principal results are summarized as follows:

(i) microseismic events are comparable to small natural tectonic earthquakes, demonstrate a self- similar scaling behavior and are associated with moment magnitudes M_W ranging from around -3 to 1;

(ii) the entirety of microseismic sources represents dominant shear faulting (standard double-couple shear model) at the cavity roof, in the Dolomite layer and in the overburden. The presence of tensile faulting could not be observed from the dataset, but cannot be completely excluded;

(iii) this observation contradicts geomechanical models predicting a dominant mode of traction failure in the center of the Dolomite layer;

(iv) source mechanisms for most microseismic events are remarkable stable and demonstrate a predominant thrust faulting regime with faults similarly oriented NW-SE, dipping around $35° - 55°$, what might be related to the presence of systematically arranged pre-existing fractures;

(v) similar to tectonic earthquake swarms, the origin of microseismic swarming is suggested in an incapacity to sustain larger strains and to release larger stresses, what seems to be related to the mechanical constitution of the rock strata overlying the cavity (i.e. low strength materials);

(vi) caving and collapsing periods at the cavity roof are associated with systematic, self-reinforcing dynamics and have a distinct microseismic response, clearly observable from statistical analysis;

The performed analysis and interpretation of the microseismicity at Cerville-Buissoncourt has shown that microseismic monitoring is a useful tool to constrain the mechanical and dynamical characteristics of an evolving and collapsing hazardous underground cavity. The here documented observations and trends provide new important constraints for the design of adequate geomechanical models that will improve hazard assessment at underground openings.

In future research, further investigation will assess the relationship between microseismic emissions and observed in-situ deformation including observations from seismic broadband data.

Résumé

Les cavités souterraines d'origine naturelle ou anthropique, comme les mines actives ou abandonnées, peuvent provoquer des affaissements importants et des effondrements qui peuvent avoir des conséquences catastrophiques au niveau humain comme économique. Pour améliorer notre compréhension des mécanismes qui régissent ces risques géologiques, l'effondrement provoqué d'une cavité saline, créée par dissolution, a été instrumentée par différentes méthodes géophysiques afin d'en tester l'efficacité. Cette expérimentation a été menée dans le cadre du « Groupement d'Intérêt Scientifique sur l'impact et la Sécurité des Ouvrages Souterrains » (GISOS) sur le site de Cerville- Buissoncourt (Lorraine, France), exploité par SOLVAY. La création de cavités de grandes dimensions sur le site est supposée possible grâce à la présence d'un banc raide (banc de Dolomite) qui jouerait le rôle d'une poutre soutenant le recouvrement et retardant ainsi son effondrement. Pendant l'expérience, un vaste ensemble de données microsismiques ($\sim$ 50.000 fichiers d'événements) a été enregistré par le réseau haute fréquence installé par l'INERIS. Cela constitue une occasion unique d'étudier en détail la réponse microsismique du développement d'une cavité souterraine jusqu'à son effondrement. Toutefois, la majeure partie ($\sim$ 80%) de ces événements microsismiques sont non-isolés, de type rafale, c'est-à-dire constitués par des superpositions complexes de groupes d'événements. Le traitement de ces signaux particuliers n'est pas possible par des approches conventionnelles de détection, localisation (basé sur les temps d'arrivée des ondes de volume) et d'analyse à la source. D'autres difficultés sont apparues dans le traitement des données, à cause de la résolution limitée du réseau à courtes distances hypocentrales et des effets de propagation et de champ proche. La thèse présente une analyse et une interprétation détaillée de cette base de données microsismiques grâce à l'adaptation de méthodologies de traitement originales, issues des études d'essaims sismiques d'origine tectonique, volcanique et minière.

La première partie de la thèse a été consacrée au développement d'une méthodologie de détection et localisation probabiliste automatique des événements en rafale. La détection des ondes P dans les séquences de rafales est réalisée grâce à une analyse automatique de la polarisation du signal, dans une bande de fréquence donnée où les ondes S ne sont pas dominantes. Puis la localisation du signal est obtenue en combinant les informations des angles de polarisation et de décroissance de l'amplitude du signal avec la distance. Cette

approche nécessite d'abord une calibration de l'atténuation élastique et anélastique du site, réalisée grâce à l'analyse d'un jeu de donnée de référence. En outre, les mécanismes à la source et leurs paramètres ont été étudiés en comparant les formes d'ondes, les spectres en amplitude et les rapports d'amplitude observés et synthétiques, en testant des modèles classiques de source sismique. D'autre part dans cette étude, il a été possible de contraindre le mécanisme à la source commun d'essaims d'événements microsismiques en utilisant une unique sonde 3 composantes.

La deuxième partie de la thèse a été consacrée à l'interprétation des résultats obtenus, complétés par une analyse statistique détaillée des attributs des essaims microsismiques d'un point de vue spatio- temporel et énergétique. Cette interprétation s'est appuyée également sur les autres données géophysiques et géomécaniques disponibles sur le site. Les résultats obtenus sont les suivants :

(i) les événements microsismiques sont comparables à des petits séismes tectoniques ayant un comportement auto-similaire et des magnitudes de moment variant entre -3 et 1;

(ii) l'ensemble des événements microsismiques montre un mécanisme unique en cisaillement (double-couple) au toit de la cavité, dans la couche de Dolomite et dans le recouvrement. Le mécanisme en traction, bien qu'il n'ait pas été observé dans les données, ne peut pas être totalement exclu;

(iii) cette observation contredit les modèles mécaniques qui proposent une déformation dominée par les modes en traction dans la couche de Dolomite;

(iv) le mécanisme de cisaillement est remarquablement stable et est associé à un régime en faille inverse d'orientation NO - SE, plongeant à environ 35°– 55°. Ce phénomène est probablement lié à la présence de fractures préexistantes sur le site;

(v) l'origine des essaims microsismiques est certainement due à l'incapacité du système à créer des fractures de grandes dimensions capables de libérer des contraintes très importantes. Cela est probablement lié aux propriétés mécaniques du toit de la cavité;

(vi) les périodes d'effondrements du toit de la cavité sont associées à une dynamique de forçage systématique et montrent une réponse microsismique particulière, qui peut-être décrite par des lois statistiques.

Les travaux de recherche de cette thèse confirment, que la surveillance microsismique peut être un outil puissant pour étudier les processus d'instabilité des cavités souterraines, même avec un nombre réduit de capteurs si des outils d'analyse adaptés sont utilisés. Ces résultats apportent des contributions importantes pour l'élaboration de modèles mécaniques, qui permettront l'amélioration de l'évaluation des risques d'instabilités de cavités souterraines. Les travaux à venir porteront sur des investigations détaillées des relations entre émissions microsismiques et mesures de déplacements in-situ (GPS, extensomètres et tachéomètre) incluant des observations sismologiques large bande.

Contents

List of Tables

List of Figures

Chapter 1

Introduction

Natural or man-made underground cavities, particularly when they are shallow, can provoke large-scale land subsidence and collapses accompanied by catastrophic social-economic impacts. The potential of passive microseismic monitoring to prevent such disasters is world widely discussed. Microseismic monitoring comprises the recording of seismic waves originating from small-sized (< 100 m) perturbations within an elastic medium associated with magnitudes $M \leq 2$ that usually cannot be felt. An evolving, "pone to collapse" underground cavity environment is supposed to incorporate significant local stress changes (e.g. ruptures, block falls etc.) which generate microseismic sources. Supposing these microseismic sources are quantitatively recorded and understood, it might be possible to identify hazardous mechanisms of the evolving underground cavity (precursor phenomena), which might allow for reliable collapsing risk assessment.

However, in practice the unambiguous identification of these precursors and reliable hazard assessment from recorded microseismic data are still far from being straightforward and represents a major topic in recent research and technology development. In the following, the potential and shortcomings of microseismic monitoring of hazardous underground cavities are introduced by reviewing fundamental contributions of more than 20 years of experience from the mining sector (Section 1.1). Then, recent attempts and challenges of microseismic monitoring about "prone-to-collapse" scenarios are introduced (Section 1.2) including studies on hazardous, inaccessible cavities produced from natural and man-made dissolution processes and abandoned mine workings. By the documentation of these two groups of microseismic studies it is aimed to demonstrate that monitoring conditions can considerably differ, and how these conditions can affect the ability to quantify and interpret microseismic signals. In mines, microseismicity is widely induced and correlated with mining activity, and therefore the potential locations and mechanisms of the microseismic sources are relatively well known and often accessible what significantly facilitate the design of efficient microseismic network configurations. In the studies presented in Section 1.2, the monitored hazardous phenom-

ena and governing trigger mechanisms can be generally poorly predicted in space and time so that the design of efficient network configurations, data processing and interpretation of microseismic signals are often more complicated and partially ambiguous.

In this thesis, the potential and shortcomings of the microseismic monitoring technique are evaluated as part of the experimental project Cerville-Buissoncourt, east of Nancy, France (Fig. 1.1), as presented in Section 1.3. This experiment comprised continuous (5 years) multi parameter geophysical monitoring of the evolution and final collapse of single salt cavern, created from salt solution mining. In contrast to mines, at Cerville, microseismicity is supposed to be rather indirectly induced from steady continual fresh water injection so that the monitored caving processes and associated hazardous mechanisms are probably comparable with many other natural and man-made underground cavity environments as karst cavities or inaccessible post-mining district. As a result, this specific exploitation method provide an unique opportunity to study the microseismic signatures of an continuously evolving hazardous underground cavity by means of a local microseismic network, whose results can be evaluated from other recorded geophysical parameters and geo-mechanical modeling back-analysis.

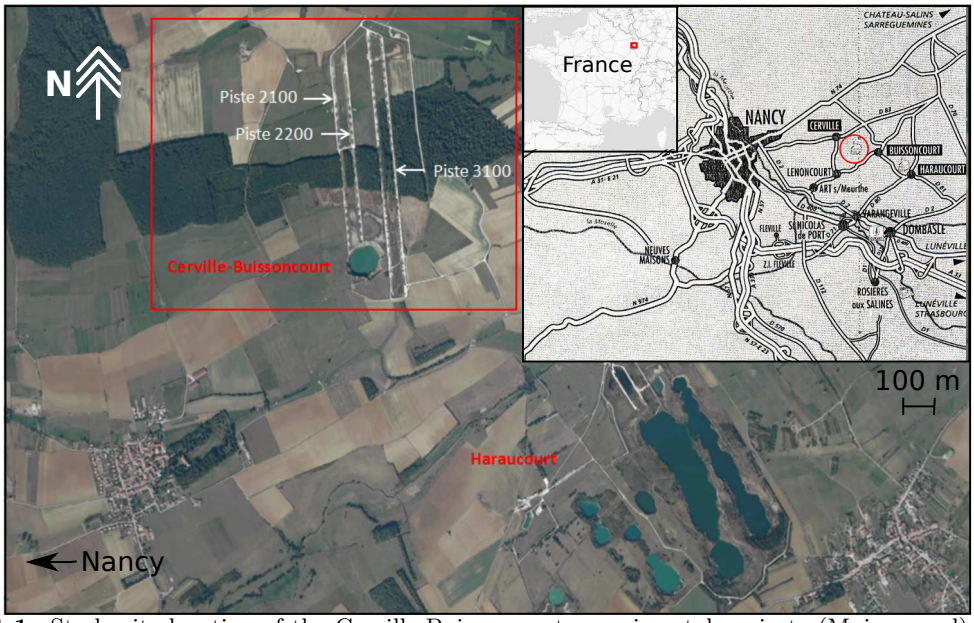

Figure 1.1: Study site location of the Cerville-Buissoncourt experimental project. (Major panel) SOLVAY solution mining site. (Right upper panels) Geographic location in France.

1.1 Routine microseismic monitoring in mines

In mines microseismic monitoring was first applied in the early sixties (Cook, 1963) and has grown to a routine tool in daily mining hazard assessment (e.g. Ge, 2005). There is a vast

quantity of scientific literature of microseismic monitoring in mines and it is beyond of this thesis to review them all here, so only major general aspects of current research in this area are presented in the following. The success of the microseismic monitoring originates from favorable conditions for this technique as provided in most mining districts:

1. Microseismicity is often strongly correlated with the ongoing mining activity what is probably the result of mining induced changes in the local stress field (e.g. newly created excavation, fluid injection) leading to readjustments of the rock mass by elastic (e.g. elastic convergence of the stope) and inelastic deformation (seismic rupture) (e.g. Boettcher et al., 2009, Cook, 1963, Gibowicz and Kijko, 1994, McGarr, 1971a,b, Spottiswoode and Milev, 1998)

2. The origin of microseismicity and the interpretation of microseismic data are often definite, since microseismic sources are often directly accessible and can be compared with geological and petrological or other geophysical in-situ measurements (e.g. Hudyma and Potvin, 2010) (Fig. 1.2).

3. Mining seismicity show similar characteristics as natural earthquakes so that data processing tools and quantitative description of the mining events can be widely adapted from global seismological research (Mendecki, 1996).

Based on these favorable conditions it is often feasible to clearly discriminate and interpret the microseismic data and to develop appropriate seismic hazard assessment strategies that significantly reduced the rate of human and economical fatalities (Gibowicz, 2009). Most of these strategies are based on the statistical analysis of the microseismic catalog where mining events are quantitatively fully described by its source location, origin time and at least two other independent source parameters (Mendecki, 1996). These statistical analysis are usually based on Gutenberg-Richter (GR) frequency-magnitude relationships (adapted from global seismology), which predict the probability that a specific value of magnitude of a seismic event will exceed during the next specific number of time units (e.g. Kijko et al., 2001, Potvin and Hudyma, 2001).

One interesting example of such efficient mining hazard assessment comprises microseismic monitoring in block or panel caving mine operations (Fig. 1.2). This mining method take advantage of the gravitational potential of a naturally fractured rock (Brady, 2004) where blasts are used to initiate caving processes arising from induced changes in the local stress

regime, stress redistribution processes and gravity cause fracturing (e.g. Simpson, 1986). In this context, microseismic monitoring is conventionally used for tracking the cave propagation and identification of abnormally fractured, or highly stressed hazardous zones in the overburden (e.g. Duplancic et al., 1999, Glazer and Hepworth, 2005, Hudyma et al., 2010, 2008). Such successful monitoring and hazard analysis is generally enabled by the installation of a comprehensive, high quality microseismic network comprising numerous stations installed in the overburden of the operation site. Thanks to these favorable monitoring conditions,

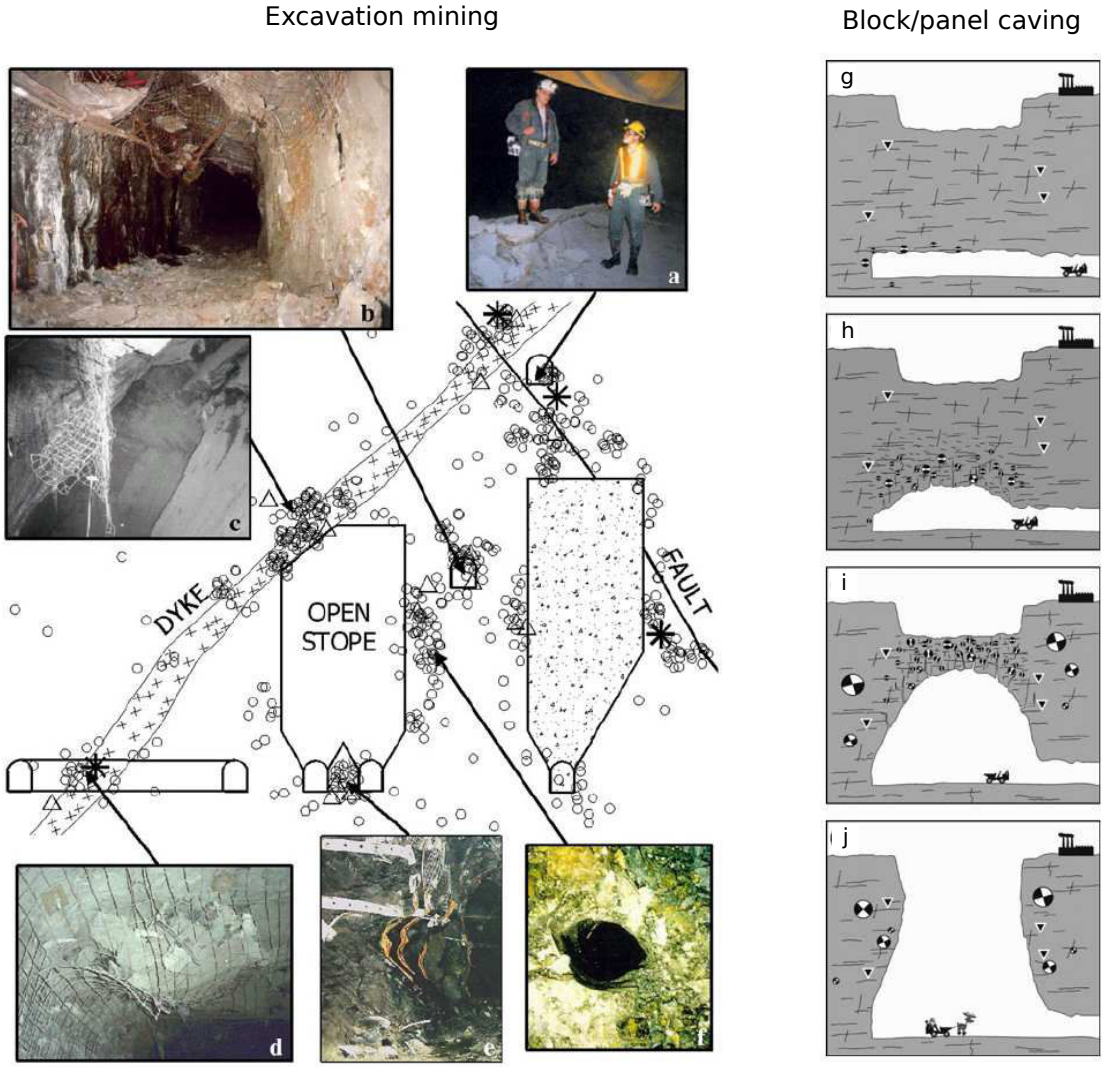

Figure 1.2: Microseismcity in mines. (left panels) (a)-(f) Example of successful microseismic event (black circles) discrimination and association with different source origins in an excavation mining environment, taken from Hudyma and Potvin (2010). (a) fault movement; (b) stress change causing rockmass fracturing near excavations; (c) stope overbreak; (d) contrast in rockmass material properties causing strain-bursting; (e) crushing of mine pillars; and (f) stress increase causing rockmass deformation. (right panels) (g)-(j) Cartoon of production and fracture evolution in the block caving Northparkes Mine, Australia, taken from Wuestefeld et al. (2011). (g) few events occur at new production tunnel; (h) tensile failure and horizontal fractures in early excavation stages; (i) tensile failure in the roof is accompanied by shear failure in the cave wall during breakthrough of the crown pillar; (j) large shear failures after production.

microseismic events can be precisely quantified in location and by their source parameters using simple traditional seismic processing methods as adapted from earthquake seismology. Based on such a high quality data set and a somewhat more advanced automatic shear wave splitting approach, it was even possible to monitor the spatio-temporal evolution of fracture orientations (Wuestefeld et al., 2010, 2011), which can provide very useful informations when analyzing the orientation and the current state of principal stresses in the overburden.

On the other hand, the seismic response and signature in mines is generally unique and depends on the quantity and geometry of mining, the mining method, geological setting, and tectonic stress field (Milev and Spottiswoode, 2002, Spottiswoode and Milev, 1998). As a result, monitoring operators from different mining districts often use different seismic hazard assessment procedures what often lead to the question of general reliability. Indeed, mining induced microseismicity show partially different behaviors compared to natural earthquakes so that universal seismic hazard procedures as developed in earthquake seismology cannot always be adapted straightforward.

One of these different behaviors is that microseismicity is often non-uniformly distributed in space and time, forms nests and swarms and partially occur in from of doublet and multiplet events (Gibowicz, 2006, Phillips et al., 1996, Riemer, 2005). Next to these particularities, a major controversy in recent research concerns the ability of appropriate source scaling of mining induced events, which is one of the major requirements for efficient and adequate hazard assessment. In this context, many studies document a breakdown in source scaling for smaller earthquakes as for examples observed from bimodal GR frequency-magnitude distributions (e.g. Gay and Ortlepp, 1979, Gibowicz and Kijko, 1994, McGarr et al., 1989, Richardson and Jordan, 2002, Spottiswoode, 1989, Syratt, 1990). These authors suggest that smaller microseismic sources in mines, often called *fracture-dominated* events, deviate significantly in their rupture process as compared to larger *friction-dominated* events (e.g. shearing on pre-existing geological structures) where stress drops are observed to be independent of the seismic event size (seismic moment M_0) (self-similarity, e.g. Aki and Richards, 2002, Scholz, 2002). In contrast, other studies found evidence that the GR-frequency-magnitude distribution holds even for nanoseismic and picoseismic mining induced events ($M \sim -4$ to 0) (Kwiatek et al., 2011, Plenkers et al., 2010). In these studies, apparent deviations from self-similar scaling are not suggested in different source characteristics, but in the presence of blasting in the data, limitations of the instrumental recording bandwidth, and detection ca-

pability of the recording system and from wave propagation effects (e.g. Boettcher et al., 2009, Collins and Young, 2000, Ide et al., 2003, Ortlepp et al., 2005, Oye et al., 2005). For a further review of studies concerning the characteristics of microseismic sources in mines see Section 3.1.

1.2 Challenges and achievements of microseismic monitoring of inaccessible underground cavities

A world wide topic in geohazard research concerns cavity environments formed by karstic or evaporitic dissolution processes which comprise a considerable hazard to produce large scale subsidence and sinkhole phenomena (e.g. Waltham et al., 2005), which can be of natural (e.g. Arkin and Gilat, 2000, Caramanna et al., 2008, Gutierrez et al., 2008, Johnson, 2005, Wachs et al., 2000) or man-made origin as commonly observed in former or active evaporite or carbonate mines (for a review see Whyatt and Varley, 2008), during salt solution mining and salt withdrawal operations (e.g. Barla et al., 1991, Ege, 1984, Mancini et al., 2009, Raucoules et al., 2003, Zamfirescu et al., 2003), as well as in artificial channel constructions (e.g. Fidelibus et al., 2011). These often catastrophic events are generally preceded by a progressively upward growing underground cavity structure, which then partially or totally collapse depending on the strength limit of the overlying rocks (Fig. 1.3a). The upward growth of the cavity is generally associated with a wide range of possible mechanisms that strongly depend on the geological setting and geochemical compositions, so that rates of cavity growth and subsidence vary significantly at each study site.

In this context, microseismic monitoring might be an attractive tool in order to detect different evolution stages of the growing cavity structure which might be interpreted in terms of collapsing hazard. Indeed, a few studies reported precursor phenomena in form of microseismic crisis before sinkhole formations (Land, 2009, Malovichko et al., 2009, Neunhofer, 1997). However, with exception of these studies, the potential of microseismic monitoring as a routine hazard assessment tool is still not sufficiently well evaluated and require further experience. It is still not well known which of the accompanying caving processes are visible or invisible for a microseismic monitoring system. Microseismic sources generated by upward migrating cavity structures are generally expected to be rather small and only detectable at rather short recording distances. In addition, some of the governing deformation processes are probably aseismic nature, especially when the cavity is progressing through unconsolidated

soils at lower depths associated with very weak elastic strengths.

In a theoretical and experimental study Malovichko et al. (2010) stated that microseismic emissions can be expected from larger rock detachment processes at the cavity roof and block falls on the cavity bottom. In their results, the authors further showed that microseismic recording and discrimination of these mechanisms is generally feasible also when accounting for significant contributions of stationary background noise. Indeed, the feasibility of measuring microseismicity apparently originating from roof fracturing, block falls, and dissolution processes in karst and evaporite environments was already demonstrated by some few studies that used standard monitoring tools (Balland et al., 2009, Dahm et al., 2011, Hardy et al., 1986, Malovichko et al., 2009). In addition, the study of Wust-Bloch and Joswig (2006) provides a good example of demonstrating the fact that the design of innovative networks, as small seismic array groups, and newly adapted processing tools can significantly help to achieve reliable recordings of pre-collapsing evolution stages of a cavity system situated in unconsolidated media. Thanks to these innovative tools and calibration experiments in the field, the authors were able to detect, locate and discriminate microseismic signals associated with different types of block falls in salt karst cavities the Dead Sea region (Fig. 1.3b).

Some more monitoring experience of dissolution and caving processes was gained during active salt solution mining operations. Microseismic monitoring was already found to be an efficient tool in cases, where the dissolution processes and the formation of solution cavities was more difficult to predict, baring the risk of ground water contamination and subsidence phenomena (Bergery and Nayman, 2007, Guarisco, 1987, Maisons et al., 1997). For this respect, generally standard detection and location procedures were applied. Interestingly, at the Arkema-Vauvert salt field, Godano et al. (2009) demonstrated that from the usage of a sparse number of three component deeper bore hole stations they were able to retrieve reliable fault plane solutions (see also Section 3.1).

Another interesting microseismic data set was recorded during down shutting of the Ocnele Mari salt solution mine in Romania. In this study, similar to Cerville-Buissoncourt, a controlled collapse was initiated by brine pumping and sterile backfilling operations of the salt caverns in order to eliminate the collapsing hazard, threatening a near densely inhabited area (e.g. Zamfirescu et al., 2003). As the concerned collapsing area was relatively well known, an efficient microseismic monitoring network was installed beforehand to survey these operations (Trifu and Shumila, 2010). By subsequent evaluation of the obtained microseismic

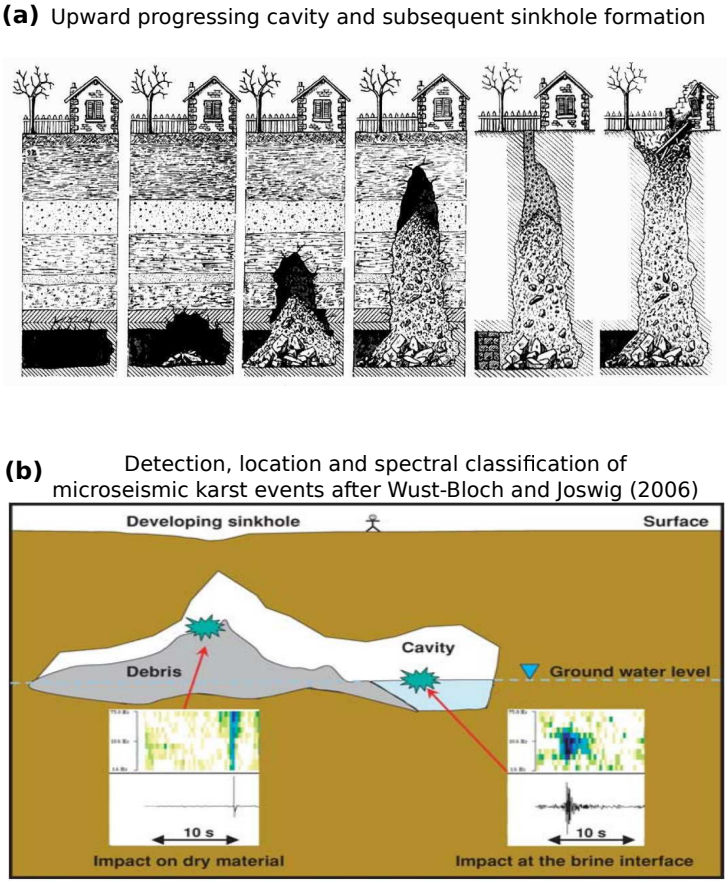

Figure 1.3: Caving processes. (a) Simplified illustration of an upward growing cavity into the overburden. (b) Qualitative spectral classification of seismic signal originating from karst processes, taken from Wust-Bloch and Joswig (2006).

data (2,392 detected events) it was stated that the results from conventional microseismic monitoring and data analysis consistently reflected the expected trends in a collapsing salt mine environment. Accordingly, the spatial distribution of estimated source mechanisms, and deformation rates showed very characteristic pattern of a typical sinkhole formation (see also Section 3.1). Furthermore, the authors outlooked that further analysis with respect to the temporal contribution might allow to detect the initiation of the expected collapsing processes which could allow for better control of the present engineering activities.

Beside these rather encouraging monitoring examples, Branston (2003) reported significant challenges of local microseismic monitoring during salt solution operations of salt cavities in the United Kingdom. By using high frequency instruments, and short recording distances, the author documented the presence of unusually strong swarming activities what caused significant problems in standard processing steps as detection and location. Similar observations of such intensive microseismic swarming sequences were also reported from salt solution min-

ing operations in Italy (Emmanuelle Nayman, pers. communication). In addition, Branston (2003) stated that also rather more simple, isolated microseismic events showed signatures that significantly differ to usual seismograms of natural earthquakes what impeded the application conventional data processing tools. For instance, body wave phases as usually used for location were apparently affected by stronger attenuation effects induced by the brine filled cavity structure. In this respect, P wave onsets were often observed to be emergent and S wave even partially absent.

Such shortcomings in local microseismic recording are widely observed in monitoring studies of dangerous rock slopes where often only a minor portion of the entire microseismic dataset can be successfully treated using routine analysis tools (e.g. Lévy et al., 2010, Mertl and Brückl, 2007, Spillmann et al., 2007). General problems of accurate body wave phase picking are related to high attenuation effects, partial lack of S wave phases due to unusual source characteristics or near-field effects, P to S wave conversions associated with strong velocity contrasts, emergent P wave onsets, and precursory signals ahead of impulsive P waves. Next to these particularities, also intensive swarming sequences, called "multiple events" (Mertl and Brückl, 2007, Spillmann et al., 2007), are frequently observed where P wave onsets are often covered by the coda of the preceding events.

1.3 The Cerville-Buissoncourt project

Recently, research started to focus on the survey of post-mining districts that represent risks to near inhabited areas, using of microseismic monitoring. Research and experience in this respect was gained among others in the United States (Miller et al., 1988, 1989, Richards and Miller, 1988), Japan (Ogasawara et al., 2002a,b), Korea (Waltham et al., 2011), United Kingdom (Toon and Styles, 2004) but mainly in France (Bigarré et al., 2011, Contrucci et al., 2010, Couffm and Bigarré, 2003, Didier, 2008, Senfaute et al., 2000, 2008). In France, investigations in risk and hazard assessment of active and closed mining districts have been intensified since the 90's, when these areas attract attention by causing ground failures and subsidence with fatal social consequences as building damages or catastrophic changes in the ground water constitution. Several of these catastrophic events occurred in the iron-ore basin in the Lorraine region, France, where decades of intensive excavation mining activity have been stopped and left old vast underground rooms and pillars beneath urban areas (e.g. Deck, 2002, Didier, 2008). The origin of these significant surface subsidence and

collapse events are generally related to a progressive rise of the ground water level into the abandoned excavated zones since water pumping was stopped with mine closure as well as to the failure of residual abandoned underground pillars.

In order to prevent these disasters, the French government initiated a post-mining risk management including in-situ monitoring in urban regions based on geodetic and microseismic networks. The efficiency of these monitoring networks for hazard assessment is generally characterized by its detection capacity of dangerous failure mechanisms as well as its identification. Current research aims continuously to improve this efficiency by studying the governing failure mechanisms and dynamics and its microseismic and geodetic signature in more detail (e.g. Didier et al., 2003). As an example, some of the governing failure mechanisms seem to be associated with aseismic deformation processes as it was observed above an abandoned mine in the town of Angevillers, NE France. A longer period of slow subsidence was detected by local geodetic measurements meanwhile no significant increase in the microseismic rate was observed (Isabelle Contrucci, pers. communication). Thus, in terms of efficient microseismic monitoring a better understanding of the recorded microseismic data is indispensable, what might be achieved by gaining more experience in its analysis and interpretation in similar environments.

In this context, microseismic and other geophysical monitoring tools were applied to a salt cavity that was created by salt dissolution mining (a SOLVAY exploitation) as part of a large multi-parameter research project founded by the research "group for the impact and safety of underground works" (GISOS, `http://gisos.ensg.inpl-nancy.fr/gisos-info-en/gisos-info-en/`) at Cerville-Buissoncourt in Lorraine, France (Cao, 2011, Contrucci et al., 2011, Daupley et al., 2010, Klein et al., 2008, Lebert et al., 2011, Mercerat, 2007, Mercerat et al., 2010) (Fig. 1.1 and 1.4). The continuous growth of the cavity was monitored from 2004 until 2009, when the cavity reached its critical size and a "controlled" collapse was initiated by brine pumping. This experimental project provides a unique opportunity to evaluate the potential of microseismic monitoring and mechanical models with respect to a growing and collapsing cavity system in a salt solution mining environment (e.g. Daupley et al., 2005), as well as similar "prone to collapse" scenarios (Section 1.2).

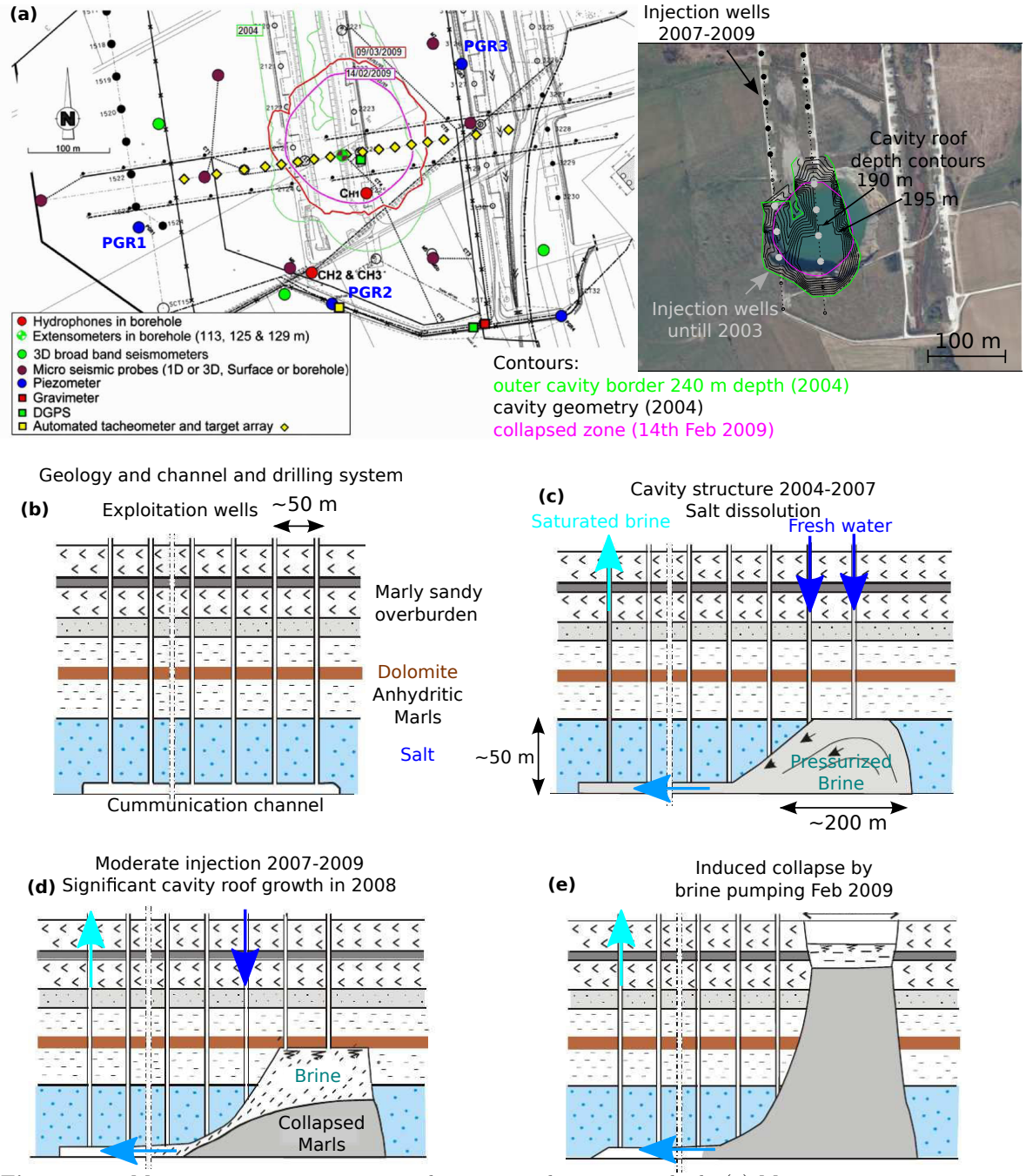

Figure 1.4: Monitoring instrumentation and mining exploitation method. (a) Monitoring instrumentation and surface and underground extensions of the solution mined cavity structure, taken from Lebert et al. (2011). (b) Simplified illustration of local geology, the "channel and dilling" technique and different evolution mining stages (c-f).

1.3.1 Geological, mechanical setting and cavity structure

At Cerville-Buissoncourt, the geology is formed by the Triassic salt formation (Mégnien, 1980), constituted of a sub-horizontal layered sub-marine sequences: a marly-sandy layer (0 to 119 m depth), a thin but competent (stiff) Dolomite layer known as the Beaumont

Dolomite (119 to 127.5 m depth), a poorly-consolidated layer of anhydritic Marls (127.5 to 183.5 m depth), and the salt deposit which reaches its final depth at 348 m (Fig. 1.4).

During 1997–2003, mining was initiated using the channel and drilling technique where water was injected via two parallel, aligned well casings into the base of the salt deposit what caused significant dissolution processes that formed a cavity structure. In the beginning of monitoring in 2004, the cavity was located at a depth of around 250 m, within the salt layer. Its geometry was initially evaluated using sonar measurements obtained by SOLVAY (2004), revealing 150 – 200 m of lateral extensions and a maximum cavity height of around 50 m (Fig. 1.4). The shape of the cavity structure is rather asymmetric with smaller vertical extensions to the west and the highest extensions to the east.

By means of mechanical numeric modeling, it could be shown that the mechanical stability of the cavity and the overburden is mainly controlled by the elastic strength of the Dolomite layer (Daupley et al., 2005, 2013, Mercerat, 2007) (Fig. 1.4). This Dolomite layer is generally more stiff and competent compared to other stratigraphic units in the study area and generally enables the creation of larger underground cavity formations. Mercerat (2007) found critical value of maximal flexure (< 10 cm) for this layer that when overcome, would lead to its complete failure and a subsequent collapse of the overburden. In addition, the cavity is further stabilized by the pressurized brine, inducing a significant pressure on the cavity walls and on the overburden (~ 2.0 MPa) (Mercerat, 2007).

1.3.2 Local monitoring systems

From 2005 to 2009 the evolution and final cavern collapse was monitored by a SYTGEM multi-parameter system (Klein et al., 2008) including a high-resolution microseismic network linked to a surface displacement measurement system (Fig. 1.4 and 1.5). Since March 2005, the microseismic network constituted three one component, plus two installed in 2008 (station 7 and 8; Fig. 1.5), and four 3-component 40 Hz geophones (GS-20DH, Geospace). The geophone's frequency response is flat and clean up to 400 Hz, and declines towards lower frequencies below 40 Hz. Geophones were cemented into boreholes and equally distributed around the solution cavern where three geophones were installed in a single vertical bore hole directly at the center above the cavern.

Due to the considerable number of channels and the high sampling frequency, the acquisition system operated in a triggering mode adjusted to the static background noise level. Two data

sets, one consisting of triggered event files (1 s length and 10 kHz sampling before 12 February 2008 and 1.5 s and 5 kHz after 12 February 2008), and one consisting of continuous data with 200 Hz sampling was recorded in February 2009. In this thesis, temporally overlapping triggered event files were merged. In addition, later in summer 2008, three Guralp CMG40-TD broadband seismometer (0.016 to 50 Hz frequency band, 100 Hz sampling rate) have been installed in 1 m deep holes (Jousset and Rohmer, 2012).

A surface displacement monitoring system was installed in 2008 (Klein et al., 2008) (Fig. 1.4). The system constituted a high resolution infra-red tacheometer (±5 mm, vertical and horizontal) associated with a recording line (17 targets) across the expected collapse area and a high resolution GPS-Real Time Kinematic (RTK) instrument (1 measurement/second ; ±5 mm) to precisely monitor subsidence.

Deformation measurements at deeper levels were provided by a set of three extensometers installed in the same drill hole as microseismic station 62 and 63 which were placed above (113 m), inside (125 m), and below (129 m) the Dolomite layer (Fig. 1.4 and 1.5). In addition, also one gravimeter (15 s sampling rate), and hydro-mechanical measurements were obtained by means of three hydrophones (30 Hz to 3 kHz, 3 to 30 kHz, and 30 to 180 kHz frequency bands), and piezometers placed in the Rhaetian aquifer inside a sandstone at 60 m depth (Fig. 1.4).

1.3.3 Monitoring data and different cavity evolution and mining stages

The different mining and cavity evolution stages and the associated monitoring data is briefly introduced in the following sections. For a more detailed review of the entire project history, see Cao (2011).

The project history can be generally classified into three different periods. The first period of the project comprised a pressure transient experiment in 2005 and 2007 by partially lowering the brine in the cavity which was widely analyzed and modeled by Mercerat (2007). The second period comprised a major microseismic crisis recorded in 2008 where simultaneously a significant vertical growth of the cavity roof was monitored (Fig. 1.6 and 1.7). The third period comprised the major microseismic crisis in 2009 associated with the controlled cavity collapse (Fig. 1.6 and 1.8).

For the two latter major crises a total data set of around 50,000 triggered event files was recorded while for the first project period only a minor amount of microseismicity was

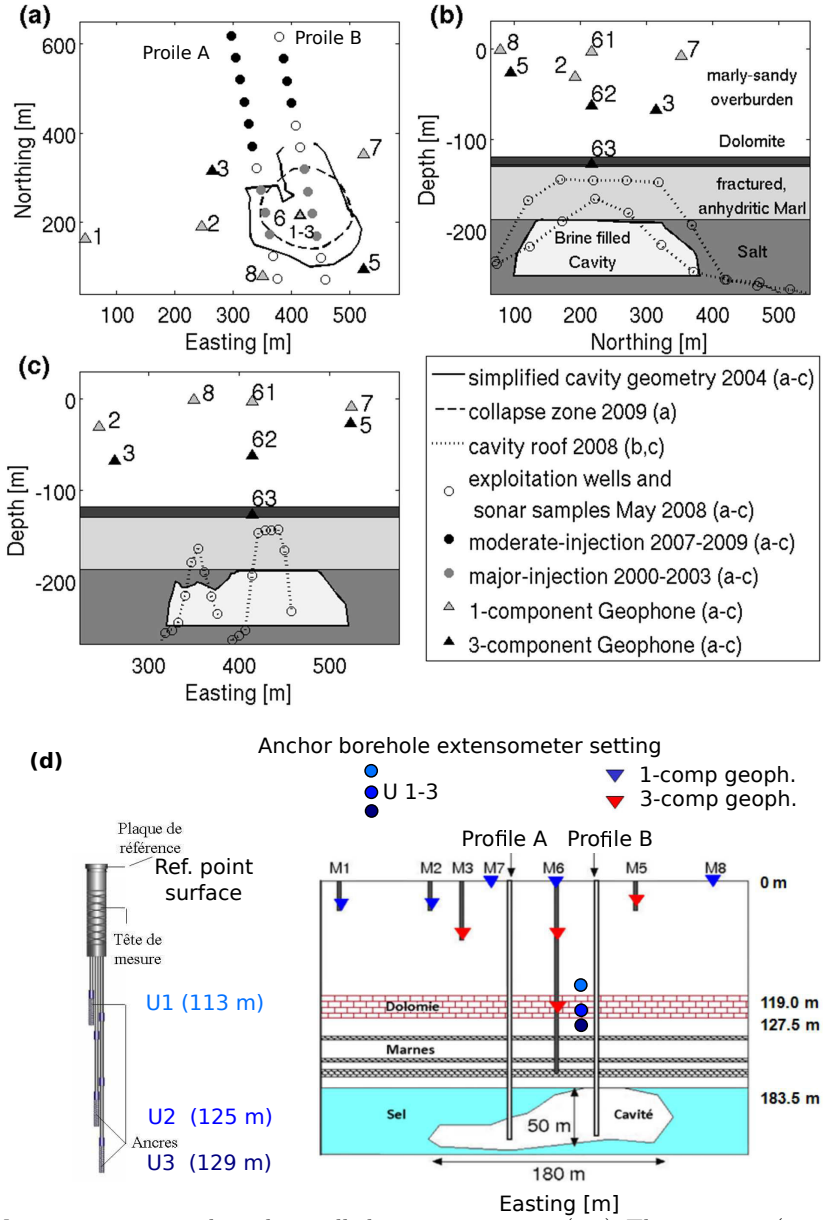

Figure 1.5: Microseismic network and installed extensometers. (a-c) The stations (triangles, named by numbers) of the microseismic network, cavity structure, and the major geologic layers. The border of the collapsed cavity area (dashed circle) in 2009 (a) is taken from Lebert et al. (2011). Northing and easting are given in meters relative to a reference point X = 892900 m and Y= 116000 m defined by the Lambert 1 Nord (NTF, Paris) coordinate system. (b,c) Sonar measurements (small circles) demonstrate the extension of the cavity roof (dotted lines) after the microseismic crisis in 2008, compared to the initial cavity roof extension in 2004 (thick black continuous lines). (d) Image of the used anchor borehole extensometer instrument type (left panel) and the illustration of the three anchor points fixed above, within and below the Dolomite layer measuring the displacement U relative to a reference point at the surface (right panel).

recorded. This thesis generally focused only on the last two periods in 2008 and 2009, when the monitoring network installation was completed. If interested in the first project period the reader is mainly referred to the study of Mercerat (2007), and Mercerat et al. (2010).

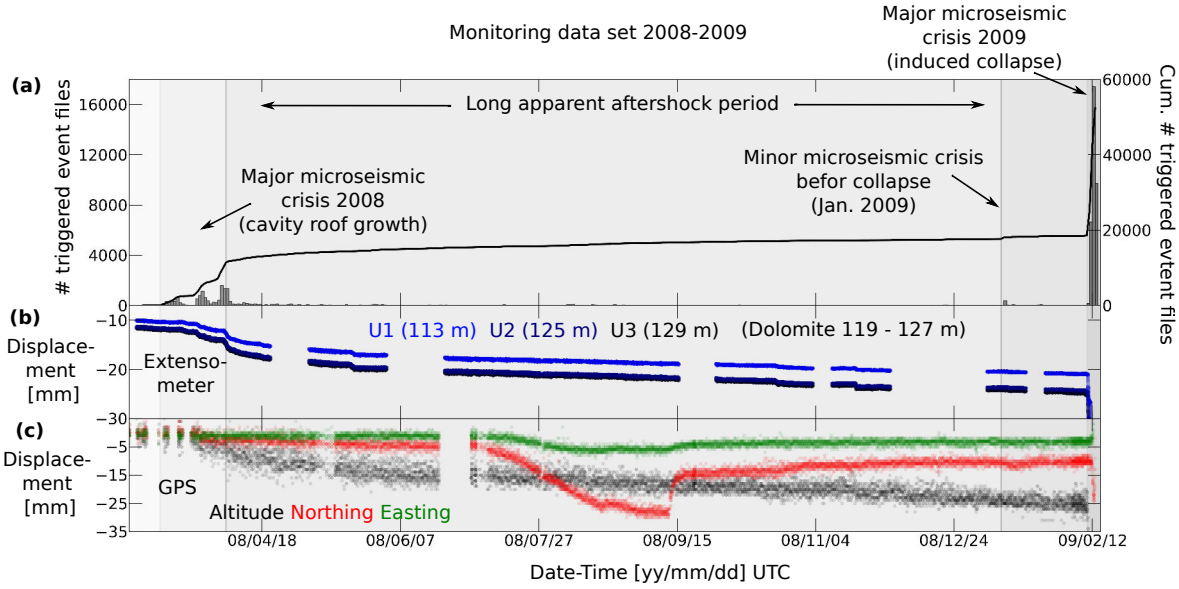

Figure 1.6: Monitored data in the period February 2008 to February 2009. (a) Number and cumulative number of recorded triggered event files. (b) Displacement recordings U of the anchors of the borehole extensometer installed above (U_1), inside (U_2), and below (U_3) the Dolomite layer (e.g. Fig. 1.4 and 1.5). (c) Data of one GPS station placed above the center bore hole close to microseismic station 61 (Fig. 1.4). Negative displacement values in altitude (black points) indicate downward soil movements (subsidence).

1.3.3.1 Microseismic crisis 2008 (cavity roof growth)

After solution mining was placed in a standby mode from 2004 to 2007 (Mercerat, 2007, Mercerat et al., 2010), it was resumed in June 2007 by moderate water injections at well cases located $200 - 300$ m further north of the cavity structure (Fig. 1.4 and 1.5). In the following period, between March and May 2008, a significant vertical development of the cavity height, of about 50 m, was recorded by periodic sonar measurements obtained along two profiles A and B (Fig. 1.5 and 1.7). This cavity growth was mainly associated with the caving processes and failures of the anhydrite Marl layer at the cavity roof located below the Dolomite layer (e.g. Fig. 1.4), striking an estimated volume of $\sim 500,000$ m^3 of material (Klein et al., 2008).

The ~ 50 m heightening of the cavity roof in 2008 was accompanied by a clear cascade-like increase in the seismic activity of around $6,000$ event files recorded in March, $7,000$ files recorded in April, and around $1,000$ files recorded in May (Fig. 1.7) (Klein et al., 2008). The microseismic activity can be classified into three major periods with apparent continuously increasing microseismic activity while the third period can be interpreted as a mainshock as associated with two major seismic activity peaks on the 3rd and 4th of April 2008, at 9 p.m. and 8 a.m., respectively, which are then followed by an apparent aftershock sequence (Fig.

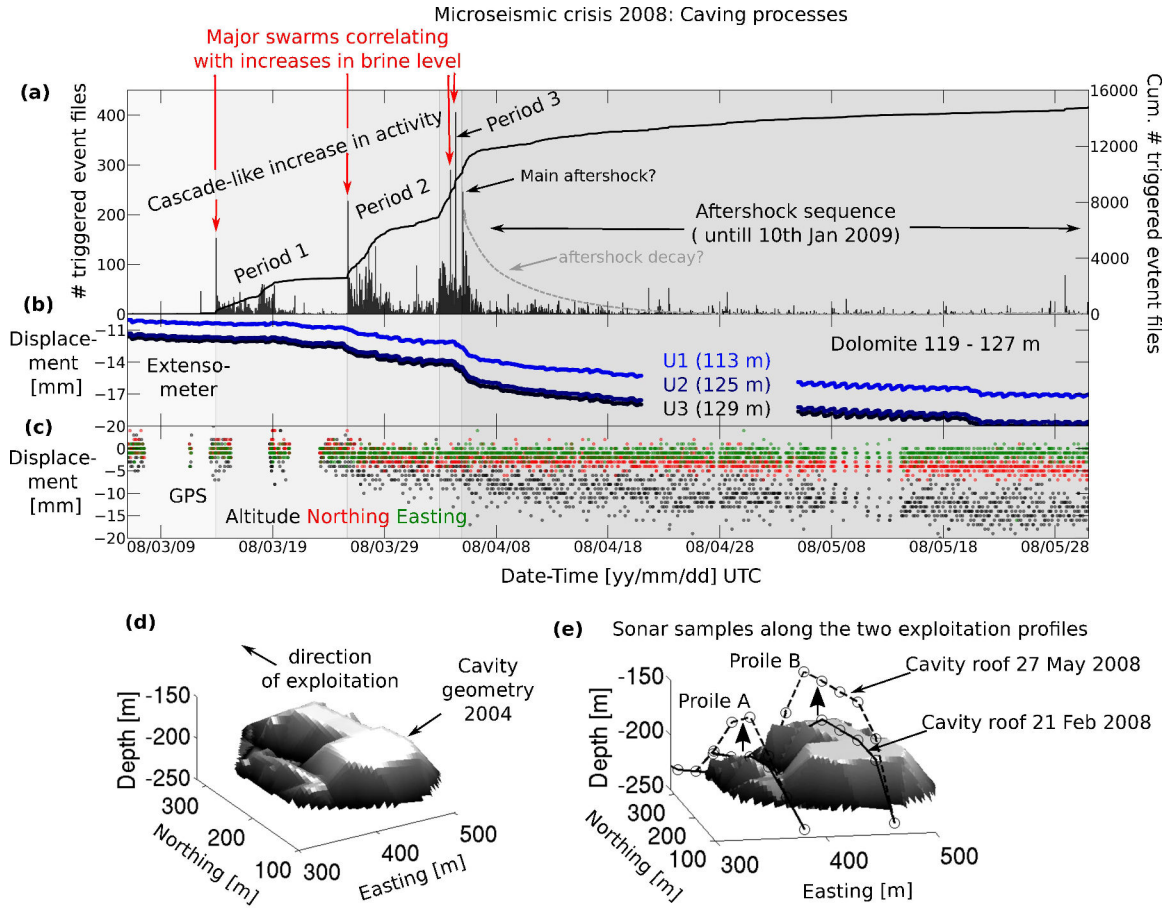

Figure 1.7: Monitored data in the period March to May 2008. (a)-(c) For data description see caption of Figure 1.6. (d)-(e) Vertical cavity roof growth (max. ~ 50) observed from periodic sonar measurement along the exploitation profiles A and B (e.g. Fig. 1.4 and 1.5).

1.6 and 1.7).

It is very interesting to note that almost each major peak of apparent activity in each period correlated with a simultaneous increase in the brine level observed at the exploitation wells which are without any doubt related to massive block falls into the cavity. From this observation it can be generally concluded that microseismicity has a clear relation to the governing caving processes.

In addition, also small magnitudes of surface subsidence (in the order of 1 cm) could be observed from the GPS curve, which become more important after the microseismic crisis (Fig. 1.6 and 1.7) (Klein et al., 2008). This observation already indicate that some deformation mechanisms in the overburden seem to be rather aseismic or dominated by lower frequencies, as not resolvable form the high frequency geophones. Contrastingly, smaller extensive deformation rates could be observed from the extensometer data (in the order of 1 cm) that seem to be roughly correlated with microseismic activity (Cao, 2011). This observation fur-

ther confirmed the idea that microseismicity is mainly related to failure processes at the cavity roof (Cao, 2011, Contrucci et al., 2011) which is followed by an elastic response of the Dolomite layer (possibly elastic flexure) which was consistently observed and modeled during the transient pressure experiments in 2005 and 2007 (Mercerat, 2007).

1.3.3.2 Microseismic crisis 2009 (induced cavity collapse)

In February 2009 the cavern reached its critical size which risked to provoke a gravity collapse from the load of the overburden so that finally the cavern collapse was induced by progressively lowering the brine level (Fig. 1.8). Before brine pumping started, a minor microseismic crisis was recorded in January 2009 (Fig. 1.6). When brine pumping was initiated (10th February 2009 at 06:00 a.m.), more than 30.000 triggered event files were recorded during three days before the final occurrence of the surface collapse (13th of February) (Fig. 1.8). From the number of triggered event files, three major peaks in microseismic activity could be observed starting the 11th of February after the second pumping stage (11th February 2009 at 04:00 a.m.) (Contrucci et al., 2011). These three major episodes are also associated with clear increases in the subsidence rate with up to several meters per day (Fig. 1.8).

The first major peak of microseismic activity is considered to be due to massive marly cavern roof falls from below the Dolomite layer (Contrucci et al., 2011). In addition, this first peak in apparent microseismic activity was consistently observed from broadband records by Jousset and Rohmer (2012) and was interpreted to be triggered by Rayleigh wave trains generated from a distant large earthquake ($M \sim 7$) in Indonesia. The most important factor in the causation of the induced collapse in February 2009 is seen in the failure of the Dolomite layer (Contrucci et al., 2011, Jousset and Rohmer, 2012). Its failure is probably associated with the second and highest peak in microseismic activity observed during the collapse initiation (Fig. 1.8). Correspondingly, loud acoustic noises could be heard on the study site, which were followed by significant acceleration in the subsidence rate (e.g. GPS data Fig. 1.8), the breakdown of station 63, and a successive breakdown of the extensometer stations (Fig. 1.8). The third peak in microseismic activity, is marked by highest acceleration in the subsidence rate and represents the final ground surface collapse leaving a circular crater with a diamter of ≤ 150 m (Fig. 1.4).

As a general interpretation of the entire microseismic data set it was concluded that microseismicity before the collapsing stage in $2005, 2007, 2008$ and 2009 is related to rock falls, debris

flows, and dropped rocks from the cavern roof below the competent Dolomite layer (e.g. Cao, 2011, Contrucci et al., 2011, Klein et al., 2008, Mercerat et al., 2010). Data analysis of the collapsing period in 2009, somewhat surprisingly, did not indicate significant changes in the microseismic data characteristics and no precursor pattern could be identified (Cao, 2011, Contrucci et al., 2011). Most significant changes in the microseismic regime are mainly seen in the increasing amounts of cumulative energy, event number and partial rapid increases of the dominant frequency in the seismograms. However, such pattern have been also observed in microseismic crisis before the collapse period (Cao, 2011, Mercerat et al., 2010). This observation is in contradiction with local mechanical models (Daupley et al., 2005, Mercerat, 2007), stating that the deformation and failure of the competent Dolomite layer should be clearly associated with brittle ruptures, and therefore significantly differ from deformation mechanisms expected in the less consolidated, fractures marls layers at the cavity roof.

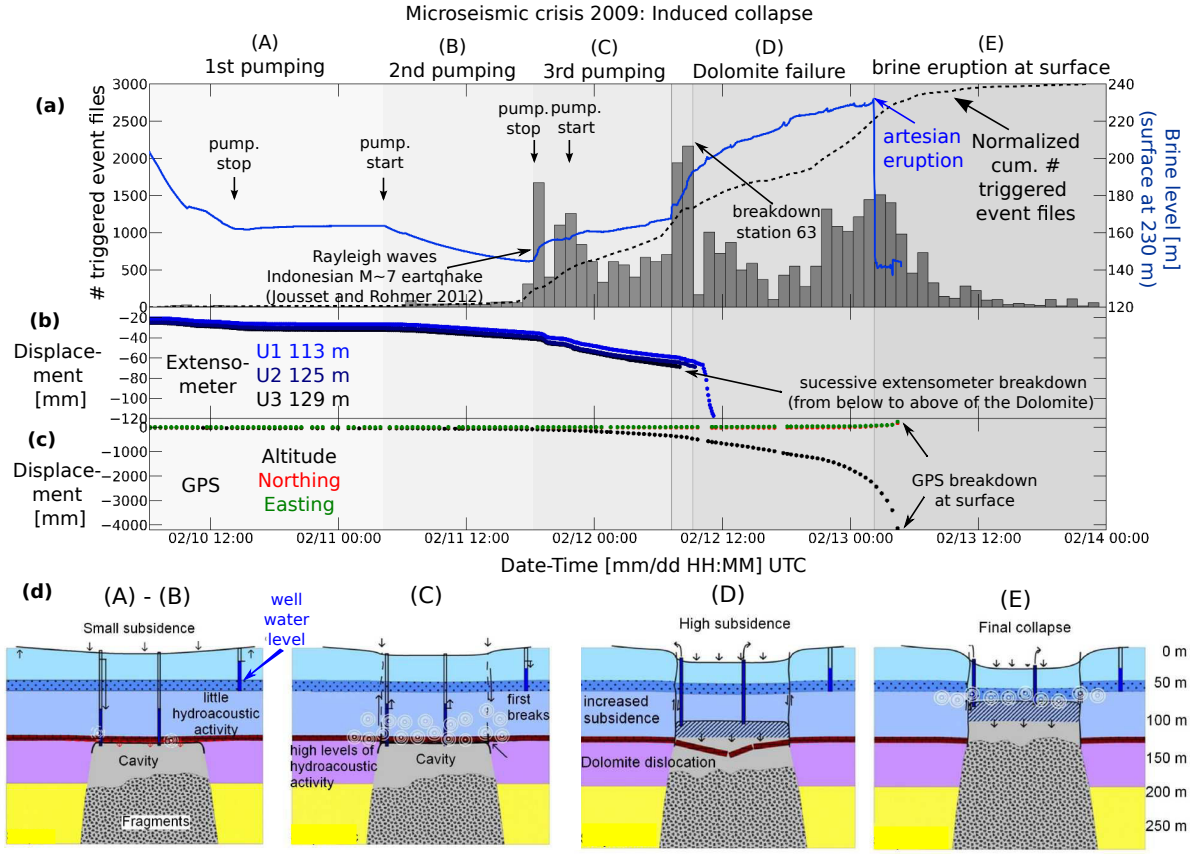

Figure 1.8: Monitored data in the period 10th to 13th February 2009. (a)-(c) For data description see caption of Figure 1.6. (a) the cumulative number of triggered event files is normalized (dashed line), while the brine level (blue line) is shown on the right Y axis. (d) simplified block model showing the different evolution stages of the induced collapse in February 2009, taken and modified from Daupley et al. (2010) and Lebert et al. (2011).

1.3.4 Challenges in analysis and interpretation of microseismicity

Initial analysis of the microseismic data set implied various applications of body wave phase-based detection and location routine tools as they are commonly used in mining and global seismology (Cao, 2011, Contrucci et al., 2011, Klein et al., 2008, Mercerat, 2007, Mercerat et al., 2010). Among others, these analyses comprised automatic P-wave phase picking approaches based on the STA/LTA technique by Allen (1982). In addition, several 1-D and also 3-D velocity models were developed to improve event location by means of calibration shots (Cao, 2011, Contrucci et al., 2011, Mercerat, 2007, Mercerat et al., 2010) , active seismic tomography (Kosecki et al., 2010, Piwakowski et al., 2006, Suffert, 2006), as well as constraints from other geophysical parameters (Coccia et al., 2013). For hypocenter determination, in all studies a probabilistic maximum likelihood inversion approach was applied (Tarantola and Valette, 1982) by considering misfits ($l2$-norm but also the EDT-norm (Pinsky et al., 2008)) between observed and synthetic body wave arrival times (mostly P waves) and optionally of their polarization angles (Contrucci et al., 2010) that were minimized by means of the Oct-Tree nonlinear location method (Lomax and Curtis, 2001).

However, similarly to the study of Branston (2003) (Section 1.2), only a minor portion of the entire microseismic dataset, approximatively 20%, could be successfully treated using these analysis tools. One major problem in this respect is the dominance of unusual swarming sequences (Fig. 1.9) which are alike to "multiple events" as observed in rock slope studies (Mertl and Brückl, 2007, Spillmann et al., 2007). These microseismic swarms are formed by dense and complex event clusters, where P wave onsets are often covered by the coda of the preceding events what impede the application of automatic body wave phase based detection and location tools. Next to microseismic swarming, also problematic event signatures, propagation effects (attenuation, refraction) and local monitoring conditions strongly hinder efficient automatic data processing which I will present and discuss in the following Sections 1.3.4.1 and 1.3.4.2, respectively. Therein, the discussion is generally based on basic spectro-temporal microseismic signal observations, partially located microseismic data sets (Cao, 2011) and synthetic seismogram calculations.

1.3.4.1 Characteristics and classification of microseismic events

Regardless of the considered periods of microseismic activity (Section 1.3.3), swarming sequences represent around 80% of the recorded data with durations of the order of 5–200 s

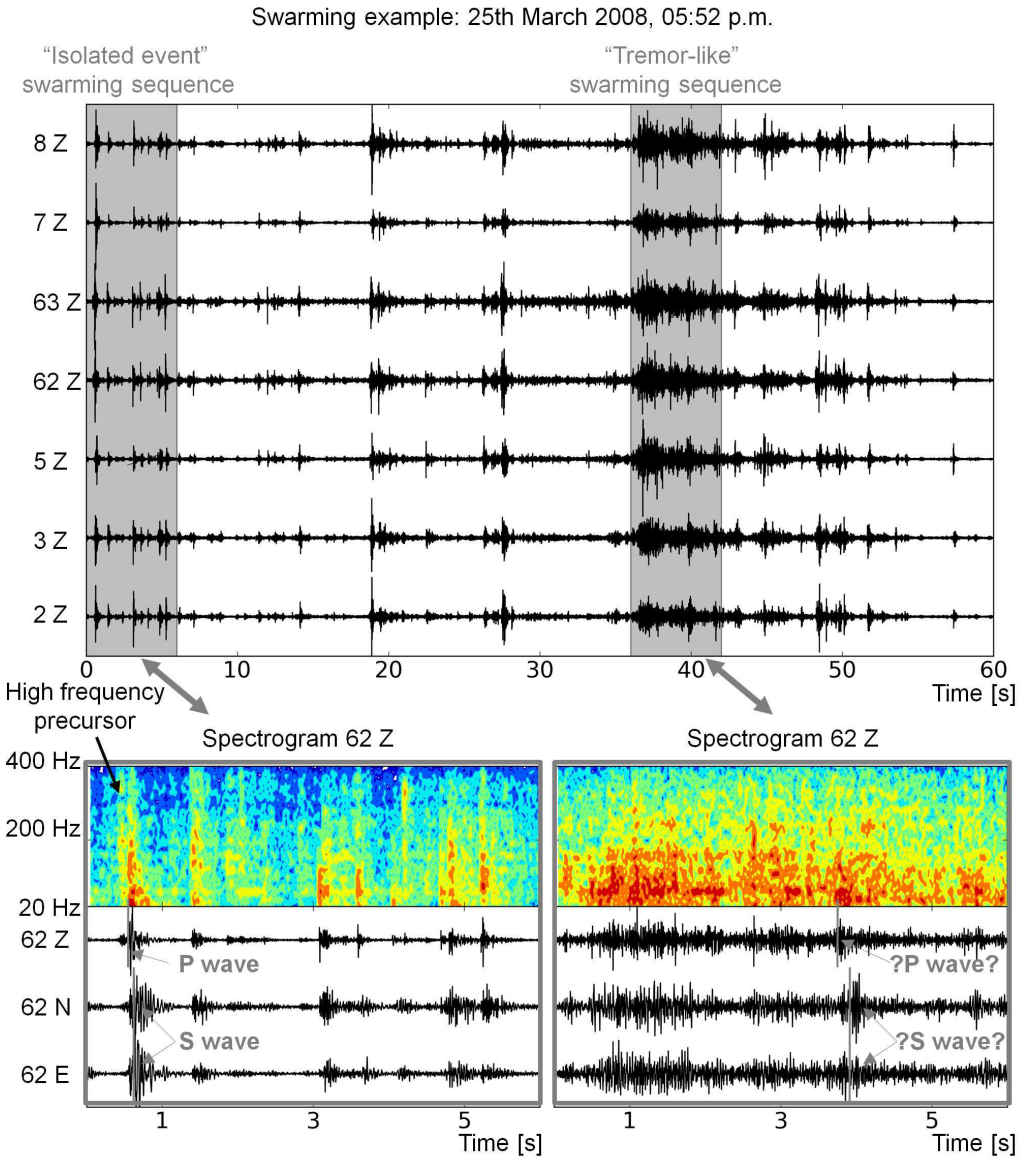

Figure 1.9: Microseismic swarm example. Example of a typical swarming sequence recorded during the microseismic crisis of 2008. (Upper panel) Seismogram traces for the Z components and examples of isolated event and tremor-like swarming sequences (gray shaded areas). Spectrograms and the 3-component traces of station 62 corresponding to the isolated event (left lower panel) and tremor-like sequence (right lower panel). Spectrograms were calculated using a 0.15 s window length with 90% overlap, while intensities are presented in a normalized dB scale for seven distinct contour levels (colored scale).

(Cao, 2011, Contrucci et al., 2011, Mercerat, 2007, Mercerat et al., 2010). Generally, two types of swarming sequences can be classified from visual inspection (Fig. 1.9): (i) a concatenation of distinguishable single events, which are hereafter called "isolated events", and (ii) partly interlaced seismic events, which are called "tremor-like" events due to their formal resemblance to spasmodic tremors commonly observed in volcanic environments (e.g. McNutt, 1992). The isolated events generally last $\lesssim 0.5$ s (Fig. 1.9) and also occur apart

from any swarming sequence. Tremor-like swarming sequences are distinguished by their quasi-continuous signals, in such a way that an event appears before the return to the background level of the previous event's coda. Tremor like swarming sequences seem to generally coincide with the peaks of major swarming activity and simultaneous brine level increases (Fig. 1.7), and therefore might be generally associated with major cavity roof failures in the pre-collapsing stage (2005-2008) (Cao, 2011, Mercerat, 2007).

However, even though to some apparent differences in the temporal occurrence of both event types, this classification is by far not straightforward when comparing the spectral content of both event types, showing a similar frequency range of $20 - 200$ Hz (Fig. 1.9). In addition, body wave phases of P and S waves seem to be generally present for both event types, even though more difficult to interpret and identify for tremor-like events. Also from standard source spectrum analysis (Brune, 1970), Mercerat et al. (2010) found no differences in terms of source dimension ($M_W - 2$ to 0) and stress drop between both event types.

Consequently, it might be generally possible to consider a tremor-like event sequences as a concatenation of isolated events (Cao, 2011, Mercerat, 2007). Accordingly, typical concatenation behavior could be observed for most of the manually inspected isolated events ($\sim 80\%$) which are commonly accompanied by precursor (Fig. 1.9 and 1.10), doublets, and multiplets phenomena (Fig. 1.10). Another concatenation behavior is suggested in a distinct event group of "cigar-shaped" isolated events which are characterized by typical emergent P wave onsets (Fig. 1.11). These events show generally a very similar signature as compared to tremor-like event types, and are associated with somewhat longer durations (up to several seconds), but show consistent spectral characteristics compared to the other event types. As a result, these events can be rather interpreted as a very dense cluster of precursor and multiplet occurrences associated with very short inter-event times which can be partially seen from distinct internal peaks in their spectrogram representation Fig. 1.11).

Nevertheless, owing to the high frequency response of the 40 Hz geophone a reliable examination for lower frequency signal contents (< 20 Hz) of the isolated and tremor-like events is not feasible but in this frequency range significant spectral differences might occur. An indication for the presence of low frequency signals was reported by Jousset and Rohmer (2012), who documented the presence of very similar microseismic swarms associated with a clear long period (LP) signature in the collapsing period in 2009.

Clear differences in the spectral content could be only observed for few portion of events

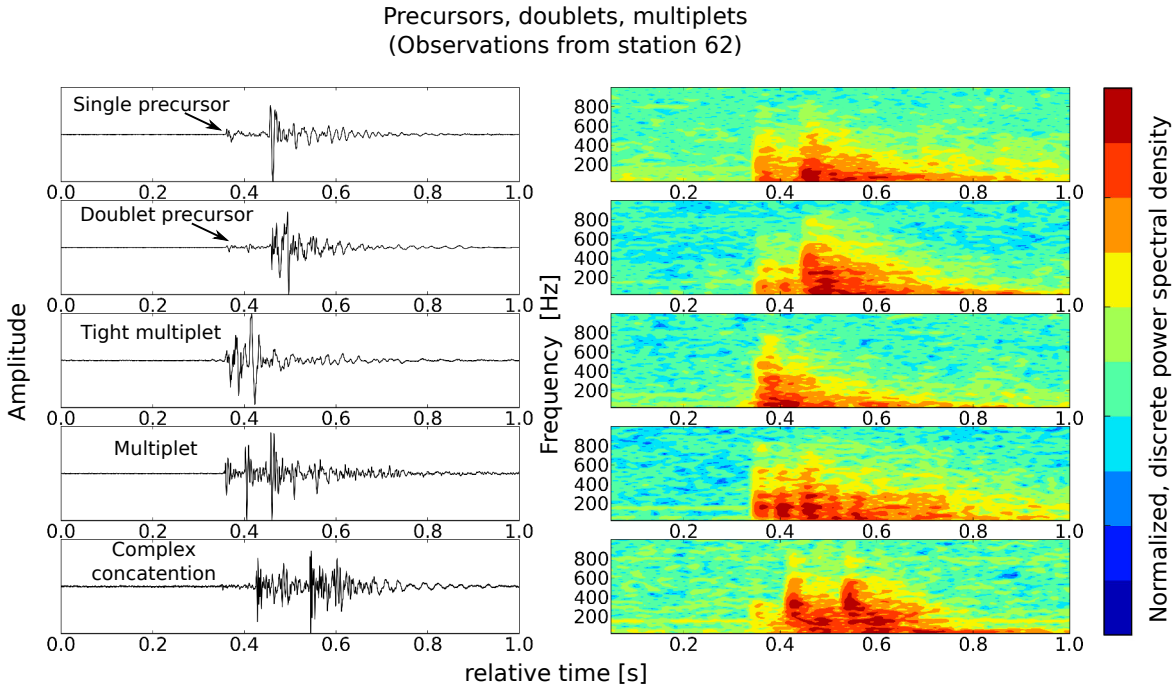

Figure 1.10: Typical precursor, doublet and multiplet phenomena as widely observed in the microseismic data. Five waveform (left panels) and spectrogram (right panels) examples observed from station 62. Spectrograms were calculated using a 0.05 s window length with 90% overlap, while intensities are presented in a normalized dB scale for ten distinct contour levels (color bar).

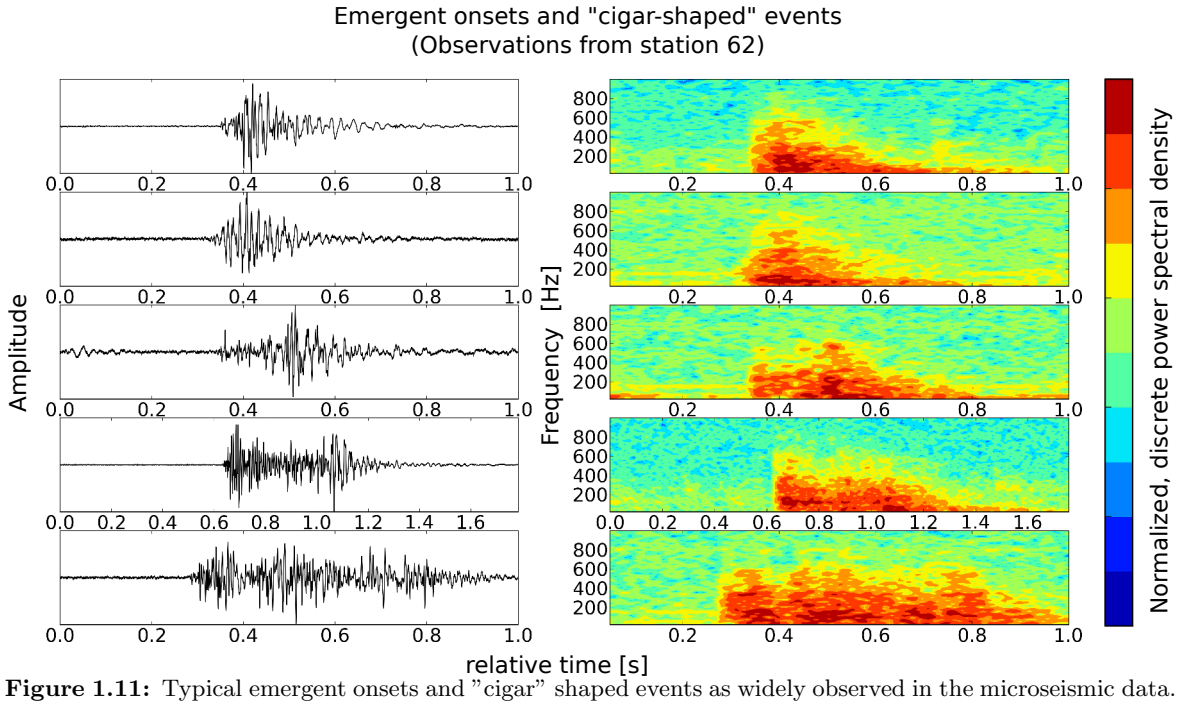

Figure 1.11: Typical emergent onsets and "cigar" shaped events as widely observed in the microseismic data. Five waveform (left panels) and spectrogram (right panels) examples observed from station 62. Spectrograms were calculated using a 0.05 s window length with 90% overlap, while intensities are presented in a normalized dB scale for ten distinct contour levels (color bar).

(around 50) which were associated with interesting resonance phenomena (Fig. 1.12). Resonance frequencies were generally observed at $40 - 90$ Hz, and $150 - 250$ Hz, while resonance frequencies with ≥ 400 Hz (Fig. 1.12) probably results from the spurious response of the geophones for higher frequencies (the geophone manufacturer reported typical spurious frequency response for ≥ 400 Hz). Next to the influence of the recording instrument, these resonance phenomena might be generally related to path effects or source phenomena which might consist in trapped wave portions in open (fluid-filled) spaces associated with a distinct geometry and dimension as e.g. interfaces of geological layers or fluid-filled opening cracks (e.g. Tary et al., 2014). A resonance phenomena associated with the complete cavity structure seems to be rather unlikely as these resonance phenomena should be visible for much more events. Nonetheless, as these events represent apparently a minority of the recorded microseismic data, their origin will not be further analyzed in this thesis, but should be the subject of more detailed future research.

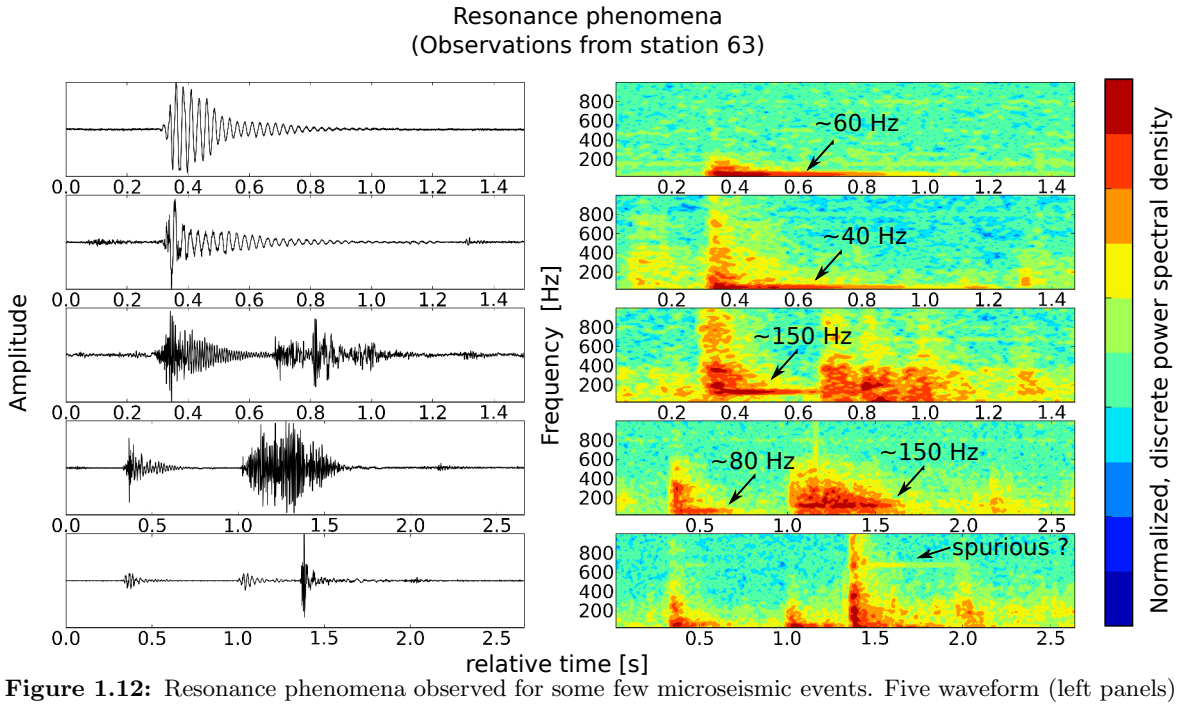

Figure 1.12: Resonance phenomena observed for some few microseismic events. Five waveform (left panels) and spectrogram (right panels) examples observed from station 63. Spectrograms were calculated using a 0.05 s window length with 90% overlap, while intensities are presented in a normalized dB scale for ten distinct contour levels (color bar).

1.3.4.2 Significant propagation effects (attenuation, refraction)

Next to these complicated microseismic event signatures clear propagation effects can be observed. The first major observable propagation effect is associated with strong attenuation

of the higher frequency portions ($\gtrsim$ 100 Hz) of the observed seismograms. Such an attenuation effect is illustrated in Figure 1.13a for one event located at the northwestern extension of the cavity structure (close to station 3) (Fig. 1.5). Regarding the spectrograms for each station it can be clearly observed that the high frequency content decreases significantly for apparently more distant stations as indicated by later P wave arrival times (for further description and discussion of attenuation effects see later Section 2.3.2).

Moreover, also significant differences in the signal and mainly in the onset shape can be observed which are very difficult to interpret due to the presence of precursor phenomena and significant attenuation effects acting on the high frequency signature. For more closer stations often clear high frequency, impulsive P wave onsets can be observed which appear rather emergent for more distant station, making consistent P wave picking a very challenging task. The origin of such strong attenuation effects is probably related to the brine-filled cavity structure as well as significantly fractured material at the cavity roof.

These difficulties in consistent P wave identification introduced from attenuation and precursor phenomena represent one of the major shortcomings in hypocenter source location using P wave phases. Hypocentral distances at Cerville are generally very small ($0 - 300$ m) with expected maximum travel times around 0.12 s, when assuming a very low average P wave velocity of $V_P = 2500$ m/s. In cases of very clear impulsive P wave onsets, picking errors are generally in the range of 0.03 s (e.g. Cao, 2011, Contrucci et al., 2011, Mercerat, 2007) but are generally much higher for the majority of events containing precursor phenomena, emergent P wave onsets or which are covered by the coda of preceding events in swarms (Fig. 1.9, 1.10, 1.11 1.13). Assuming that seismic velocities were faster than the assumed value, the picking errors are in the same range as travel times what render precise hypocenter location to an impossible undertaking.

A second major propagation effect is related to strong refraction effects associated with the Dolomite layer ($V_P \sim 5000$ m/s), which represent a significant seismic velocity contrast compared to the less consolidated, slower over- and underlying Marl layers ($V_P \sim 3000$ m/s) (e.g. Mercerat, 2007). The signature of this refraction effect can be widely seen in the microseismic data especially at station 3 and 63, where the average station incidence angles are generally larger (more horizontal) compared to other station (Fig. 1.14a, see also later Section 2.1). Both stations are placed in deeper bore holes and were actually supposed to significantly improve hypocenter location (mainly source depth) estimations. However, the

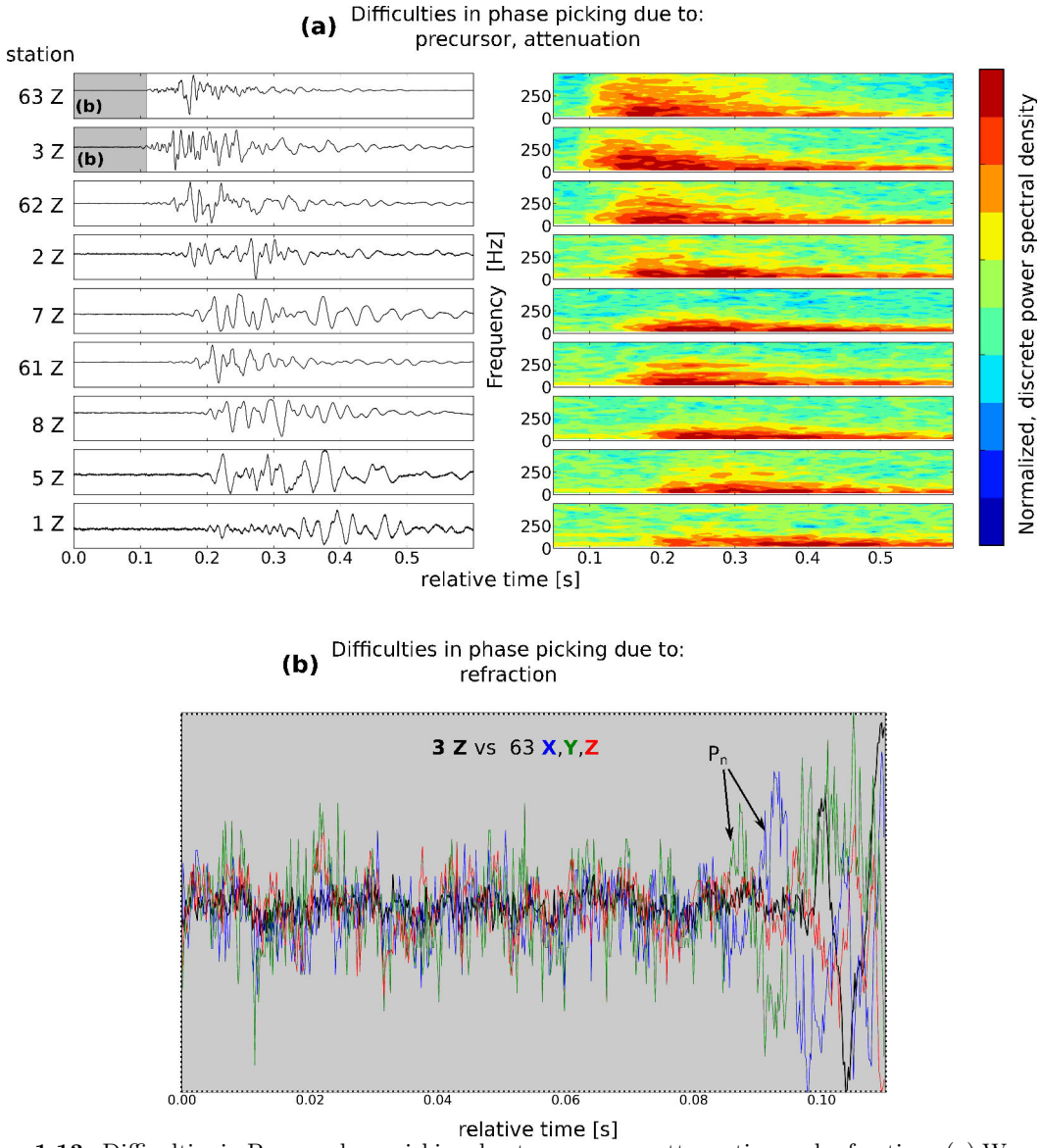

Figure 1.13: Difficulties in P wave phase picking due to precursor, attenuation and refraction. (a) Waveforms (left panels) and spectrograms (right panels) of Z components for all stations of the microseismic network with respect to a microseismic event, recorded the 5th April 2008 (08:56 a.m. UTC), which is located to the northwestern part of the cavity structure (close to station 3). Spectrograms were calculated using a 0.05 s window length with 90% overlap, while intensities are presented in a normalized dB scale for ten distinct contour levels (color bar). (b) Zoom to onsets (gray shaded areas in (a)) of station 3 and 63. Clear refraction related head wave *Pn* phases can be seen in the horizontal components of station 63 (X (blue),Y (green)).

identification of P waves at both stations is rather challenging and need to be undertaken by consideration of all station components (namely the X,Y and Z) in order to detect refracted head wave phases (P_n) (Fig. 1.13b).

Moreover, P wave incidence polarization angles tend to be close to horizontal at station 63 and remain constant around the expected critical angle of refraction ($30 - 45°$) at station 3 (e.g. Cao, 2011, Mercerat, 2007) (see also later Chapter 2). The modeling of these refracted

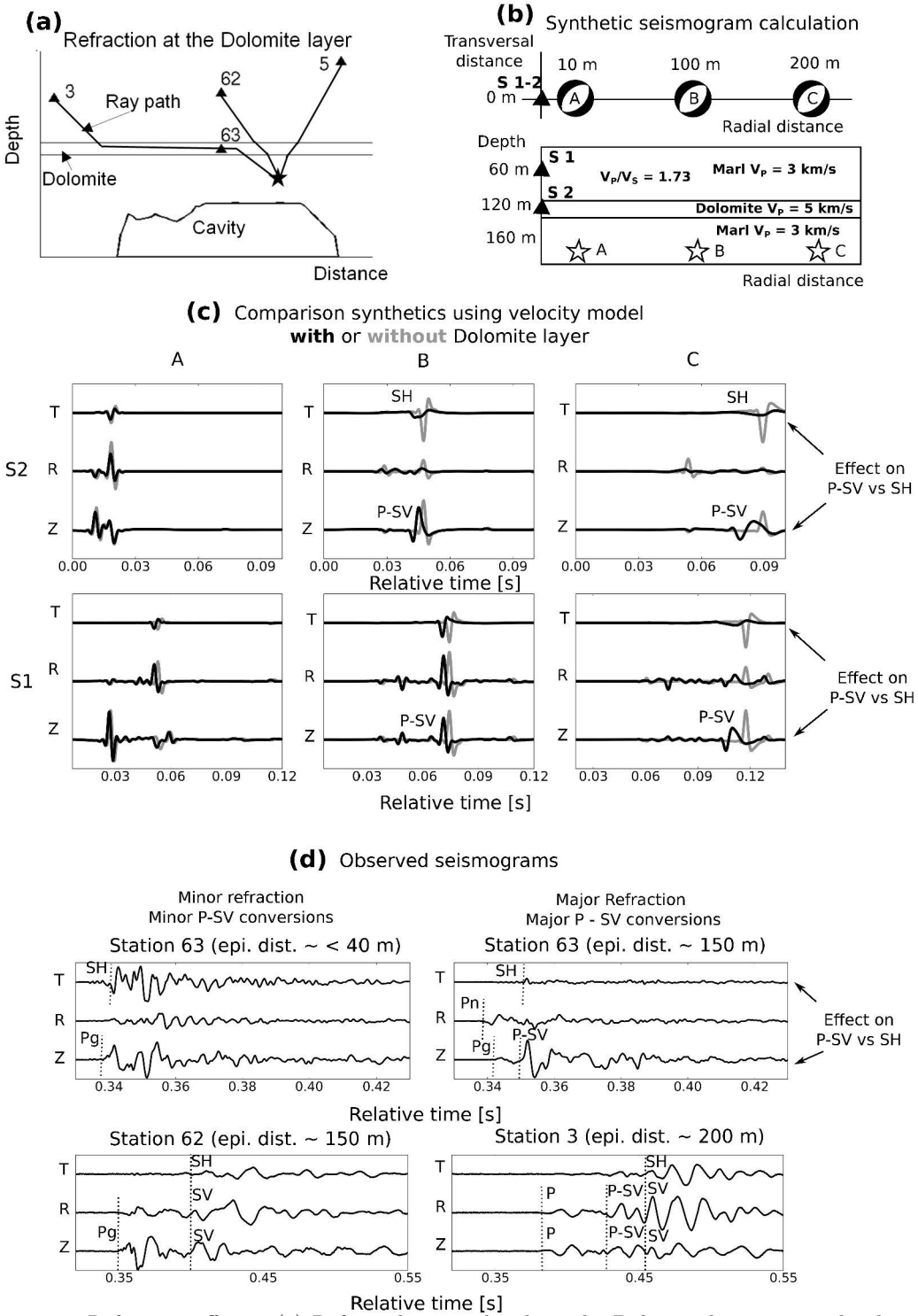

Figure 1.14: Refraction effects. (a) Refracted ray paths along the Dolomite layer as mainly observed at station 3 and 63. (b)-(c) Illustration of synthetic seismograms calculated by means of AXITRA (Coutant, 1989a,b) (see appendix D) for different source receiver locations assuming a simple double couple mechanisms (beach-balls) and a varying velocity model (b), one with (black wave forms) and one without (gray wave forms) Dolomite layer (c). (d) Four examples of observed wave forms documenting (right panels) and not documenting (left panels) the signature of refraction effects as similar to the synthetic seismograms (c).

ray paths depends strongly on the velocity model used and may bias the results, since the velocity structure and contrasts between the cavity roof and the overlying Marl and Dolomite layers are supposed to be very complex and involve temporal changes due to the evolution of the cavity roof.

Next to these complexities in the P wave signature, also S wave contributions in the observed seismogram are significantly affected by the presence of refraction effects. The influence on the wave field from refraction is demonstrated by observed and synthetic seismograms shown in Figure 1.14. Synthetic seismograms were calculated by assuming a simple normal fault mechanism at constant depth and different epicentral distances calculated for a uniform velocity model and a one layered velocity model including the Dolomite layer (Fig. 1.14b). Two different receiver positions ($S1$ and $S2$) were assumed that correspond to the actual location of receivers 3, 62, 63.

From the synthetics a clear refraction effect on the wave field can be seen, when considering larger epicentral distances, and especially for receiver $S2$ located in the Dolomite layer (Fig. 1.14c). While for the homogeneous velocity model, the SH phase amplitudes increases with respect to the SV amplitudes with increasing epicentral distance and source receiver angle, a reverse behavior can be observed when taking into account the Dolomite layer. In addition, SV wave phase show earlier arrivals as compared to SH when taking into account the Dolomite layer. These effects arise from P-SV multiple reflections and conversions that superimpose and partially interfere constructively to predominant radial and vertical particle motions.

The wave field estimated by the synthetics can be very well recognized from the observed wave forms of station 63 (Fig. 1.14d). For larger source receiver angles a dominant P-SV conversion phase evolve in the vertical Z component accompanied by a predominant P_n phase in the radial component (Fig. 1.13b and 1.14d). Clear P-SV conversion phases can be also commonly observed at station 3 (Fig. 1.14d), which is clearly confirmed by the synthetic seismograms shown for receiver $S1$ for larger epicentral distances (Fig. 1.14c). Consistently, less influence from refraction effects and rather simple P and S wave phases, can be observed for smaller (more vertical) station incidence angles (smaller epicentral distances) as shown by the observed seismograms for station 62 and 63 (Fig. 1.14d).

As a result, for interpretation of S wave phases with respect to the hypocenter source location, by using for instance S minus P wave arrival times ($t_s - t_p$), P-SV conversion needs to be generally taken into account, which is not the case in conventional ray approximation based

location approaches. Consequently, the usage of S wave phases for location, especially from stations 3 and 63, must be generally regarded with caution. In addition, also analysis and interpretation of source mechanisms of the microseismic events need to generally account for refraction as demonstrated by the strong influence of refraction on SV and SH wave amplitudes (Fig. 1.14c). This example, as well as the strong influence of attenuation on the seismogram signature demonstrate the general need for good propagation approximations before analyzing the source characteristics (e.g. location, mechanism) associated with high frequency microseismic data.

1.4 Motivation, strategy and structure of this thesis

This thesis contributes to the evaluation of the potential microseismic monitoring with respect to hazardous underground cavities based on the "Cerville-Buissoncourt" microseismic data set. The experimental setting at Cerville gives a unique opportunity to study in detail the microseismic response associated with a growing and collapsing cavity system. However, as documented in the previous Sections, analysis and interpretation of microseismic monitoring in this context is rather poorly experienced and associated with major shortcomings. Based on the results from previous studies and other geophysical parameters, this study aimed to find an appropriate way to analyze the unusual and partially complex high frequency microseismic data set, and secondly to identify and interpret the microseismic signatures to the governing caving and collapsing mechanics and dynamics. In this context, several approaches and models known from different fields of seismic research are tested, including contributions from classical tectonic, volcanic, mining and earthquake swarm seismological studies.

The major work of this thesis, namely Chapters 2 to 4, focused on the study of the microseismic data set recorded during the caving period in 2008. In contrast to the collapsing period in 2009, the installed recording instruments did not break down and apparently no dramatic changes in the elastic constitution occurred what generally simplifies microseismic analysis and interpretation. Analysis of microseismicity is mainly performed by the methods presented in Chapter 2 and 3, describing the development of a semi-automatic detection and location procedure and extensive analysis of source characteristics. The nature and origin of microseismicity and microseismic swarms associated with caving processes recorded in the period of 2008 is then discussed in Chapter 4, whose interpretation is based on the previ-

ously obtained seismic catalogue and some additional statistical analysis adapted from recent investigations of natural earthquake swarm phenomena.

Since the cavity evolution in this period was not provoked by any changes in the solution mining activity, the governing caving processes and its microseismic signature of the period in 2008 are supposed to characterize the initial mechanical state of the cavity system under constant "natural" conditions without any changes in the solution mining activity. In the collapsing period 2009, these conditions are supposed to change when the system was brought to collapse by active brine pumping operations. In order to identify potential changes in the microseismic signature or even precursor phenomena indicating the collapsing state of the cavity system, the principal analysis and interpretation steps, as performed for the period in 2008, were repeated for the collapsing period as documented in Chapter 5. Then differences and similarities of both periods are discussed in the light of hazard assessment based on microseismic observations. Finally, Chapter 6 summarizes the most important achievements of this thesis, and suggests opportunities for future research concerning the improvement and evaluation of the developed methods, the design of appropriate mechanical models and provides some recommendations for the improvement of microseismic monitoring of hazardous underground cavities.

Chapter 2

Semi-automatic event detection and location

Major contents of this chapter are published in: Kinscher et al., (2014). Location of microseismic swarms induced by salt solution mining, Geophysical Journal International, accepted.

As shown in the introduction (Section 1.3.4), around 80 % of the microseismic data at Cerville-Buissoncourt comprise unusual swarming sequences with complex clusters of superimposed microseismic events which could not be processed through standard automatic detection and location routines. The following chapter presents the design of two alternative probabilistic methods which together provide a powerful tool to assess the spatio-temporal characteristics of these complex swarming sequences in a semi-automatic manner. The first approach was designed to identify significantly polarized P wave energies and the associated polarization angles which provide very valuable information on event detection and hypocenter location. The second method uses simple signal amplitude estimations for different frequency bands, combined with an attenuation model to constrain the hypocenter location. The location results for both methods are formulated in a probabilistic manner and can be combined to solve the location problem.

This chapter is organized as follows: first, a classical event location technique is used to locate rather "simple" isolated events (Section 2.1) in order to create a representative training set. This training set is then used to calibrate and evaluate the design and potential of the developed location methods, while first the polarization-based detection and location approach is introduced in Section 2.2, which is followed by the amplitude-based location approach in Section 2.3, accompanied by a detailed discussion of the attenuation characteristics (Section

2.3.2). Then first application results of both approaches are evaluated and discussed with respect to the training set (Section 2.4) and some major swarming sequences (Section 2.5). Finally, a general semi-automatic detection and location design is presented (Section 2.6), including an additional pre-detection step (Section 2.6.1, which is applied and evaluated for the microseismic crisis recorded in 2008 (Fig. 1.7).

The choice and concentration of the 2008 data set, instead of the data set of the collapsing period in 2009 (Fig. 1.8), has the simple reason that the cavity evolution stage is well known and rather simple, what simplifies analysis and interpretation of microseismicity for the here presented methods. As already stated in Section 1.3.3.1, the microseismic crisis in 2008 is clearly related to a period of significant vertical cavity growth, what is well constrained by other geophysical data, meanwhile in 2009, the collapsing dynamics are probably associated with several evolution stages involving significant changes in the elastic medium constitution (Section 1.3.3.2).

2.1 Classical location of a training set

In order to calibrate and evaluate the later presented alternative location approaches, I generate a training set of 54 isolated (rather simple) events which were classically located based on P wave polarization angles and relatively clear and impulsive P and S waves arrival times (Fig. 2.1). These events were selected in the way that the associated hypocenters are homogeneously distributed over the entire cavity zone, and therefore are supposed to widely represent the variety of governing source and propagation effects at the study site determining the general microseismic signal constitution. In addition, all 54 microseismic events occurred all over the entire period (March to May) of the microseismic crisis in 2008 (Section 1.3.3.1), so that the robustness of the later presented location approaches can be discussed in the light of eventual changes in the propagation medium or source characteristics with time. Since isolated and tremor-like events do not differ in their spectral characteristics (Section 1.3.4.1), it is assumed that the analysis and interpretation of this microseismic training set will be also representative for tremor-like events.

2.1.1 Probabilistic inversion procedure

For hypocenter inversion, I chose a classical probabilistic location approach, where the posterior probability density σ (PDF) is denoted as (Tarantola, 2005, Tarantola and Valette,

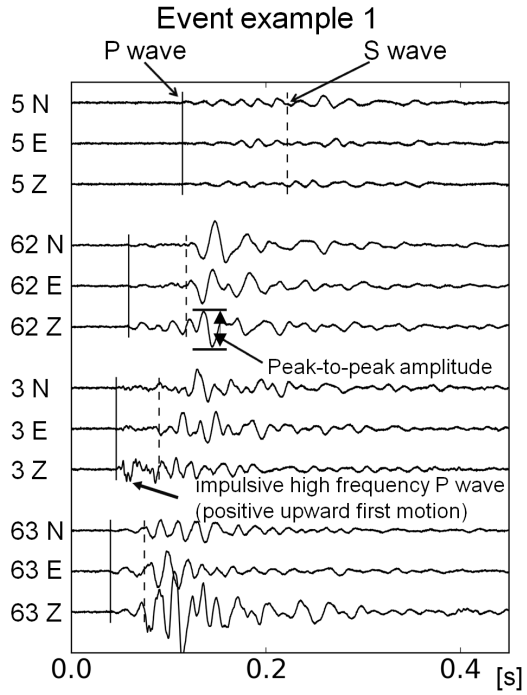

Figure 2.1: Microseismic waveform example. Unfiltered waveforms for event 1, shown for all four 3-component stations.

1982)

$$\sigma(\boldsymbol{X},\boldsymbol{Y},\boldsymbol{Z}) = \kappa\rho_M(\boldsymbol{X},\boldsymbol{Y},\boldsymbol{Z})\rho_D(g(\boldsymbol{X},\boldsymbol{Y},\boldsymbol{Z})), \tag{2.1}$$

where $\boldsymbol{X},\boldsymbol{Y},\boldsymbol{Z}$ represent the Cartesian coordinates of the potential source location, ρ_M is the prior probability density in the model space M, ρ_D the probability density, κ the normalization constant, and g the functional relationship $d = g(m)$ between the elements $m \in M$ of the model space and $d \in D$ of the data space D. The PDF of hypocenter location $\sigma(\boldsymbol{X},\boldsymbol{Y},\boldsymbol{Z})$ was expressed by the exponential distribution of the fit ($l2$-norm) of observed and calculated P wave arrival time differences $\boldsymbol{t_p}$ for a station couple i, P minus S arrival times t_{s-p} at station j, as well as polarization backazimuth φ and incidence θ angles (for 3-component stations) at stations k and l, respectively following Cao (2011), Contrucci et al. (2011), Mercerat (2007), Mercerat et al. (2010)

$$\sigma\left(\boldsymbol{X},\boldsymbol{Y},\boldsymbol{Z}\right) = \kappa\exp\Bigg\{-\sum_{i,j,k,l}\Bigg[\frac{\left(\boldsymbol{t}^{i}_{\boldsymbol{p}_{obs}} - \boldsymbol{t}^{i}_{\boldsymbol{p}_{calc}}(\boldsymbol{X},\boldsymbol{Y},\boldsymbol{Z})\right)^2}{2\sigma^2_{\boldsymbol{t_p}}} + \frac{\left(t^{j}_{s-p,obs} - t^{j}_{s-p,calc}(\boldsymbol{X},\boldsymbol{Y},\boldsymbol{Z})\right)^2}{\sigma^2_{t_p} + \sigma^2_{t_s}} + \frac{\left(\varphi^{k}_{obs} - \varphi^{k}_{calc}(\boldsymbol{X},\boldsymbol{Y},\boldsymbol{Z})\right)^2}{2\sigma^2_{\varphi}} + \frac{\left(\theta^{l}_{obs} - \theta^{l}_{calc}(\boldsymbol{X},\boldsymbol{Y},\boldsymbol{Z})\right)^2}{2\sigma^2_{\theta}}\Bigg]\Bigg\}, \tag{2.2}$$

where exp is the exponential function. The model space sampling for hypocenter location $\boldsymbol{X}, \boldsymbol{Y}, \boldsymbol{Z}$ was defined by a grid search for a $10 \times 10 \times 10$ m grid, over the coordinate system $X = 220 - 550$ m, $Y = 40 - 400$ m, $Z = -(100 - 250)$ m (Fig. 2.2).

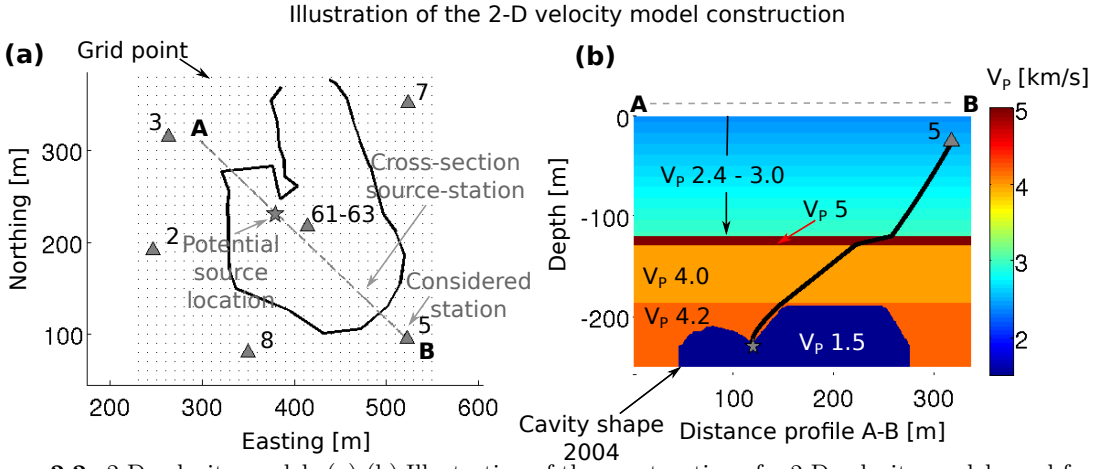

Figure 2.2: 2-D velocity model. (a)-(b) Illustration of the construction of a 2-D velocity model, used for the calculation of travel times and ray paths (black line in (b)) for one grid point (gray star) of potential hypocenter location and station 5 (gray triangle). The geometry of the cavity roof is taken from sonar measurement by SOLVAY (Section 1.3.1). References for seismic velocities are given in Table 2.1 and D.1.

I used the fast marching method (e.g. Sethian, 1999) implemented in a Matlab code (provided by the website `https://sites.google.com/site/patricknraanespro/fast-marching-method`) in order to calculate ray paths and body wave arrival times based on a 2D velocity model taking into account the true cavity geometry for each station-source path way (Fig. 2.2). As a result, compared to a 1-D model I generally accounted for the 2-D vertical extension of the cavity structure with respect to the direct station-source path way. On the other hand, lateral pathways introduced by the 3-D cavity structure were not accounted, but lower computation times are achieved than when using a complete 3-D velocity model. The layers of the velocity model and the associated P and S wave velocities were taken from Mercerat et al. (2010) and are shown in Table 2.1.

Uncertainties in P and S wave arrival time picking ($\sigma_{\boldsymbol{t_p}}$, σ_{t_p}, and σ_{t_s}) were defined with ± 0.03 s for P, and ± 0.05 s for S waves, and correspond to the maximum uncertainties observed from manual phase picking analysis. P wave phase picking was mainly done with respect to the vertical station components, while frequently refracted P wave phases (P_n) were picked from the horizontal component of station 63 (Fig. 1.13). S wave phases could be only reliably picked on 3-component stations.

During inversion P wave travel time differences $\boldsymbol{t_p}$ were considered for all station couples of

Table 2.1: Elastic characteristics for the major geological units (Fig. 1.5, Section 1.3) estimated from laboratory analysis and calibration shots, as carried out by Mercerat (2007), Mercerat et al. (2010), Nothnagel (2003).

	Depth [km]	V_p [km/s]	V_p/V_s	ρ [g/cm^3]
Marls and sands	$0.0 - 0.119$	$2.4 - 3.0$	1.83	2.5
Dolomite	$0.119 - 0.128$	5.0	1.73	2.89
Anhydritic marls	$0.128 - 0.185$	4.0	1.83	2.657
Salt	$0.185 - 0.3$	4.2	1.8	2.15
Brine filled cavity		1.5		1.0

the network (Table B.1). In contrast, P minus S wave arrival times t_{s-p} were exclusively considered for station 62 (Table B.1). This choice was made in order to avoid any bias in the inversion results arising from erroneously picked P-SV conversions (Fig. 1.14, Section 1.3.4.2), which are often difficult to distinguish from the direct S wave phases. Since ray incidence angles at station 62 are generally more vertical compared to other 3-component stations 3, 5, and 63, refraction effects and P-SV conversion are clearly less important.

Polarization angles were carefully determined from the first period of P wave onsets (Table B.1) using the SYTMIS software (Cao, 2011, Contrucci et al., 2011, Mercerat, 2007, Mercerat et al., 2010), and the implemented conventional eigenanalysis of the seismic data matrix (e.g. Flinn, 1965), where polarization angle uncertainties (σ_φ and σ_θ) were observed with $\pm 10^\circ$ from regarding the maximum scatter in the polarization analysis window (0.05 s). The mis-orientation of the horizontal station components (deviation from North-East orientation) was corrected by means of the results of a detailed polarization analysis within a calibration shot campaign (Mercerat, 2007).

During inversion all backazimuth polarization angles for all 3-component stations were considered. However, as similar to the travel time inversion procedure, only the incidence polarization angles of station 62 were considered since refraction effects are less important (Section 1.3.4.2), and thus polarization incidence angles more similar to the true vertical source-receiver angle. In this way, biases in the inversion results arising from mis-modeling of refracted ray paths (as mainly observed for station 3 and 63, but also expected for station 5) are generally avoided. Modeling of refracted ray paths is generally complicated since the velocity structures and contrasts between the cavity roof and the overlying Marl and Dolomite layers are supposed to be very complex and involve temporal changes due to the evolution of the cavity roof, what could easily lead to misinterpretation when using a simple, constant 1-D velocity model (Table 2.1).

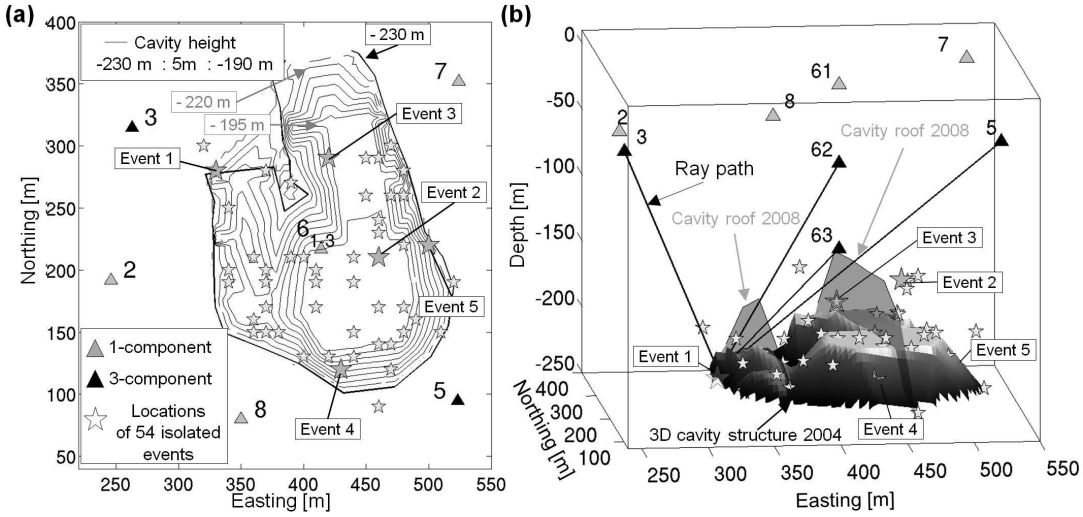

Figure 2.3: Results from classical location for the training set of 54 located isolated events (small stars), used later for the calibration of the developed location approaches. Numbered larger gray stars mark isolated events partially discussed in more detail in the text. (a) Top view of the 3-D cavity structure shown by the contours (solid black and gray lines). (Right panel) Side view of the 3-D cavity structure determined in 2004, and the cavity growth registered in 2008 (gray shaded areas) (Section 1.3).

2.1.2 Results and discussion

The maximum likelihood locations of the 54 analyzed events are shown in Figure 2.3. The PDF with respect to event 1 (Fig. 2.1 and 2.3) is shown in Figure 2.4 which is generally very representative for the other event location results as the shape and extension of the cumulative probability functions and contours (Φ) are very similar. From this location result, it can be generally seen that epicenter locations are relatively well resolved. The error in epicenter location is estimated to be generally $\leq$ 50 m which corresponds to the maximum distance between the maximum-likelihood location and the most distant location covered by the 0.68 Φ contour (Fig. 2.4). Slightly increased epicenter location errors were observed for event locations to the northern and eastern parts of the cavity zone which is logical, since the receiver coverage is less dense as compared to the southern and western parts (e.g. Fig. 2.2). It must be stressed that the resolution of epicenter locations is widely controlled by the information on the polarization angles (station backazimuths). As already mentioned in Section 1.3.4.2, the inversion of travel time differences at the study site, is often ill-posed, as the observed picking errors are generally too high (or partially in the same range) with respect to the observed travel time differences which are very small due to short hypocentral distances and relatively fast seismic velocities (up to 5000 m/s).

Not surprisingly, source depths are associated with a larger uncertainty (Fig. 2.4) and should be regarded with caution. The only information in source depth comes from the t_{s-p} time residuals and P wave incidence polarization angles from station 62 (Section 2.1.1). However, the estimated source depths seem to be generally not unreasonable, since most hypocenters are found between the cavity roof and the overlying Dolomite layer, where microseismicity is generally expected (Section 1.3.3.1).

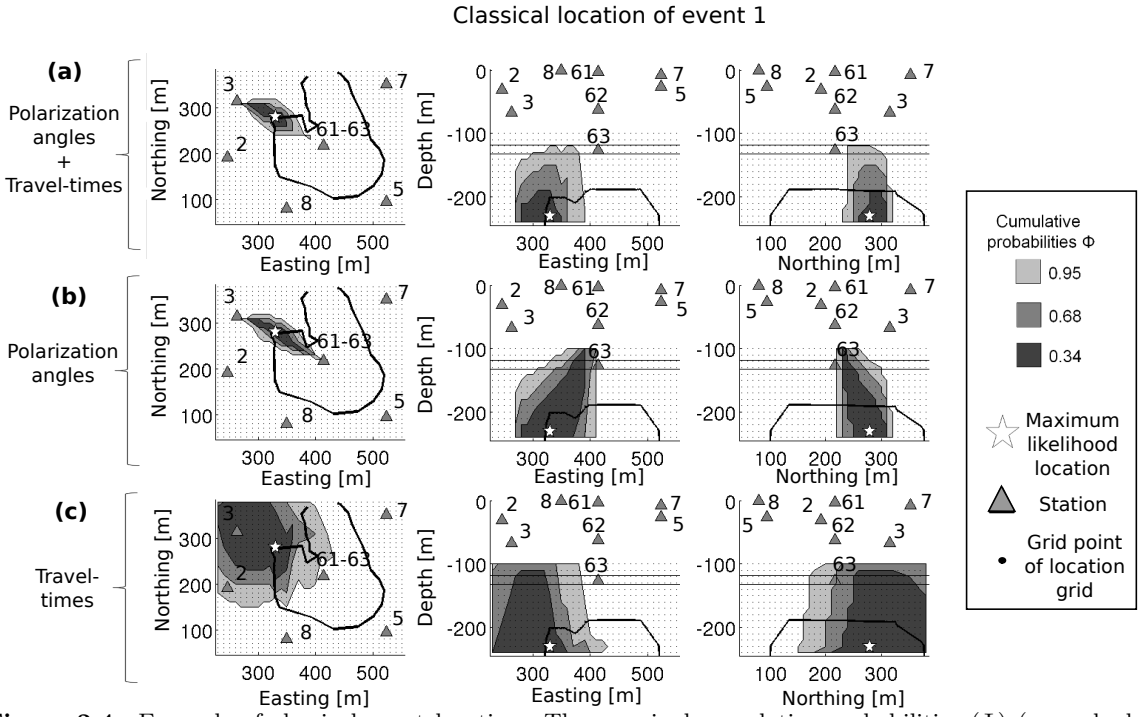

Figure 2.4: Example of classical event location. The marginal cumulative probabilities (Φ) (gray shaded areas) for location of event 1 (white star) (Fig. 2.1) as shown for the horizontal plane (right panels) the eastern vertical plane (middle panels) and the northern vertical plane (left panels) by using (a) body wave arrival time differences $\boldsymbol{t_p}$, t_{s-p}, and P wave polarization angles, (b) P wave polarization angles only, (c) and arrival time differences $\boldsymbol{t_p}$ and t_{s-p} only.

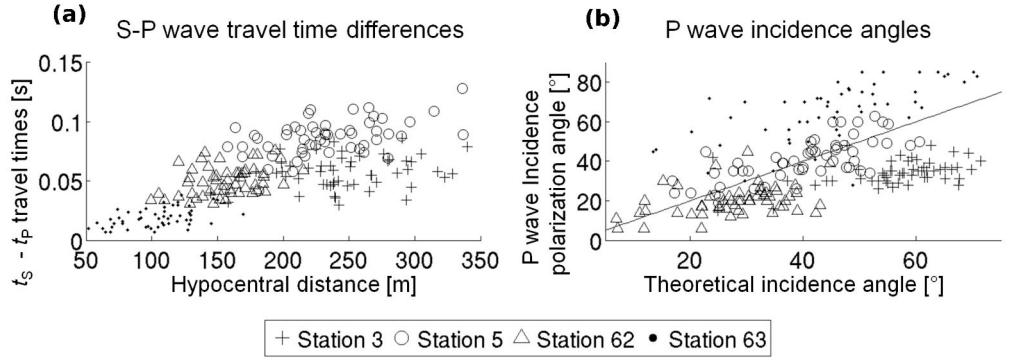

Figure 2.5: Travel times and polarization angles. S minus P t_{s-p} travel time differences (a) and the estimated the P polarization incidence angles as a function of theoretical incidence angles calculated from the hypocenter locations (b) (Fig. 2.3).

Corresponding to the event locations, Figure 2.5 shows the P minus S arrival times t_{s-p} as

function of hypocentral distance as well as the P wave polarization incidence angles as a function of theoretical incidence angles calculated from the hypocenter locations (Table B.1). From this illustration once again the importance of refraction effects in the microseismic signals is demonstrated (Section 1.3.4.2), especially seen at station 3 and 63. Accordingly, body wave travel time residuals t_{s-p} at stations 3 and 63 are significantly smaller compared to those recorded at stations 5 and 62 (Fig. 2.5a), although their hypocentral distances are similar. The smaller t_{s-p} time residuals result from erroneously picked P-SV conversions (Fig. 1.14, Table B.1) and longer wave propagation distances in the Dolomite layer, which is associated with higher velocities and a smaller V_P/V_S–ratio as compared to the Marl layers (Table 2.1). Moreover, P wave incidence polarization angles tend to be close to horizontal at station 63, and remain constant around the critical angle of refraction (30-45°) at station 3 (Fig. 2.5b, Section 1.3.4.2).

These observations generally underline the here used location strategy (Section 2.1.1), by considering only P wave incidence angles and S wave phase picks of station 62. On the other hand, refraction effects seem to be also negligible at station 5 where t_{s-p} time residual seems to be consistent with station 62 and where P wave incidence angles are linearly related to the theoretical ones (Fig. 2.5). As a result, I also tested the location approach by taking into account these estimates from station 5, what however did not significantly improved nor changed the location results.

2.2 Detection and location using signal polarization characteristics

The following method was developed in order to identify automatically P wave phases and their associated polarization angles for 3-component stations, providing fundamental information with respect to hypocenter source location. The development of this method was inspired by a fundamental characteristic observed during detailed inspection of the microseismic training data set (Fig. 2.3, Section 2.1). This characteristic is illustrated in Figure 2.6, showing the S and P wave peak-to-peak amplitude ratios (S/P) for different frequency bands. By this illustration it can be clearly seen that the P waves become more dominant compared to S waves when regarding higher frequencies ($\gtrsim$ 100 Hz). One fundamental origin of this characteristic is suggested in an abnormal high S wave attenuation behavior as compared to P waves, what will be later analyzed and discussed in more detail in Section

2.3.

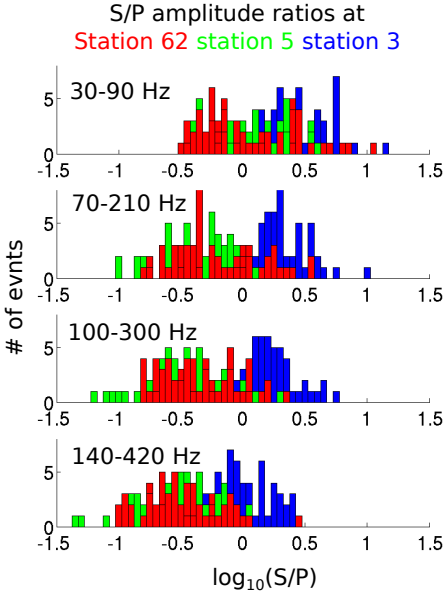

Figure 2.6: S and P wave amplitude ratios. Histograms of the S/P amplitude ratios shown for the 54 events of the training set (Fig. 2.3) at station 3 (red bars), station 5 (green bars), and station 62 (blue bars) for distinct frequency bands with increasing higher frequencies from top to bottom. S and P wave amplitudes are estimated by the peak-to-peak phase amplitudes (e.g. Fig. 2.1) after station component rotation to an LQT (ray oriented) coordinate system (e.g. Plesinger et al., 1986).

2.2.1 Estimating the degree of linearly polarized energies

Different from conventional polarization analyses that use eigenanalysis of particle motion (e.g. Flinn, 1965), this approach instead uses simple peak-to-peak amplitudes estimates (e.g. Fig. 2.1) to determine the degree of linearly polarized energy in the signal. In conventional polarization analysis, the window of analysis (signal covariance matrix) need to be generally larger than the average signal period of the analyzed phase but if the window is too large or too small the degree of polarization degrades due to the influence of noise and other wave phase contributions (e.g. Jurkevics, 1988). Using peak-to peak amplitudes permits to identify the highest degree of polarization is more robust with respect to the choice in the length of the window of analysis and the considered wave periods. For a time window t, the maximum polarized energy L, associated with a specific receiver backazimuth φ and an incidence angle θ, is approximated as the maximum of the ratio (logarithmic subtraction)

$$L_{t,\varphi,\theta} = \arg\max_{\boldsymbol{\varphi}\times\boldsymbol{\theta}} \left\{ \log_{10}\left(\boldsymbol{l}_t(\boldsymbol{\varphi}\times\boldsymbol{\theta})\right) - \frac{1}{2}\left[\log_{10}\left(\boldsymbol{q}_t(\boldsymbol{\varphi}\times\boldsymbol{\theta})\right) + \log_{10}\left(\boldsymbol{t}_t(\boldsymbol{\varphi}\times\boldsymbol{\theta})\right)\right] \right\}, \qquad (2.3)$$

where $\boldsymbol{l}$, $\boldsymbol{q}$, and $\boldsymbol{t}$ (please do not confuse with t) represent the peak-to-peak amplitudes (e.g. Fig. 2.1) estimated from each axis of the LQT (ray oriented) coordinate system (e.g. Plesinger et al., 1986). The axes of the LQT system and the respective $\boldsymbol{l}$, $\boldsymbol{q}$, $\boldsymbol{t}$ amplitudes are explored with respect to all directions of the half space below the considered receiver

(Fig. 2.7). The directions are discretized by direction vectors defined by the Cartesian product $\times$ of a set of potential backazimuths $\boldsymbol{\varphi} = \{0, 10, \ldots, 340, 350\}$ and incidence angles $\boldsymbol{\theta} = \{0, 10, \ldots, 80, 90\}$. Consequently, I assume that the seismic energy always originates from below the receiver, resolving the $\pm 180°$ ambiguity for the backazimuth angle. The resulting L-value can be seen as a measure of the degree of linearly polarized energy.

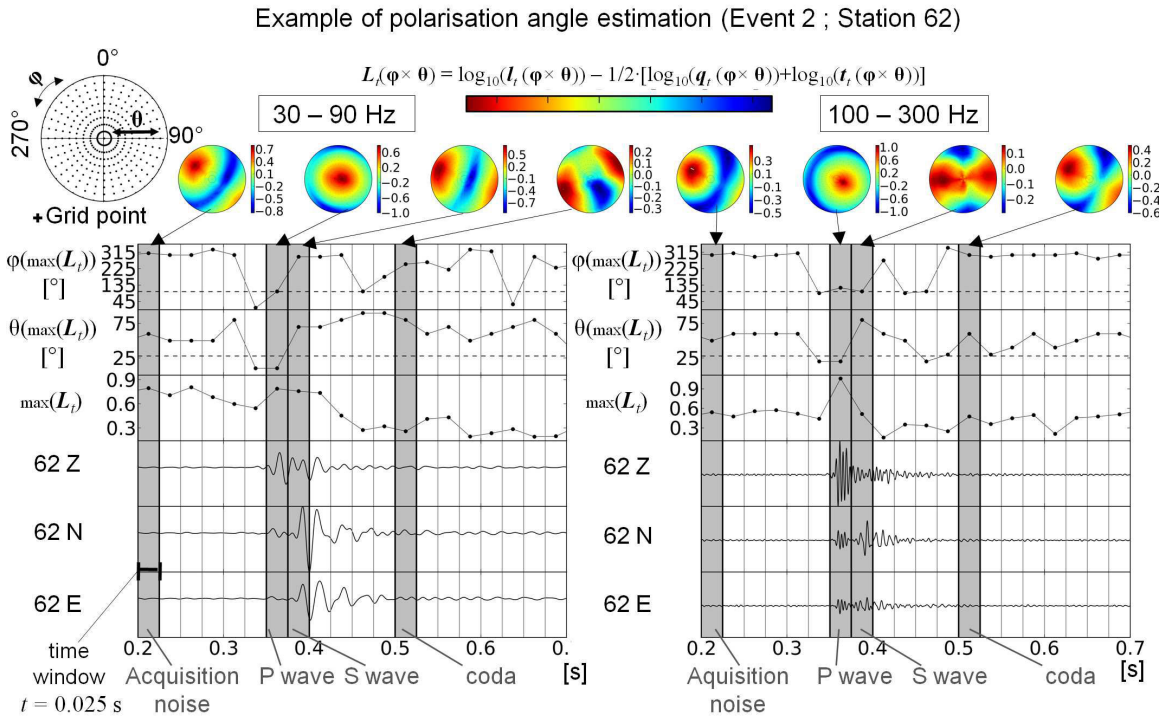

Figure 2.7: Example of P wave polarization analysis. Demonstration of P wave phase identification and polarization angles at station 62 for event 2 (Fig. 2.3) for the frequency bands of $30 - 90$ Hz (lower left panel) and $100 - 300$ Hz (lower right panels) using the L-value method (Eq. 2.3, Section 2.2.1). L-values were calculated for 0.025 s time windows (grey and black vertical lines) corresponding to a backazimuth φ and incidence angle θ. Dashed lines mark the actual backazimuth and incidence angles with respect to event 2 (Fig. 2.3). L-value calculation is illustrated (upper hemisphere plot) for four windows (gray shaded areas) showing the maximal L-value corresponding to acquisition noise, P and S waves and coda portions.

2.2.2 P wave phase identification

As it was shown by the S/P amplitude ratios in Figure 2.6, P wave energies become dominant in the body wave field when considering higher frequencies ($\gtrsim 100$ Hz). Figure 2.7 shows the ability of the L-value method (Eq. 2.3) to successfully identify such cases of dominating P wave energies at higher frequencies, with respect to event 2 (Fig. 2.3). At higher frequencies, the degree of polarization for S waves (L-value $= 0.6$) is significantly lower compared to P waves (L-value $= 1.1$), while at lower frequencies the degree of polarization is in the same order of magnitude for P and S waves (L-value $= 0.7$) (Fig. 2.7). Furthermore, the degree of

linear polarization with respect to the acquisition noise is weaker at higher frequencies (L-value = 0.5) compared to lower frequencies (L-value = 0.8), so that the P wave contribution in the seismogram is represented by significantly higher L-values, relative to noise.

Next to the observation that P waves can be better identified and distinguished at higher frequency (using the L-value method), it can be observed that also the degree of linear polarization increases with higher frequencies for P waves with L-value = 0.8 for lower and L-value = 1.1 for higher frequencies (Fig. 2.7). The increasing degree of polarization with higher frequencies might be explained by the fact that the observed wavelengths become smaller, and therefore the wave field is better approximated by assumed ray theory (high frequency approximation). The hypocentral distance with respect to station 62 and event 2 is probably smaller than 150 m (Fig. 2.3), which is almost in the same range as the expected wavelength $30 - 90$ m when considering $30 - 90$ Hz and a average V_P of 2700 m/s (Fig. 2.7, Table 2.1). Thus, also near-field effects might play a role in this respect which is later discussed in Section 3.2.3.

The capability of the L-value method to automatically identify significantly polarized high frequency P wave energy portions is demonstrated in Figure 2.8a. The method was applied to the seismograms of the 54 located events (including noise, seismic events, and codas) (Fig. 2.3) for the 3-component stations 3, 5, and 62, at a high ($100 - 300$ Hz) and a low ($30 - 90$ Hz) frequency band, using a time window t of length 0.025 s gliding stepwise along 0.0125 s intervals. In Figure 2.8a, the errors of the estimated direction vectors and the related backazimuth and incidence angles are shown as a function of the corresponding L-values (degree of polarization). The errors in the polarization angles are represented by the differences between the estimated (using the L-value method) and the calculated direction vectors and of their related backazimuth and incidence angles for the hypocenter location of the training set (Fig. 2.3), assuming a homogeneous velocity model (for further explanations regarding the choice of a homogeneous velocity model see later Section 2.2.3).

In this method, station 63 is completely neglected, because P wave phases could not be sufficiently well distinguished from the degree of linear polarization (L-value) with respect to other seismic wave phases. Arrival time residuals between P and S waves are very short (≤ 0.01 s) at station 63 (Fig. 2.5a) and even shorter for P-SV conversion phases (Fig. 1.14c-d). To estimate the polarization degree and identify P wave phases, an even very smaller analysis time window t than ≤ 0.025 s would be required, what is often smaller than the

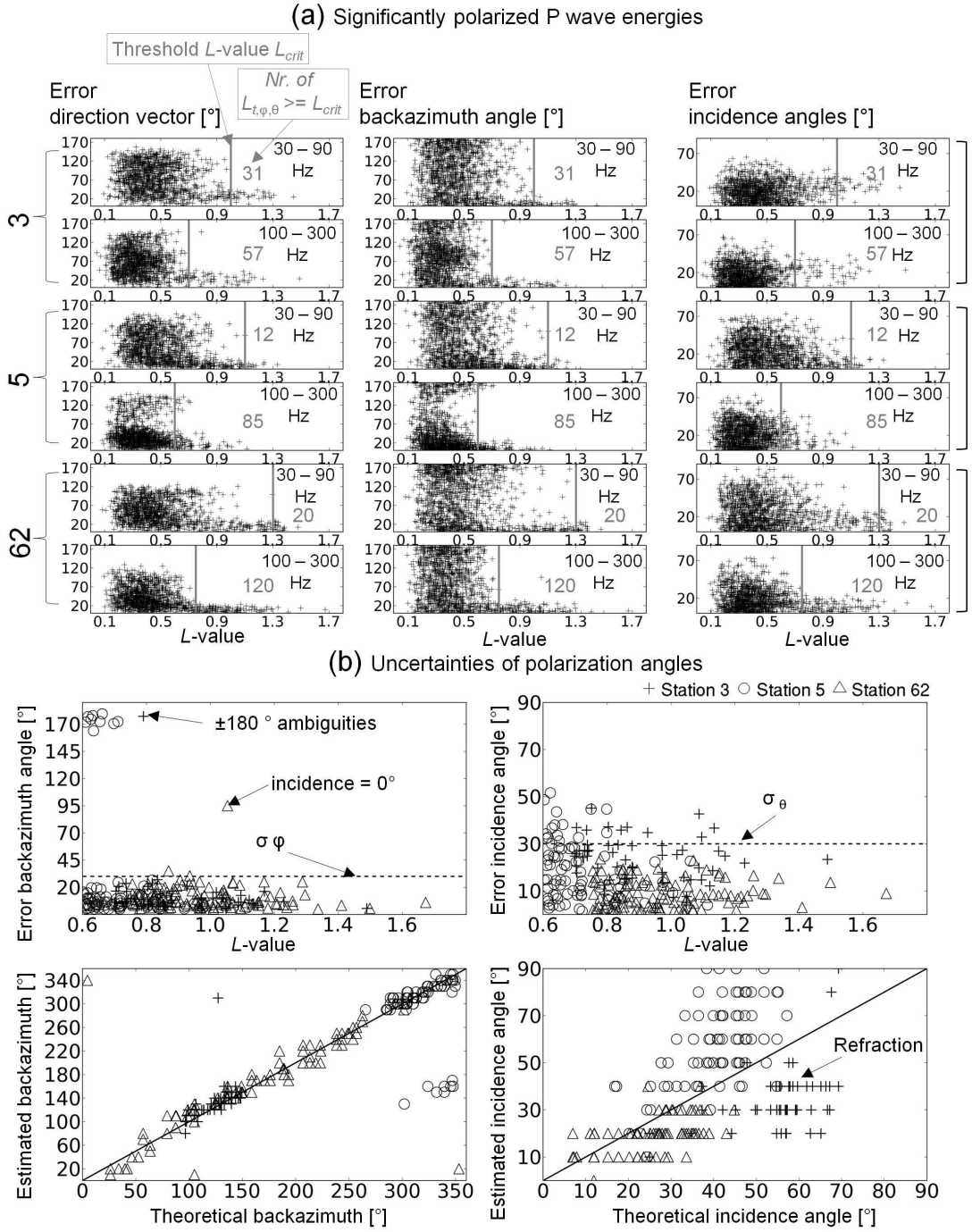

Figure 2.8: Distribution of linearity and polarization angles. (a) Errors in the estimated direction vectors (left panels), the related backazimuths (middle panels) and incidence angles (right panels), as a function of the corresponding L-values (black points) calculated for 0.025 s time windows for all seismograms of the 54 located events (Fig. 2.3) and for 3-component stations 3, 5 and 62, at frequency bands of $30 - 90$ Hz and $100 - 300$ Hz. Errors in polarization angles were calculated by the absolute deviation of the estimated polarization angles with respect to the expected backazimuth and incidence angle found from the location of the 54 events. L-values greater than the thresholds (gray lines) (Lcrit) indicate significantly polarized P wave energies. (b) Quality and errors of the determined polarization angles associated with L-values $\geq$ Lcrit for the $100 - 300$ Hz frequency band. Theoretical incidence angles correspond to the angles pointing towards the source at 0° and 90° in vertical and horizontal directions, respectively, with regards to the station.

average signal period of P waves, so that estimates of the estimated degree of polarization become noisy.

In contrast, regarding the L-values and the corresponding errors in the polarization angles in for the other stations 3, 5, and 62 (Fig. 2.8a), it can be observed that P wave phases are clearly distinguishable from other phases by significant high degrees of linear polarization (L-values). For a specific L-value (degree of polarization), the errors in the polarization angles remain significantly small compared to errors associated with lower L-values. For each station and frequency band, this specific L-value is defined as the threshold value Lcrit. In addition, the quantity of L-values $\geq L$crit is much larger at higher frequencies than at lower frequencies, what is consistent with the observations stated above that P wave become more dominant at higher frequencies compared to S waves and show a higher degree of linear polarization as probably a result of a different attenuation behavior, and better ray approximation, respectively.

In the following, the threshold values shown for each station are used for the detection of significantly polarized P wave energies within the considered time windows by considering higher frequencies. Most polarized P wave energies can be detected at station 62, using the defined threshold of Lcrit = 0.75 (Fig. 2.8a). The lowest amount of L-values beyond the threshold Lcrit is observed at station 3 (Fig. 2.8a). In addition, a noticeable cluster of polarized SH wave energies is observed at higher frequencies and L-values below the threshold value (Lcrit = 0.7) associated with an indicative error of $\sim 90^\circ$ in the backazimuth angle, which cannot be observed from stations 5 and 62. The origin of this differences in P wave detection quantity and significant SH wave energy contribution in the seismograms is probably related to a systematic source effect, which will be later shown and discussed in Section 3.3. The lowest critical P wave detection value was found for station 5 with Lcrit = 0.6, what is consistent with the significant decrease in the S/P ratios at station 5 for increasing frequencies as shown by Figure 2.6. The origin of this particular strong decrease in the S/P ratios at station 5 (which is located at shallower depth than stations 3, 62 ($\sim$ 35 m), and 63 $\sim$ 102 m)) is assumed in an extra intensification of the abnormal attenuation behavior of S waves in the upper ($\leq$ 50 m in depth), less consolidated sedimentary layers in the overburden as later shown and discussed in Section 2.3.2.2 and 3.3. On the other hand, the estimated polarization angles are partially erroneous with $\pm 180^\circ$ ambiguities in the backazimuth angles and overestimated incidence angles (Fig. 2.8b). Since station 5 is located at shallower depth,

these errors might be also related to secondary P wave phases reflected at the free surface which, when contained in the particle motion, lead to misestimations of the true incidence angles (e.g. Neuberg and Pointer, 2000).

2.2.3 Probabilistic location based on polarization angles

In this section, I explain how I use the identified P wave polarization angles (Fig. 2.8a) to constrain hypocenter locations. I chose a probabilistic approach in order to render location results comparable with the later presented amplitude-based approach (Section 2.3), and to account for the varying detectability and quality of the P wave phases and their polarization angles, at each station (Fig. 2.8).

As stated above, P wave phase and polarization angle determination is generally performed using the high frequency band, because comparatively more P waves phases can be identified (Fig. 2.7 and 2.8). For several cases amongst the 54 considered events of the training set, more than one P wave phase and polarization angle was identified (Fig. 2.8a). For station 62, the total number of determined polarization angles (120) is more than twice the total of events considered (54). On the other hand, polarization angles for certain events could not be identified for all stations. It should be noted that not all of the identified P phases are related to the 54 events but also to small precursor and multiplet events (Fig. 1.10) appearing before and after the main seismic event as commonly observed for isolated events (Section 1.3.4.1).

In order to relate the polarization angles, determined at each station, to the same seismic event, all the corresponding time windows per station (*stat.*) $t^{stat.} = \{t_1, t_2, \ldots, t_n\}$ are combined to a set representing the potential source origin times $\boldsymbol{T}_0^{stat.}$

$$\boldsymbol{T}_0^{stat.} = t^{stat.} - \frac{\boldsymbol{R}^{stat.}}{V_p}, \tag{2.4}$$

where $\boldsymbol{R}^{\boldsymbol{stat.}}$ represents the distances between the station and the grid points of potential hypocenter source location, as defined by a 10 m grid $\sigma(\boldsymbol{X}, \boldsymbol{Y}, \boldsymbol{Z})$ represented by the Cartesian product $\times$ of the coordinate sets $X = \{220, \ldots, 590\}$ m, $Y = \{40, \ldots, 450\}$, and $Z = \{-250, \ldots, -60\}$ (e.g. Fig 2.2). Then, the sets of source origin times for all stations are united to one set, T_0 representing all potential source time origins

$$\boldsymbol{T}_0 = \boldsymbol{T}_0^3 \cup \boldsymbol{T}_0^5 \cup \boldsymbol{T}_0^{62}, \tag{2.5}$$

where $\cup$ marks the set's theoretic union. In the final step, the source origin times for one

event are represented by a time τ defined from the spacing intervals of the time samples T_i in $\boldsymbol{T}_0$ from the conditional functional relationship

$$\tau_{start-end} = \begin{cases} \text{if } i = 0 \vee T_i - T_{i-1} \geq \quad 0.05 \text{ s then } \tau_{start} = T_i \\ \text{if} \qquad\qquad T_i - T_{i+1} \leq -0.05 \text{ s then } \tau_{end} = T_i, \end{cases} \tag{2.6}$$

where $\vee$ denotes the logical disjunction (or). In other words, a new event associated with the source origin times τ is identified in the set $\boldsymbol{T}_0$, when the difference between two adjoined time samples exceeds 0.05 s, corresponding to double the length of the chosen time window t (0.025 s) used for the L-value method.

For every seismic event associated with the time interval τ, the posterior probability density of the hypocenter location (Eq. 2.1) is then expressed by the $l2$-norm misfit between m observed and calculated backazimuth φ and incidence θ angles obtained for one station with uncertainties σ_φ and σ_θ

$$\sigma_{stat.}(\boldsymbol{X},\boldsymbol{Y},\boldsymbol{Z}) = \frac{1}{m}\sum_{k}^{m} \kappa \exp\left\{ -\frac{\left(\varphi_{obs}^{k} - \varphi_{calc}(\boldsymbol{X},\boldsymbol{Y},\boldsymbol{Z},\tau)\right)^2}{2\sigma_\varphi^2} - \frac{\left(\theta_{obs}^{k} - \theta_{calc}(\boldsymbol{X},\boldsymbol{Y},\boldsymbol{Z},\tau)\right)^2}{2\sigma_\theta^2} \right\}. \tag{2.7}$$

The index k refers to those polarization angles whose time window $t^{stat.}$ satisfies the condition

$$\tau \cap t^{stat.} - \frac{\boldsymbol{R}^{stat.}}{V_p} \neq \varnothing, \tag{2.8}$$

where $\varnothing$ denotes an empty set. In other words, I choose those polarization angles whose set of potential source origin times is compatible with the event time τ. Finally, the conjunction of probability densities for all stations gives the posterior probability density σ_{pol} for one event location

$$\sigma_{pol}(\boldsymbol{X},\boldsymbol{Y},\boldsymbol{Z},\tau) = \sigma_3(\boldsymbol{X},\boldsymbol{Y},\boldsymbol{Z},\tau)\sigma_5(\boldsymbol{X},\boldsymbol{Y},\boldsymbol{Z},\tau)\sigma_{62}(\boldsymbol{X},\boldsymbol{Y},\boldsymbol{Z},\tau). \tag{2.9}$$

The parameter setting chosen for the practical implementation of this probabilistic location scheme is summarized in Figure 2.8b, which illustrates the quality of the obtained polarization angles and the definition of their uncertainties σ_φ and σ_θ. These uncertainties are defined by comparison with the theoretical backazimuth and incidence angles with $\sigma_\varphi = \pm 30°$ and $\sigma_\theta = \pm 30°$ (Fig. 2.8b). For simplification, all theoretical polarization angles φ_{calc} and θ_{calc} (Fig. 2.8b, Eq. 2.7) and their potential source origin times $\boldsymbol{T}_0$ (Eq. 2.4-2.5) are calculated

using a homogeneous velocity model with an expected minimum mean velocity of $V_P = 2900$ m/s (Mercerat et al., 2010), Table 2.1).

Misinterpretations of the incidence angles due to effects of the free surface are not taken into account during the estimation of polarization angles neither during the location procedure, but are expected to be mostly smaller as compared to the assumed uncertainty σ_θ. As shown by Neuberg and Pointer (2000), for a planar surface (as given at the study site) and small P wave incidences ($< 50°$), the misinterpretation of the true incidence angle from particle motion is maximally 10° but can be significant ($\sim 30°$) when assuming a horizontal P incidence. Even though, the here assumed error σ_θ would even account for the extreme case of incidence angle misinterpretation, we generally excluded incidence angles larger than 50° from inversion (see below).

In addition, the choice of a homogeneous velocity model to interpret the observed polarization angles implies that we do not account for refraction effects of the Dolomite layer that strongly affect the estimated incidence angles (Fig. 2.8). However, the use of a more sophisticated layered velocity model would introduce a significant bias to our results, since the actual velocity structure is complex and associated with strong velocity contrasts, which may change over time due to the developing cavity structure (Section 1.3.4.2 and 2.1.1). As a result, we decided to simply exclude those incidence angles from the inversion procedure that are apparently affected by refraction effects what was evaluated by the comparison to the theoretical incidence angles (Fig. 2.8). This polarization angle selection procedure is described in the following paragraph.

The estimated backazimuth angles at stations 3 and 5 show some ±180° ambiguities. Consequently, for each backazimuth angle determined from these stations, an analogue angle at ±180° was added to the location scheme (Eq. 2.7). At station 62, the backazimuth angle becomes erroneous for sources directly located below it, when the estimated incidence angle is $\theta = 0°$ (Fig. 2.8b). In these cases, the estimated backazimuth angle is excluded from the location scheme (Eq. 2.7). The incidence angles at station 3 are completely excluded from the hypocenter location inversion, due to the presence of predominantly refracted ray paths (Fig. 1.14, 2.5, and 2.8b, Section 1.3.4.2 and 2.1.1). For station 5, the incidence angles with $\geq 50°$ and estimated with respect to a L-value < 0.8 were also excluded from inversion (Fig. 2.8b).

2.3 Location of microseismicity using amplitudes and an attenuation law

The here presented location method was developed in order to provide microseismic event location without using body wave phase arrival times, whose identification is often problematic (Section 1.3.4 and 2.1.1). In this method, simple peak-to-peak amplitudes are used to constrain the hypocenter source location by taking advantage of the amplitude decay with distance as described by a simple attenuation law. Originally, amplitude-based location was introduced by Battaglia and Aki (2003) and was so far applied to volcanic environments (e.g. Battaglia et al., 2005, Di Grazia et al., 2006, Jolly et al., 2002, Taisne et al., 2011, Yamasato, 1997), and ice-quakes (Jones et al., 2013). Compared to these studies, the achievements of the here presented method are generally the inclusion of several frequency bands and an advanced attenuation law calibration procedure, providing a probabilistic solution of the source location problem.

This Section is organized as followed: first the attenuation model is introduced (Section 2.3.1), which represent the fundamental basis of the location approach. Then, the validity of the attenuation law and the underlying attenuation parameters are investigated by means of detailed signal inspections, synthetic seismograms and common attenuation methods (Section 2.3.3), before the probabilistic calibration step is presented in Section 2.3.4. Finally, the probabilistic location scheme is presented in Section 2.3.5. Note that the influence from source radiation on amplitudes and on the location results is discussed in the next Chapter in Section 3.3.

2.3.1 Attenuation model

The influence of attenuation (Section 2.3.2) is assumed to follow a simple attenuation law (e.g. Battaglia and Aki, 2003)

$$A(f) = s(f)A_0(f)\frac{1}{r^n}\exp\left(\frac{\pi f r}{Q V_P}\right), \tag{2.10}$$

describing the exponential amplitude decay with distance, where A, A_0, s, and r are the corresponding signal amplitudes, the source amplitude, the receiver amplification site effect, and the hypocentral distance, respectively. The coefficient n represents the degree of amplitude loss due to geometric spreading, V_P the medium's specific P wave velocity, f the considered

frequency, Q the Quality factor, and exp the exponential function. In order to avoid any assumption about A_0, the attenuation law can be considered for amplitude ratios of a station couple with stations i and j, as proposed by Taisne et al. (2011), that is here expressed in its logarithmic form

$$\log_{10}\left(\frac{A_i(f_k)}{A_j(f_k)}\right) = \log_{10}\left(\frac{s_i(f_k)}{s_j(f_k)}\right) + n\log_{10}\left(\frac{r_j}{r_i}\right) - \frac{\pi f_k}{QV_P}(r_i - r_j)\log_{10}(exp(1)) \quad (2.11)$$

where f_k is the considered frequency band.

2.3.2 Constraints on the attenuation parameters and propagation effects

As introduced in Section 1.3.4.2 and shown by Figure 1.13, the spectral characteristics of the microseismic events reflect significant attenuation and scattering effects. Thanks to the obtained hypocenter locations of the training set (Fig. 2.3), these attenuation effects can be illustrated in more detail with respect to the source and receiver positions and the influence of the brine filled cavity structure (Section 2.3.2.1). In addition, another training data set of isolated 20 events is presented in Section 2.3.2.2, where all events are located below stations 6 1-3 and show very similar waveforms, what allows for detailed determination of seismic velocities and Q-factors. Finally, the characteristics of geometric spreading related to refraction effects at the Dolomite layer are investigated in Section 2.3.2.3.

2.3.2.1 Attenuation and scattering effects for differing source-receiver positions

A typical attenuation effect arising from the cavity structure can be seen by comparing the P waveforms of event 1, recorded at stations 3 and 62 (Fig. 2.1), both located at similar hypocentral distances (Fig. 2.3). The wave field observed at station 3 did not pass through the cavity structure, and therefore the P wave onset appears impulsive and contains significant high frequency energy (Fig. 2.1). In comparison, the wave field recorded at station 62 and 63 clearly traversed the cavity structure or the overlying fractured Marl layer at the cavity roof, such that its higher frequency content almost vanishes and the P wave onsets appear emergent. In addition, peak-to-peak P and S wave amplitudes are significantly reduced at the most distant station 5, clearly documenting the presence of strong attenuation effects.

In Figure 2.9, the spectral characteristics of the 54 isolated events are represented by their smoothed average Fast Fourier transform (fft) spectra, calculated for each station. The average spectra are calculated for the frequency range of $10 - 1000$ Hz, describing the mean

spectral amplitudes for each 10 Hz interval. The average spectra of the 54 events show the usual frequency content of around $20 - 200$ Hz as consistent with observations from Section 1.3.4.1. The mean of the relative standard deviation (RSD) of the 54 event spectra with respect to the average spectrum at frequencies of 20–200 Hz is similar for all stations and smallest at station 2 RSD $\sim 72\%$ and highest at station 62 RSD 88%. As a result, it can be concluded that the average spectra represent a relative good first order approximation of the general spectral characteristics of the 54 events.

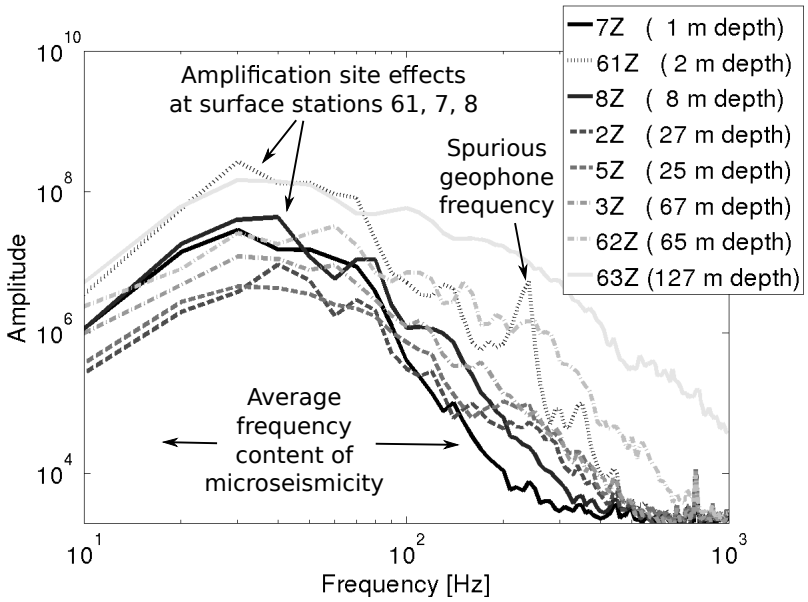

Figure 2.9: Spectral signal characteristics. Smoothed average spectra calculated for the Z component at each station for the 54 located events (Fig 2.3). The average spectra are calculated over the frequency range of $10 - 1000$ Hz, representing the mean spectral amplitudes for each 10 Hz interval.

The average spectra illustration provides a first constraint for the quantification of the governing attenuation characteristics (Fig. 2.9). All average spectra at each station show a consistently decreasing spectral shape especially at higher frequencies of > 100 Hz. Secondly, the absolute spectral amplitudes at each station are clearly related to the mean hypocentral distance, reflected by the increasing amplitudes at deeper stations (stations 3, 62, 63) and the decreasing mean seismic energies at stations located along the cavity borders and at shallower depths (stations 2, 5). In addition, at lower frequencies < 100 Hz, clear amplification site effects can be observed at surface stations 61, 7 and 8, probably resulting from resonance inside the unconsolidated soil.

2.3.2.2 Seismic velocities and Q factors

In order to constrain the parameters of the attenuation law of Equation (2.11), an additional data training set of 20 isolated events was selected and analyzed in more detail whose results are here briefly summarized, and will be continuously discussed in the following thesis

Chapters. The 20 events show similar phase and spectral signatures as compared to the 54 events (Section 2.1), occurred all over the entire the microseismic crisis in 2008 (March-May) (Table B.2) and comprise the largest events directly located below stations 6 1-3 (size was approximated from $30 - 90$ Hz, peak-to-peak amplitudes at station 62). Event selection was performed by using the polarization-based approach (Section 2.2), looking for events associated with an incidence angle of $\theta = 0$ from station 62. Event source depths were defined from manually picked S minus P $t_p - t_s$ travel time differences observed from station 62 (using seismic velocities $V_{p,s}$ as documented below), where an almost continuous decrease in source depth can be observed (Table B.2, see also Chapter 4). In addition, for all events, P wave amplitudes are much stronger in amplitude as compared to S waves what is related to systematic source radiation characteristics as later discussed in in detail in Chapter 3.

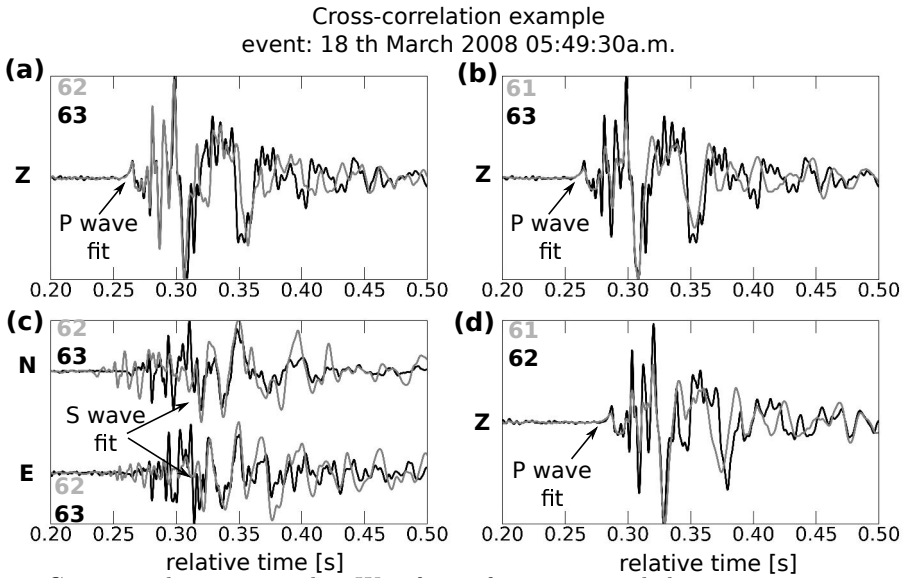

Figure 2.10: Cross-correlation example. Waveforms for one event below stations 6 1-3 with respect to the vertical (Z) and horizontal station components (N (North), E (East)) for (a),(b),(d) P and (c) S waves. Waveforms for both stations of one considered station couple (black and gray lines) are aligned using the time lags $\tau_{p,s}$ obtained from the maximum correlation coefficient $C(\tau_{p,s})$.

The major benefit of these events for attenuation parameter determination is that at stations 6 1-3, waveforms for P wave are mainly contained in the vertical station components and S waves in the horizontal components, and that waveforms are remarkably similar among the stations. (Fig. 2.10). From the similarity of waveforms it is possible to precisely estimate travel time difference of P and S waves (τ_p and τ_s, respectively) by looking for the maximum

correlation coefficient $C(\tau)$ of the cross-correlation between stations i and j

$$C(\tau_{p,s}) = \sum_{k=0}^{n} \tilde{u}_i[t]\tilde{u}_j[t + \tau_{p,s}], \tag{2.12}$$

where $\tilde{u}$ is the normalized (divided by maximum magnitude sample), $10 - 400$ Hz filtered component trace, containing n time samples (sampling rate is 5 kHz). The wave travel paths are very similar and close to vertical for all events so that the seismic velocities between the stations 6 1-3 can be directly calculated from the differential travel times ($\tau_{P,S}$) and the differences in receiver depth for each station pair Δr by $V_{P,S} = \Delta r/\tau_{P,S}$, as shown by Figure 2.11.

P wave velocities V_P were estimated using the Z components of all stations couples 61-62, 61-63, and 62-63 and all of the 20 events (Fig. 2.11a). For all events, the estimated velocities are very similar (Fig. 2.11a, Table 2.2 and B.2), demonstrating that velocities are constant over time during the microseismic crisis in 2008. P wave velocities between station 62 and 63 are found with $V_P = 2900$ m/s, what is consistent with the velocity model of Table 2.1. However, P wave velocities at smaller depth (using station 61 and 62) are found with $V_P = 1690$ m/s, which is significantly smaller as compared to this model (Table 2.1). On the other hand, this results is consistent with results from an high resolution tomography campaign, documenting velocities of $V_p = 1700$ m/s for the uppermost layers (< 50 m depth) of the overburden (Kosecki et al., 2010, Piwakowski et al., 2006) (Table B.2).

Next to the low P wave velocities for the uppermost layers, I found very small S wave velocities ($V_s = 1300$ m/s) for the layer between stations 62 and 63 (Fig. 2.10 and 2.11b, Table 2.2), yielding a significantly increased V_p/V_s-ratio of ~ 2.3 as compared to the results of laboratory measurements (Nothnagel, 2003) (Table 2.1). S wave velocities were estimated from the horizontal components (North (N) and East (E)) (Fig. 2.10), but could not be reliably estimated for all of the 20 events (Fig. 2.11b, Table B.2). Difficulties in its determination arose especially for events of shallow source depths, where $t_p - t_s$ travel time differences become very small at station 63 and slight refraction effects (P-SV conversions) appear. Nonetheless, S wave velocity estimates are reliable (Fig. 2.10c) and temporally constant (Table B.2). Since no horizontal component are available at station 61 unfortunately no S wave velocities could be determined for the uppermost sedimentary layers.

Finally, the obtained velocities are used to find constraints on the Q-factor using the spectral

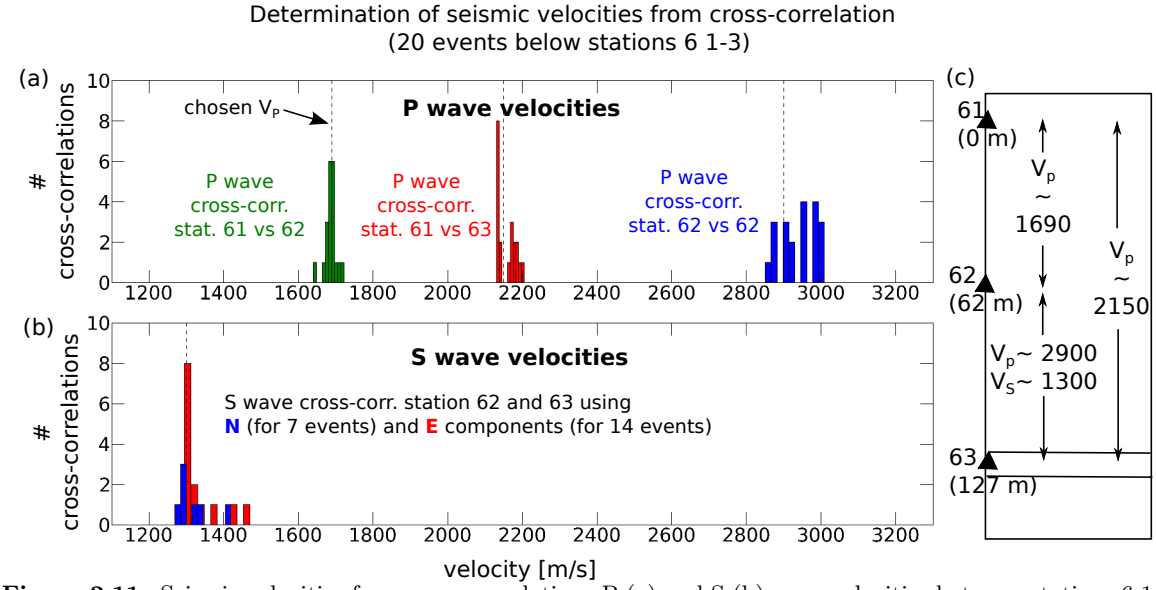

Figure 2.11: Seismic velocities from cross-correlation. P (a) and S (b) wave velocities between stations 6 1-3 (colored histograms) were obtained from time-lags of P and S wave arrival, determined from waveform cross-correlation (Eq. 2.12 and Fig. 2.10) for 20 events located below stations 6 1-3 (Table B.2). Cross-correlations and velocity determination for S waves, based on the horizontal components (N (North), E (East)) was not possible for all of the 20 events (see Table B.2).

amplitude ratio technique (e.g. Feustel, 1998, Mercerat, 2007) based on Equation (2.11)

$$Q_{p,s} = \pi \Delta r / (V_{p,s} \mu), \tag{2.13}$$

where μ is the slope of the regression curve of the amplitude spectral ratios for P and S waves for the 20 events as a function of frequency f (Fig. 2.12, Table 2.2). Before the fft spectrum calculation, P and S wave phase were isolated using a hanning window of 0.2 s length, providing a spectral resolution of 5 Hz, while the regression analysis for $A_i(f)/A_j(f)$ was applied for reliable, noise-free frequency bands f_k (Fig. 2.12). The final values for Q_p and Q_s were determined by using the average of the spectral ratio for all 20 events (Fig. 2.12). In order to estimate the variability and error of these average Q-factor values, Q-factors were also calculated for each single event (Table 2.2 and B.2).

The most reliable result is obtained for the Q-factor for P waves by using the spectral ratio of stations 62 and 63 (Fig. 2.12a, Table 2.2 and B.2) where the slope μ is remarkably stable for a wide frequency band ($50 - 500$ Hz). The estimates for Q_s (Fig. 2.12b) were obtained by using all horizontal station components (N and E) for stations 62 and 63, but are less reliable, since the frequency band for regression needed to be restricted to $50 - 300$ Hz. The finally estimated value Q-factor for S waves was found with $Q_s \sim 24$ what is almost the half of the Q-factor found for P waves.

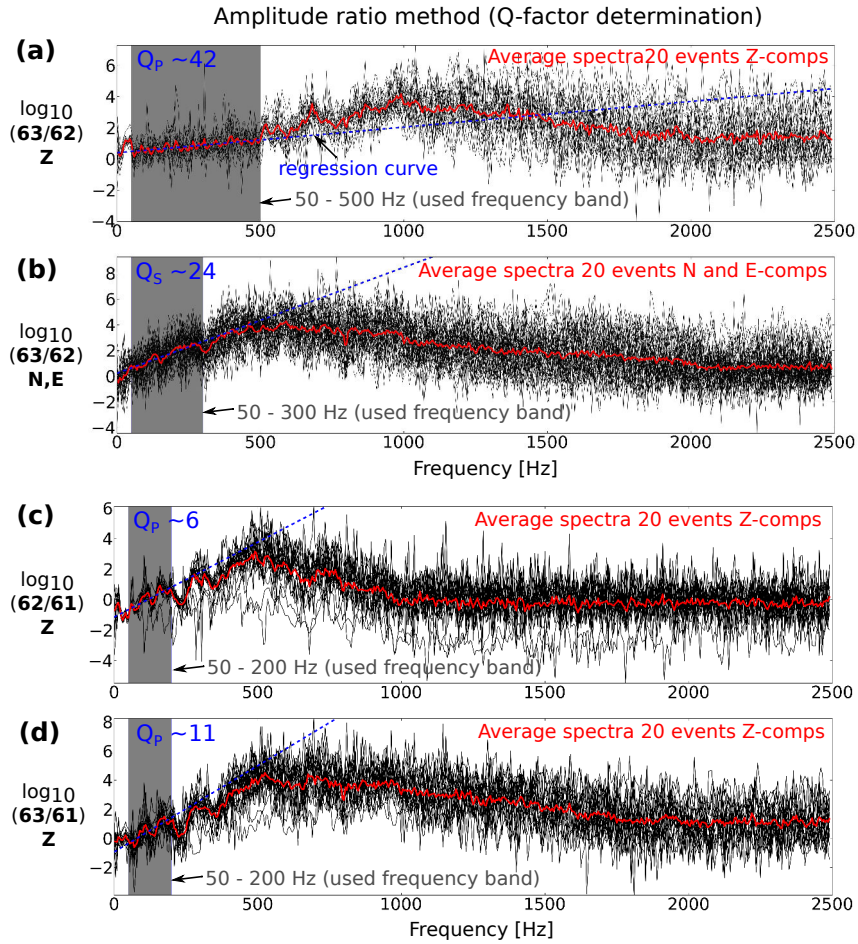

Figure 2.12: Q-factor determination. (a)-(d) Spectral ratios between stations 6 1-3 for the 20 events (black lines) and the average spectral ratio (red line). Indicated Q factors were calculated from the slope μ of the regression curve (dashed blue line) for a chosen frequency band (gray shaded area) using Equation (2.13) and velocities from Table 2.2 and B.2. For Q_s calculation, horizontal station components N and E for all 20 events were used.

Small Q_p factors around a value of 10, as obtained by using station 61 (Fig. 2.12c-d), need to be regarded with caution, since station 61 is located at the surface where frequency dependent site effects are observed, which might affect the estimation of μ, and thus Q (Fig. 2.9, Eq. 2.11). As visible from the average spectrum of station 61 (Fig. 2.9), strong amplification effects can be seen for lower frequency, but much less for higher frequencies (> 100 Hz), what might significantly in increase/decrease the slope of the regression curve obtained from the ratio to the "none" amplified spectra of stations 62 and 63. In addition, the frequency band needed to be chosen very narrow with $50 - 200$ Hz in order to avoid the influence of spurious geophone frequencies visible at around 250 Hz at station 61 (Fig. 2.9). On the other hand, these estimates are consistent with the findings of Mercerat (2007), Mercerat et al. (2010) who documented $Q_p = 10 - 30$ by using calibration shot data.

Taking these results together, there are three major observations when regarding the obtained elastic parameters (Table 2.2). (i) First, P wave velocities are very low in the uppermost sedimentary layers ($\lesssim 62$ m depth), which generally corresponds to P wave propagation in

Table 2.2: Estimated velocities and Q-factors. First column indicates the stations used for the cross-correlation and the spectral ratio approach. Errors for estimated velocities corresponds to the widest deviation in velocity values observed for all analyzed event as shown in histograms in Figure 2.11 and listed in Table B.2, while final velocity values correspond to the mean of all determined velocity values. Errors for Q-factors correspond to the standard deviation of all Q-factor values determined for the 20 events (Table B.2), while the optimal values were determined by using the average spectrum of the 20 events (Fig. 2.12).

used station pairs	Depth [km]	V_p [km/s]	V_s	V_p/V_s	Q_P	Q_S
61 and 62	$0.0 - 0.62$	1.69 ± 0.05	/	/	6 ± 3	/
61 and 63	$0.0 - 0.127$	2.15 ± 0.05	/	/	11 ± 3	/
62 and 63	$0.62 - 0.127$	2.9 ± 0.1	1.3 ± 0.12	2.3 ± 0.3	42 ± 14	24 ± 7

water. Even though the origin of these very low P velocities remains rather speculative it can be assumed that these sedimentary layers represent the major groundwater aquifer what is consistent with piezometric ground water level measurements obtained by SOLVAY (Fig. 1.4), documenting ground water levels at approximately $\sim$ 30 m depth (e.g. Cao, 2011). Another hypothesis might be also that groundwater accumulated due to subsidence of the overburden over the cavity formation building a kind of groundwater trough (Mercerat, 2007).

(ii) Secondly, S wave velocities and Q factors are almost two times smaller than for P waves (Table 2.2), documenting an abnormally high S wave attenuation behavior, what is consistent with the observed decreasing S/P amplitude ratios with increasing frequency (Fig. 2.6). S waves are generally more sensitive with respect to the consolidation and saturation state of sedimentary layers. As a result, it must be concluded that also sedimentary layers between station 62 and 63 are in an advance unconsolidated or fluid-saturated state.

(iii) Thirdly, it is important to note that the attenuation characteristics, as velocities and Q-factors (Table 2.2 and B.2), for the sedimentary layers above the Dolomite layer do not change within the microseismic crisis in 2008 (see also Chapters 4 and 5). Thus, the attenuation behavior seems to be constant with time, what is a pre-requisite for the reliability of amplitude-based location.

2.3.2.3 Determination of the theoretical coefficient of geometric spreading

As introduced in Sections 1.3.4.2 and 2.1, the presence of the stiff, high-speed Dolomite layer is the origin of significant refraction effects observed in the seismic body wave field (Fig. 1.13, 1.14 and 2.5). In this Section it is aimed to quantify the influence of these refraction effects on the shape of the propagating wave front, and thus the geometric attenuation behavior. In a homogeneous medium, the geometric spreading coefficient is generally $n = 1$ for body waves describing a spherically propagating front (e.g. Aki and Richards, 2002). However, in

cases of refracting wave fields geometric attenuation can become more complicated and more important, resulting in n values of bigger than one. Theoretical studies showed that $n = 2$ for critically refracted P waves (head waves) (Aki and Richards, 2002), and $n = 1.5$ for direct P waves emitted from sources located below a refractor (Campillo et al., 1984). Also regional empirical studies reported increased geometric spreading coefficients $n = 1.77$ as estimated from Moho head waves Pn (Zhu et al., 1991).

In order to test for such complexities in geometrical spreading at the study site, a simple analysis based on synthetic seismograms was performed (Fig. 2.13). The test is very similar to the one already presented in Figure 1.14 (Section 1.3.4.2), while a simple isotropic (explosion) source mechanisms was used (Fig. 2.13). Consequently, in this approach only P wave characteristics are studied. In order to determine the coefficient of geometric spreading n_{dol} related to refraction effects, I compared the apparent radiated energies (temporal amplitude integration over all seismic traces) for a homogeneous E_{hom} and a layered velocity E_{dol} model. When regarding Eq. (2.11) and assuming that the differences in intrinsic attenuation are negligibly small for both velocity models (right-hand side terms in Eq. (2.11)), n_{dol} can be determined by

$$\begin{aligned} \log(E_{hom}/E_{dol}) &= \log(r^{n_{dol}-n_{hom}}) \\ n_{hom} &= 1 \\ n_{dol} &= (\log(E_{hom}/E_{dol}) + \log(r))/\log(r), \end{aligned} \tag{2.14}$$

where r is the hypocentral distance (Fig. 2.13).

In the results in Figure 2.13c, it can be observed that n_{dol} is always bigger than 1 reflecting the refraction related complexities in the wave front and stronger magnitudes of geometric spreading. In addition, magnitudes of geometric spreading significantly increase when going to larger epicentral distances of around 75 m, where the coefficient n increases from ~ 1.2 to ~ 1.5 (Fig. 2.13c).

2.3.3 Amplitude calculation, correction, and distribution

Signal amplitudes are determined by the peak-to-peak amplitudes on the vertical station components (Fig. 2.1) for four different frequency bands f_k with increasing center frequency: $f_1 = 30$–90 Hz, $f_2 = 70$–210 Hz, $f_3 = 100$–300 Hz, and $f_4 = 140 - 420$ Hz. The root mean square (RMS) amplitude approximation is less appropriate to determine signal energy from

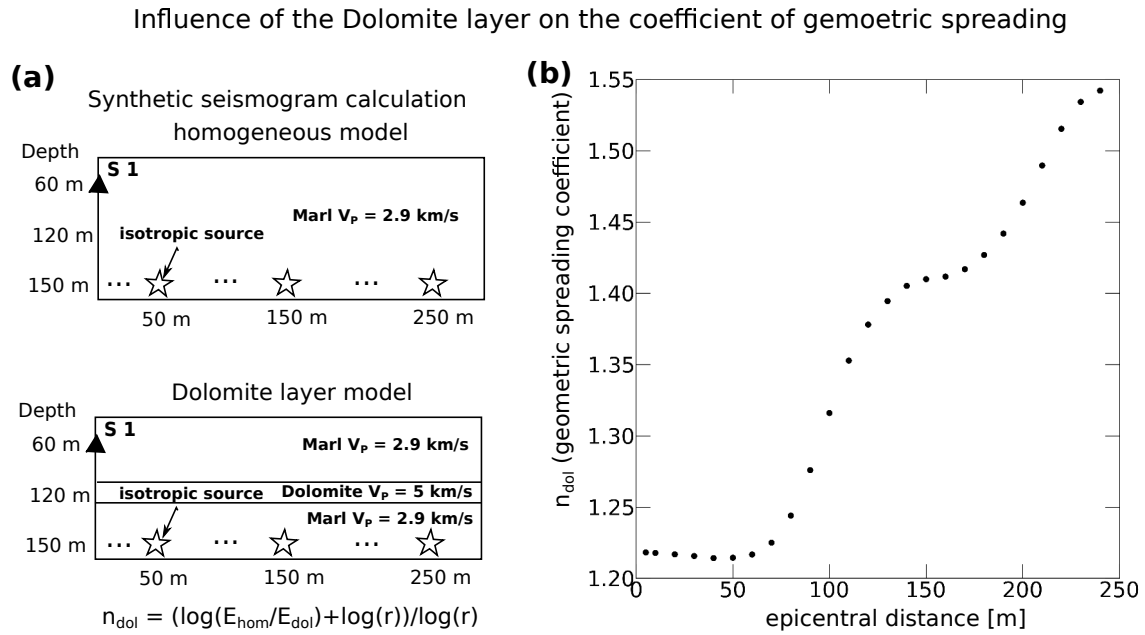

Figure 2.13: Refraction related coefficient of geometric spreading n_{dol}. (a) Illustration of synthetic seismograms calculated by means of AXITRA (Coutant, 1989a,b) (see appendix D) for different source receiver locations assuming an isotropic source (explosion), for one homogeneous and one layered velocity model. (b) Coefficient of geometric spreading for the layered velocity model n_{dol} as a function of epicentral distance, calculated from Equation (2.14).

the observed microseismic data as it depends on the chosen time window for a seismic event. Regarding the complicated and strongly varying phase signature of tremor-like swarming sequences (Section 1.3.4), an accurate determination of the starting and end time of a seismic event is generally difficult.

Using the 54 isolated events of well constrained hypocenter locations (Fig. 2.3), the ratio of amplification site effects (Eq. 2.11, Fig. 2.9, Section 2.3.2.1) with respect to one station couple was determined by using the amplitude ratios for those events that are located at very similar hypocentral distance (±20 m) with respect to both stations. If both station-hypocenter distances are of same order, the attenuation effects can be neglected and the observed amplitude ratios represent a first approximation of the ratio of amplification site effects (Eq. 2.11). In this way, the amplification site effect ratio was determined with respect to each station pair by using the mean of the amplitude ratios of the selected events.

Even though this correction for amplification site effects as well as the assumed attenuation law do not account for 3-D attenuation effects introduced by the cavity zone (e.g. Fig. 2.1, Section 2.3.2), the final amplification corrected amplitude ratios for the 54 events show a clear functional relationship with the distance-depending terms of Equation (2.11) (Fig. 2.14). As a result, the amplitude decay with distance is smooth, and the 1-D attenuation law seems

to be an appropriate choice to model the observed attenuation effects (Section 1.3.4.1 and 2.3.2) without accounting for 3-D attenuation effects (Section 2.3.2.1). At higher frequencies, variations of amplitude ratios become significantly larger compared to lower frequencies, which agrees with the observed increase of attenuation effects at frequencies of $\geq$ 100 Hz (Fig. 2.9 and 2.14, Section 2.3.2.1).

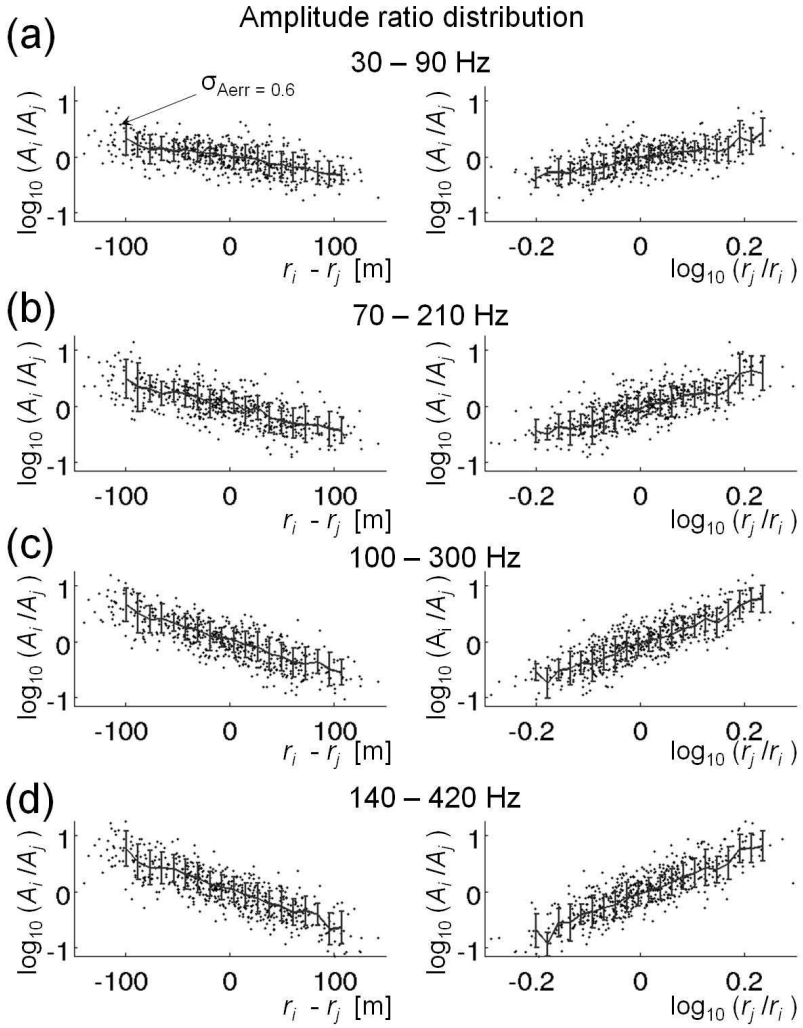

Figure 2.14: Effects of attenuation on amplitudes. Peak-to-peak amplitude ratio distributions versus distance terms described in Equation (2.11), with respect to all station couples and neglecting the stations at the cavity center (6 1-3). Error bars indicate the measure of the uncertainty in the amplitude ratio determinations σ_{Aerr} and represent the standard deviations related to a mean value (continuous black line) calculated at 30 points along the amplitude ratio distribution.

2.3.4 Calibration of an attenuation law (probabilistic forward model)

The 54 located events were used to calibrate the attenuation law represented by the parameters n and Q (Fig. 2.3, Eq. 2.11). I used a probabilistic formulation for the parameter search of n and Q, represented by the posterior probability density σ, analogically to Equation (2.1)

(Tarantola, 2005, Tarantola and Valette, 1982)

$$\sigma(Q,n) = \kappa\rho_M(Q,n)\rho_D(g(Q,n)), \tag{2.15}$$

where the functional relationship $d = g(m)$ between the elements of the model M and data space D is given by Equation (2.11). It is assumed that the uncertainties in the forward simulation of Equation (2.11) are generally negligible compared to the errors in the observed amplitude ratios and expected hypocenter locations (Fig. 2.3, Section 2.1). In the attenuation model, V_P is valued as the expected minimum mean velocity of 2900 m/s (Mercerat et al., 2010) (Table 2.1) what is generally consistent with the V_P velocities obtained in Section 2.3.2. Furthermore, ρ_M is considered to be uniform with equal a priori probabilities within the intervals of the Cartesian product $\boldsymbol{Q} \times \boldsymbol{n}$ of the parameter sets $\boldsymbol{n} = \{0.3, 0.4, \ldots, 2.9, 3.0\}$ and $\boldsymbol{Q} = \{1, 2, 3, \ldots, 299, 300\}$. Model space sampling is based on a grid search where the probability density ρ_D is defined as the exponential distribution of absolute differences ($l1$-norm) of the observed and calculated amplitude ratios $\boldsymbol{A}$, so that it follows

$$\sigma(f_k, \boldsymbol{Q} \times \boldsymbol{n}) = \kappa \exp\left\{ -\sum_j \sum_i \frac{|\boldsymbol{A}^i_{obs}(f_k, x_j, y_j, z_j) - \boldsymbol{A}^i_{calc}(f_k, x_j, y_j, z_j; \boldsymbol{Q} \times \boldsymbol{n})|}{\sigma_{Aerr}} \right\}, \tag{2.16}$$

where i is the number of observed amplitude ratios for all station couples with respect to an event j from the 54 located events with coordinates x, y, z (Fig. 2.3), and σ_{Aerr} represents the uncertainties in the observed amplitude ratios, the assumed attenuation model, and the hypocentral location errors (Section 2.1). The value for σ_{Aerr} was estimated at ± 0.6, corresponding to the maximum observed amount of scattering in the amplitude ratios (maximal standard deviation), relative to the receiver distance ratios and differences (Fig. 2.14).

The shapes of the resulting PDFs indicate a trade-off between parameters $n(f_k)$ and $Q(f_k)$ for each frequency band f_k (Fig. 2.15a). As a result, the stated inverse problem (Eq. 2.15) is severely ill-posed with respect to the assumed attenuation model. In order to resolve this trade-off, it was assumed that the parameter n (geometric spreading) is frequency-independent, as predicted by the attenuation model (Eq. 2.11). As a result, I calculated the marginal PDF for n with respect to all frequency bands f_k by

$$\sigma_{\boldsymbol{n}}(\boldsymbol{Q} \times \boldsymbol{n}) = \int_{\boldsymbol{Q}} \sigma(f_1; \boldsymbol{Q} \times \boldsymbol{n})\sigma(f_2; \boldsymbol{Q} \times \boldsymbol{n})\sigma(f_3; \boldsymbol{Q} \times \boldsymbol{n})\sigma(f_4; \boldsymbol{Q} \times \boldsymbol{n}), \partial\boldsymbol{Q} \tag{2.17}$$

which is shown in Figure 2.15b with a maximum likelihood at $n = 1.7$. The increased value of the coefficient of geometric spreading, departing from $n = 1$ for a spherically expanding body wave, is consistent with the findings presented in Figure 2.13 and Section 2.3.2.3, and thus documents probably complexities in the wave front introduced by refraction at the Dolomite layer.

The marginal probability for n, as representative for all frequency bands, was then used in order to determine the marginal probabilities for $Q(f_k)$ at each frequency band f_k by

$$\begin{aligned}
\sigma_{\boldsymbol{Q}}(f_1; \boldsymbol{Q} \times \boldsymbol{n}) &= \int_{\boldsymbol{n}} \sigma(f_1, \boldsymbol{Q} \times \boldsymbol{n}) \sigma_{\boldsymbol{n}}(f_{2-4}, \boldsymbol{Q} \times \boldsymbol{n}) \partial \boldsymbol{n} \\
\sigma_{\boldsymbol{Q}}(f_2; \boldsymbol{Q} \times \boldsymbol{n}) &= \int_{\boldsymbol{n}} \sigma(f_2, \boldsymbol{Q} \times \boldsymbol{n}) \sigma_{\boldsymbol{n}}(f_{1,3-4}, \boldsymbol{Q} \times \boldsymbol{n}) \partial \boldsymbol{n} \\
\sigma_{\boldsymbol{Q}}(f_3; \boldsymbol{Q} \times \boldsymbol{n}) &= \int_{\boldsymbol{n}} \sigma(f_3, \boldsymbol{Q} \times \boldsymbol{n}) \sigma_{\boldsymbol{n}}(f_{1-2,4}, \boldsymbol{Q} \times \boldsymbol{n}) \partial \boldsymbol{n} \\
\sigma_{\boldsymbol{Q}}(f_4; \boldsymbol{Q} \times \boldsymbol{n}) &= \int_{\boldsymbol{n}} \sigma(f_4, \boldsymbol{Q} \times \boldsymbol{n}) \sigma_{\boldsymbol{n}}(f_{1-3}, \boldsymbol{Q} \times \boldsymbol{n}) \partial \boldsymbol{n}
\end{aligned} \tag{2.18}$$

The marginal probabilities for $Q(f_k)$ at each frequency band are shown in Figure 2.15b. The obtained maximum likelihoods indicate a slight dependence of Q with frequency. Q factors are generally found in the range of 40–60, which generally agrees with the results obtained in Section 2.3.2.2 for P wave of $Q_P \sim 42$ (Table 2.2). As a result, it can be concluded that most analyzed peak-to-peak amplitudes, estimated from the vertical station components, are related to P wave amplitudes, what is probably also favored by the abnormal high attenuation behavior of S for higher frequencies (Fig. 2.6, Table 2.2, Section 2.3.2.2).

The uncertainties in Q's maximum likelihoods decrease at increasing frequencies, as shown by the bell-shaped PDF curves that clearly become less dispersive and have more symmetric geometries (Fig.2.15b). This observation might indicate that intrinsic attenuation dominates at higher frequencies. For lower frequencies, between 30 and 90 Hz, the maximum likelihood for Q converged to infinity, indicating that attenuation is predominantly contributed by geometric spreading, while intrinsic attenuation is negligible (Fig. 2.15b). The predominance of geometric spreading at lower frequencies and predominance of intrinsic attenuation at higher frequencies is quite reasonable considering Equation (2.11). For lower frequencies, hypocentral distances and wavelengths are of the same order of magnitude such that the magnitude of intrinsic attenuation becomes comparatively small.

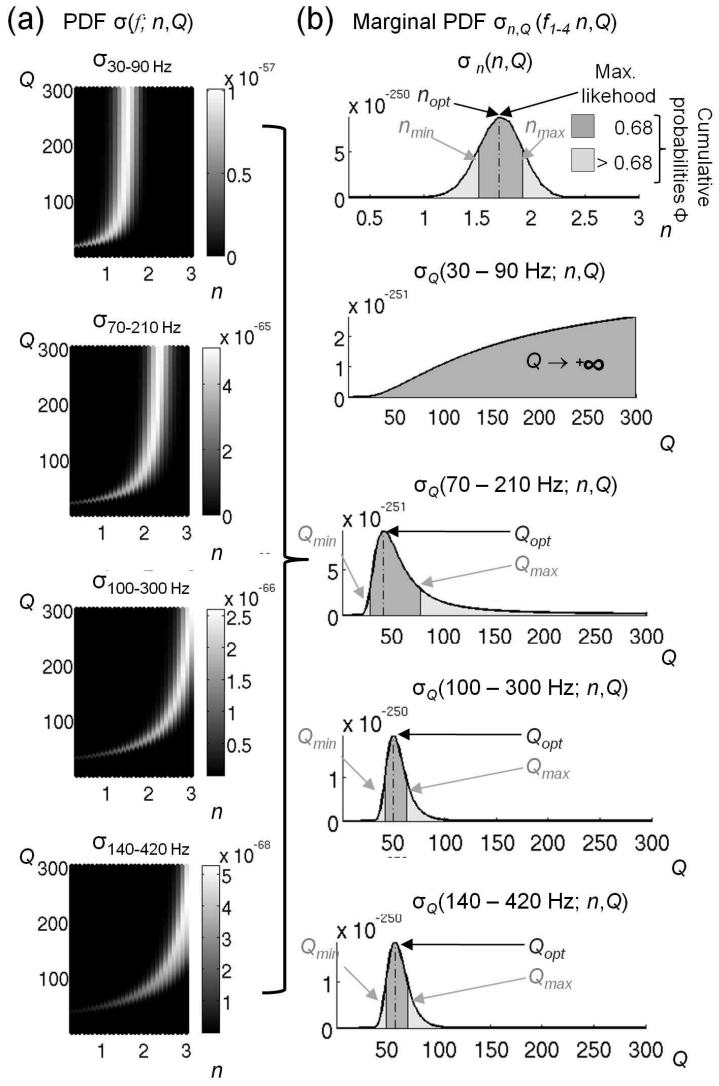

Figure 2.15: Probabilistic estimates of n and Q. Parameter estimation for n and Q; (a) PDFs with respect to parameters n and Q are calculated for four frequency bands using Eq. (2.16). (b) Marginal PDFs for n calculated from Equation (2.17) (upper panel), and for Q with respect to all frequency bands as calculated from Equation (2.18) (panels below). Named indices (min, opt, max) for n and Q correspond to the parameters values (Table 2.3) which represent the region (dark gray shaded area) of the maximum likelihood (opt) (dashed line) and those located next to it (min and max) (light gray shaded areas) defined by the cumulative probability equal to 0.68 (Section 2.3.4).

For the attenuation estimations, and in the following location approach, stations 61, 62 and 63, located at the center of the cavity, were not considered, because amplitudes observed at both stations are more sensitive to absolute source depths compared to stations located along the cavity border. Source depth estimations by our classical location approach for the 54 events are based on significant uncertainties (Section 2.1), which might introduce a bias in our results when including stations 62 and 63.

Furthermore, in the case of station 63, the wave field observed on its vertical component is complicated and not dominated by P waves, as the case for the other stations, but comprises multiple P-SV conversions or inhomogeneous waves (Fig. 1.14 and 2.5, Section 1.3.4.2 and 2.1). For station 62, incidence angles of the wave field and epicentral distances are significantly smaller than compared to stations surrounding the cavity zone (Fig. 2.5). As a result, station

62 is generally less affected by refraction related complexities in the observed expanding wave front so that geometric attenuation in the wave field is less significant as compared to the other stations (Fig. 2.13, Section 2.3.2.3). Correspondingly, I found significantly smaller values for n when repeating the calibration procedure including amplitude ratios of station 62.

2.3.5 Probabilistic location based on amplitudes

The calibrated attenuation law, based on parameters n and Q, can now be used to calculate the theoretical amplitude ratios, which will then be compared with the observed ratios to determine the hypocenter locations. The location procedure is formulated in a probabilistic manner with consideration of uncertainties in n and Q. The formulation of the corresponding PDF expression $\sigma_{amp}(\boldsymbol{X}, \boldsymbol{Y}, \boldsymbol{Z})$ is analogue to Equation (2.7) (Tarantola, 2005, Tarantola and Valette, 1982) as stated for the polarization-based approach, using the same Cartesian coordinates of the potential source locations $\boldsymbol{X}, \boldsymbol{Y}, \boldsymbol{Z}$ associated with equal a priori probabilities to equal volumes (Section 2.2.3).

For simplification, the uncertainties to be given to the parameters n and Q were not the continuous marginal PDFs, but were extracted from the PDFs as three possible values for each parameter, defined as the "min", "opt" and "max"' values of the respective PDF shown in Figure 2.15b and Table 2.3. These values are calculated from the PDFs so that the "opt" corresponds to the maximum likelihood, and the "min" and "max" bracket the 0.68 probability level. For the three highest frequency ranges, both Q and n, are thus represented by $m = 3$ possible values, each of them having a specific weight (see Table 2.3), leading to $m = 9$ possible combinations; for the lowest frequency range, Q is not defined, so that only $m = 3$ possible cases arise (values of n).

Thus, for inversion, a set of $m = 9$ entries $\boldsymbol{E}(f_k) = \{(n_1, Q(f_k)_1), (n_2, Q(f_k)_2), \ldots, (n_m, Q(f_k)_m)\}$, represent all possible combinations of the three parameter values for n and Q obtained for each frequency band, except for the frequency band of $30 - 90$ Hz for which $m = 3$. Each entry of $\boldsymbol{E}(f_k)$ is associated with a weight $\boldsymbol{w}(f_k)_m = \Phi(\boldsymbol{E}(f_k)_m)/\Phi(\boldsymbol{E}(f_k))$ corresponding to the cumulative probabilities Φ found for each parameter combination (Table 2.3). Then the posterior probability density for one frequency band f_k and one seismic event is obtained by the weighted product of independent probability densities calculated for each parameter combination and the $l1$-norm distances between the observed and calculated amplitude

ratios $\boldsymbol{A}$ for a station couple i

$$\sigma(f_k;\boldsymbol{X},\boldsymbol{Y},\boldsymbol{Z}) = \prod_i \left[\frac{1}{m} \sum_m \boldsymbol{w}(f_k)_m \kappa \exp\left\{ \frac{|\boldsymbol{A}^i_{obs}(f_k) - \boldsymbol{A}^i_{calc}(\boldsymbol{E}(f_k)_m;\boldsymbol{X},\boldsymbol{Y},\boldsymbol{Z})|}{\sigma_{Aerr}} \right\} \right]. \tag{2.19}$$

The final posterior probability density of hypocenter location σ_{amp} is then found by the conjunction of the probability densities (Tarantola, 2005, Tarantola and Valette, 1982) for all frequency bands

$$\sigma_{amp}(\boldsymbol{X},\boldsymbol{Y},\boldsymbol{Z}) = \frac{1}{\upsilon} \prod_k \sigma(f_k;\boldsymbol{X},\boldsymbol{Y},\boldsymbol{Z}), \tag{2.20}$$

where υ is a normalization constant.

Table 2.3: Three n and Q values, and their corresponding weights are shown for each frequency band, related to the region of the maximum likelihood locations and those next to it (Fig. 2.15b, Section 2.3.4).

Frequency [Hz]	n_{min}	$\boldsymbol{w}_{nmin}$	n_{opt}	$\boldsymbol{w}_{nopt}$	n_{max}	$\boldsymbol{w}_{nmax}$	Q_{min}	$\boldsymbol{w}_{Qmin}$	Q_{opt}	$\boldsymbol{w}_{Qopt}$	Q_{max}	$\boldsymbol{w}_{Qmax}$
$30-90$	1.51	0.17	1.7	0.67	1.92	0.16						
$70-210$	1.51	0.085	1.7	0.335	1.92	0.08	28	0.025	41	0.325	78	0.15
$100-300$	1.51	0.085	1.7	0.335	1.92	0.08	42	0.04	50	0.335	63	0.125
$140-420$	1.51	0.085	1.7	0.335	1.92	0.08	49	0.05	58	0.34	70	0.11

2.4 Re-location of the training set

In order to estimate the performance and associated uncertainties of the developed location methods, I re-located all 54 selected events (Fig. 2.3) using (i) the probabilistic amplitude-based method $\sigma_{amp}(\boldsymbol{X},\boldsymbol{Y},\boldsymbol{Z})$ (Section 2.3), (ii) the probabilistic polarization-based method $\sigma_{pol}(\boldsymbol{X},\boldsymbol{Y},\boldsymbol{Z})$ (Section 2.2) and (iii) the probabilistic conjunction of the latter two $\sigma_{amp+pol}(\boldsymbol{X},\boldsymbol{Y},\boldsymbol{Z}) = \frac{1}{\upsilon}\sigma_{amp}(\boldsymbol{X},\boldsymbol{Y},\boldsymbol{Z})\sigma_{pol}(\boldsymbol{X},\boldsymbol{Y},\boldsymbol{Z})$ where υ is a normalization constant. Figure 2.16 shows examples of two good location results (events 3 and 4, Fig.2.3), and two less accurate location results (events 1 and 5, Fig.2.3).

For the good location results, epicenter locations are well resolved from the amplitude- and polarization-based approaches and consequently are very well resolved when using the conjunction of both methods (Fig. 2.16). In contrast, source depth estimations are poorly constrained using the amplitude approach, visible from the 0.34, 0.68, and 0.99 contours of the cumulative probabilities that generally cover the entire range of explored source depths. The weak constraint on source depths from this approach is generally due to the poor resolution with depth of used stations. Accurate estimates of the source depths can be partially

obtained from the polarization-based approach, when backazimuth angles are available for all three stations and when reliable incidence angles are available for stations 5 and 62. When combining the probability densities for both approaches, the source depth estimations are biased by the amplitude approach. The strong effect of the amplitude-based approach on the maximum likelihood source depth estimations is related to the fact that the cumulative probabilities are spatially more extended for the polarization-based approach compared to the amplitude-approach.

A resulting deviation from the expected epicenter location is shown for event 5 using the amplitude-based approach, and for event 1 using the polarization-based approach (Fig. 2.16). In the case of event 5, the epicenter location error probably results from local heterogeneities at the cavity roof, leading to wave scattering effects (Fig. 2.1 and 1.13, Section 2.3.2), which are not considered in our simple 1D attenuation law (Eq. 2.11). In the case of event 1, the epicenter location is uncertain using the polarization-based approach due to the absence of calculated polarization angles at stations 5 and 62. Also in this case, local attenuation and wave scattering effects might be be responsible for the non-determination of polarization angles at stations 5 and 62 (Fig. 2.1 and 1.13, Section 2.3.2). As already mentioned, also source effects play a role in this respect, which are later discussed in Section 3.3.

Nonetheless, the shortcomings and epicenter misestimations for both location methods can be significantly improved by combining them (Fig. 2.16). Correspondingly, for event 5, the shape of the 0.34 cumulative probability contour of the amplitude-based approach significantly reshapes towards the expected epicenter location when combining it with the polarization-based approach. Similarly, a well constrained epicenter location is drawn from the cumulative probabilities for event 1 upon combining both approaches.

The absolute epicenter and hypocenter location errors are calculated from the distance deviations between the maximum likelihood locations obtained by the used method and the classical location approach (Fig. 2.3, Section 2.1). The absolute errors in the hypocenter locations for all 54 events are presented in Figure 2.17. It should be noted that the calculated absolute errors are additionally affected by the uncertainties in the event locations calculated by the classical approach, being of the order of ± 50 m in the horizontal and even larger in the vertical coordinates, respectively (Section 2.1).

The absolute errors in the maximum likelihood epicenter and hypocenter locations determined by the amplitude-based approach are $< \pm 100$ m and $< \pm 160$ m, respectively (Fig. 2.17). For

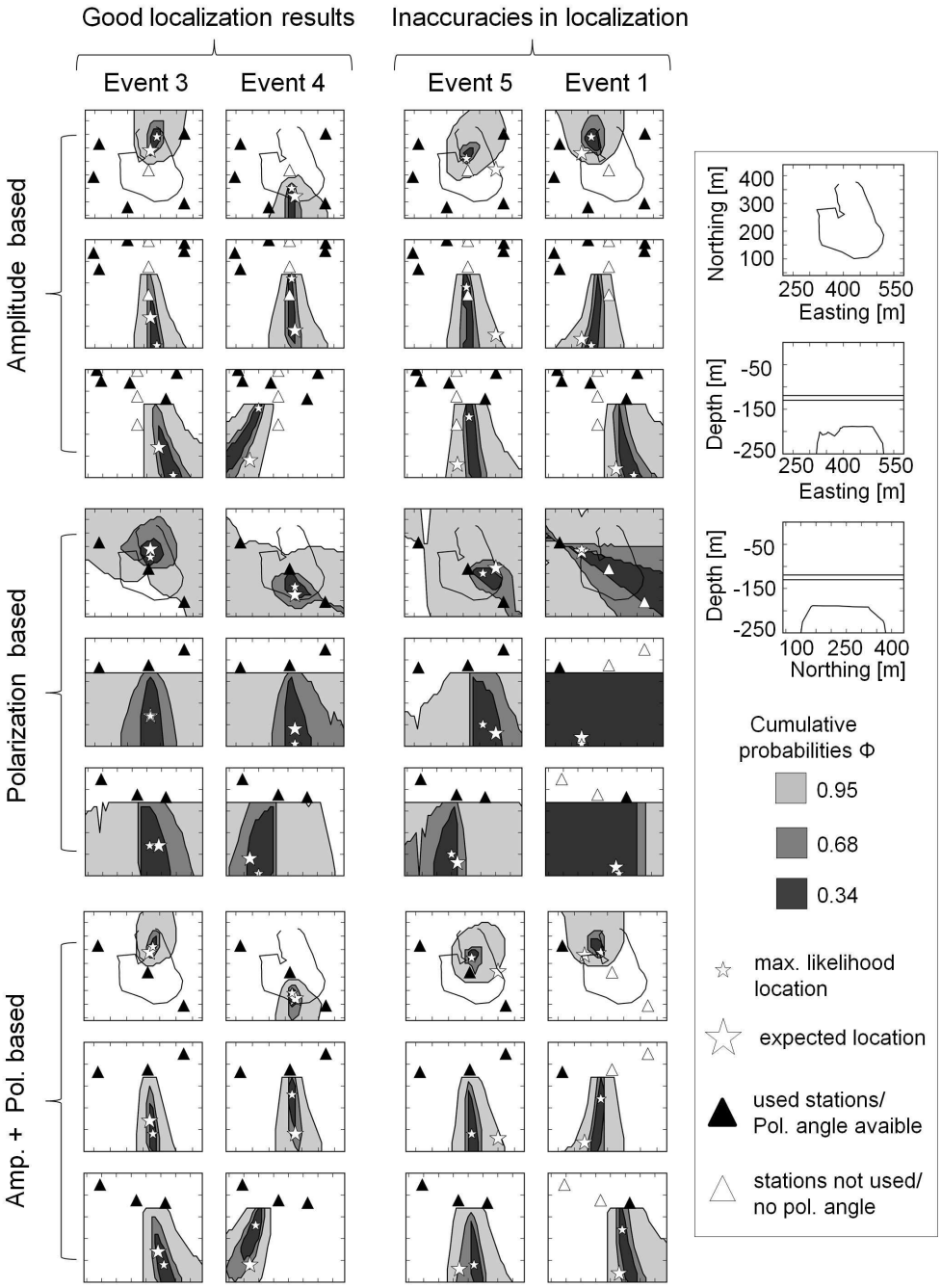

Figure 2.16: Probability density functions for location. Cumulative probabilities (Φ) with contours equal to 0.34, 0.68, and 0.95, and the maximum likelihood locations (small stars), for two good (left panels) and two problematic (right panels) location results using the amplitude-based (upper panels), the polarization-based (middle panels), and the combination of the latter two (lower panels) in comparison with the expected hypocenter location (big star) estimated from the classical location approach for the 54 events.

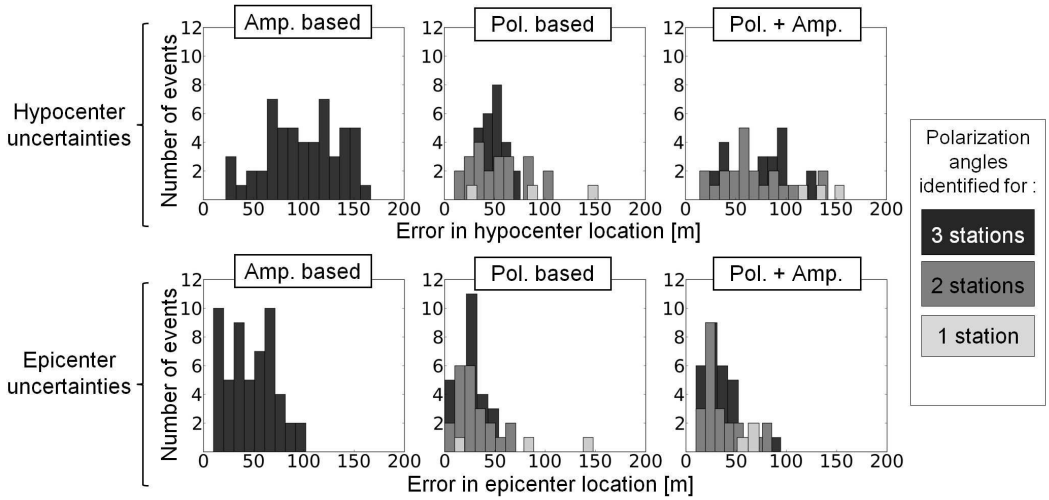

Figure 2.17: Statistics of location errors. Location errors for the 54 events of the training set using the amplitude-based, polarization-based, and the combined location approach. The errors are estimated from the absolute distance differences between the calculated hypocenter (upper panel) and epicenter (lower panel) locations and the ones obtained from the classical location approach (Fig. 2.3).

the polarization-based approach, the quality of the location results depends on the quantity of identified polarization angles at each station. The epicenter and hypocenter locations are significantly more accurate using this method compared to the amplitude-based approach, under the circumstance that polarization angles are available for all three stations, which is the case for 51% of the 54 events. For the combined approach, the epicenter errors, with at least two available stations, are significantly reduced. In contrast, as already stated above, the source depth estimations using the polarization-based approach become inaccurate when combined with the amplitude-based approach.

2.5 Detection and location in dense microseismic swarms

The two developed location approaches were applied to resolve the spatio-temporal characteristics of the observed two types of swarming sequences, isolated and tremor-like (Fig. 1.9, Section 1.3.4.1). In order to identify single seismic events in isolated and tremor-like swarming sequences, I used the polarization-based P wave automatic detection scheme for 3-component stations 3, 5, and 62 (Section 2.2.2 and 2.2.3).

For the amplitude-based approach, the event-specific time window was defined by the minimum source origin time τ^{i}_{start} and the maximum source origin time τ^{i+1}_{end} of the subsequent identified event (Eq. 2.4-2.6). This event window definition assures that amplitude estimates for more distant stations (e.g. 7 and 8) are always related to the entire seismic event duration,

in order to determine the true event-specific maximum peak-to-peak amplitude.

In Fig. 2.18 and 2.19, the location results for both approaches are shown, individually and combined, for swarming sequence example 1 (Fig. 1.9). Consistently observed, using both location schemes, this entire swarming sequence is associated with distinct spatio-temporal epicenter migration trends. During the preceding isolated event swarming sequence, the epicenters migrate from the northwestern to the southeastern cavity region (Fig. 2.18g-i). During the subsequent tremor-like swarming sequence, the epicenters migrate reversely from the southeastern to the northwestern cavity region (Fig. 2.19g-i). These cyclic spatio-temporal epicenter migrations are clearly identified at stations 5 and 62 by the calculated backazimuth and incidence angles (Fig. 2.18b,d and 2.19b,d). In contrast, the exact dimension of the epicenter migration trends cannot be completely resolved using this approach, due to the significant uncertainties in the epicenter locations, averaging around ± 50 m (Fig. 2.17). For both swarming sequences, hypocenter depths are poorly resolved and very noisy, and hence, are not shown in the figures.

Similarly, distinct spatio-temporal epicenter migrations are observed for two other main swarming sequences, namely examples 2 (Fig. 2.20) and 3 (Fig. 2.21), which correspond to the two major last peaks of activity in the microseismic crisis in 2008 (Fig. 1.7). For the swarming sequence example 2, cyclic epicenter migration trends are observed with an initial migration direction towards the west and a subsequent migration towards the east (Fig. 2.20).

However, for both swarming sequence examples 2 and 3, the locations for the tremor-like event sequences are related to bigger uncertainties due to the lack of polarization angles available at station 62 (Fig. 2.20 and 2.21). The quantity of P wave detections at this station decreases significantly, as P wave onsets are widely covered by the coda of the preceding event and by the general increase in the high frequency noise level associated with comparatively stronger and more frequent seismic energy releases (Fig. 2.20a and 2.21a). On the other hand, P waves are frequently detected at the more distant station 5, where high frequency noise widely vanishes due to attenuation (Fig. 2.20c and 2.21c).

The amplitude-based location approach appears generally robust for the tremor-like event sequences, however remains more sensitive to isolated event sequences when these are associated with close concatenations of individual events that strongly vary in amplitude (Fig. 2.20). In these cases, the amplitudes estimated at each station can be related to different isolated

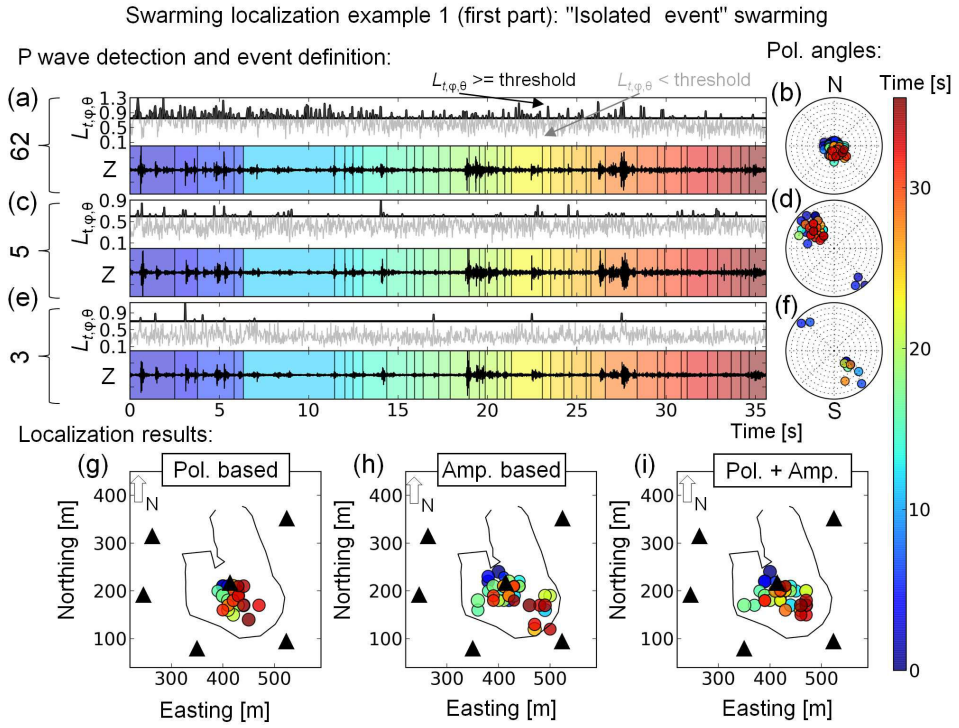

Figure 2.18: Location of an isolated event swarming sequence. Location results for the isolated event swarming example 1 (Fig. 1.9). (a,c,e) Z component traces of stations 3, 5, and 62, and the L-values below (gray) and above (black) the critical threshold value Lcrit. Trace background colors mark the current time and black lines denote the minimum expected source origin times τ^i_{start} for the identified events (Eq. 2.6 Section 2.5). (b,d,f) Lower station hemisphere plots of the determined polarization angles with current time (colored scale). (Lower panels) Results for the polarization-based (g), amplitude-based (h), and combined location approaches (i).

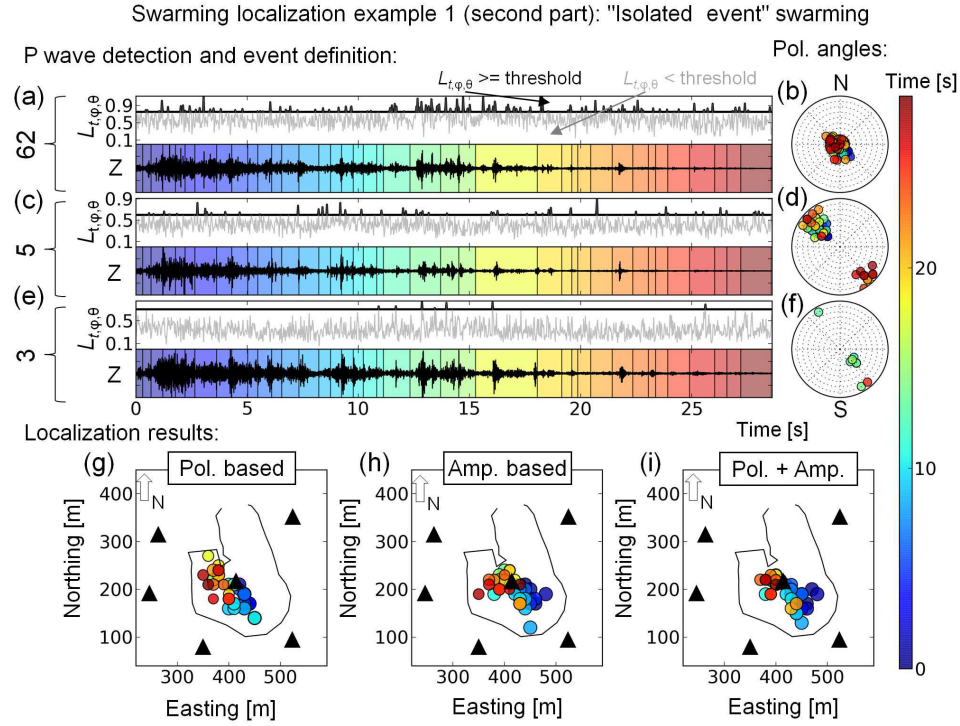

Figure 2.19: Location of a tremor-like swarming sequence. Location results for the tremor-like swarming sequence example 1 (Fig. 1.9). For further description see Fig. 2.18.

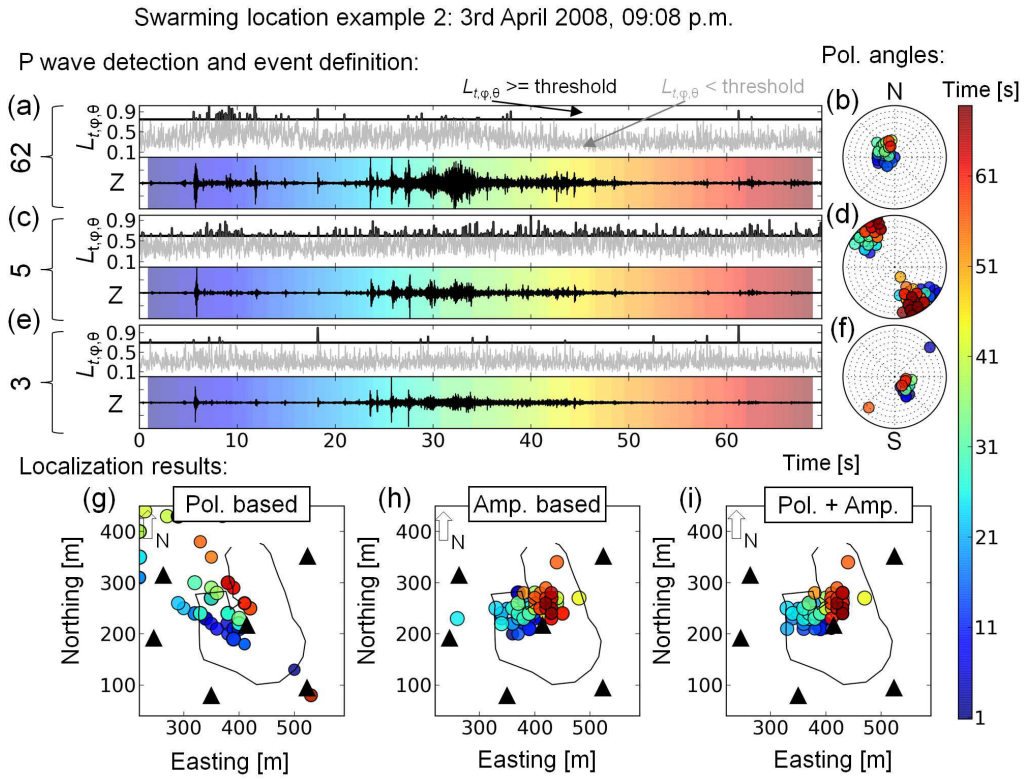

Figure 2.20: Location results for swarming sequence example 2. Further descriptions are given in Fig. 2.18. For a better illustration, the minimum expected source origin times τ^i_{start} of the identified events are not shown here.

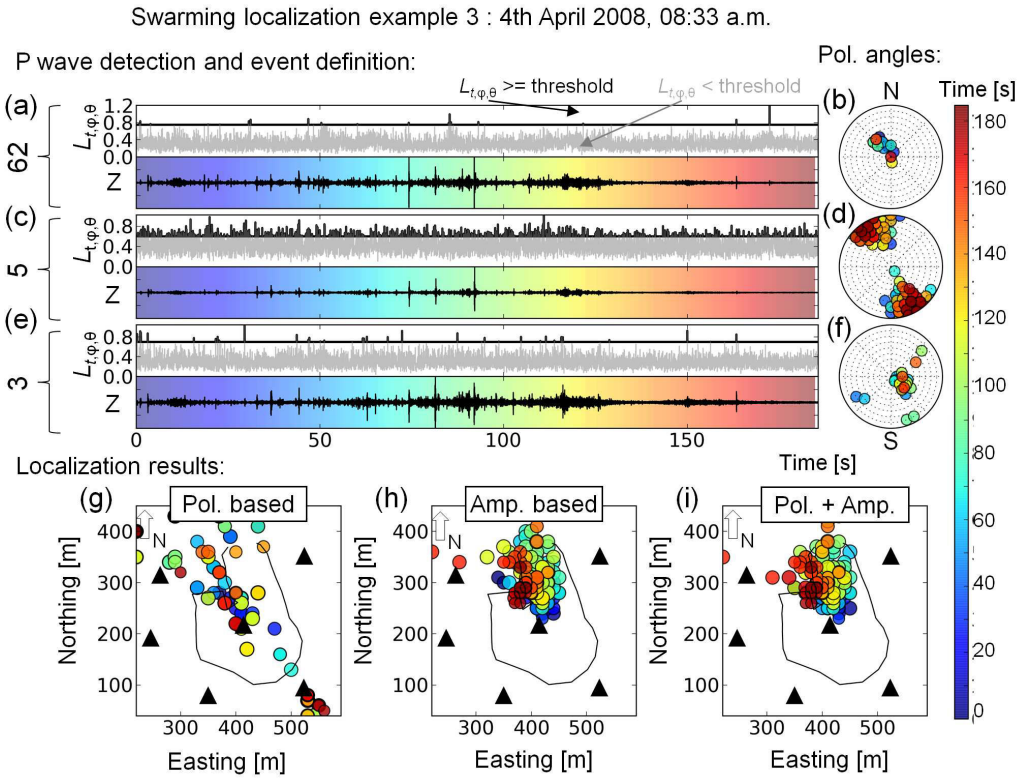

Figure 2.21: Location results for swarming sequence example 3. Further descriptions are given in Fig. 2.18. For better illustration, the minimum expected source origin times $\tau^i_{start}$of the identified events are not shown here.

events, leading to erroneous locations when the amplitudes of the different events vary significantly. Such an effect and limitation are visible from the more scattered nature of located events using the amplitude-based approach (Fig. 2.20h), compared to the polarization-based (Fig. 2.20g) or combined approaches (Fig. 2.20i).

2.6 A Semi-automatic detection and location design

As shown in the previous Section 2.5, based on the two developed methods, namely the polarization- and amplitude-based approach (Section 2.2 and 2.3), it is now generally possible to process the microseismic data in a semi-automatic manner to obtain a seismic catalog containing the source origin times as well as source location. However, event detection by the polarization approach alone might be precarious as the detection capability is only representative with respect to stations 3, 5 and 62, and is generally sensitive to changes in the wave field characteristics, as mainly produced by changing source radiation pattern or propagation characteristics (see later Section 3.3). In order to review the detection behavior of the polarization-based approach, a simple pre-detection step is applied before phase identification, as presented in Section 2.6.1. This approach generally uses spectral seismogram envelopes in order to ensure event detection with respect to all network stations, and therefore guarantees that amplitude estimations from more distant stations 2, 7 and 8 do contain seismic event signals, which is a pre-requisite for the amplitude-based location approach (Section 2.3.5). Thanks to this pre-detection step, it is possible to locate microseismic events by means of amplitudes, even though no reliable polarization angles are available.

In order to demonstrate the functionality and to evaluate this semi-automatic detection and location design, some first detection (Section 2.6.2) and location results (Section 2.6.3) are shown with respect to the microseismic crisis in 2008 (Section 1.3.3.1), what is followed by a preliminary interpretation of these results in Section 2.6.4. As shown in Section 2.3.2, in this period the attenuation characteristics appear to be generally stable, what is a precondition for reliable amplitude-based location results. Furthermore, the cavity evolution stage in 2008 is relatively well constrained by other geophysical measurements (Section 1.3.3.1), which will be compared with the obtained location results.

2.6.1 Detection and signal characterization using a spectral envelope

For each station, the considered seismogram is band pass filtered for $10-250$ Hz (as consistent with the expected event frequency range, Section 1.3.4.1) and is then divided into small time windows w with 0.025 s length. For each time window, the logarithmic maximum spectral amplitude is calculated from a low resolution (128 samples) fft spectrum, what yield a spectral envelope function (SEF) of the seismogram

$$SEF(w) = \arg\max\{\log_{10}(|\mathrm{fft}(w)|)\}. \tag{2.21}$$

For each station a critical detection value λ was determined which correspond to the maximum SEF value found in the background noise level of the 54 events of the training set (Section 2.1). Then the SEF is subtracted by λ (Fig. 2.22) and the resulting function is transformed to a "2-valued" function $(SEF(w) - \lambda)_{0,1}$, containing exclusively ones and zeros, where a value of 1 corresponds to a spectral envelope above λ, and thus to a detection of a potential seismic event, while a value of 0 correspond to values of the SEF smaller than λ, and thus to background noise.

By this SEF representation, contributions of noise and seismic events can be clearly distinguished (Fig. 2.22). In the following, it is aimed to combine the information of the SEF for each seismogram for each network station, to a single network detection function (NDF), which represent event detection in agreement with the network detection capability, meaning that one event is detected if it has been simultaneously observed at all stations. In this respect, station 1 was neglected, since it is generally not used for location and is much more distant to the cavity structure compared to the other stations, and therefore would significantly reduce the number of detected events. For the calculation of the NDF, the detection functions $(SEF(w) - \lambda)_{0,1}$ at each station are elongated by convolution with a step function χ_A

$$SEF^*(w) = (SEF(w) - \lambda)_{0,1} * \chi(w)_A \tag{2.22}$$

where

$$\chi(w)_A = \begin{cases} 1 \text{ if } w \in A \\ 0 \text{ if } w \notin A, \end{cases} \tag{2.23}$$

where $*$ denotes the convolution. The length of the step function was chosen with 0.3 s,

$\chi(w)_{[0,0.3\ \mathrm{s}]}$, what is four times the value of the expected maximum of the difference in P wave travel times (0.075 s) when assuming an average velocity of $V_P = 2900$ m/s. As a result, the obtained convolved spectral envelope function $SEF^*(w)$ elongates the time window of the detected potential event ($(SEF(w) - \lambda) > 0$) with the double maximal P wave travel times difference (± 0.15 s) to both sides of the event (Fig. 2.22). Then all convolved spectral envelope functions of all network stations $SEF^*_{stat.}(w)$ are multiplied yielding the NDF

$$NDF(w) = \prod_i SEF^*_{stat.}(w), \tag{2.24}$$

which is then also transformed to a "2-valued" $NDF_{0,1}(w)$ where

$$NDF_{0,1}(w) = \begin{cases} \text{if } NDF(w)_j > 0 \text{ then event detected } \Rightarrow NDF(w)_j = 1 \\ \text{if } NDF(w)_j \leq 0 \text{ then no event detected } \Rightarrow NDF(w)_j = 0 \end{cases} \tag{2.25}$$

The detection results using the NDF for swarming example 1 (Fig. 1.9, 2.18 and 2.19) are shown in Figure 2.23. As seen from these results, potential seismic events are consistently detected by all stations. However, not surprisingly, the spectral envelope method is clearly more limited in the detection of single events as compared to the polarization-based approach (Fig. 2.18 and 2.19), so that often several events are detected as one event, when the inter-event times are too short. On the other hand, this method is very useful for quantification and classification of the microseismic data, being whether of tremor-like or isolated character (Fig. 2.23, Section 1.3.4.1).

2.6.2 First application to the 2008 microseismic crisis: detection results

The detection results for the spectral envelope (Section 2.6.1) and the polarization-based approach (Section 2.2), as well as the number of recorded triggered event files (fix trigger value, Section 1.3.2) are shown in Figure 2.24 for the microseismic crisis (March-April) in 2008.

As seen by the absolute and cumulative number of detected events, the relative detection capacity seems to remain almost constant for the spectral envelope and polarization-based approach (Fig. 2.24). Constantly, few events are detected by the spectral envelope approach as compared to the number of recorded triggered event files. The percentage of non-detected events in merged trigger event files remains constant at $\sim 38\%$, what means that the number of "non-detected events" increase proportionally with increasing microseismic activity

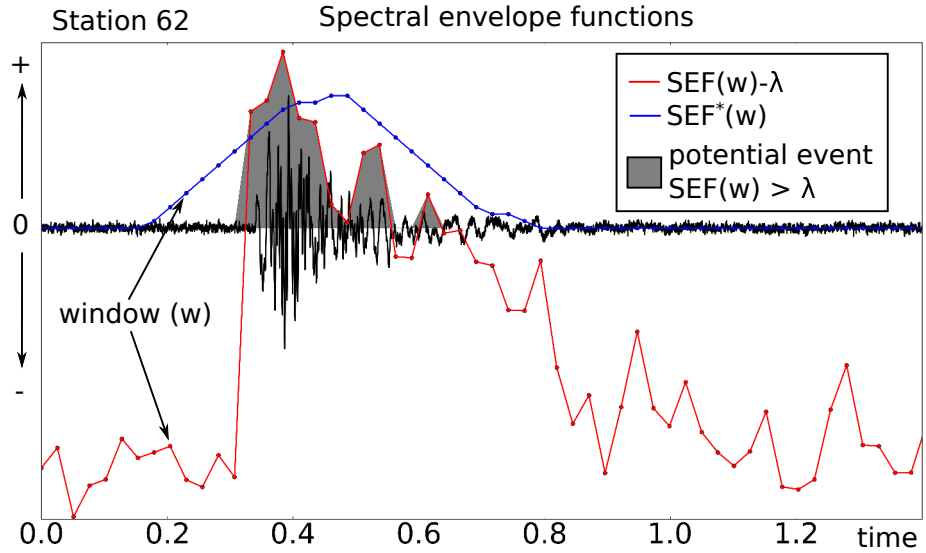

Figure 2.22: Spectral envelope function. Seismic event example from station 62 (black lines) and the corresponding spectral envelope function SEF (Eq. 2.21) subtracted by the critical detection value λ (red line), where values > 0 (gray shaded area) indicate a detected event. The convolved spectral envelope $SEF^*(w)$ (blue line) (Eq. 2.23) is used for calculation of the NDF (Eq. 2.24).

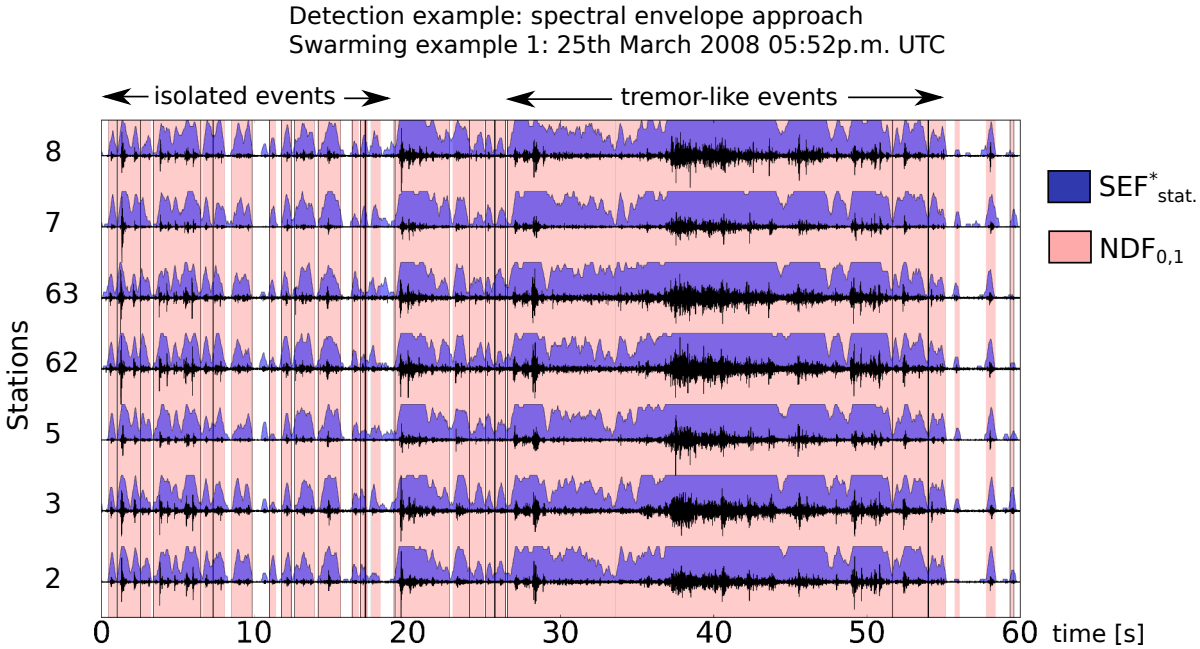

Figure 2.23: Spectral envelope detection in swarms. Detection results by using the "2-valued" network detection function $NDF_{0,1}(w)$ (Eq. 2.25) for swarming example 1 (Fig. 1.9, 2.18, and 2.19), where detected events are shown by red shaded areas which were obtained from the product of the convolved spectral envelope function $SEF^*_{stat.}(w)$ (Eq. 2.24) calculated at each station (blue shaded areas) (Eq. 2.23).

(Fig. 2.24a-b). Constantly more events are detected by the polarization-based approach as compared to the number of recorded files and events detected by the spectral envelope approach (Fig. 2.24a). For $\sim$ 10% of the events detected by the spectral envelope, almost independent of microseismic activity, no events or P wave phases could be detected from the polarization-based approach (Fig. 2.24a,c)

Taking these observations together it can be concluded that the number of events, detected from the polarization-based approach, increases with the duration of the events detected from the spectral envelope approach as well as with the number of merged triggered triggered event files (Fig. 2.24a). This conclusion implies that swarming sequences, also of tremor-like character, can be interpreted as a superposition of isolated events, what is consistent with the results from microseismic signal characterization and classification in Section 1.3.4.1. This issue will be analyzed and discussed in detail in Chapter 4.

The detection capability of the polarization-based approach is slightly depend on the degree of swarming or tremor-like event activity, as already discussed in Section 2.5. The degree of linear polarization can degrade due to small inter-event times and coda superpositions. Accordingly, in periods of intensive tremor-like event activity, as mainly associated with the swarming example 1-3 (Fig. 1.7, 2.18-2.21, and 2.24c), the amount of "non-detected events" increases (Fig. 2.24c). In addition, from Figure 2.24d, it can be consistently observed that for swarming examples 2 and 3 the detection rate at station 62 significantly decreases as compared to station 5. This detection behavior is related to the detection dependency on hypocentral distances. Station 62 is generally closer to the swarming sequences (Fig. 2.20-2.21), and therefore more (small-sized) events are recorded, which superpose and overlap, decreasing the degree of linear polarization.

Next to this distance dependency in the detection capability of the polarization-based approach, it can be seen that the detection rate at station 3 is almost constantly smallest and highest for station 62, as it was already observed with respect to the 54 events of the training set (Fig. 2.8, Section 2.2.2). This behavior will be later discussed in the light of a systematic source effect in Section 3.3.

2.6.3 First application to the 2008 microseismic crisis: location results

The automatic event identification and location approaches (polarization- and amplitude-based), as used for the swarming sequences (Fig. 2.18-2.21), are applied to all pre-detected

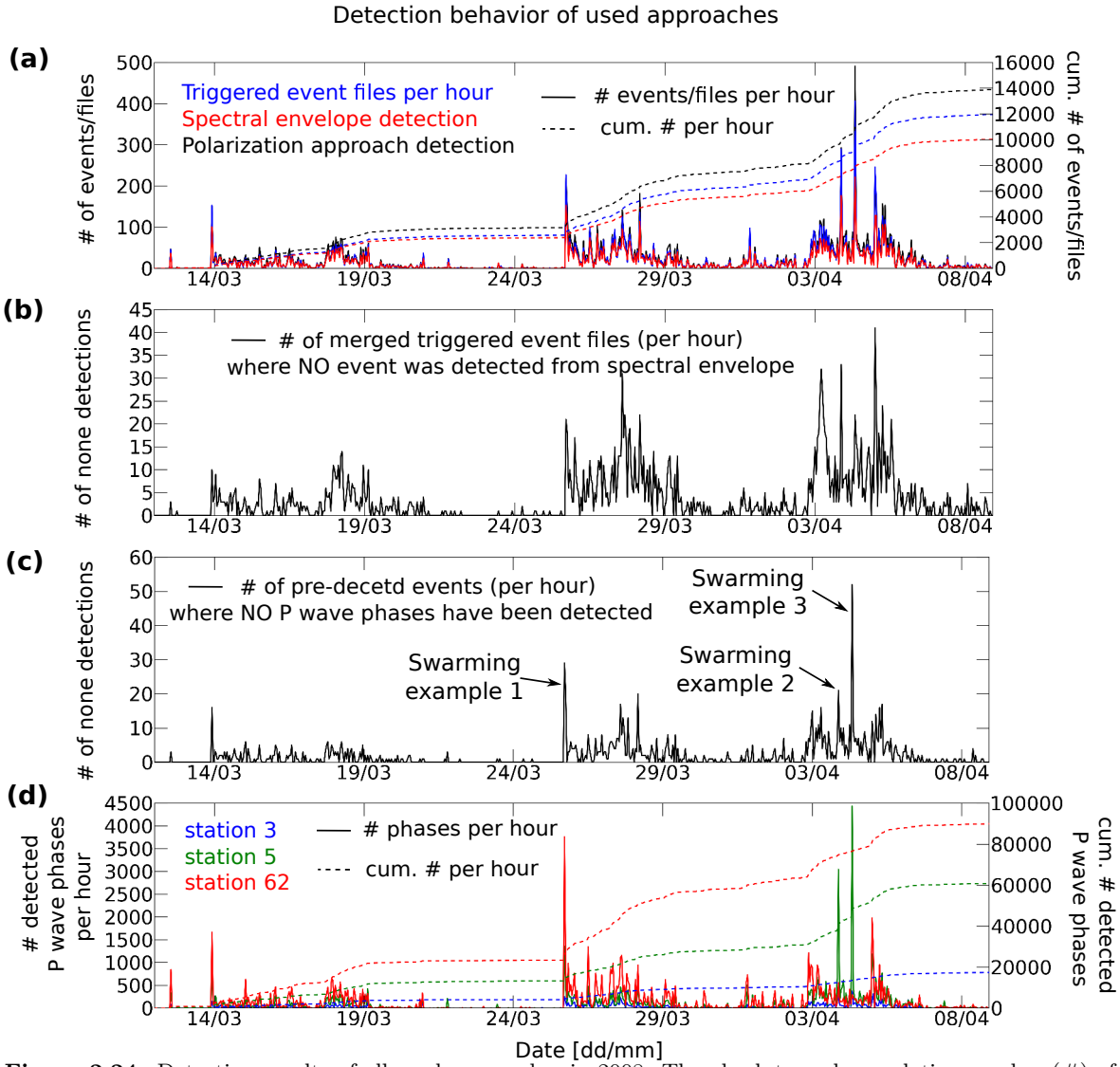

Figure 2.24: Detection results of all used approaches in 2008. The absolute and cumulative number (#) of (a) triggered events files (blue) (Section 1.3.2), the spectral envelope approach (red) (Section 2.6.1), and the polarization-based approach (black) (Section 2.2). (b) # of no-event detections using the spectral envelope approach with respect to the merged triggered event file data base (Section 1.3.2). (c) # of no-event detections using the polarization-based approach with respect to detected events of the spectral envelope approach. (d) # of detected P wave phases using the polarization-based approach with respect to station 3 (blue), 5 (green), and 62 (red).

events (spectral envelope approach, Section 2.6.1) of the 2008 microseismic data set (Fig. 1.7). Figure 2.25 shows the apparent spatio-energetic distribution of the microseismic crisis in 2008, based on the maximum likelihood locations obtained from the polarization-based (Fig 2.25a) and the combined approach (Fig. 2.25b-c). As stated in Section 2.4, the polarization-based approach provides better location results for the source depths, while the combined approach provides better epicenter location resolution. The apparent seismic energy E_{app} for

each grid point $(\boldsymbol{X}, \boldsymbol{Y}, \boldsymbol{Z})$ was approximated by

$$E_{app}(\boldsymbol{X}, \boldsymbol{Y}, \boldsymbol{Z}) = \log_{10}\left(N(\boldsymbol{X}, \boldsymbol{Y}, \boldsymbol{Z})A^2(\boldsymbol{X}, \boldsymbol{Y}, \boldsymbol{Z})\right), \tag{2.26}$$

where N is the number of events, A the peak-to-peak amplitudes estimated from station 62 for the frequency band $30 - 90$ Hz and corrected for attenuation by multiplying $r^{-1.7}$ (Table 2.3), where r is the epicentral distance. Seismic events with amplitudes below an apparent magnitude of completeness ($\sim 50\%$) are excluded from the distribution shown in Figure 2.25. The apparent magnitude of completeness was defined by finding the amplitude bin with the highest number (frequency) of events identified from a frequency-amplitude plot.

The spatio-energetic distribution as a function of depth, shown in Figure 2.25a, marks very well the vertically evolved cavity roof measured after the crisis by sonar measurements. Even the asymmetry in the vertical roof extension between the eastern and the western part of the cavity zones is reproduced (Fig. 2.25a). The spatio-energetic distribution in the horizontal plane, as seen from Fig. 2.25b, clearly agrees with the lateral extensions of the cavity zone. Also, microseismicity nicely redraws the asymmetric shape of the cavity associated with a larger N-S extension along the eastern side, compared to the western side. The major seismogenic zone, as marked by the maximum of released microseismic energy, is found in the transition zone lying between the highest cavity roof extension to the E-S-E and the lower cavity roof extension to the W-N-W.

Fig. 2.25c shows the cumulative seismic energy along the two exploitation profiles in comparison with the cavity roof growth obtained by sonar measurements realized before and after the microseismic crisis in February and May 2008, respectively. From this illustration it can be clearly seen that the amount of cumulative seismic energy increase almost proportionally with the respect to the size of collapsed cavity roof portions during the crisis in 2008. Accordingly, the largest cavity roof collapse was measured at the northern cavity zone along profile A, what agrees with the location of maximum cumulative seismic energy.

Taking all these results and observations together, it can be concluded that the developed semi-automatic location approach is a very useful tool in order to resolve the spatio-temporal characteristics of complex swarming sequences recorded in a growing cavity environment, at a local-scale. Absolute locations are associated with clear uncertainties, but appear widely reasonable especially with respect to the epicenter locations.

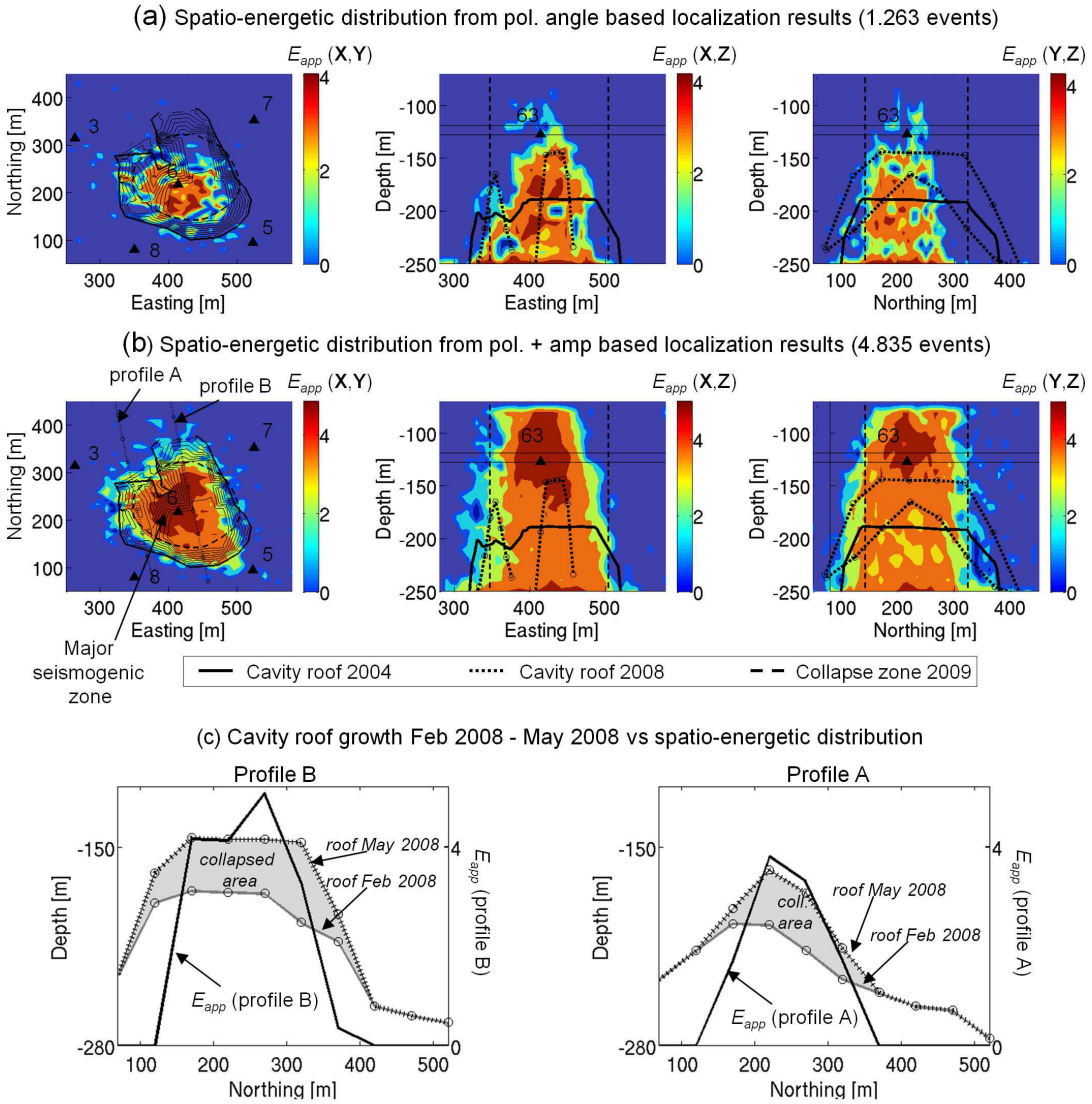

Figure 2.25: Spatio-energetic distribution of the 2008 microseismic crisis, representing the apparent seismic energy E_{app} (Eq. 2.26) calculated for seismic events below a apparent magnitude of completeness (Section 2.6.3) located using polarization angles from all three stations 3, 5 and 62, and incidence angles $< 50°$ at station 5 (a), using the combined location approach with polarization angles available for at least two stations for one seismic event (b). (c) Cavity roof growth during the crisis in 2008 (left ordinate) and the cumulative apparent seismic energy E_{app} calculated along two profiles A and B (a, Fig. 1.5). The collapsed area of the cavity roof (gray shaded area) is represented by the difference between to sonar measurements (black circles) along the two profiles obtained before and after the microseismic crisis 2008, in February and May 2008, respectively.

2.6.4 First application to the 2008 microseismic crisis: preliminary interpretation

The presented location results of the swarming sequences (Fig. 2.18-2.21) and the spatio-energetic distribution of the micrsoeismic crsis in 2008 (Fig. 2.25), agree very well with the hypothesis from previous studies arguing that microseismicity, before the cavity collapse in

2009, generally represents rock detachment cracking and breakage processes along the cavity roof (Section 1.3.3). Accordingly, microseismic activity is concentrated to zones where the cavity structure has significantly evolved during the crisis in 2008 (Fig. 2.25). Microseismicity located inside the cavity structure should be interpreted as poorly resolved source depth location (Fig. 2.25a). Seismic energy released by the impacts of falling blocks on the cavity floor is rather unlikely, since the brine-filled and pressurized cavity should reduce significantly the fall velocity of detached Marl or salt blocks. In addition, the sunken Marl blocks along the cavity floor are widely fractured and brine-saturated, forming an unconsolidated viscous interface which is expected to significantly damp the impacts of falling blocks.

The spatio-temporal epicenter migrations associated with the swarming examples (Fig. 2.18-2.21) indicate, that both, isolated and tremor-like swarming sequences clearly interact with each other, maybe in a way that isolated, local detachment cracks initiate a self reinforcing chain reaction which forms a failure zone, succeeded by rock breakage. Consistently, each of these tremor-like swarming sequence coincides with significant increases in the brine pressure level measured at the exploitation wells located about 1 km to the north of the cavity structure (Fig. 1.5 and 1.7). The most noticeable event of such chain reaction cavity roof failure is represented by the distinct northward epicenter migration happening on the 4th of April 2008 associated with the swarming example 3 (Fig. 2.21). At the same time of this major microseismic swarming activity a significant increase in the brine level of $\sim$ 13 m was measured (Klein et al., 2008). This observation indicates that the observed swarming activity might represent the major collapse of the northern cavity roof as shown by the sonar measurements shown in Figure 2.25c.

The fact that the observed distinct spatio-temporal epicenter migrations cover laterally larger areas of the total cavity zone (Fig. 2.18-2.21) indicates that the triggering mechanism for detachments and rock failures are probably related to processes of bulk stress accommodation and redistribution. Generally, the cavity roof is supposed to be in a critical state of stress, and the partial release of stress in one zone provokes stress concentrations and subsequent failures in adjacent zones, and vice versa. A major factor in these stress redistribution processes might be seen in the distinct relief of the cavity roof. Accordingly, the major seismogenic zone is located in the transition zone between the highest cavity extension to the S-S-E and the lowest to the N-N-W (Fig. 2.25b) which might be a key zone prone to the initiation of cavity roof failure.

In order to confirm these preliminary interpretations with respect to the origin of microseismicity, more constraints on the microseismic source mechanics need to be investigated from further analysis which is presented in the next Chapter 3. Within this analysis, it will be furthermore shown that the here obtained location approach and results provide a very useful prerequisite for efficient source analysis, but are also affected by a governing systematic source effect (Section 3.3). More constraints on these preliminary results and interpretation are presented in Chapter 4, analyzing and discussing the origin of microseismic swarming in more detail.

Chapter 3

Microseismic source characteristics: evidence for consistent shear source mechanics

Major contents of this chapter are in preparation for publication: Kinscher et al., Evidence for consistent shear source mechanics in microseismic swarms induced by salt solution mining.

As introduced in Chapter 1, the source mechanical interpretation of microseismicity in growing and collapsing, inaccessible underground cavity environments is poorly understood so far. In order to gain experience in this context, this chapter aims to constrain the source characteristics of the recorded microseismic events at Cerville-Buissoncourt. For this analysis, I generally used the source detection and location results from the previous Chapter and tested classical seismic source models and scaling approaches as commonly used in global and mining seismology. As a result, the major achievement of the analysis performed in this Chapter is the generation of a complete seismic catalogue, who quantitatively fully describes the microseismic occurrences in space and time, which are further analyzed and interpreted in the following Chapters. If not familiar with general seismic source theory and related scientific terms, I refer the reader to a brief overview in Appendix C, as well as to standard textbooks.

The structure of this Chapter is organized as follows: firstly, the state of the art and the principal results of source analysis are reviewed in Section 3.1, focusing on numerous studies in excavation mines, as well as some few studies reported from salt-solution and block mining environments and natural karstic and evaporitic caving contexts. Secondly, source character-

istics are analyzed for the Cerville microseismic data set of 2008 (Section 3.2). Therein, the source mechanisms are investigated by a comprehensive step-by-step procedure constraining first of all the fundamental body wave field observations (Section 3.2.2 and 3.2.3), before several source inversion approaches are applied (Section 3.2.4), whose results are summarized and discussed in the light of theoretical mechanical models and other comparable microseismic studies (Section 3.2.5). Then in Section 3.3, the influence of the observed source mechanics on the developed detection and location approaches (Chapter 2) and their results is discussed. In the last Section 3.4, a classical source parameter scaling approach is tested to the Cerville microseismic dataset accounting for the findings in source mechanism and location.

3.1 Previous microseismic source studies at near underground openings

3.1.1 Seismic source models and challenges

From a seismological point of view, source mechanisms of natural earthquakes can be successfully approximated by a point source shear-dislocation model represented by two equivalent body force double-couples (DC) (e.g. Burridge and Knopoff, 1964). Also many source mechanisms in mines are clearly associated with shearing, especially larger events ($M > 0$), and can be modeled assuming a DC-source as usually applied for natural earthquakes (e.g. Gane et al., 1946, Gay and Ortlepp, 1979, McGarr, 1971b, McGarr et al., 1989, Richardson and Jordan, 2002, Šílenỳ, 1989, Spottiswoode and McGarr, 1975). On the other hand, the DC-source model is not always representative for mining sources and sometimes requires additional model terms respecting volume changes at the source, as a result of cavity collapse, pillar burst, crack opening or cavity closing (e.g. Hazzard and Young, 2002, Julià et al., 2009, McGarr, 1992). Figure 3.1 shows six generally used source models for induced seismicity in underground mines, applicable for many mining environments (Horner and Hasegawa, 1978): (a) normal fault, (b)tensile faulting, (c) thrust fault, (d) pillar burst, (e) cave collapse fault, (f) Shallow (near horizontal) thrust faulting, arising either from either a normal (g), tensile (h), or thrust (i) stress regime. In terms of seismic source theory, models (b), (d) ,(e) require non-DC portions to explain source deformation (Fig. 3.1).

These source mechanisms are often described by the full moment tensor formulation (Gilbert,

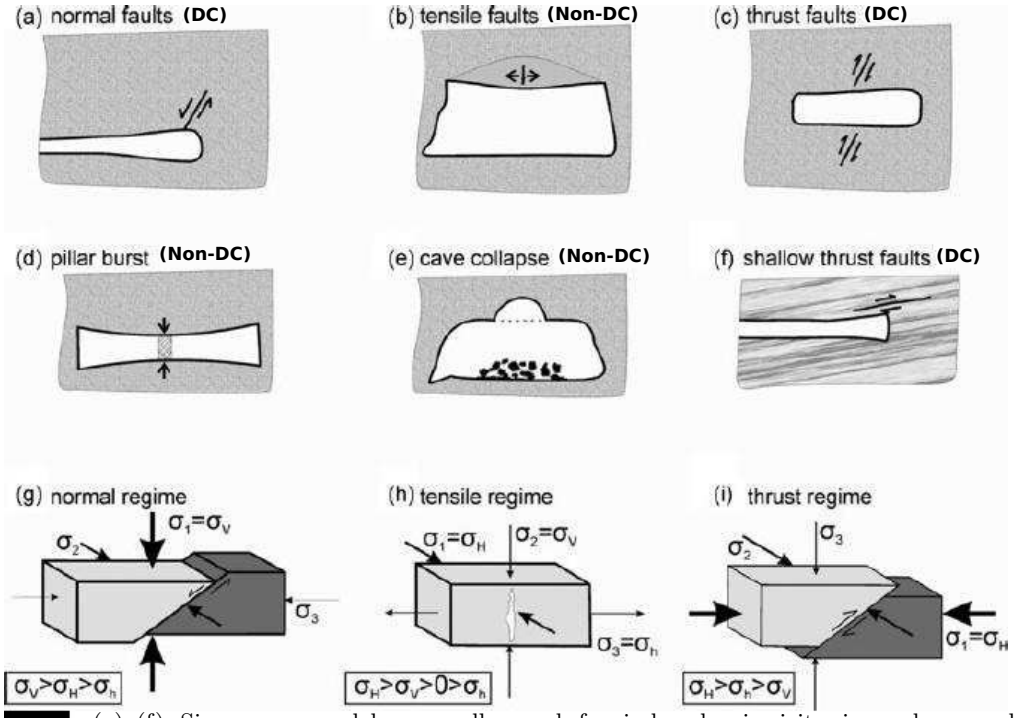

Figure (a)–(f) Six source models generally used for induced seismicity in underground mines (Horner Hasegawa, 1978). (g)–(i) Anderson's stress regimes associated with faulting (Anderson, 1905, 1951). I is taken from Wuestefeld et al. (2011)

1971), where the moment tensor is usually decomposed into a DC, compensated linear vector dipole (CLVD) (Knopoff and Randall, 1970) and isotropic component (ISO). The CLVD and ISO components can then be interpreted in terms of source related complexity in rupture geometry, rapid phase changes, volume changes and tensile components (tensile angle, Vavryčuk, 2001, 2011), which are often associated with induced fluids in hydrothermal or volcanic and oil/gas extraction environments (e.g. Julian et al., 1998, Miller et al., 1998). Further testing of such possible physical origins can also include e.g. higher-order moment tensor approaches (Dahm and Krueger, 1999) or appropriate single force distributions (Šílenỳ and Milev, 2008, Takei and Kumazawa, 1994).

However, in several studies it was shown that spurious non-DC portions can reflect uncertainties of the inferred DC-components, the presence of noise, a mismodeling of the surrounding and source medium and/or an inappropriate source representation (e.g. Kawasaki and Tanimoto, 1981, Kuge and Lay, 1994, Sileny, 2004). So, the discrimination of different source mechanisms by moment tensor inversion techniques is not always straightforward. In fact, source inversion of microseismic events ($M < 2$) is an even more challenging task, compared to large natural earthquakes. For higher frequencies the seismic wave field is much more affected by local heterogeneities in the propagation medium, which can introduce

significant trade-offs between medium and source characteristics, when Green's functions are not of sufficient quality. For example, the usage of body wave amplitudes can lead to significant misinterpretation of the source mechanism, if P and S wave attenuation is not completely known (e.g. Eisner et al., 2011). The resolution of the full moment tensor from inversion of microseismic data generally requires a high Signal-to-Noise ratio, precise source location, and a very good station coverage, while the DC portions can be generally well resolved from sparse networks (e.g. Eaton and Forouhideh, 2010, Eisner et al., 2011, Godano et al., 2011, 2009, Jechumtálová and Šílenỳ, 2005, Jechumtálová et al., 2014).

3.1.2 Solution mining and block caving

Studies of source characteristics for seismicity induced from salt solution mining are rare in literature. Trifu and Shumila (2010) analyzed the source mechanisms of 1,518 events ($Mw-2.6-0.2$) recorded from 36 one-component 15 Hz borehole geophones within an induced collapse scenario in Field II at Ocnele Mari, Romania. For the source analysis they used an automatic moment tensor inversion scheme in the time domain, based on low frequency amplitudes and first arrival P-wave polarities. In their results they documented pure DC normal and strike-slip failures while the majority of the events showed up to 30% explosive failure components, which they refer to roof caving under gravitational collapsing (Fig. 3.1e). In addition, the authors observed a systematic quasi-circular and radial orientation of the tension and pressure axes for the major DC components with respect to a major sinkhole, which were associated with predominantly normal and strike slip faulting. In a further study, Jechumtálová et al. (2014) investigated the resolution and quality of these mechanisms in terms of network performance and additional usage of S wave amplitudes and confirmed the presence of pure shearing and tensile fracturing events. In their results, they found that the orientation of the pure shear fracture component is almost always well resolved, especially when including S wave amplitudes. The resolution of the non-DC components was found to be only reliable for high quality data sets and very sensitive to contributions of noise.

In the salt solution mining study of Branston (2003) (Section 1.2), the microseismic events were characterized by a significant lack of S wave energy. However, the authors could not unravel if the lack of S wave radiation is related to a source effect (tensile mechanism) or strong attenuation effects on S waves from the brine filled cavities. In a more recent study, Godano et al. (2012) analyzed focal mechanisms of seismic events in microseismic swarms

(1,214 events of a total of 125,000, $Mw - 3 - 0.5$) recorded during injection operations in the Arkema-Vauvert salt field by two 3-component 28 Hz velocimeters. In their results, they found primarily dip-slip fault mechanisms that correlated well with the spatio-temporal distribution of the seismic activity located between two vertical cavities along the wells. It was assumed that seismic activity is associated with faulting on regional thrust fault structures or on stratigraphic interfaces between salt beds and the beds of insoluble rocks.

During continuously block mining operations in Northparkes, Australia (Fig. 1.2b), Wuestefeld et al. (2011) observed temporal changes in the fracture orientation, by using an automatic shear-wave splitting method. The authors interpreted these changes as changes in the stress regime depending on the thickness of the overburden. Accordingly, tensile fracturing (vertical aligned fractures) dominate in the initial state of the mining operations when the overburden is partially undermined. With increasing cave propagation to the surface, the overburden becomes less thick and horizontal stress becomes dominant, producing a thrust fault regime (horizontal fracture orientation).

3.1.3 Karst cavitation processes

Dahm et al. (2011) analyzed the seismic source characteristics of an unusual $Mw0.6$ event close to the city of Hamburg, Germany, which probably originated from the formation of a cavity structures caused by salt dissolution or gypsum karst. The seismic event was located at a depth of about 100 m representing a vertical linear dipole and 73° dipping normal fault shear crack associated with an unusual long rupture duration of 0.3 s.

In addition, some seismic observation were reported for man-made and natural karst processes. A serious accident happened in the Berezniki-1 potash mine (October 2006, Russia), which led to uncontrolled mine flooding, followed by karst processes in the rock mass above the mine and sinkhole formations (Malovichko et al., 2009). The recorded microseismic events were related to seismic sources originating from the governing karst processes, as indicated from the spectral signal content and by a clear space-time correlation of seismicity in direction of the sinkhole growth. In a later study, Malovichko et al. (2010) investigated the feasibility for recording the seismic effect of dynamic phenomena accompanying the karst processes based on synthetic seismograms (Section 1.2). For their simulation they formulated a seismic source model with respect to two major mechanisms associated with karst processes (Fig. 3.2, Section 1.2). One major source process was considered in with shear and detachment

cracking at the cavity roof. A second one is represented by the collapsing wall rocks at the karst cave bottom. For different modeled sources it was found that the signal generally lies in the frequency range from $10 - 100$ Hz, which was consistent with the characteristics of microseismic events ($M_L - 3$ to -1.5) recorded in evaporite cavity formations in the Dead Sea region (Wust-Bloch and Joswig, 2006). In both studies, it was stated that the frequency range changes significantly to lower frequencies ($\leq 10Hz$) for rock impacts on a brine filled cavity bottom.

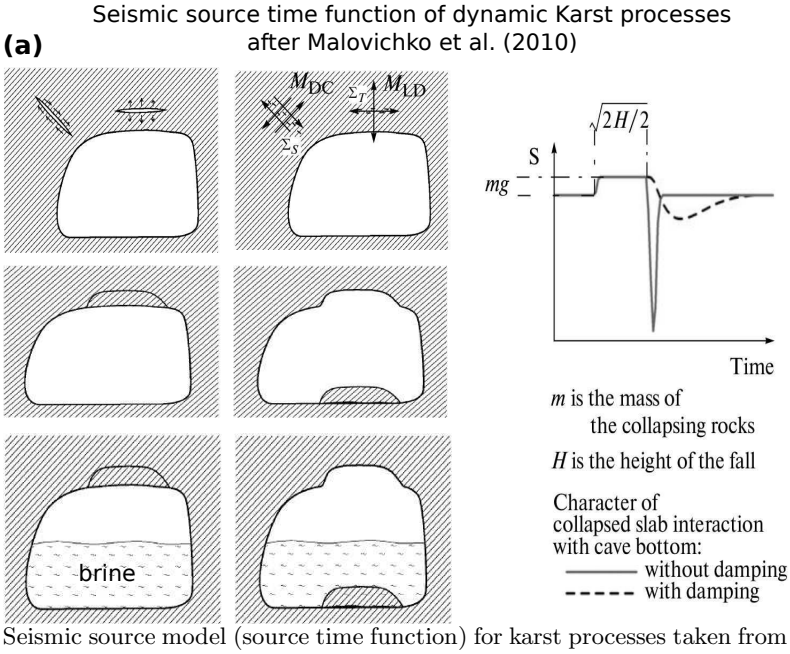

Figure 3.2: (a) Seismic source model (source time function) for karst processes taken from (Malovichko et al., 2010).

3.2 Cerville-Buissoncourt: evidence for consistent shear source mechanics

At the Cerville-Buissoncourt study site, it was so far discussed that both microseismic event types, isolated and tremor-like events, seem to represent fracturing processes at the cavity roof (Section 1.3.3.1, 1.3.4.1 and 2.6.4). The spectral content for both event types is dominated by higher frequencies in the range $20 - 150$ Hz (e.g. Fig. 2.9), what agrees with the expected range for shearing and detachment cracking at the cavity roof or undamped rock collapses at the cavity bottom (Malovichko et al., 2010, Wust-Bloch and Joswig, 2006) (Fig. 3.2). The latter one, namely the impact of falling blocks, is rather unlikely at Cerville, since the brine-filled and pressurized cavity should reduce significantly the fall velocity of detached Marl or salt blocks. Moreover, microseismic events seem to be generally associated with simple and

short rupture process, as demonstrated by the pulse-like, short lasting event shown in Figure 3.3. In cases of rock falls or collapses, generally longer signal durations ($\gtrsim$ 0.1 s) would be expected (e.g. Lenti et al., 2012, Malovichko et al., 2010, Miller et al., 1989, Phillips et al., 1996, Wust-Bloch and Joswig, 2006).

Considering the energetic constitution of body wave phase for the event example in Figure 3.3, already some first insights into the governing rupture mechanism can be observed. The shown event is directly located below receiver 62 (Section 2.3.2) and shows a dominant short, pulse-like P wave signal in the vertical component (Fig. 3.3). S waves can be seen in the horizontal components, but show significantly lower amplitudes. Similar low S/P wave ratios have been also observed for the other considered events located directly below station 62 and 63 (Section 2.3.2.2). Consequently, the underlying mechanism is apparently similar for the considered events and is characterized by a predominant P wave radiation vertically upwards or simply radiates few S wave energy.

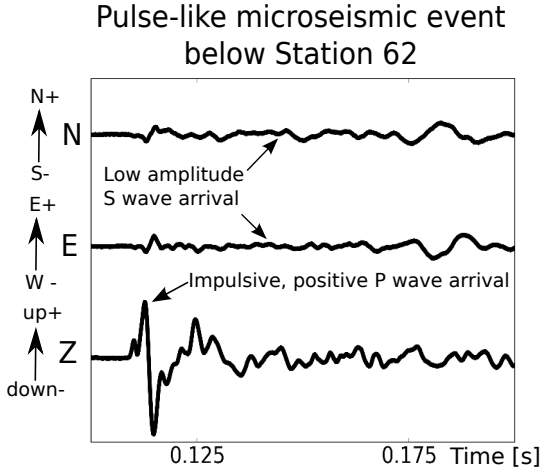

Figure 3.3: Typical short, pulse-like shaped event located below stations 62 and 63, documenting rather simple source rupture processes as shearing or detachment at the cavity roof. Note the dominant amplitude of the P wave compared to S waves.

In the following it is aimed to further constrain the underlying mechanism and further investigate the apparent similarity in source mechanism observed for these few events as well as for the entire dataset of the microseismic crisis in 2008 at Cerville. However, the application of classical event specific source analysis tools, like automatic moment tensor inversion approaches (e.g. Dahm et al., 1999, Sen et al., 2013), is supposed to be very challenging and limited for the Cerville microseismic dataset. Microseismic events appear preliminary in form of swarms, where single microseismic events cannot be sufficiently isolated from the preceding and following ones (Section 1.3). Moreover, the usage of high frequency data ($\gtrsim$ 40 Hz) and the limited station coverage strongly affects the robustness of such inversion approaches

(Section 3.1).

Therefore, in this Section, a comprehensive source analysis is presented, constraining step-by-step the governing source mechanisms by means of (i) qualitative observations (Section 3.2.2 and 3.2.3) and (ii) quantitative source inversion (Section 3.2.4). In the qualitative analysis, I refer to major trends, indicating the presence of a systematic source effect, what is observed from spectral characteristics (Section 3.2.2) and from peak-to-peak amplitude ratio distributions (Section 3.2.3), which are compared with observations from synthetic seismograms. The calculation of synthetic seismograms is briefly introduced in the following Section 3.2.1 and further documented in Appendix C.

In the quantitative analysis, then the observed trends are evaluated and quantified by means of three different inversion approaches. The first approach represents the conventional inversion (Fig. 3.4), using the observed amplitude spectra of different stations in order to explore the best source model with respect to one single event (Section 3.2.4.1). For the second and third approach, it is generally assumed that the source mechanism remains constant for all considered events. If this assumption holds, it is then theoretically feasible to use the microseismic data of several events observed at one single station in order to constrain a common source mechanisms (average source mechanism), as schematically shown in Figure 3.4. In this manner, in the second inversion approach I used several amplitude spectra of around 90 events observed at one station in order to find the best average source model (Section 3.2.4.2). Analogically, in the third approach, simple peak-to-peak amplitude ratios for around 6000 events observed at one single station are compared with synthetic ones in order to find the best representing average source model (Section 3.2.4.3).

3.2.1 Synthetic calculations

In the following Sections, synthetic seismograms are used in order to investigate the source mechanics. The synthetics were calculated using the QSEIS code (Wang, 1999) (Appendix D). It should be noted that from this approach only 1-D propagation media can be considered, while all introduced source models can be modeled (Fig. 3.1). For a reliable estimation of the governing source mechanisms through the comparison of observed and synthetic data, it is important to use a well constrained 1-D velocity model. The inclusion of observed signals strongly affected by 3-D propagation effects, e.g. scattering, multipathing at the 3-D cavity structure etc. (Section 2.3.2.1), should be avoided.

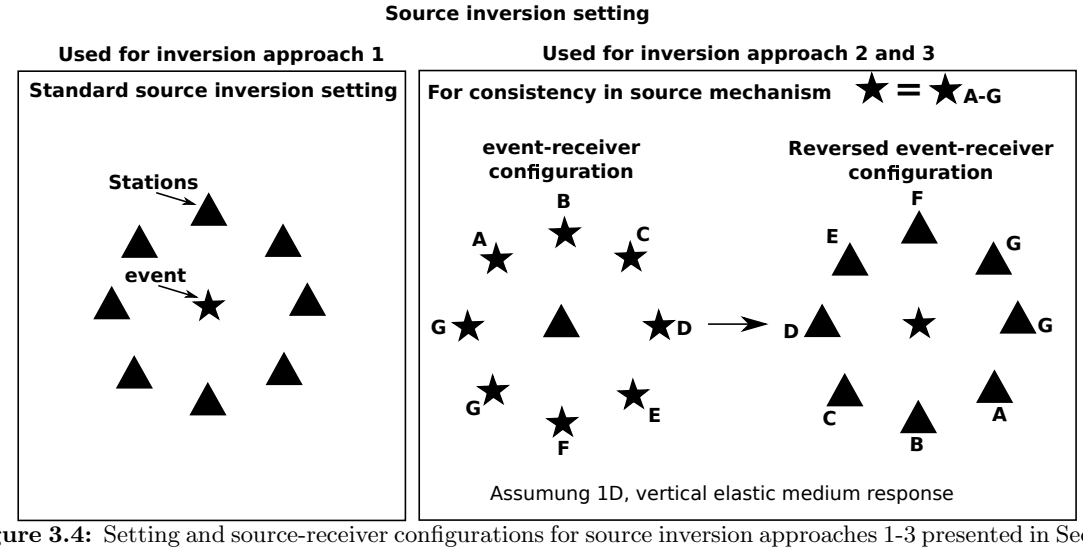

Figure 3.4: Setting and source-receiver configurations for source inversion approaches 1-3 presented in Section 3.2.4.

In the entire following section, I used the velocity model as shown in Table 3.1. This model is a readjusted version of the original velocity model proposed by Mercerat (2007), where I accounted for the newly obtained elastic parameters V_P, V_S, Q_P and Q_S from observation of stations 6 1-3 for the 20 events located below these stations (Section 2.3.2). In addition, P and S wave travel time distances for the other stations were also used to improve the velocity model. The details of this procedure are explained in Appendix D.2.

As it will be seen below, observed and synthetic wave forms, amplitude spectra and peak-to-peak amplitudes will be systematically compared for each station. In this context, a Green's function database was computed using the minimizer KIWI tool (Heimann, 2011) in order to account for different receiver depths. KIWI Green's function databases are extremely convenient to rapidly calculate the synthetic seismograms for different source models and to compare them with observed data (see also Appendix D.3). The comparison of synthetic and observed data is measured by standard misfit norms, $l1$-norm and $l2$-norm. For misfit minimization, I made use of the Levenberg-Marquardt minimization technique as provided by the KIWI tools to solve non-linear square problems. On the other hand, no tools for comparison for synthetic and observed peak-to-peak amplitudes are so far implemented in the KIWI tools. To obtain the synthetic amplitudes, I first calculated the displacement seismograms using the minimizer KIWI tool and differentiate them to velocity. Then peak-to-peak amplitudes were estimated for different frequency bands in the same way as done for the observed ones. The used fitting procedure to compare synthetic and observed amplitudes will be explained below.

Table 3.1: Readjusted velocity model (Appendix D.2) used for synthetic seismogram calculations.

	Depth [km]	V_p [km/s]	V_s [km/s]	Q_P	Q_S	ρ [g/cm^3]
Soil	$0 - 0.02$	1.1	0.5	40	20	2.3
Marls and sands	$0.02 - 0.06$	2.0	0.9	40	20	2.3
Marls and sands	$0.06 - 0.118$	2.9	1.3	40	20	2.3
Dolomite	$0.118 - 0.13$	4.9	2.6	40	20	2.5
Anhydritic marls and Salt	$0.13 - 0.3$	4.1	2.0	40	20	2.4

3.2.2 Spectral characteristics

The apparent simplicity and consistency of the governing source process, at Cerville, is documented by the comparison of the average spectra shown for the 54 events of the location training set (Section 2.1), and for around 2000 arbitrary chosen events, including both, isolated and tremor-like events, which were located located homogeneously over the entire cavity structure (Fig. 3.5). The average spectra were calculated for the frequency range of $10 - 500$ Hz, describing the mean spectral amplitudes for each 5 Hz interval, for the vertical components of most stations. As a surprising result, the individual as well as the average spectral shape is almost identically for each station for the 54 and the 2000 arbitrary chosen events (Fig. 3.5).

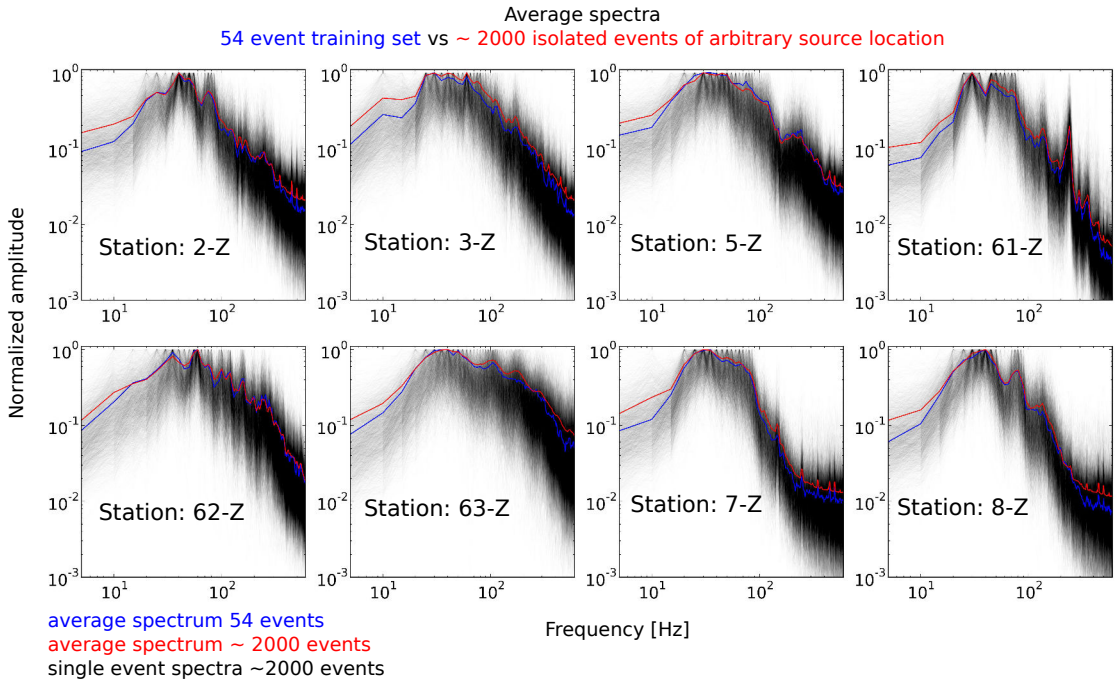

Figure 3.5: Station's Z-component average spectra. The average spectra of the 54 located events of the training set (blue lines) (Section 2.1) and $\sim$ 2000 arbitrary chosen events (red lines) calculated from the individual normalized event spectra (black lines). See text for calculation procedure.

These observations suggest some preliminary conclusions. First, they suggest that the spectral characteristics cannot be used to distinguish between isolated and tremor-like events (this

point will be further discussed in Chapter 4). Secondly, the similarity in the shape of the average spectra indicates that the size and type of the rupture processes are similar everywhere in the cavity zone. Hence, the distinct average spectral shape observed at each station is likely to represent its characteristic average Green's function, which is the average elastic response of the dominant source-receiver pathway for each station, while the excitation for different seismic sources remain constant.

Following these first results, it can be assumed that the differences in the individual event spectra (Fig. 3.5) are mostly controlled by the event location and its source size. This hypothesis is tested in Figure 3.6, where the difference in event location is compared with the estimated difference in the spectral shape for selected event pairs using observations from station 62. In total, I chose around 750 of the largest events, homogeneously distributed over the cavity zone. The chosen events were of isolated character (no event appears before and after 2 sec of the considered event), and all events occurred in the crisis of 2008. The spectral comparison for each event pair was based on the P wave spectra determined from the L component of the LQT coordinate system (e.g. Plesinger et al., 1986) obtained upon rotation of the N, E, Z components using the determined polarization angles (Section 2.2). Before calculating the fft spectrum, P waves were isolated by a hanning window multiplied around the maximum P wave amplitude (see later Section 3.4, Fig. 3.25 for a detailed illustration). For each event pair, the normalized P wave spectra were compared using a least mean square fit ($l2$-norm) (Fig. 3.6).

In Figure 3.6c, the misfits for all event pairs (total of $283,881$ for 754 events) are shown as a function of the difference in the epicentral distances and in the incidental and the backazimuthal angles. In addition, colors denote the difference of the peak frequency for each event pair. This figure shows a better fit for event pairs with similar peak-frequency. Moreover, the spectral fit improves significantly for event pairs with similar incidence angles and epicentral distances and slightly improves for those with similar backazimuth angles. In other words, the spectral fit between two events is very good when both events are located at the same spot and are of similar size. The event size can be roughly approximated by the peak frequencies which is also affected by attenuation (e.g. Eisner et al., 2013). Contrastingly, the spectral fit is worst when events have different size, epicenter location and/or source depth.

The knowledge of event location and event size is thus sufficient to explain spectral differences, what implies certain stability in source mechanism. More precisely, spectral differences are

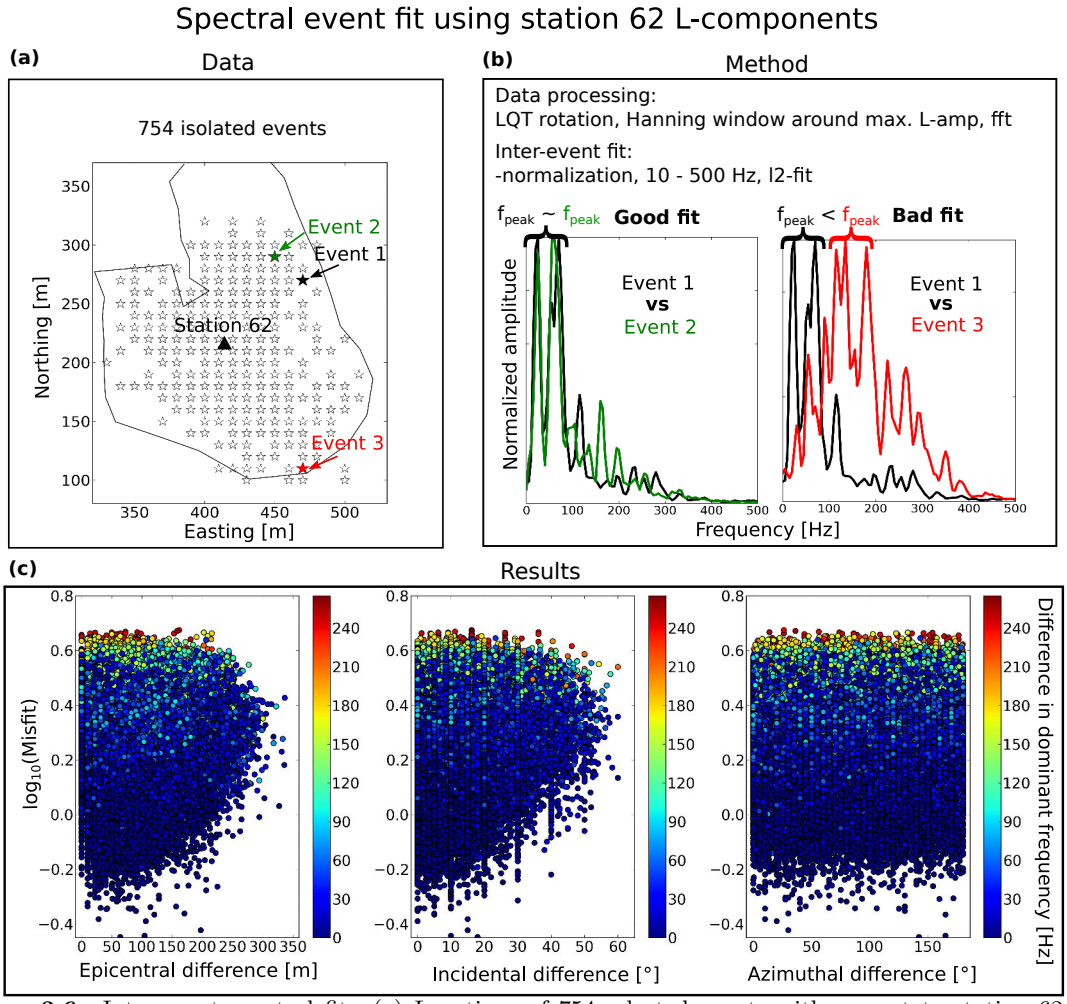

Figure 3.6: Inter-event spectral fit. (a) Locations of 754 selected events with respect to station 62. (b) Example of a good (right panel) and bad (left panel) spectral spectral fit with respect to events 1-3. (c) The logarithmic misfit for all fitted event pairs (a) shown as a function of their corresponding differences in epicentral distance (right panel), incidence (middle panel), and backazimuth (left panel) angle with respect to station 62. Colors show the respective difference in the estimated peak frequency.

principally dependent on the incidence angle at station 62. Knowing that the elastic medium is horizontally layered, and thus symmetric, its elastic response recorded at station 62 does probably not change significantly regarding different incidence angles. It seems thus probable that the change in the spectral shape as a function of different incidence angle is directly related to the source P wave radiation pattern. Consequently, the source mechanism is probably associated with a dominant upward P wave radiation what was already documented for the event example shown in Figure 3.3.

3.2.3 Peak-to-peak amplitude characteristics

The apparent consistency among source mechanisms is further investigated modeling peak-to-peak amplitudes (see e.g. Fig. 2.1). In this approach, the peak-to-peak amplitudes where

determined for a fix frequency range of $30-90$ Hz, where signals are most energetic (Fig. 2.9) and in accordance with the frequency range proposed by Malovichko et al. (2010). In order to fulfill the effective point source approximation (Appendix C.3) and to avoid the influence of small-scale heterogeneities in the propagation medium, it would be desirable to consider lower frequencies. However, low frequencies are here widely damped by the instrumental high pass response with a cutoff frequency at 40 Hz.

Given that the seismic wave velocities are in the order of 1600–3000 m/s (e.g. Table 3.1), in the frequency range 30–90 Hz we obtain wavelengths of the order of $17-100$ m. As a result, wavelengths are in a similar order as the expected hypocentral distances, and therefore the influence of the wave propagation and refraction (Section 1.3.4) on the amplitude ratios is expected to be smaller. However, Mercerat et al. (2010) found that the source radius is in the order of one to several ten meters ($6-31$ m) for eight events recorded in $2005-2007$. Assuming that these estimations are correct, it cannot be completely excluded that in some cases the estimated amplitudes reflect near-field or directivity effects, especially in cases of short source-receiver distance. This can be a common case for station 63.

Figure 3.7 shows the observed T/ZR amplitude ratios determined for the 54 events of the location training set (Fig. 2.3 and Section 2.1) and the 20 events located below station 62 and 63 used to constrain attenuation and velocity characteristics (Section 2.3.2). The T/ZR amplitude ratio generally reflects the relative energy of SH compared to P and SV waves and was calculated from rotation of the horizontal components N and E into the directions radial (R) and transversal (T) to the source–receiver travel path (RTZ radial-coordinate system). Three dimensional component rotation, including the vertical Z component, to the LQT (ray oriented) coordinate system is generally impeded by uncertainties in source depth (Section 2.1 and 2.3.2), erroneous incidence angle estimations (refraction affected) (Fig. 2.5 and 2.8) and since no polarization angles are available for station 63 (Section 2.2.3). Full component rotation and calculation of P/SV, as well as SV/SH amplitude ratios is generally feasible for stations 5 and 62 as shown later below.

From the shown amplitude ratios, it can be observed that the T/ZR-ratio remains relatively stable for values between -1 and 1 over the entire range of apparent station incidence angles (based on uncertain source depth), while the ratios seem to be generally somewhat smaller for lower incidence angle as compared to higher ones (with exception of station 63). In order to roughly approximate which kind of source mechanisms might be responsible for this T/ZR-

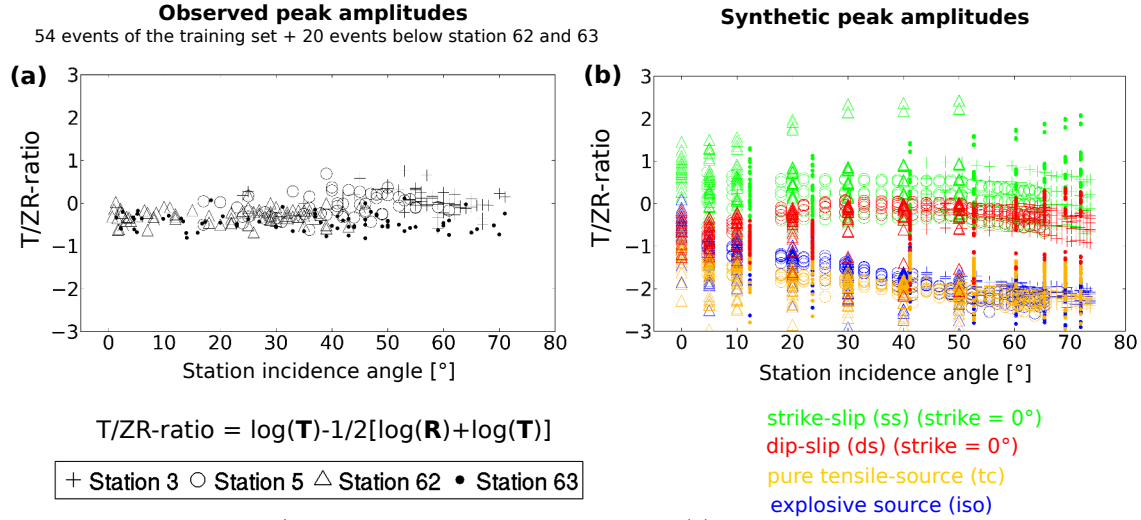

Figure 3.7: Observed T/ZR peak-to-peak amplitude ratios. (a) Observed ratios for located events of the training sets introduced in Sections 2.3 and 2.3.2. Station incidence angle were calculated based on the estimated source depth, which is relatively uncertain, and therefore need to be regarded with caution. (b) Synthetic ratios calculated for four potential source models (Fig. 3.8). The synthetic ratios were calculated for source locations being in agreement with the range of observed source locations. These "synthetic" source locations were determined by assuming a fixed source depth at 150 m, while the epicenters corresponded to locations around station 62 given by a grid defined by the Cartesian product of a set of backazimuth angles ranging $\{0, 10, \ldots, 340, 350\}$ and incidence angles $\{0, 5, 10, 20, 30, 40, 50\}$.

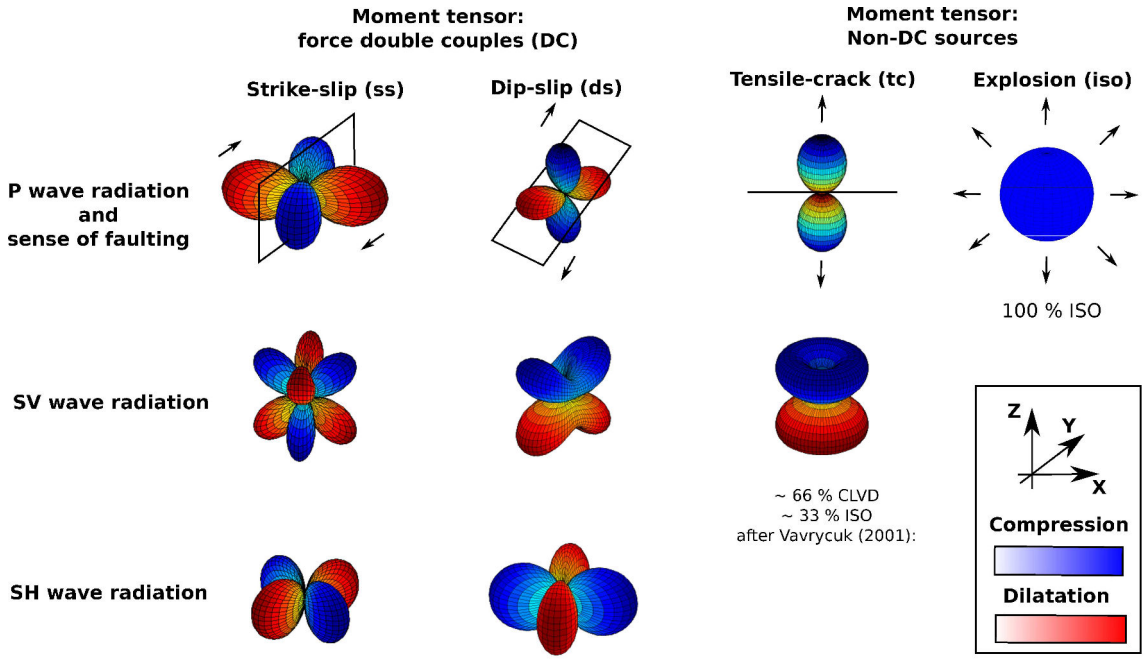

Figure 3.8: Radiation pattern for four potential source models. Radiation coefficients used for radiation pattern illustration were calculated by using the approach by Boore and Boatwright (1984) for DC sources, the approach by Vavryčuk (2001) for a pure tensile source with an tensile angle of $\alpha = 90°$, and basic formulas for an isotropic (e.g. Lay and Wallace, 1995) which all were implemented in the matlab codes by Kwiatek and Ben-Zion (2013) (`http://www.mathworks.fr/matlabcentral/fileexchange/authors/201090`) and SEIZMO (`http://epsc.wustl.edu/~ggeuler/codes/m/seizmo/`)

ratio distribution, I discuss some pattern of synthetic amplitudes (Fig. 3.7b, Section 3.2.1). Four potential source models are considered (Fig. 3.8): a strike-slip fault (*ss*), a dip-slip fault (*ds*), a tensile source (*tc*) with horizontal crack geometry, and an explosion (*iso*) (Fig. 3.7b). By this comparison of synthetic and observed T/ZR-ratio, it can be clearly seen that the *ds* model is the only model able to approximate the observed amplitude ratio distribution. Thus, the observed systematic source effect can be apparently best approximated by a simple shear source as represented by classical DC-model with clear tendency to *ds* faulting.

On the other hand, the existence of predominating mixed source model associated with a dominant DC-component and minor *tc* or *iso* component cannot be completely excluded from these results (Fig. 3.7). Mercerat et al. (2010) reported the presence of extensive source components suggested by a low ratio between the P and S wave displacement spectra (Ω_S/Ω_P) of < 4 (Walter and Brune, 1993) for eight analyzed isolated events. In addition, a large number of laboratory tests indicated extremely low tensile strengths with respect to some Marl samples, located at the cavity roof (Mercerat, 2007, Mercerat et al., 2010, Souley et al., 2008). However, compared to the results of this study (Table 3.1 and Section 2.3.2) S wave attenuation was significantly underestimated in the study by Mercerat et al. (2010) who used $V_S = 2.0$ km/s (in this study $V_S = 1.28$ km/s) and equal Q factors for P and S waves, which significantly decrease the estimated S/P ratio (e.g. Eisner et al., 2011).

In order to demonstrate that these results are also valid with respect all the other events of the microseismic crisis in 2008, I examined the T/ZR amplitude ratios for around 6000 events recorded during the period of the crisis (March-April 2008) and in the following aftershock sequence up to December 2008 (Fig. 3.9). All these 6000 events represent both isolated and tremor-like event types and for all of them polarization angles could be determined using the polarization-based approach for stations 3, 5, and 62 (Section 2.2). Backazimuth angles obtained from station 62 are generally used for the T/ZR amplitude ratio calculation at station 63. From Figure 3.9a-d, it can be seen that the range of the T/ZR amplitude ratios is similar with respect to all stations equally for the 6000 and the well located events. The comparison with synthetically calculated range of T/ZR amplitude ratios for the four investigated source models strongly supports the idea that the governing source effect can be best approximated by a simple DC-source model with clear preference to a *ds* faulting model. The *tc* and the *iso* source models might explain some T/ZR amplitude ratios observed at station 62 and 63, but fail to reproduce observations at station 3 and 5. The *ss* model

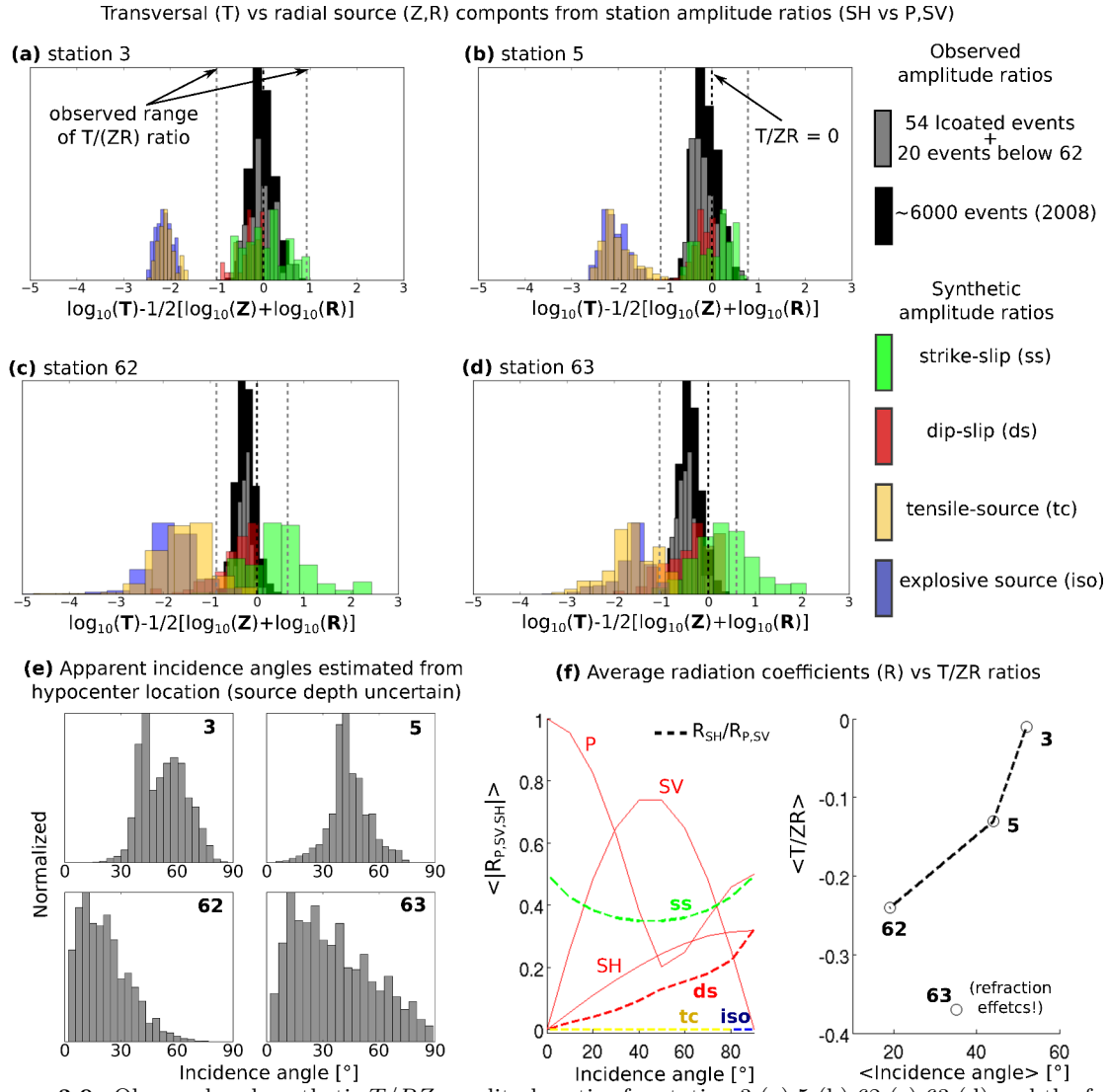

Figure 3.9: Observed and synthetic T/RZ amplitude ratios for station 3 (a) 5 (b) 62 (c) 63 (d) and the four potential source models (Fig. 3.7 and 3.8). (e) Station incidence angles for the $\sim$ 6000 events corresponding to source depth estimates using the polarization- and amplitude-based approach (Section 2.6), which are uncertain (see text). (f) (left panel) Average of the absolute values of ray-theoretical radiation coefficients $\langle|R_{P,SV,SH}|\rangle$ for P, SV and SH waves (e.g. Boore and Boatwright, 1984) shown for the *ds* model (red continuous lines) and the $R_{SH}/R_{P,SV}$ ratio $= 2\langle|R_{SH}|\rangle/(\langle|R_P|\rangle + \langle|R_{SV}|\rangle)$ shown for all four tested source models (thick dashed lines) plotted as a function of incidence/takeoff angles, while radiation azimuths were considered for $\{0, 10, \ldots, 340, 350\}$. (f) (right panel) The average T/ZR amplitude ratios for all stations (a)-(d) shown as function of the average incidence angle (e).

agrees well with T/ZR amplitude ratios of stations 3 and 5, while most of the lowest T/ZR amplitude ratios observed at stations 62 and 63 cannot be explained by this model.

Also in terms of quantity, a clear preference to the *ds* model is recognizable in Figure 3.9. There is a clear trend with respect to the quantitative distribution observed T/ZR amplitude ratios for each station, which generally correspond to different receiver depth and thus, different average incidence angles (Fig. 3.9e,f). Correspondingly, it can be observed that the

average T/ZR amplitude ratio for each station increase with increasing average incidence angle (Fig. 3.9f) as it was already observed in Figure 3.7. The highest average T/ZR amplitude ratio is observed for station 3, for which the average incidence angle is supposed to be larger compared to other stations (Fig. 3.9e,f). Reversely, the lowest average T/ZR amplitude ratios is observed for station 62, where the average incidence angle is supposed to be smaller compared to other stations (Fig. 3.9e,f). It must be noted that the shown absolute incidence angles in Figure 3.9e,f are erroneous, since they were calculated based on the estimated source depths, which are highly uncertain (Section 2.4). Nonetheless, the relative difference of the average incidence angles observed at each station should be relatively well represented by the shown distributions (Fig. 3.9e).

The observed trend of increasing SH wave energy with increasing incidence angle can be well explained by considering the P, SV, SH radiation pattern associated with a *ds* source (Fig. 3.8) as represented by their radiation coefficients $R_{P,SV,SH}$ (e.g. Boore and Boatwright, 1984) in Figure 3.9f. For smaller incidence angles the wave-field is generally dominated by P and SV wave contribution, while SH wave energy becomes more important for higher incidence angles as principally radiated in the horizontal plane where SV wave radiation is smallest. This trend is very well reflected by the observed T/ZR amplitude ratios for stations 3, 5 and 62. In contrast, observations from station 63 deviate from this trend, where T/ZR ratios and SH wave energies are lowest compared to the other stations even though the average incidence angle is clearly higher as compared to station 62. This behavior can be explained by the presence of significant refraction effects at the Dolomite, which lead to a decrease in the SH/P,SV wave amplitude ratio as observed from synthetic seismograms in Figure 1.14 (Section 1.3.4.2). In addition, near-field effects might play a role in this respect.

Taking all these observations together, spectral (Section 3.2.2) and peak-to-peak amplitude examination clearly documented a significant change in the wave-field depending on the considered incidence angle which can be best explained by a *ds* source model. When assuming a *ds* source model, P, SV and SH wave radiations are not symmetrical into all directions, change significantly with fault orientation (e.g. Fig. 3.8), and thus with respect to the considered backazimuth angle (Fig. 3.6, Section 3.2.2). In order to investigate this issue, the P, SV and SH wave amplitude ratios of the 6000 events (estimated from peak-to-peak amplitude of the LQT components) are shown in Figure 3.10 projected to the lower station hemisphere with respect to station 5 and 62. The incidence angles for both stations are

supposed to approximatively represent the true source-receiver angle with the exception of erroneously high incidence angles estimated from station 5, when the true incidence angle exceeds 50° (Fig. 2.8 and Section 2.2.3). The shown SV/P and SH/SV amplitude ratios are distributed in a remarkably systematic manner, which consistently reflects the expected source radiation pattern of a pure *ds* fault striking approximatively with $150 - 330°$.

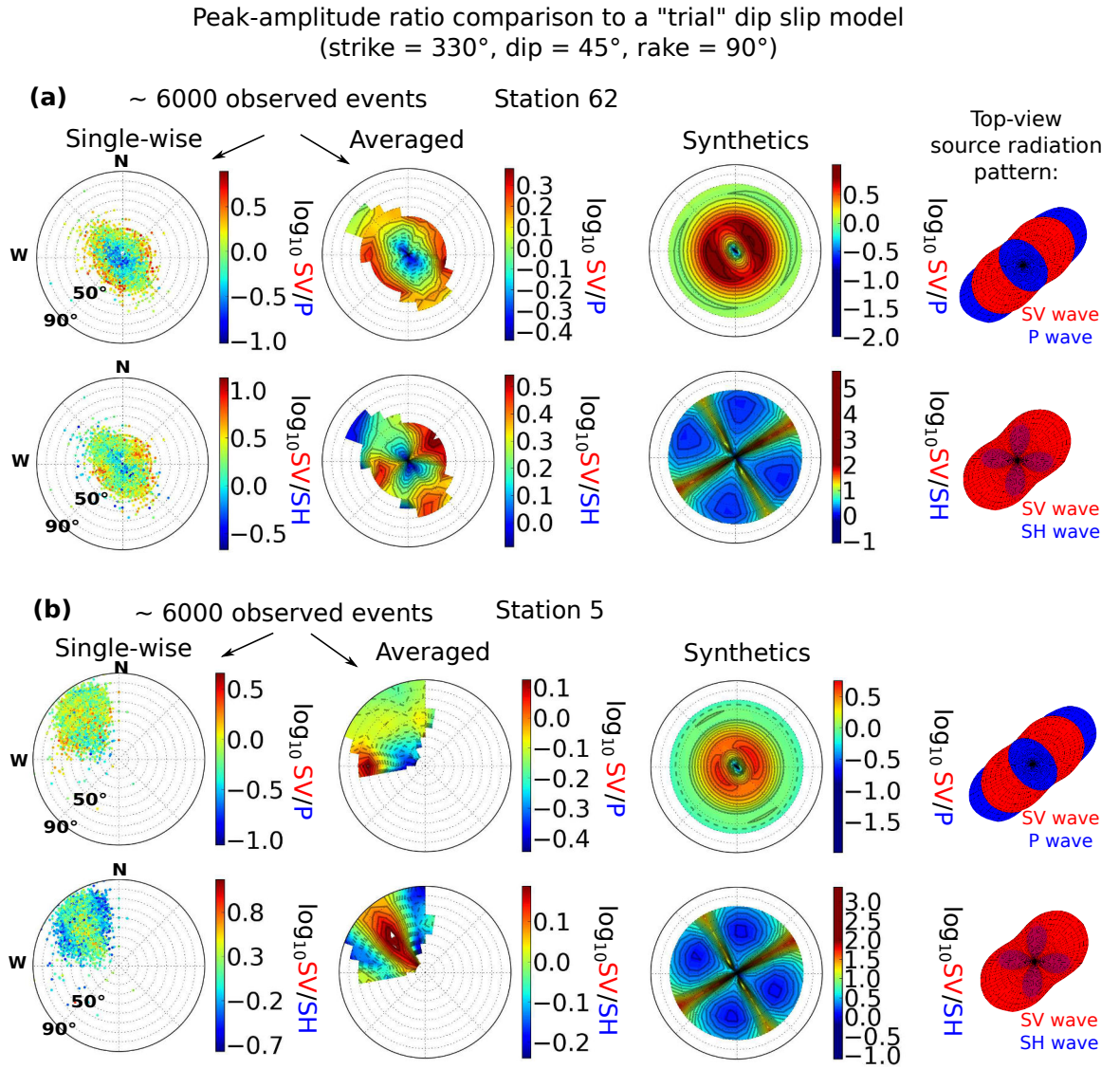

Figure 3.10: Body wave amplitude ratios for stations 5 and 62 for the ~ 6000 events compared to synthetics of a "trial" *ds* model. Station lower hemisphere plots and SV/P and SV/SH amplitude ratios shown as a function of the incidence and backazimuth polarization angles for station 62 (a) and 5 (b). From the left to the right, shown are (i) the observed individual amplitude ratios for each event (colored points), (ii) contours of the observed averaged amplitude ratios (color shaded contours) calculated for a discrete grid defined by the Cartesian product of a set of backazimuth angles ranging $\{0, 10, \ldots, 340, 350\}$ and incidence angles $\{0, 10, \ldots, 80, 90\}$, (iii) the synthetic amplitude ratios (color shaded contours) calculated for a grid defined by the Cartesian product of a set of backazimuth angles ranging $\{0, 10, \ldots, 340, 350\}$ and incidence angles $\{0, 10, \ldots, 60, 70\}$ for each station, respectively and (iv) the top view of radiation pattern for the used "trial" *ds* model.

Even though the observed SV/P and SH/SV amplitude ratios clearly reproduce the general trends as proposed by the synthetics, the extreme values and the range given by the synthetic ratios is often significantly larger, especially for the observed averaged amplitude ratio distribution. This lack of extreme values is generally related to errors and limited resolution in the estimated polarization angles ($\pm 30^\circ$ and 10°, respectively). Moreover, the observed amplitude ratios do not probably represent distinct ray phases directly comparable to the ray-theoretical radiation pattern, but include several seismic phases and rays, as well as scattering effects, which are not reproducible from the synthetics.

Consequently, the shown "trial" *ds* mechanism is a first order approximation and represents one possible solution. The robustness of this solution and the consideration of other solutions is investigated and discussed in the following Sections. In addition, it would be desirable to present quantitative estimates describing the amount of specific events associated with the apparent predominant source mechanism. Unfortunately, such estimates could not be presented in this study and should be the subject of future research.

3.2.4 Source mechanism inversion

It is aimed to quantify the space of possible solutions explaining the systematic source effect as observed from spectral and peak-to-peak amplitude characteristics (Section 3.2.2 and 3.2.3). Qualitatively, the best approximative source model seems to be represented by a classical double couple shear dislocation model with strong preference to a pure *ds* model (Fig- 3.10). By means of the following inversion approaches the stability of this solution will be explored by comparing systematically observed and synthetic, spectral and temporal amplitudes for different source models.

Even though the presence of minor portions of tensile components cannot be completely excluded (Section 3.2.2 and 3.2.3), in the following approaches only DC source models will be considered. As a result, it is assumed that the possible minor tensile component will not affect the result of the investigated DC-source model. Jechumtálová and Šílenỳ (2005) showed that the resolution of the DC-model is mainly affected, when the true source component is predominantly composed of Non-DC portions, what can be excluded for the majority of the considered dataset.

In addition, it is widely known that in non-optimal inversion scenarios, full moment tensor inversion (six source parameters) can also bias the resolution of the DC-moment tensor,

especially when considering microseismic data. The full moment tensor resolution is very sensitive with respect to the quality of source location, to the knowledge about the propagation medium, the data quality (signal-to-noise ratios), and the station coverage (e.g. Eaton and Forouhideh, 2010, Eisner et al., 2011, Godano et al., 2011, 2009). In addition to these limitations, in the present study it cannot be guaranteed that source mechanisms are exactly the same for all events, which might significantly bias the finally obtained moment tensor solution.

3.2.4.1 Inversion approach 1: conventional use of amplitude spectra

In this approach the best DC-source-model is investigated for one single event observed from different station data (Fig. 3.4a). One of the largest events was chosen that occurred in the very beginning of the microseismic crisis in 2008, when the cavity roof is expected to be less fractured compared to later periods. The event is one of the 20 events directly located below stations 62 and 63 (Section 2.3.2). Correspondingly, also predominant P amplitudes are observed, as very similar to the pulse-like event shown in Figure 3.3. The source inversion for this event aims to demonstrate whether the observed significant P wave radiation can be quantitatively describe by a DC source model.

Inversion was performed by using the observed amplitude spectra in the frequency range of $20-90$ Hz for four three component stations (3, 5, 62, and 63) as well as three one component stations (2,7,8) (e.g. Fig 1.5). The use of amplitude spectra compared to waveforms has the advantage of being independent on time/phase shifts between calculated Green's functions and observed seismograms arising from mismodeling of seismic velocities, an thus, erroneous travel times, source time origin and mislocation. On the other hand, due to the lack of phase information in the amplitude spectra inversion, the polarity of the source mechanism cannot be resolved. Since the difference in S-P travel times are generally very small ($\lesssim 0.1$ s, Fig. 2.5), P and S waves were not separated for inversion, but the complete Z,N,E component amplitude spectra are considered.

The best DC-source was investigated by means of a grid search with grid points defined by the Cartesian product of strike $= \{0, 10, \ldots, 340, 350\}$, dip $= \{5, 15, \ldots, 75, 85\}$, and rake $= \{0, 10, \ldots, 170, 180\}$ according to the conventions set forth by Aki and Richards (2002). The misift of observed at synthetic amplitude spectra was obtained by a standard least-mean square fit ($l2$-norm) using the minimizer tool of the KIWI tools (Heimann, 2011)

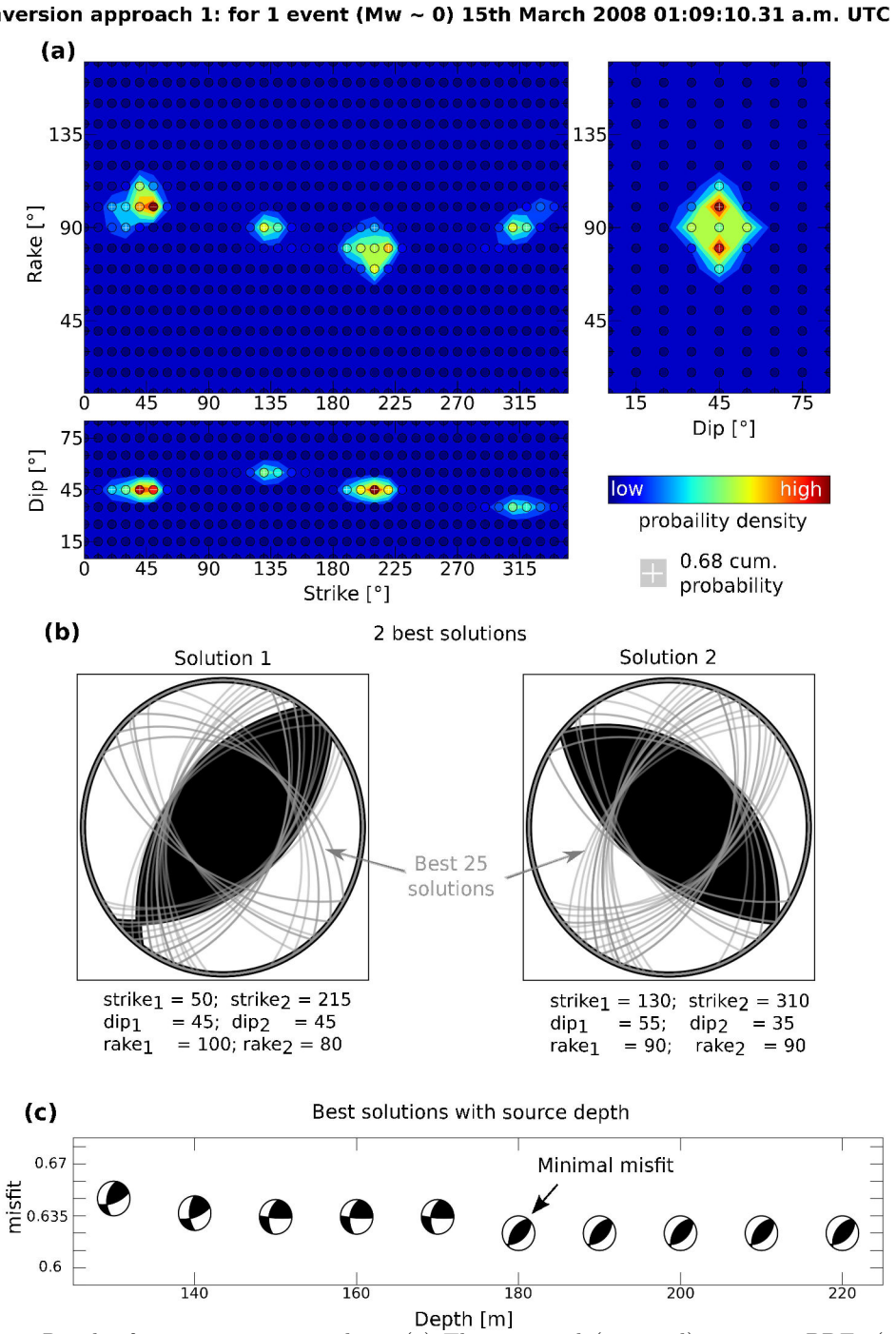

Figure 3.11: Results for inversion approach 1. (a) The marginal (summed) apparent PDFs (see Section 3.2.4.1) are shown for the strike-rake plane (upper left panel), the strike-dip plane (lower left panel) and the dip-rake plane (upper right panel). White crosses indicate the respective grid points covered by the apparent cumulative probability equal to 0.68. (b) The two best solutions (beach-ball plots) and the 25 next best solutions (gray circles). Note that compressive (black shaded area) and dilatational (white shaded area) are only shown for visualization, but are not known from this inversion approach. (c) Misfit and best DC solutions as a function of assumed source depth.

(Section 3.2.1, Appendix D.3). In order to account for receiver depth characteristic amplification effects as very important with respect to surface stations 7, and 8 (Fig. 2.9 and

Section 2.3.2), the Levenberg-Marquardt minimization technique was used (Heimann (2011) and references therein) to minimize at each grid point for the best fitting seismic moment scalar separately for each station.

The inversion results are summarized in Figure 3.11. In order to visualize the space of possible solutions, I calculated the marginal apparent probability densities for the entire model space M spanned by the defined grid of strike, dip, and rake (Fig. 3.11a). The probability densities function PDF was calculated assuming the error between model and data is Gaussian distributed $PDF(M) = \exp(-Misfit(M)/\sigma)/\sum \exp(-Misfit(M)/\sigma)$, where the normal distribution was parametrized using the variance σ. The variance was defined by the difference of the minimum misfit and the misfit value, being 3% higher relative to the entire misfit range. Even though, this formulation does not consider the actual uncertainties associated with data and model, and thus only represent an apparent probability, it is helpful to distinguish between more and less probable solutions and will be very useful, when comparing the results of this and the other following inversions approaches and their robustness.

As seen from the marginal PDFs in Figure 3.11a, the inversion results clearly converge for two solutions both demonstrating almost pure *ds* (Fig. 3.11a-b), while the minimal misfit is found for a source depth of 180 m, which is consistent with observations from S-P wave travel time differences (Fig. 3.11c). The first solution (*solution 1*) indicate *ds* faulting with a strike of $\sim 50 - 230°$, while the second solution (*solution 2*) indicates striking with $130 - 310°$, which is consistent with results shown in Figure 3.10.

Both solutions differ not significantly in misfit and their probability density (Fig. 3.11a) and reproduce the observations similarly well. The quality of the fit between observed and synthetic amplitude spectra and waveforms for *solution 1* is illustrated in Figure 3.12a and b, respectively. The fits for *solution 2* are very similar, and are therefore not shown here. The best fit with respect to waveforms and amplitude spectra is obtained for the Z components of stations 62 and 63, which show the largest amplitudes dominated by P wave energy. In conclusion, this approach demonstrated that dominant P wave radiation in vertical direction can be sufficiently well explained by a classical *ds* source model. The strike of the *ds* source model is ambiguous and cannot be completely resolved from this approach, which is probably a result of rather noisy data with respect to other stations and very limited azimuthal coverage. On the other hand, *solution 2* is consistent with the "trial" *ds* model shown in Figure 3.10, and is thus considered the preferred model. This result supports the idea of an

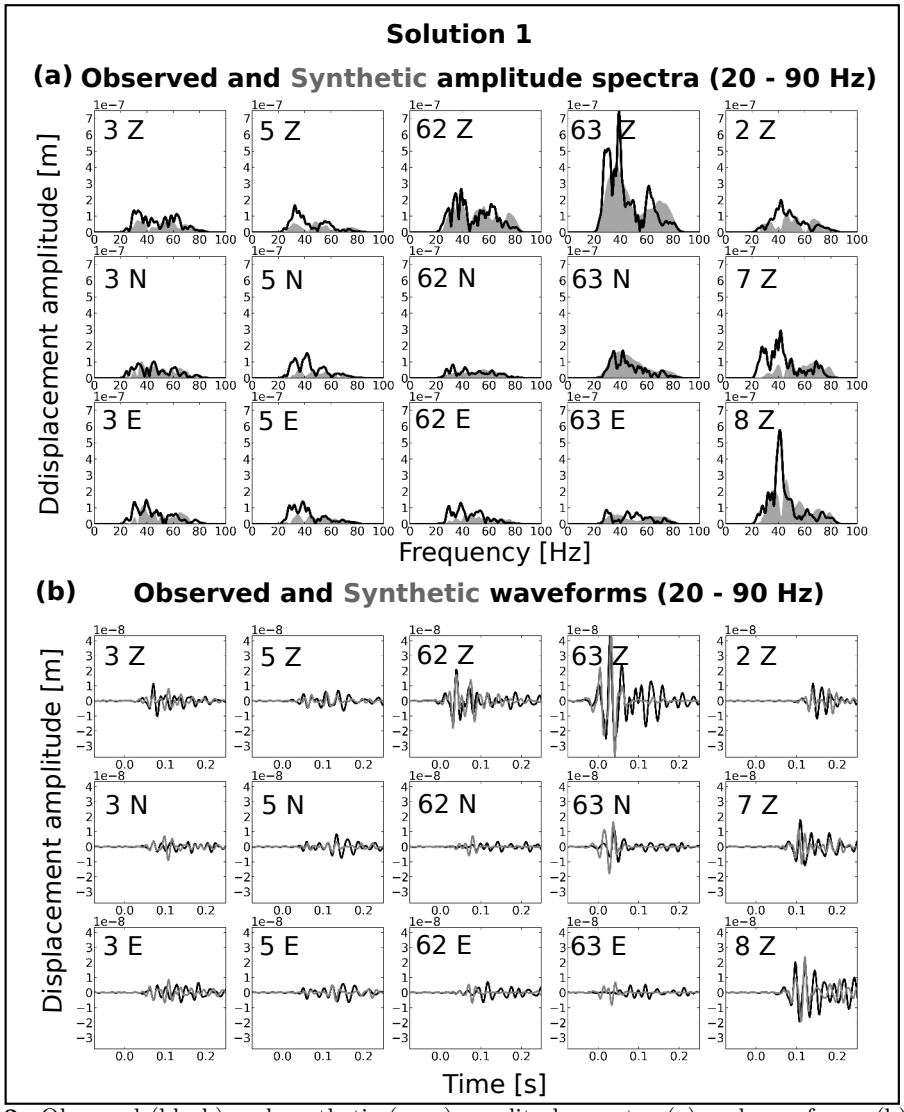

Figure 3.12: Observed (black) and synthetic (gray) amplitude spectra (a) and waveforms (b) with respect to the best DC solution (Fig. 3.11)

overall consistency in source mechanism. Correspondingly, the average mechanism indicated by most of the considered events in 2008 (e.g. Fig. 3.10) is also found when regarding one single event observed form different station observations (Fig. 3.4 and 3.11).

3.2.4.2 Inversion approach 2: reverse source-receiver setting

This approach uses the observations of several events at one station in order to derive a common focal mechanism and to test if a single mechanism can be used to reproduce observations of multiple events (Fig. 3.4). To test this issue, I chose 91 seismic events observed from station 62 that occurred randomly during the crisis in 2008 (Fig. 3.13 and Table B.4). The use of observation from station 62 has two significant advantages compared to the other stations.

First, observations (event seismograms) are available from all azimuths. Secondly, the majority of events is recorded at lower incidence angles so that lateral heterogeneities introduced by the 3D cavity structure (which cannot be explained by our synthetic 1D calculations, Section 3.2.1) play a minor role as compared to other stations.

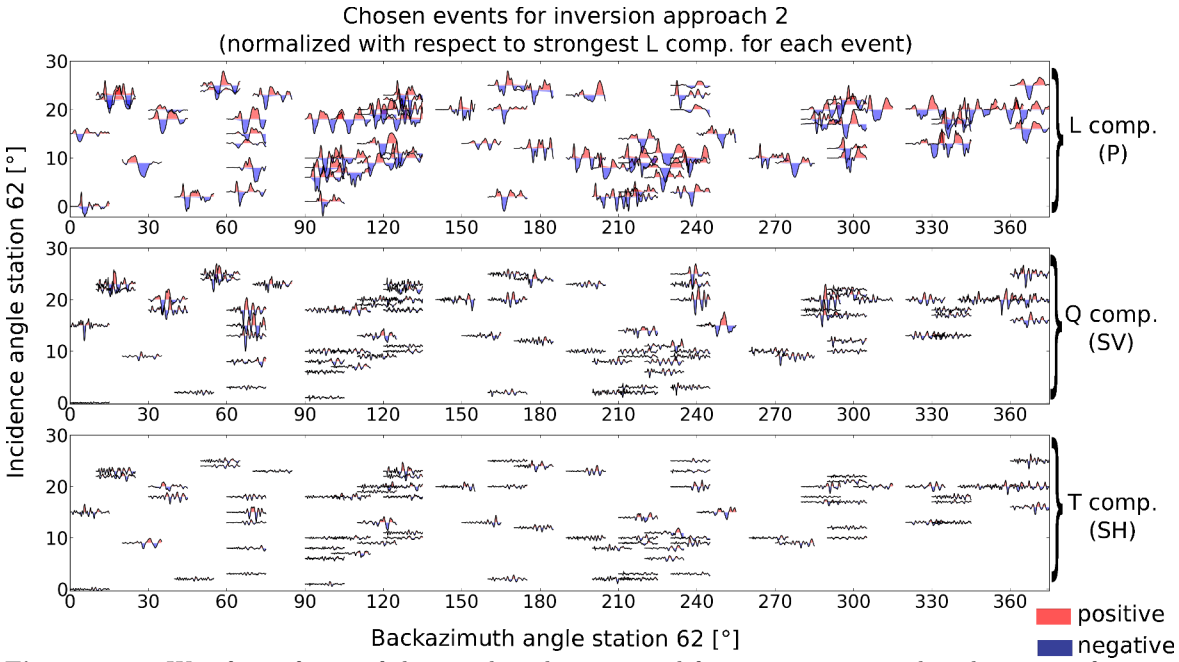

Figure 3.13: Waveforms for 81 of the 91 selected events used for inversion approach 2 shown as a function of backazimuth and incidence polarization angles with respect to station 62.

The major difficulty in event selection was to provide a wide range of events observed for different backazimuth and incidence angles and to choose events associated with similar magnitudes and hypocentral distances. The first criterion is very important with respect to the inversion resolution of the source mechanism. The second criterion is necessary to guarantee that attenuation effects are consistent for all events as a function of hypocentral distance. Therefore, I used the inter-event spectral-fit method used in Section 3.2.2, in order to find a preliminary event database, limited to events that showed similar peak-frequencies but different incidence and backazimuthal angles and that were located relatively close to station 62 (< 50 m) (Table B.4). Then, a further event selection was considered, choosing those with simple waveforms, comparable to the pulse-like shaped, where no precursor signals (Section 1.3.4) were visible.

81 velocity waveforms of the selected events are shown in Figure 3.13 as a function of the observed incidence and backazimuth angle of station 62 (the remaining 10 other waveforms are not shown to improve the visibility of the illustration). By considering the shown waveforms,

already similar characteristics can be recognized as they were stated in Section 3.2.3 and interpreted by the final *ds* model in Figure 3.10: P waves are very dominant compared to S waves for smaller incidence angles, SV wave amplitudes are dominant to the NE and SW, and SH wave amplitudes are comparatively very small.

During the inversion the events were treated as stations and the location of station 62 as the event location in order to determine the average source mechanism of all selected events (Fig. 3.4). As the estimated source depths are highly uncertain and differ significantly for the chosen events (estimated from the polarization- and amplitude-based location approach Section 2.2.3 and 2.3.5), a fix source depth at 150 m was assumed for that a new epicenter location was obtained using the incidence and backazimuth polarization angles (Table B.4). In order to scale these events for a similar event size, I normalized the Z, N ,E traces for each event by division of the absolute maximum found at $30 - 90$ Hz, which were then multiplied by the hypocentral distance to simulate attenuation. Then, the inversion procedure and parametrization was the same as documented for the first inversion approach (Section 3.2.4.1), with the exception that the seismic moment was not minimized at each grid point (source model).

This source inversion procedure, namely the usage of several event observations instead of station observations (Fig. 3.4), was not applied so far in seismic source analysis, and is presented for the first time by this study. On the other hand, it must be noted that this approach is based on strong uncertainties contained in the polarization angles (e.g. Fig. 2.8), and probably introduced by the kind of radical event trace normalization procedure. Next to these uncertainties, this approach is based on the very strong assumption of consistency in source mechanism. Nonetheless, the result as summarized in Figure 3.14 show surprisingly very similar trends as compared to the first inversion approach (Section 3.2.4.1) and the "trial" *ds* model shown in Figure 3.10. Similar to the first inversion approach, the inversion results converge for two very similar solutions (*solution 1* and *solution 2*) both demonstrating *ds* solutions with different fault strike of NW-SE and NE-SW, respectively.

From the marginal PDFs, calculated in the same manner as explained for inversion approach 1 (Section 3.2.4.1), a clear tendency towards *solution 1* is indicated (Fig. 3.14a), which is the solution consistent with with the "trial" *ds* model shown in Figure 3.10. Compared to inversion approach 1, the apparent cumulative probability, equal to 0.68, spans a very large space of possible solutions for this approach (Fig. 3.14a). This observation indicates that

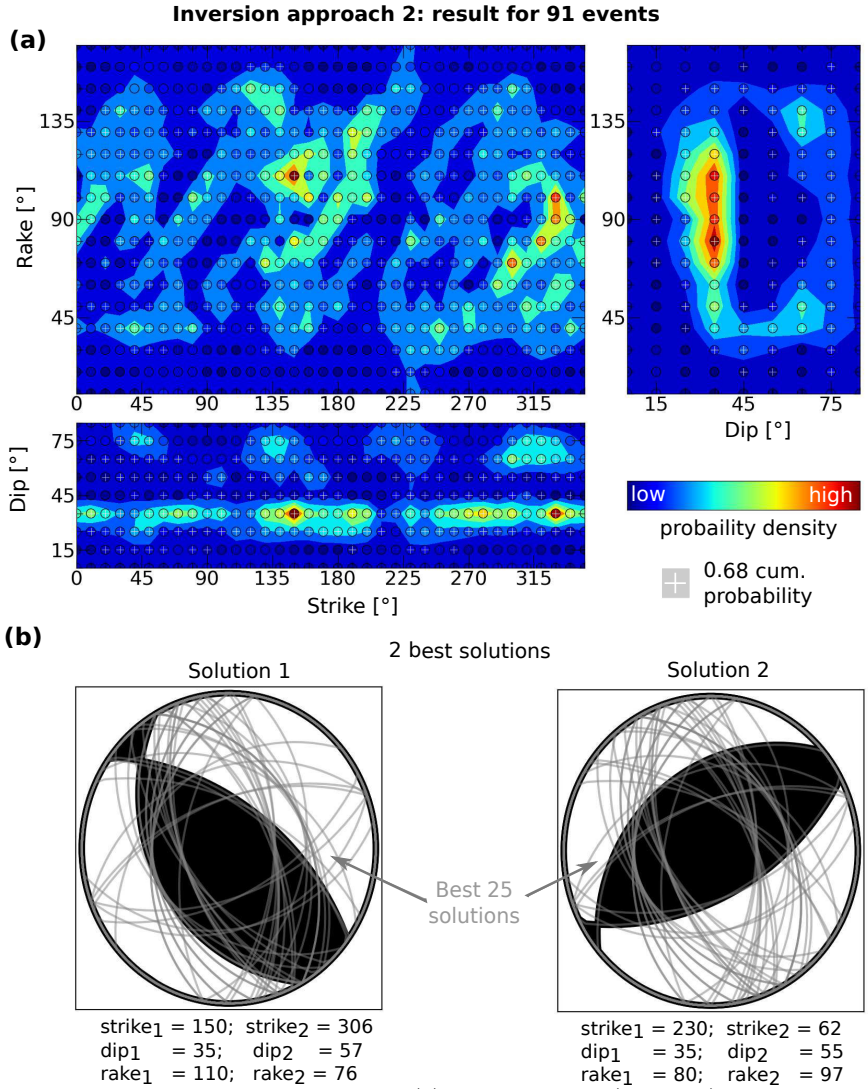

Figure 3.14: Results for inversion approach 2. (a) The marginal (summed) apparent PDFs (see Section 3.2.4.1) are shown for the strike-rake plane (upper left panel), the strike-dip plane (lower left panel) and the dip-rake plane (upper right panel). White crosses indicate the respective grid points covered by the apparent cumulative probability equal to 0.68. (b) The two best solutions (beach-ball plots) and the 25 next best solutions (gray circles). Note that compressive (black shaded area) and dilatational (white shaded area) are only shown for visualization, but are not known from this inversion approach.

there is a generally much lower robustness and stability in the results of this approach as compared to inversion approach 1. Accordingly, also the fit between observed and synthetic amplitude spectra is clearly worse (Fig. 3.15) than the fit shown for inversion approach 1 (Fig. 3.12).

Moreover, the dip of the *ds* solution is clearly concentrated at 35° (Fig. 3.14a,b) and not at 45° as shown for the "trial" *ds* model and for the results of inversion approach 1 (Fig, 3.11). This preference for a dip of 35° and strictly not 45° is possibly related to the fact that in this inversion approach only very small incidence angle (from station 62) have been considered

($\leq 30°$, Table B.4) and represents probably an artifact. As already discussed in Section 3.2.3, the ray-theoretical radiation pattern for small incidence angle predict generally extremely high or low body wave amplitudes especially for rays emitted from the lobes and nodes of the radiation pattern (as the case for vertical incidence angles) (Fig. 3.10). These extreme values are not resolved in the observed amplitudes, since seismic rays are significantly more scattered at the study site as in the theoretical case and polarization angle estimation is limited in resolution. As a result, the inversion tends to solutions close to these extreme values, what would be probably different, if higher incidence were included as done for inversion approach 1.

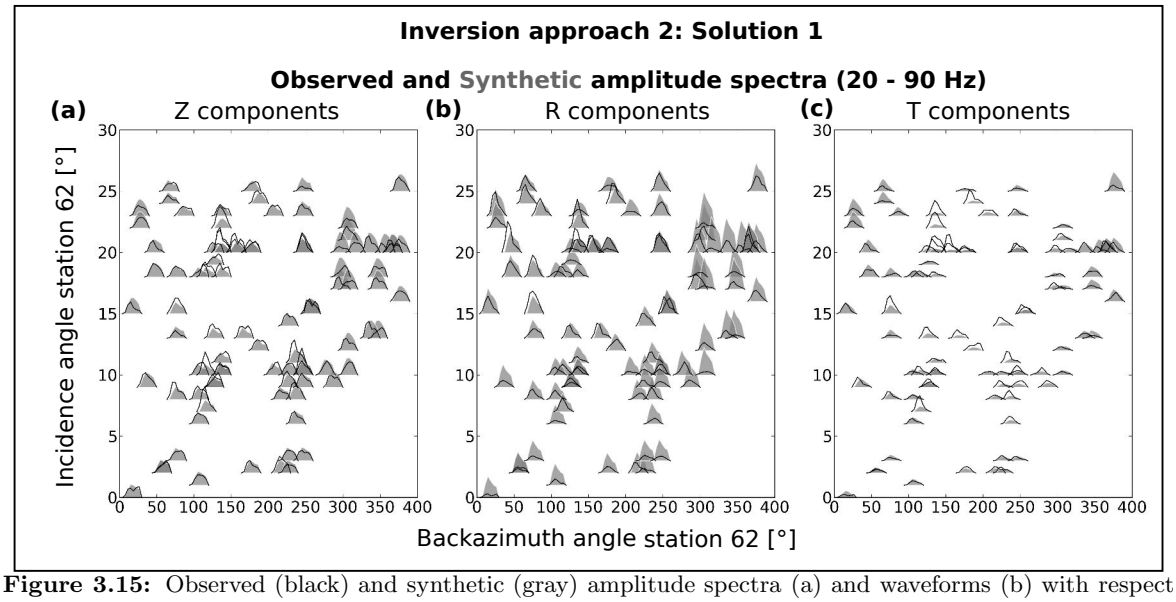

Figure 3.15: Observed (black) and synthetic (gray) amplitude spectra (a) and waveforms (b) with respect to the best DC solution (Fig. 3.14) shown as a function of incidence and backazimuth angle with respect to station 62

3.2.4.3 Inversion approach 3: using peak-to-peak amplitudes

In this third inversion approach, it is aimed to explain quantitatively the systematic distribution of observed amplitude-ratios of the $\sim$ 6000 events (Section 3.2.3) as a function of backazimuth and incidence angle (e.g. Fig. 3.10) using synthetic amplitude ratios calculated for the DC-source models considered in the other inversion approaches (Section 3.2.4.1 and 3.2.4.2). For similar reasons as stated in the inversion approach 2 (Section 3.2.4.2), for this approach only the observations from station 62 were used, since they represent the widest range of observed polarization backazimuth angles ($0 - 360°$), and reliable incidence angles (e.g. Fig. 2.8).

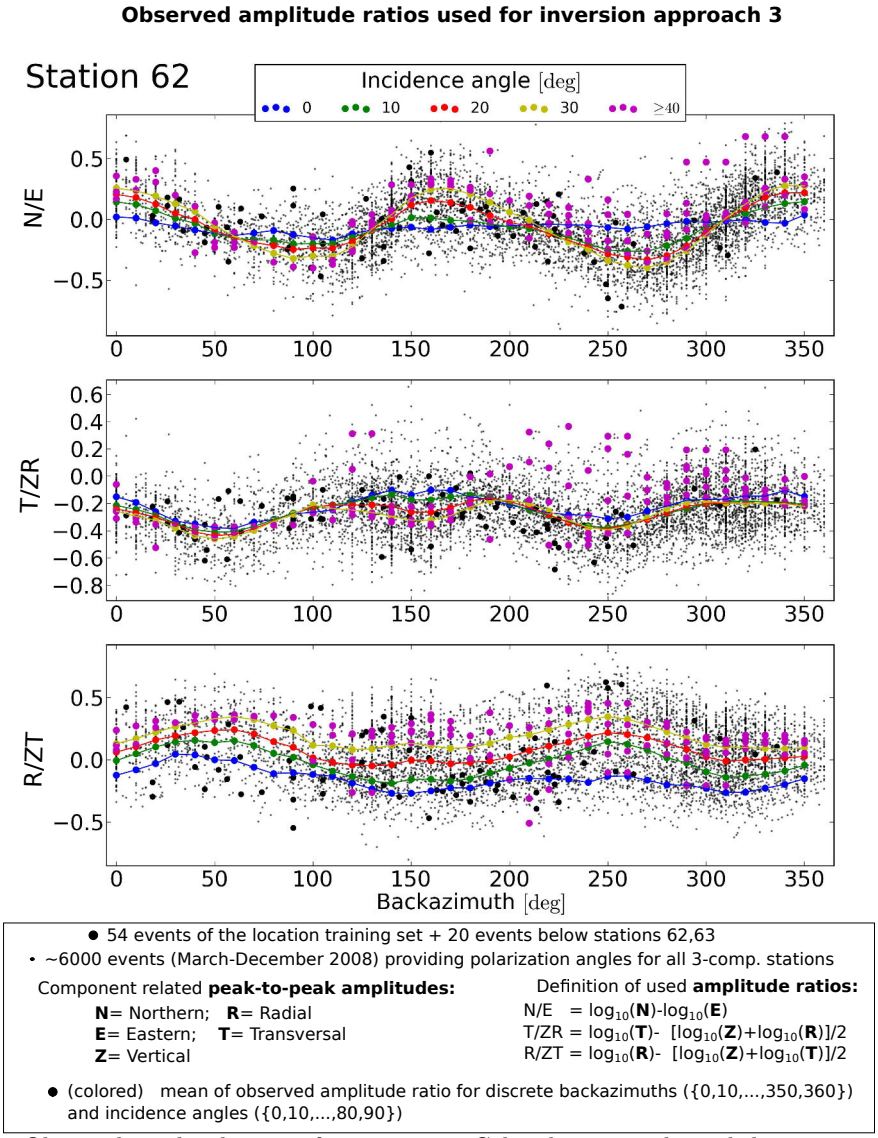

Figure 3.16: Observed amplitude ratios for station 62. Colored points indicated the average amplitude ratio with respect to a distinct grid of incidence and backazimuth angles (see text).

The observed amplitude ratio distribution of station 62 is shown in Figure 3.16 for N/E (northern vs eastern horizontal component), the T/ZR (transversal vs radial and vertical component), and the R/ZT (radial vs vertical and transversal component) amplitude ratios as a function of backazimuth and incidence angles. The reason for the choice of these specific ratios was the evidence of clear dependencies between the observed amplitude ratios and the backazimuth and incidence angles. The N/E ratio generally represents the degree of radial wave field components in the horizontal components which was observed to be strong at station 62 (Section 3.2.2 and 3.2.3). The dominance of radial components in the horizontal components is clearly indicated by a significant dependence of the N/E ratio on the backazimuth angles forming distinct local minimum and maximum at specific backazimuth

angles with varying absolute values, depending on the considered incidence angle. As already explained in Section 3.2.3, the T/ZR ratio reflects the relative energy of SH compared to P and SV waves, while the R/ZT ratio generally reflects the relative quantities of P and SV wave amplitudes in the radial and vertical components. Also here, clear local minimum and maximum of the amplitude ratios at distinct backazimuth angles can be observed. Using the LQT coordinate system would permit to study directly the P, SV, SH amplitudes. However, it was found that an erroneously assumed incidence angle bias the comparison of P with SV wave amplitude contribution (see also Section 3.2.3), what produce less distinct amplitude ratio distributions as compared to the ones shown in Figure 3.16.

The colored lines and points in Figure 3.16 represents the mean of the amplitude ratio as observed for a similar backazimuth and incidence angle discretized by a grid of backazimuth and incidence angles. The inversion aimed to simulate the curves representing incidence angles at $0°, 10°, 20°$, and $30°$ (blue, green, red, and yellow curves in Figure 3.16, respectively) where backazimuth angles were completely available for $0 - 360°$. As a result, each observed amplitude ratio dataset (N/E, T/ZR, R/ZT) was represented by 140 observation points (mean amplitude ratios). Then, synthetic amplitude ratios were calculated for the grid of DC-models rthe(Section 3.2.4.1), while for each of these models, the source was placed at 140 different locations that corresponded to the observed backazimuth and incidence angles, assuming a fixed source depth at 150 m.

The fit between the observed and synthetic data set for one considered amplitude ratio $ampratio_k$, at the observation point A_i of a total of n ($n = 140$), was estimated by the absolute misfit ($l1$-norm)

$$Misfit_{ampratio_k} = \frac{\sum_{i}^{n} \sqrt{(A_{obs,i} - A_{syn,i})^2}}{\sum_{i}^{n} \sqrt{A_{obs,i}^2}}, \tag{3.1}$$

$$\tag{3.2}$$

where A represent the normalized observed and synthetic amplitude ratios found by division of the maximum in each dataset. Hence, the fit of equation 3.2 can be regarded as a measure of how well the trends and relationships between amplitude ratios and corresponding backazimuth and incidence angles are reproduced by the synthetic data. This normalized fitting procedure was preferred, since the average of observed amplitude ratios differed in their ab-

solute value. The difference in the absolute values of the averaged observed and synthetic amplitude ratio is due to the deviation from ray theory, as discussed in Section 3.2.3 (Fig. 3.10), and possibly due to some events slightly differing source mechanism. The total misfit with respect to one source model and all three amplitude ratios was then simply estimated as:

$$Misfit_{total} = \frac{1}{3}(Misfit_{N/E} + Misfit_{T/ZR} + Misfit_{R/ZT}), \tag{3.3}$$

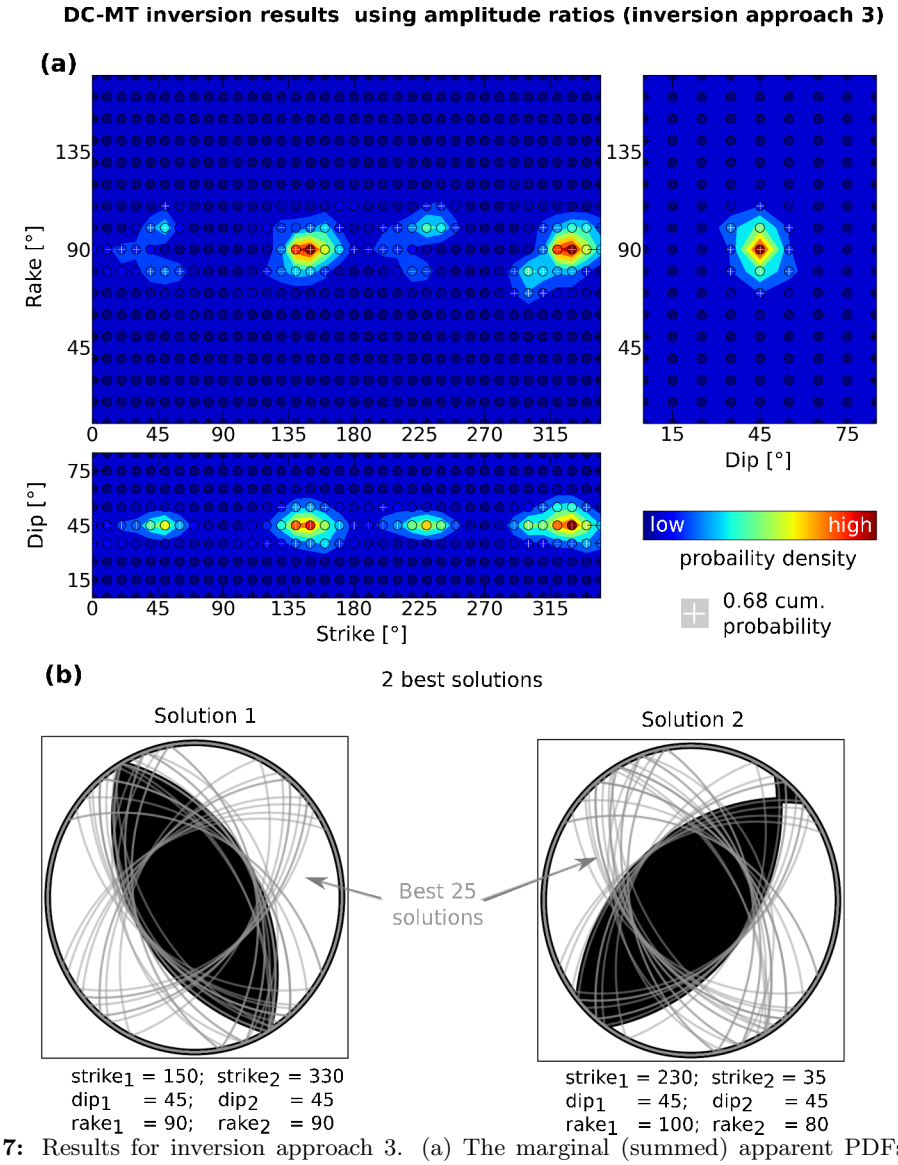

Figure 3.17: Results for inversion approach 3. (a) The marginal (summed) apparent PDFs (see Section 3.2.4.1) are shown for the strike-rake plane (upper left panel), the strike-dip plane (lower left panel) and the dip-rake plane (upper right panel). White crosses indicate the respective grid points covered by the apparent cumulative probability equal to 0.68. (b) The two best solutions (beach-ball plots) and the 25 next best solutions (gray circles). Note that compressive (black shaded area) and dilatational (white shaded area) are only shown for visualization, but are not known from this inversion approach.

The inversion results are shown in Figure 3.17. They are consistent with the results of inversion approach 1 and 2 (Section 3.2.4.1 and 3.2.4.2, respectively), and correspond almost exactly to the "trial" *ds* solution shown in Figure 3.10 differing by 10° in strike. Regarding the well constrained PDFs and generally small covered area by the cumulative 0.68 PDF (Fig. 3.17), it can be assumed that the results of this approach are almost as well as the ones presented for inversion approach 1 (Fig. 3.11) and generally much more robust and stable as compared to inversion approach 2 (Fig. 3.14). Better constraints in the results as compared to inversion approach 2 are generally due to the normalized misfit procedure, where extreme amplitude ratio values given from the synthetics (not observable in the observed ones) have less influence on the results (Figure 3.18, Section 3.2.3 and 3.2.4.2).

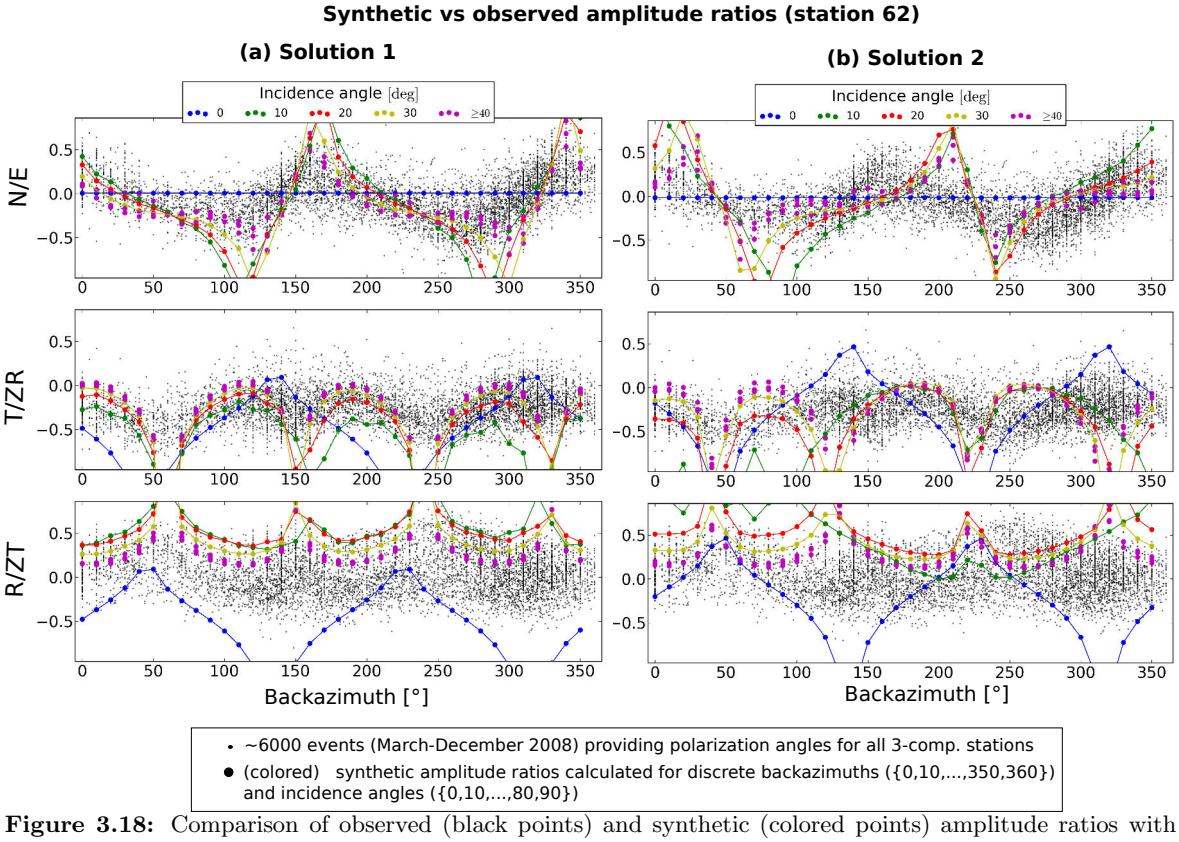

Figure 3.18: Comparison of observed (black points) and synthetic (colored points) amplitude ratios with respect to *solution 1* (c) and *solution 2* (Fig. 3.17).

Also in this approach, two possible solutions are found (Fig. 3.17). These are associated with almost pure *ds* faulting with NE-SW and NW-SE strike. The comparison of observed amplitude ratios and synthetic ones, for both solutions, explain well the observed trends and dependencies of the observed amplitude ratios with backazimuth and incidence angle (Fig. 3.17b). From comparison of *solution 1* and *solution 2*, it must be stressed that probabilities

for *solution 1* are somewhat higher (Fig. 3.17a), and the observed amplitudes are better reproduced (Fig. 3.18). Nonetheless, *solution 2* cannot be completely excluded as a possible solution, since the corresponding synthetic amplitude ratio does not categorically differ from *solution 1* and the observed amplitude ratios.

Synthetic and observed amplitude ratios for *solution 1* are shown for station 63 in Figure 3.19, where the observed amplitude ratios are supposed to sample the entire station's lower hemisphere, and thus in case of a consistent mechanism the complete upper source hemisphere. The observed amplitude ratio show similar trends and absolute values as compared to station 62, especially with respect to the N/E ratio but less distinct for the T/ZR and R/ZT ratios as a result of refraction effects (Fig. 1.14, Section 1.3.4.2 and 3.2.3). The synthetic amplitude ratios reproduce quite well the absolute ratio values and the distribution of observed amplitude with backazimuth and incidence angle especially with respect to the N/E ratio.

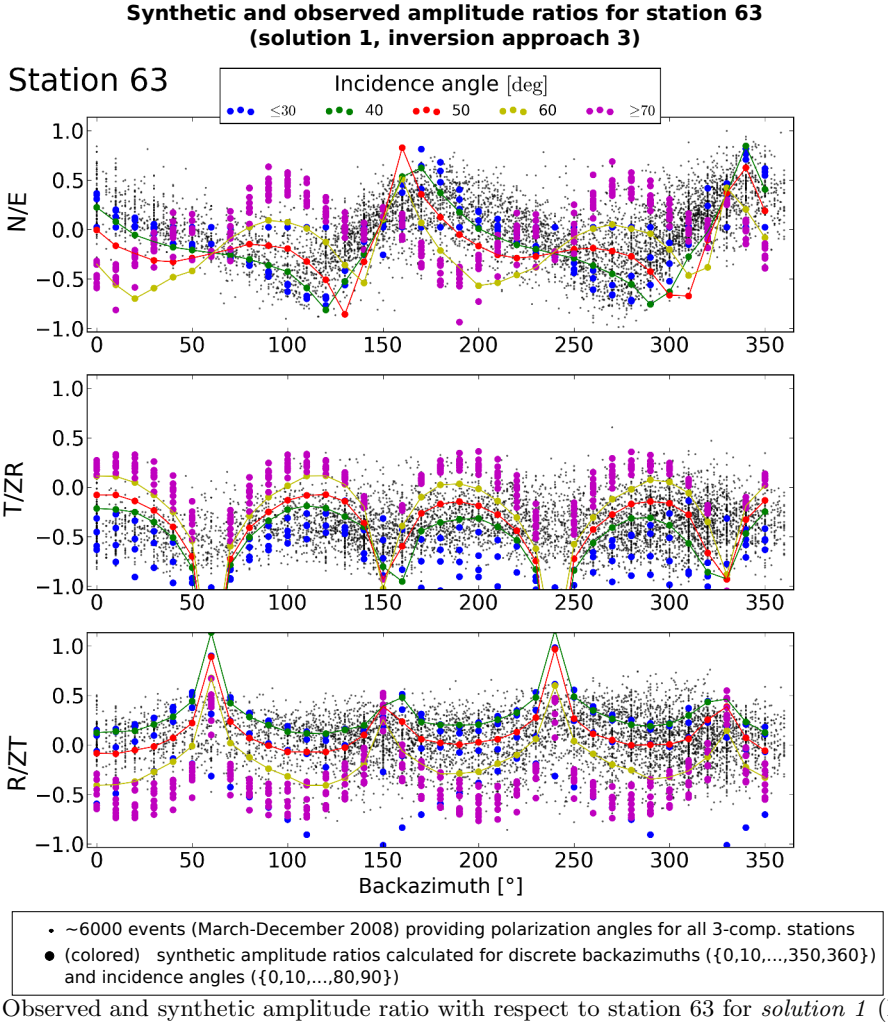

Figure 3.19: Observed and synthetic amplitude ratio with respect to station 63 for *solution 1* (Fig. 3.17).

3.2.5 Synthesis and discussion

In the preceding Sections, it was shown that the microseismic events recorded from March to December 2008 appear to be associated with a very similar source mechanism. The results of the three performed independent inversion approaches (Fig. 3.11, 3.14, and 3.17) are remarkably consistent and indicate dominant *ds* faulting with dips ranging from $35 - 55°$, and slip directions (rake) ranging from $80 - 110°$, while two dominant strike directions are documented trending NE-SW and NW-SE. From the observations in Figure 3.10 and from the inversion approach 2 and 3 a preference for the NW-SE *ds* striking source is suggested. Only inversion approach 1 shows a slightly better fit for the NE-SW striking mechanism, although a visual inspection reveals no clear improvement in the waveform and amplitude spectra fit among the two proposed solutions.

It was still not discussed if the *ds* source is associated with normal faulting or thrust faulting. This issue cannot be answered by quantitative analysis as no method was available to determine automatically P wave polarities. On the other hand, most of the eye inspected events, including the 54 events of the training set and the 20 events below station 62 and 63, demonstrated clearly positive upward P wave polarities as shown in Figure 3.3 and 3.13, while no event with unambiguously negative P polarity was observed. As a result, it is assumed that *ds* faulting is mainly associated with thrust faulting.

The hypothesis that the entire microseismic data set of 2008 is dominated by thrust faulting has two important implication with respect to the interpretation of the local stress field in terms of Anderson's fault theory (Anderson, 1905, 1951) (Fig. 3.1). Firstly, this implies that the minimal principal stress is vertically oriented ($\sigma_3 = S_V$) producing significant vertical displacement. Thus, it might be possible that dominant vertical displacement at Cerville is constituted by sets of conjugated thrust faults as illustrated in Figure 3.20a. Secondly, the presence of a pure dominant thrust fault mechanism implies that the maximal horizontal stress (S_H) is clearly confined along a specific direction, ideally perpendicular with respect to the fault orientation (e.g. Fig. 3.1). This second implication bares a clear paradox when assuming both *ds* solutions of perpendicular strike (NE-SW and NW-SE) are valid and associated with thrust faulting. Assuming a perpendicular orientation of S_H with respect to one of the two *ds* fault orientations would exclude the other solution. Another option would be to interpret the less favored NE-SW striking *ds* solutions as normal faults or oblique fault

segments (Fig. 3.20b). Such faulting types might appear in regions of the cavity, where the relation to the minimal horizontal stress S_v is smaller or similar with respect to the vertical stress S_V as maybe due to the asymmetry of the cavity roof structure producing stronger gravitation gradients.

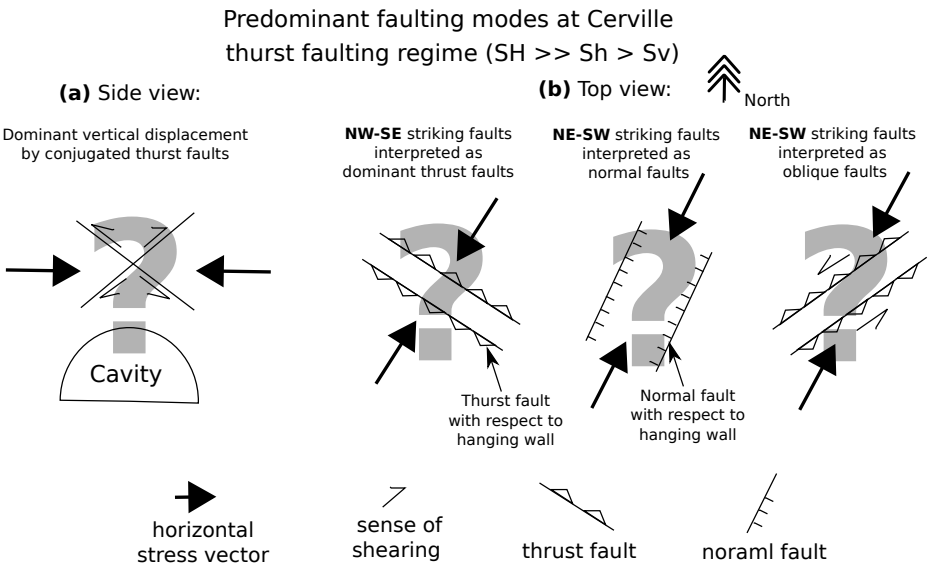

Figure 3.20: Simplified fault model at Cerville interpreted from the results of the inversion approaches 1-3 (Fig. 3.11, 3.14, and 3.17).

The dominance of thrust faulting above underground openings is not new and was frequently observed in shallow mines (Fig. 3.1), but also in fluid filled underground cavity at more important depth ($\geq$ 2000 m). For instance, Godano et al. (2012) found clear evidence for thrust faulting induced from solution mining in the in the Arkema-Vauvert salt field (France), which occurred mostly along pre-existing fault structures. In addition, (Bardainne et al., 2008) documented dominant thrust faulting above an gas filled anticline structure in the Lacq gas field (France). As a result, the observation of $\sigma_3 = S_V$ and dominant thrust faulting is actually quite reasonable at Cerville regarding the fact that the cavity is at shallow depth, as well as pressurized with brine keeping the thin overburden additionally stable.

In contrast, rather unclear remains the stability in orientation of thrust faulting at Cerville implying an apparent strong alignment of S_H. Unfortunately, at Cerville, after my knowledge no in-situ stress measurements are available. The most nearby in-situ stress measurements were obtained at an ANDRA (French national radioactive waste management agency `www.andra.fr`) study site around 150 km to east of Cerville, documenting a very stable NW-SE orientation of S_H equally at shallow ($\sim$ 100 m) and deeper ($\sim$ 1700) depth of $\sim$ N150° E (Cornet and Röckel, 2012, Gunzburger and Magnenet, 2014, Wileveau et al., 2007) (Fig.

3.21), what consistent with other regional measurements within the underlying basement (Heidbach et al., 2010), indicating mechanical coupling between the basement and the overlying sedimentary layers. The geology at this study site is akin to Cerville, constituted by the Triassic salt formation (Mégnien, 1980) and younger Jurassic units, while the geological layers at Cerville are located at more important depth ($\sim$ 1000 m) at the ANDRA site (Fig. 3.21b). Assuming a consistent orientation of S_H at Cerville, would mean that the maximum horizontal stress is parallel to the NW-SE striking preferred *ds* model what contradicts with Andersonian fault theory. However, this suspicious good correlation between structure orientation and regional stress leaves room for a speculative scenario as shown in Figure 3.21. After this scenario, it might be possible that anisotropic structures as aligned tensional joints formed in the study site due to regional stress before exploitation started. When exploitation finally started and a cavity structure was formed, vertical stresses at the cavity were significantly reduced. what maybe leaded to preferential thrust faulting along the pre-existing joint structures.

Interestingly, André et al. (2006) found systematic distributions of joint structures at the ANDRA study site which show distinct NW-SE orientations in younger Oxfordian geological units located at $\lesssim$ 400 m depth which are linked to the Alpine orogenese (Fig. 3.21c). Even though, the measured joint structure show a vertical dip and differ from the range of *ds* fault dips of $35 - 55°$ at Cerville, the coincidence in structure orientation should be evaluated by future structural geological analysis at the Cerville study site. So far no significant anisotropies from laboratory rock sample analysis neither geological faults have been documented (Mercerat, 2007), even though some systematic NW-SE striking regional fault structures have been observed close (in ther order of some kilometers) to Cerville (e.g. André, 2003, Mégnien, 1980). Another possibility to further constrain the presence of pre-existing structure might be performed by detailed shear wave splitting analysis in future research. Such a method was already successfully applied during block-caving operations by Wuestefeld et al. (2011), who found consistently to Cerville, very stable strike orientation of apparent thrust fault structures at the cavity roof that the authors referred to shearing events on pre-existing structures (Fig. 1.2b). Even though not shown and analyzed in this study, during signal inspection, I often observed clear S wave splits at station 3.

In addition, there is probably an influence of the 3-D shape of the fluid-filled (brine pressurized) cavity on the orientation of the local stress field that need to be further analyzed

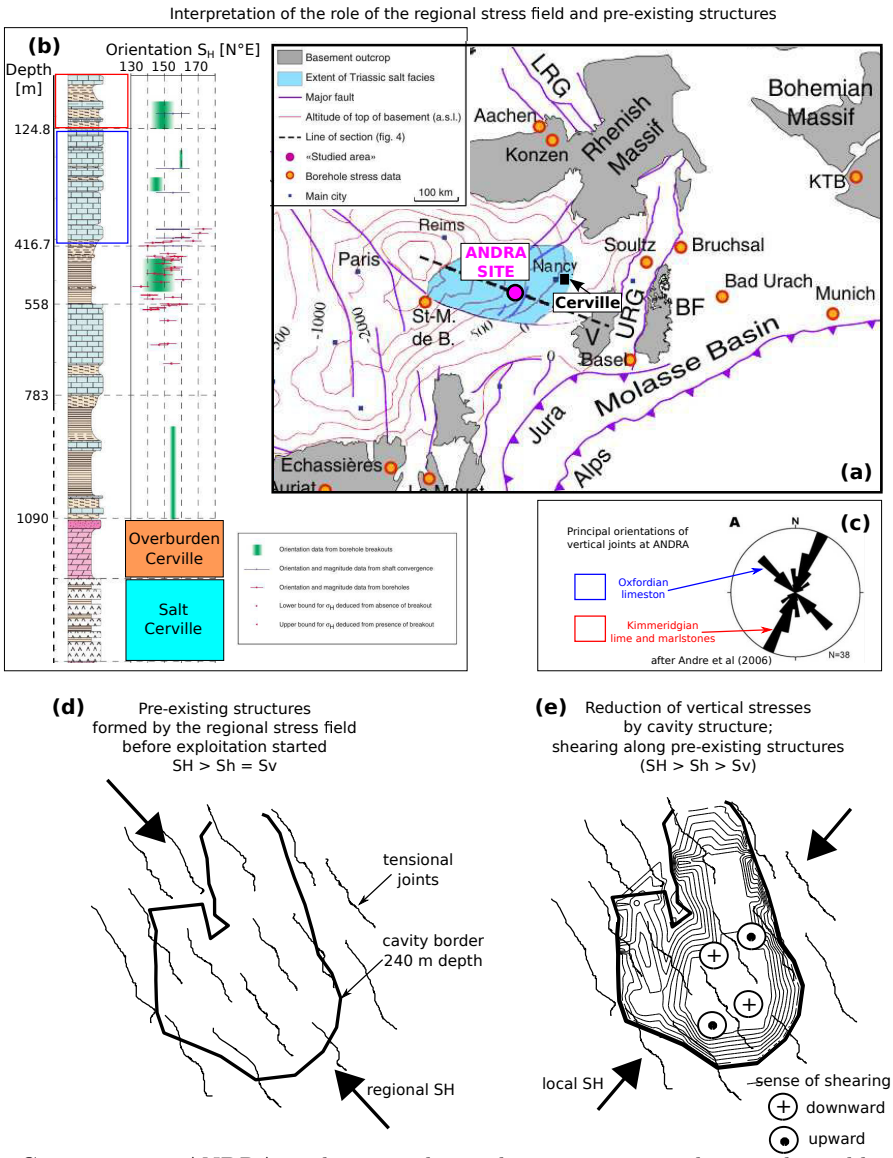

Figure 3.21: Comparison to ANDRA study site and speculative scenario explaining the stable *ds* orientation at Cerville. (a) Geographical Map taken and modified from Gunzburger and Magnenet (2014) (see also references therein) showing the Cerville and ANDRA study site. (b) Geology and S_H measurement obtained at the ANDRA study site taken and modified from Gunzburger and Magnenet (2014) (see also references therein). Blue and red squares mark the Oxfordian and Kimmeridgian lithological units, respectively, where systematic joint fractures has been measured as shown in (c) (rose diagram), which was taken from André et al. (2006).

and understood, as e.g. by means of numerical mechanical modeling approaches. It seems however rather unlikely that the cavity geometry alone might produce such a distinct alignment of S_H, since the geometry is rather complicated and is supposed to evolve significantly in time. Moreover, when following e.g. Kirsch's theory for theoretical stress accumulation along excavated regions, the maximum horizontal stress is generally oriented along the most elongated axis of the excavated object. Correspondingly, at Cerville, the cavity structure can be approximatively described by an ellipsoid elongated to the NW-SE, what would produce a

maximum horizontal stress also oriented NW-SE, and therefore contradicts with the observed orientation of the preferred *ds* model.

3.3 Re-consideration of the detection and location results

The consistency in source mechanism found for the majority of analyzed microseismic events has an important impact on the interpretation of the detection and location results of the developed polarization- and amplitude-based approaches (Section 2.2 and 2.3), which are discussed in the present section.

3.3.1 Polarization-based detection

Event detection upon the polarization-based approach is supposed to be sensible to the amplitude of the P wave radiation, since a trigger value was used in order to detect well polarized P wave energy (Section 2.2). The spatial distribution of P wave amplitudes is affected by the source location, its magnitude and its focal mechanism. As a result, it might be possible that the detection capacity of this approach is affected by the repeated source mechanism found for most of the microseismic events in 2008. To investigate such an effect, Figure 3.22 shows the radiation coefficient for P waves (R_P) (Boore and Boatwright, 1984), calculated for the *ds* mechanism striking NW-SE (Figure 3.22f) and a Poisson's ratio of $\sigma = \frac{1}{2}\frac{\left(V_P^2 - 2V_S^2\right)}{\left(V_P^2 - V_S^2\right)} = \frac{1}{2}\frac{\left(2.9^2 - 21.28^2\right)}{\left(2.9^2 - 1.28^2\right)} = 0.379$, and compare it to the number of detected P wave phases and the degree of polarization (L-value) as a function of the backazimuth and incidence angles observed from station 62 (Figure 3.22a-c). From the comparison of these images, a clear similarity can be observed between zones of high number of P wave detections, and L-values, with high R_P, and vica versa. This correlation is more clearly shown by the direct functional relationship of R_P with the detected event number (Figure 3.22d), and the L-value (Figure 3.22e), where a linear dependency can be observed. Hence, the source mechanism clearly affects the detection capability, what in turn clearly supports the previously presented results of Section 3.2, documenting a clear stability in the source mechanisms for most of the observed events.

On the basis of the significant influence of the source mechanism on the results of the polarization-based approach, it is now possible to re-interpret observed differences in the detection behavior of station 3, 5 and 62, as shown in Figure 2.8 and 2.24d. Most significantly polarized P wave energies are detected at station 62 (Fig. 2.8a and 2.24d), what is

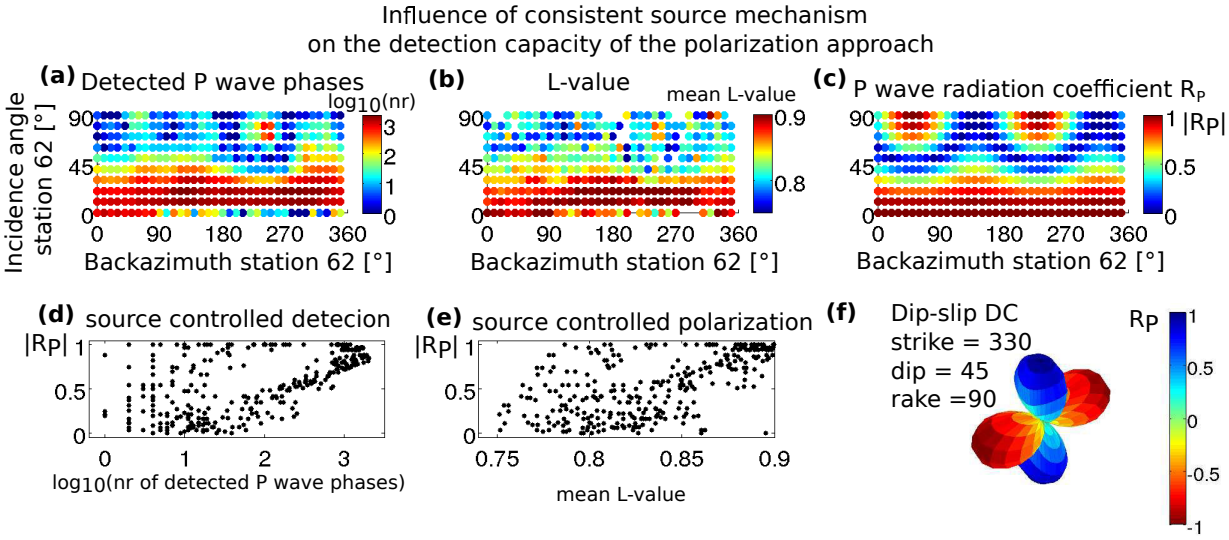

Figure 3.22: Comparison of detection capability of the polarization-based approach and radiation coefficients for P waves (R_P) for the *ds* source model striking NW-SE (e.g. Fig. 3.10). (a)-(c) For comparison the number of detected events (a), the degree of polarization of P waves (L-value) (b), and the radiation coefficients of the *ds* model (c) are shown as a function of the backazimuth and incidence angles with respect to station 62. (d)-(e) Direct functional relationships of R_P with the average of the detected event number and the L-value calculated for a discrete grid defined by the Cartesian product for the set of the backazimuth ($\{0°, 10°, \ldots, 340°, 350°\}$) and the incidence angles ($\{0°, 10°, \ldots, 80°, 90°\}$). (f) Radiation coefficient were calculate using the approach of Boore and Boatwright (1984) assuming Poisson's ratio of $\sigma = 0.379$.

expected, since P waves radiates predominantly upwards and incidence angles at station 62 are smallest (Fig. 3.9 and 3.22). Consistently, the lowest amount of significantly polarized P wave energies is observed at station 3 (Fig. 2.8a and 2.24d), which is consistent with the fact that S waves dominate for larger theoretical incidence angles (as the case for station 3) (Fig. 3.7, 3.9, and 3.10). In addition, at station 3 a noticeable cluster of polarized SH wave energies is observed in Figure 2.8 at higher frequencies and L-values below the threshold value (Lcrit), associated with an indicative error of $\sim 90°$ in the backazimuth angle. Also this observation is consistent with the assumed *ds* model, where SH become more important for larger station incidence angles (Fig. 3.9 and 3.10).

However, similar results should be expected with respect to station 5, where incidence angles are also larger (e.g. Fig. 3.9), but where no comparable SH wave energy cluster can be observed for higher frequencies (Fig. 2.8a). Some significant SH wave energies might be assumed by some few samples of increased L-value seen for lower frequencies. This lack of SH wave energies might be related to the abnormal attenuation behavior of S compared to P waves ($V_P/V_S = 2.25$, $Q_P/Q_S = 2$, e.g. Section 2.3.2). This abnormal attenuation behavior for S waves might play a significant role at station 5, which is at shallower depth (~ 25 m) than stations 3, 62, and where P wave velocities were found to decreases to equal values as

water (V_P = 1.69 km/s), documenting the presence of the ground water aquifer (Section 2.3.2, Table 3.1), where S wave are expected to be very strongly attenuated.

All these observations underline the hypothesis of a strong consistency in source mechanism for the microseismic events analyzed in 2008. (Note: the detected events and polarization degree shown in Figure 3.22 actually comprise the complete Cerville data set including events in 2009, see Chapter 5 for further discussion.) In addition, these results demonstrate that the detection capability of a seismic network can be significantly affected by the governing source mechanisms. As observed in Section 2.5, the number of detected events by the polarization-based approach generally increases with the number of recorded triggered event files, as recorded from the triggered network operation mode (Fig. 2.24, Section 2.6.2). Detection of the triggered network was mainly controlled by the detection capacity of station 63 (closest station), where P and SV waves are most dominant, when assuming a constant *ds* mechanism. As a result, it might be possible that actually the entire recorded data set or seismic catalogue at Cerville represents a biased portion of microseismic emissions confined by source radiation pattern as observed for the polarization-based approach. Hence, relatively more microseismicity is detected at locations, where the maximum of P and SV wave source radiation points toward the recording station and vica versa.

These results might be of significant relevance for recently used methods and procedures to estimate local seismic hazards. These procedures are generally based on the determination of the magnitude of completeness (M_C), which is the lowest magnitude at which 100% of the events in a space-time volume are detected (e.g. Rydelek and Sacks, 1989, Woessner and Wiemer, 2005) and which characterize the network detection capacity. For the determination of M_C usually network characteristics as well as medium attenuation characteristics are taken into account (e.g. Matsumura, 1984, Papanastassiou and Matsumura, 1987). However, few studies (e.g. Stabile et al., 2013) considered the influence of source radiation pattern so far, what encourage for more future research in this respect.

3.3.2 Amplitude-based location

The effect of source radiation on the amplitude-based location approach was not discussed yet (Section 2.3), what will be cached up in this section. As illustrated by Figure 3.8 and 3.23a-b, with exception of the pure tensile or isotropic source, source radiation pattern are not symmetric. Therefore, they have a strong influence on the amplitude ratio observed

for a certain station couple. The effect of radiation pattern on the amplitude ratio can be even larger when one station receives seismic energy associated with a source radiation lobe and the other station is located in the direction of source radiation node. As in this study, the source radiation pattern is supposed to be common for most of the located events, the influence of the source radiation may significantly bias the location results. It is expected that the location errors vary depending on the backazimuth and incident angles.

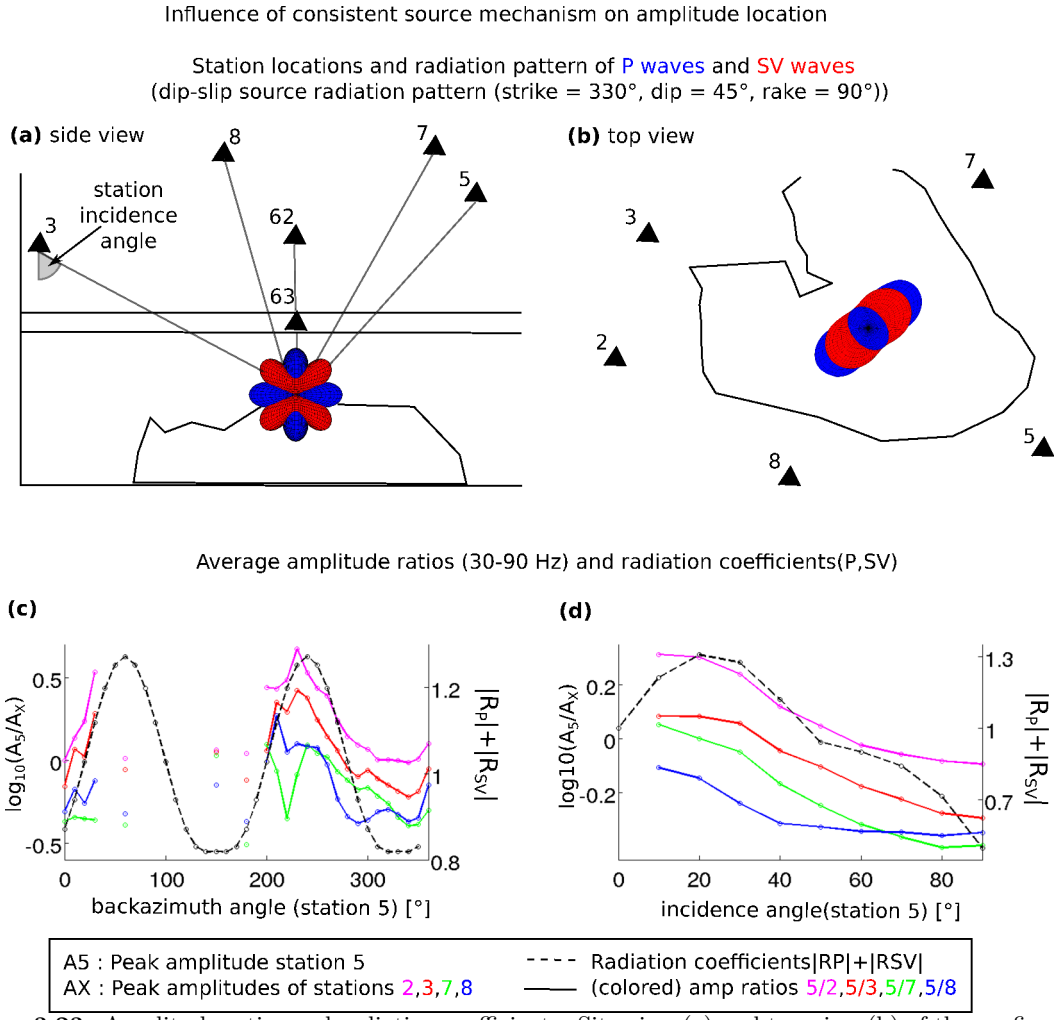

Figure 3.23: Amplitude ratios and radiation coefficients. Site view (a) and top view (b) of the configuration of the microseismic network and the expected dominant radiation pattern calculated for NW-SE striking *ds* model. (c)-(d) The average radiation coefficients for P and SV waves ($R_{P,SV}$) (dahed black line) and the average peak-to-peak amplitude ratios (vertical component) for $\sim$ 6000 events of station 5 with other stations (colored continuous lines) are shown as a function of the backazimuth angles ($\{0, 10, \ldots, 340, 350\}$) and incidence angles ($\{0, 10, \ldots, 80, 90\}$), respectively. Backazimuth angles and incidence angle corresponding the shown amplitude ratios are the polarization angles determined at station 5 (based on the polarization approach Section 2.2).

In order to investigate such a possible bias, I show in Figure 3.23c-d the average of amplitude ratios of station 5 with other station used for location for $30 - 90$ Hz as a function of the backazimuth and incidence angles estimated from the polarization-based approach based on

station 5 for the $\sim$ 6000 events already discussed in the previous Sections. The observed amplitude ratio distribution is then compared to the average of the radiation coefficients $R_{P,SV} = |R_P| + |R_{SV}|$ for P and SV waves (Boore and Boatwright, 1984) (projected to the receivers lower hemisphere) calculated for the NW-SE striking *ds* model (Fig. 3.23c-d). Naturally, SH radiation pattern were ignored here, since signal amplitudes were estimated from the Z components.

By this comparison, it can be clearly seen that amplitudes at station 5 for a backazimuth angle around $> 310°$ become significantly smaller when compared to the other stations, what agrees with the expected minimum of P and SV wave amplitudes at similar angles as observed by the radiation coefficients (Fig. 3.23c). Similar correlation can be observed, when considering the amplitude ratios and radiation coefficients as a function of the incidence angle. This correlation suggests that the amplitude ratios are affected by the dominant radiation pattern of the *ds* source. Moreover, the amplitude ratios for station 5 and surface stations 7 and 8 are generally smaller than amplitude ratios for deeper stations 2 and 3. Even though smaller amplitude ratios for surface stations are related to amplification effects at the surface (e.g. Fig. 2.9), they probably also result from source radiation pattern, since incidence angles at station 7 and 8 are generally smaller, and therefore contain more P and SV energy than deeper stations (e.g. 2, 3, 5).

From this obvious influence of radiation pattern in the amplitude ratios, it is likely that the location results from the amplitude-based approach are biased by the presence of a dominant source radiation pattern. In order to roughly quantify this bias on the location results, these are shown for the $\sim$ 6000 events in Figure 3.24. From the shape of the border formed by the epicenter locations in Figure 3.24a, one can observe distinct lineaments as well as a significant part of epicenter locations that cross the outer cavity contour towards station 5. I suggest that these results are biased by the radiation pattern effect.

To test the possible influence of source radiation, I repeated the location procedure using again the amplitude-based approach for the same events, but considering a slight modification in Equation (2.11):

$$log_{10}\left(\frac{A_i(f_k)}{A_j(f_k)}\right) = \log_{10}\left(\frac{R^i_{P,SV}}{R^j_{P,SV}}\right) \text{Radiation coefficients} + \log_{10}\left(\frac{s_i(f_k)}{s_j(f_k)}\right) + \log_{10}\left(\frac{r_j}{r_i}\right) - \frac{\pi f_k\,(r_i - r_j)}{Q_P V_P}\log_{10}\left(exp(1)\right), \qquad (3.4)$$

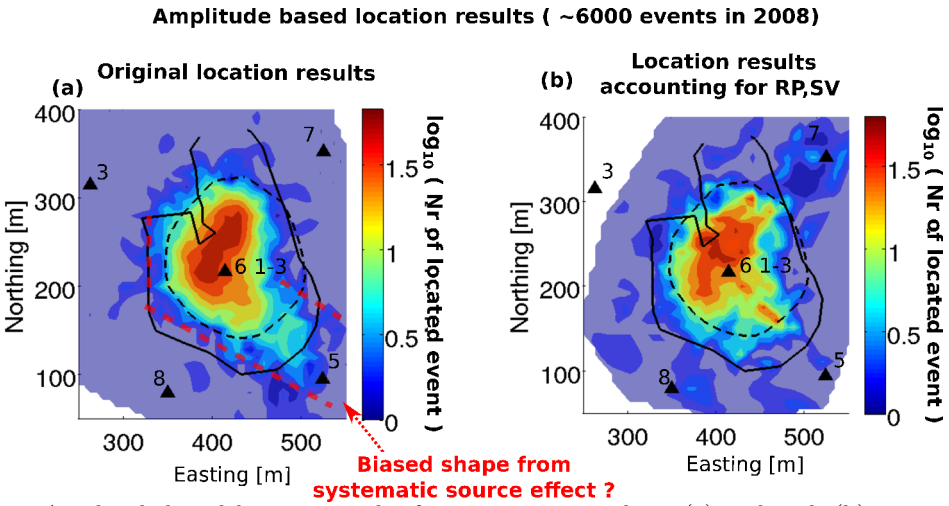

Figure 3.24: Amplitude-based location results for 6000 events without (a) and with (b) correction for a systematic source effect.

where now the systematic effect of the source radiation pattern is approximated by the ratio $R_{P,SV}$ with respect to station i and j. When comparing these location results (Fig. 3.24c) with the original ones (Fig. 3.24a), it can be seen that the shape of the borders formed by the epicenter locations are no longer linear and the epicenter locations elongated towards station 5 are vanished.

This observation, as well as the result in Figure 3.23, clearly confirm that the source radiation pattern are stable for the considered events and introduce a bias in the location results. On the other hand, it seems that the bias mostly affects events located at the cavity borders, as the epicenter location cluster in the cavity does not change significantly (Fig. 3.24). This hypothesis seems reasonable, when considering $R_{P,SV}$ as a function of backazimuth and incidence angles. Differences in $R_{P,SV}$ with respect to two stations of one station couple can be significant in cases of significant differences in the incidence angle (vertical versus horizontal), or when the backazimuth angles differ with 90°. These conditions often apply when events are located at the cavity borders.

Furthermore, the effect of radiation pattern also explains why it was not possible to include amplitudes of stations 62 and 63 in the amplitude-based location approach (Section 2.3). These stations were excluded, as the observed amplitude decay with distance was different to the other stations. So far this behavior was interpreted as a result of differences in geometric spreading at station 62 (Section 2.3.4) and significant refraction effects at station 63 (Section 1.3.4.2 and 2). Now, it cannot be excluded that the systematic source radiation pattern effect plays a major role in this respect. Compared to other stations, the backazimuth angle varies

significantly more at station 62 and 63, as well as the incidence angle at station 63, so that the radiation pattern play a dominant role in the amplitudes observed at these two stations (Fig. 3.23). Instead, amplitudes observed at stations surrounding the cavity zone are less concerned by the source radiation pattern, as the incidence and backazimuth angle remain relatively stable. As a result, the differences in $R_{P,SV}$ for the station couples surrounding the cavity zone remain unchanged and were probably taken into account, when correcting for apparent amplification site effects (Section 2.3). In future research, this hypothesis might be tested by a re-calibration procedure of the amplitude-based location approach using Equation (3.4) and including observed amplitudes from station 62 and maybe 63. On the other hand, the sensitivity of amplitude-based approach to radiation pattern might provide also great potential for the development of future location approaches providing information of source locations (Eq. 3.4) and mechanism at once, especially in cases of dense station distributions or microseismic clusters.

Regarding the significant influence of the source radiation pattern on the amplitude-based location as demonstrated in this section, the interpretation of the corresponding location results need to be generally considered with caution. A fair and reliable interpretation of these location results is later presented in Chapter 4, when discussing the spatial distribution of microseismicity.

3.4 Source scaling

In this section, the determination of source parameters of the microseismic events is discussed. In addition, an automatic scaling approach is presented that gives a first approximation of the size and spatial dimension of the analyzed microseismic events. In this context, I followed the results of Mercerat (2007) and Mercerat et al. (2010), who showed that the spectra of microseismic events at Cerville are smooth an can be apparently well approximated by a simple far-field shear source model, "omega-squared" (ω^{-2}) model, assuming linear rupture propagation (Aki, 1967). The fact that microseismic sources seem to be predominantly associated with shearing (DC-source), supports these results (Section 3.2). Based on the (ω^{-2}) model the size of the seismic source can be derived from two parameters: the corner frequency (f_c) and the seismic moment (M_0) (Brune, 1970). Mercerat (2007) and Mercerat et al. (2010) found that these parameters can be approximated from acceleration spectra with uncertainties of 20 % and 50 % for M_0 and f_c, respectively.

3.4.1 Method

I adapted the ω^{-2}-model approach in a automatic manner which is based on observations from station 62 and identified P waves, based on the polarization-based approach (Section 2.2). The choice of station 62, and not e.g. station 3, 5, has the reason that P wave are most dominant at this station (3.2), and thus provides the highest amount of P wave detections ($\sim 15,000$) and polarization angles. The automatic processing, as illustrated by Figure 3.25 and 3.26, is very similar to P wave spectrum calculations performed in Section 3.2.2. In order to calculate the source spectra for one event, for an isolated P wave phase, the station components were first rotated to the LQT (ray oriented) coordinate system by means of the polarization angles (Fig. 3.25). Then the maximum peak-amplitude of the L component was identified which was then multiplied with a hanning window of 0.2 s length, before the fft velocity spectrum ($\dot{u}(f)$) was calculated associated with a spectral resolution of 5 Hz.

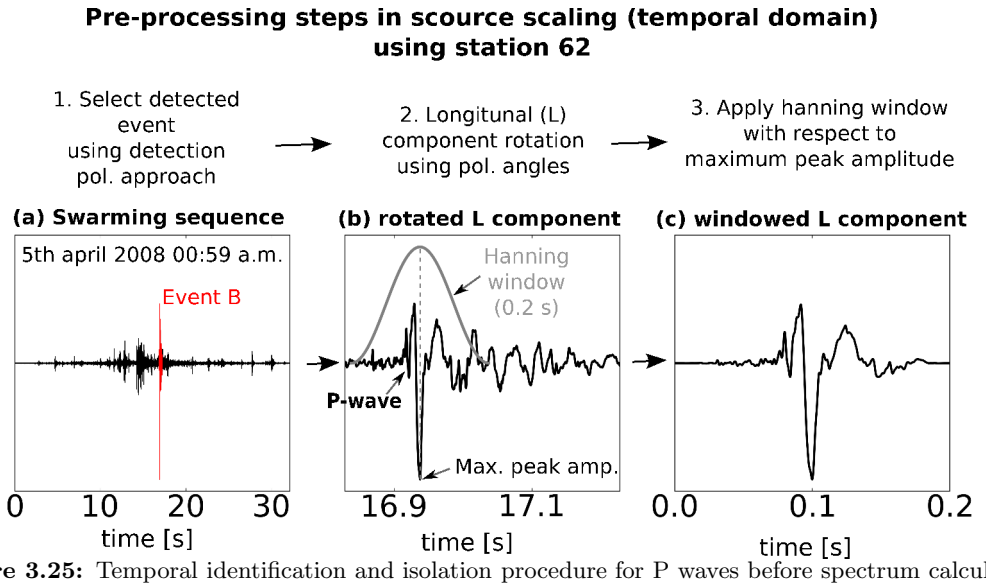

Figure 3.25: Temporal identification and isolation procedure for P waves before spectrum calculation.

In order to determine source parameters (seismic moment M_0, corner frequency f_c), the obtained P wave spectrum is inverted by fitting synthetic spectra (Fig. 3.26) calculated by the Brune's model (Brune, 1970) and its extension for P waves (Hanks and Wyss, 1972) given by

$$u(f) = M_0 \frac{2R_P}{4\pi\rho V_P} \frac{1}{1+\left(\frac{f}{f_c}\right)^2} \left[\exp\left(\frac{-\pi r f}{Q_P V_P}\right)\frac{1}{r}\right], \tag{3.5}$$

where $u(f)$ is the displacement spectrum, ρ the density, r the hypocentral distance and M_o

the seismic moment as defined as (Brune, 1970)

$$M_0 = \Omega_P 4\pi\rho V_P^3 R_P^{-1}. \tag{3.6}$$

Ω_P is the low frequency plateau of $u(f)$. To improve the robustness in the fitting procedure between observed and synthetic source spectra, the spectra are converted to moment magnitude spectra (following the SOURCESPEC approach by Claudio Satriano IPG, Paris, in preparation), where the synthetic spectrum reads

$$u_{synt}^{M_w}(f) = M_W + \frac{2}{3}\left[-\log_{10}\left(\frac{1}{1+\left(\frac{f}{f_c}\right)^2}\right) - \pi f t^* \log_{10}\exp(1)\right] \tag{3.7}$$

wherein the moment magnitude M_w is defined as (Kanamori, 1977)

$$M_w = \frac{2}{3}\log M_0 - 6.1. \tag{3.8}$$

Consequently, the synthetic spectra $u_{synt}^{M_w}(f)$ are calculated by the three parameters: M_0, f_c, and the anelastic attenuation term $t^* = \frac{r}{Q_P V_P}$, which are all optimized during inversion to fit the observed spectrum. In turn the observed moment magnitude spectrum reads

$$u_{obs}^{M_w}(f) = \frac{2}{3}\log_{10}\left(\frac{\dot{u}(f)}{2\pi f} I(f)^{-1} 4\pi\rho V_P^3 R_P^{-1} r\right) - 6.1, \tag{3.9}$$

where $I(f)$ is the instrumental response. For its calculation, the density was assumed with $\rho = 2300$ kg/m^3 and $V_P = 2900$ m/s (Table 3.1), while R_P was calculated with respect to the polarization angles of station 62 and the NE-SW striking *ds* model (Fig. 3.10). Major uncertainties are associated with the assumptions on the hypocentral distances r, since no reliable informations of source depths are available (Section 2.5). In this respect, I decided to calculate r by assuming a fixed source depth of 160 m, while the epicenter location is taken from the location results of the polarization- and amplitude-based approaches.

Both, observed and synthetic spectra, were smoothed using the "Konno-Ohmachi" method. The misfit of the compared magnitude spectra was formulated using the $l2$-norm

$$Misfit = \sqrt{\frac{\sum w(f)(u_{obs}^{M_w}(f) - u_{synt}^{M_w}(f))^2}{\sum w(f)(u_{obs}^{M_w}(f))^2}} \tag{3.10}$$

$$w(f) = (u_{obs}^{M_w}(f)/u_{noise}^{M_w}(f))/\arg\max(u_{obs}^{M_w}(f)/u_{noise}^{M_w}(f)),$$

where the $w(f)$ is a weight function which describes the quality of spectral samples as a

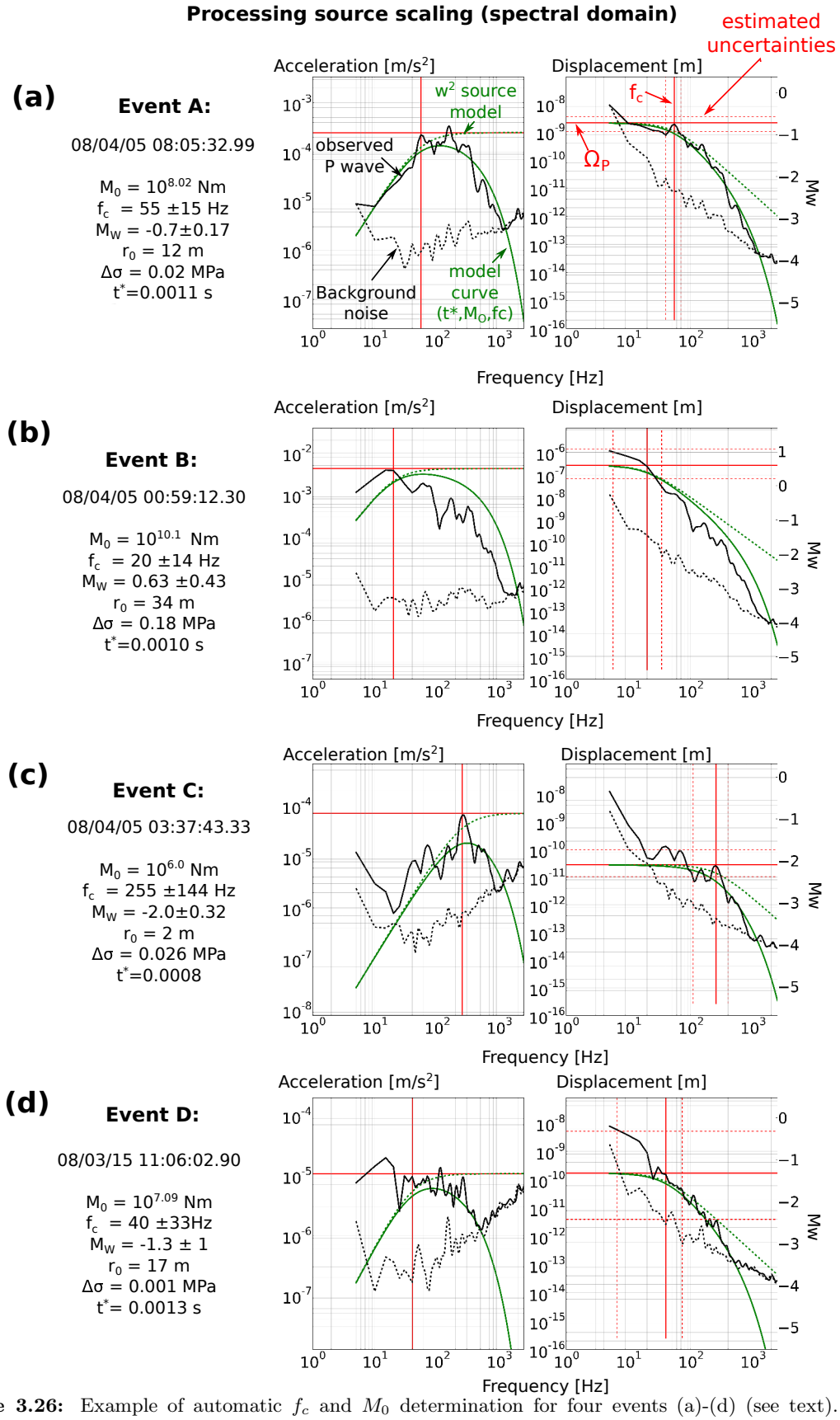

Figure 3.26: Example of automatic f_c and M_0 determination for four events (a)-(d) (see text). Right and left panels show the acceleration and displacement (moment magnitude) spectra observed for P waves (continuous black line), for background noise (dashed black line), and synthetic data based on the Brune's model, accounting (continuous green line) and not accounting (dashed green line) for attenuation, calculated from the optimal parameter values of M_0, f_c (continuous red lines), and t^*, determined during inversion. Uncertainties for M_0 and f_c (dashed red lines) are shown for the displacement spectra (see text).

function of the signal-to-noise ratio, which was obtained by the ratio of the P wave magnitude spectrum $u_{obs}^{M_w}(f)$ and the noise spectrum $u_{noise}^{M_w}(f)$. The noise spectrum was calculated for the first 0.2 s of the merged triggered event file in the same way as the P wave magnitude spectrum (Eq. 3.9).

Non-linear minimization and parameters optimization was performed by using the "Truncated Newton" gradient method, which allows for predefined parameter configuration. The parameter bounds were defined as follows: M_W with $-4-2$, fc with $1-2500$ Hz, while the range for t^* was chosen by assuming an error of ± 100 m for r, $V_P = 2900 \pm 100$ m/s and $Q_P = 42 \pm 14$ (Table 2.2). The inversion result is generally sensible with respect to the initially chosen parameter values. The most robust way was found by using the peak frequency of the corrected observed velocity spectrum ($\dot{u}(f)$) as an initial value for f_c and the maximum of the observed magnitude spectrum $u_{obs}^{M_w}(f)$ multiplied by the weight function $w(f)$ as an initial value for Mw. The initial value for t^* was estimated using $V_P = 2900$ m/s and $Q_P = 42$ (Table 2.2) and the hypocenter distance r assuming the fix source depth.

The uncertainties of the finally obtained parameters, M_W^{opt} and f_c^{opt}, as shown in Figure 3.26, were estimated by repeating the inversion approach for a set of starting solutions, using a more constrained parameter search for M_W (generally more robust estimates as compared to f_c), and to consider the scatter of parameters values obtained from these inversion results. Nine starting solutions were considered in this respect, which are defined by all combinations of two sets, M_W^0 and f_c^0, containing three initial values. The three values for M_W^0 are defined by $M_W^0 = \{M_W^{opt} - Misfit, M_W^{opt}, M_W^{opt} + Misfit\}$, where the $Misfit$ value is related to M_W^{opt} calculated in the first inversion run. f_c^0 is defined by assuming an error of 90% in the estimation of f_c^{opt} yielding $f_c^0 = \{f_c^{opt} - f_c^{opt}0.9, f_c^{opt}, f_c^{opt} + f_c^{opt}0.9\}$. f_c^0.

The parameter bounds during the nine inversion runs were the same as in the first inversion run with exception of the of the range for M_W, which was set equal to the upper and lower bounds of M_W^0. Then, the uncertainties M_W^{err} and f_c^{err} were estimated from the obtained parameter values for each inversion run i using

$$M_W^{err} = \sum_{i=1}^{9} \frac{Misfit_i}{\sum_{i=1}^{9} Misfit_i} |M_W^{opt} - M_W^i|$$
$$f_c^{err} = \sum_{i=1}^{9} \frac{Misfit_i}{\sum_{i=1}^{9} Misfit_i} |f_c^{opt} - f_c^i|, \tag{3.11}$$

where parenthesis || refer to the absolute value.

The optimal parameter estimates M_W^{opt} and f_c^{opt} were used to calculated the characteristic source radius r_0 and corresponding stress drop $\Delta\sigma$ according to Brune's model for P waves Hanks and Wyss (1972) by

$$r_0 = \frac{k_P V_S}{2\pi f_c} \tag{3.12}$$

$$\Delta\sigma = \frac{7}{16}\frac{M_0}{r_0^3}, \tag{3.13}$$

where $k_P = 3.36$ is the model constant and $V_S = 1300$ m/s the S wave velocity (Fig. 3.26). In addition to these source parameters, also the radiated seismic energy E_p of P waves is calculated with respect to each event by (Boatwright and Fletcher, 1984)

$$E_P = 4\pi\rho V_P R_P^{-2} r^2 \int_{\omega_{min}}^{\omega_{max}} \dot{u}_{corr}(\omega)^2 d\omega, \tag{3.14}$$

where $\omega = 2\pi f$. To calculate the energy flux from integration of the velocity spectrum, the velocity spectrum was corrected for attenuation and instrumental response by $\dot{u}_{corr}(\omega) = \dot{u}(\omega) I(\omega)^{-1} \exp(-\omega t^*/2)$, where t^* represent the optimal parameter value obtained from source spectrum inversion. The range of the integral defined by ω_{min} and ω_{max} was defined by the spectral range where the signal fell below the noise level for higher and lower frequencies, respectively. Integration of the squared corrected velocity spectrum was then performed using the Simpson's rule algorithm.

From E_P, the apparent stress σ_{app} was estimated which can be seen as the fraction of the effective applied stress on the fault (ignoring other local energy consumptive processes) (Wyss and Brune, 1968)

$$\sigma_{app} = \mu E_P / M_0, \tag{3.15}$$

where μ is the shear modulus estimated with $\mu = V_S^2 \rho = 3768.32$ MPa.

3.4.2 Results and discussion

The results of automatic source parameter determination are summarized in Figures 3.27 (see also Table B.5) and are presented for the two training sets of well located events from chapter 2 and the 15,000 events of uncertain source depths. As shown by Figure 3.26 and 3.28, estimations of f_c and M_0 are associated with uncertainties. These uncertainties are generally controlled by the signal-to-noise ratio, determined by event size and attenuation

and the limited instrumental response for lower frequencies. Best results are obtained for events associated with M_W around $-2-0$ and f_c with $\gtrsim 20$ Hz which concerns the majority of the analyzed events (Fig. 3.28).

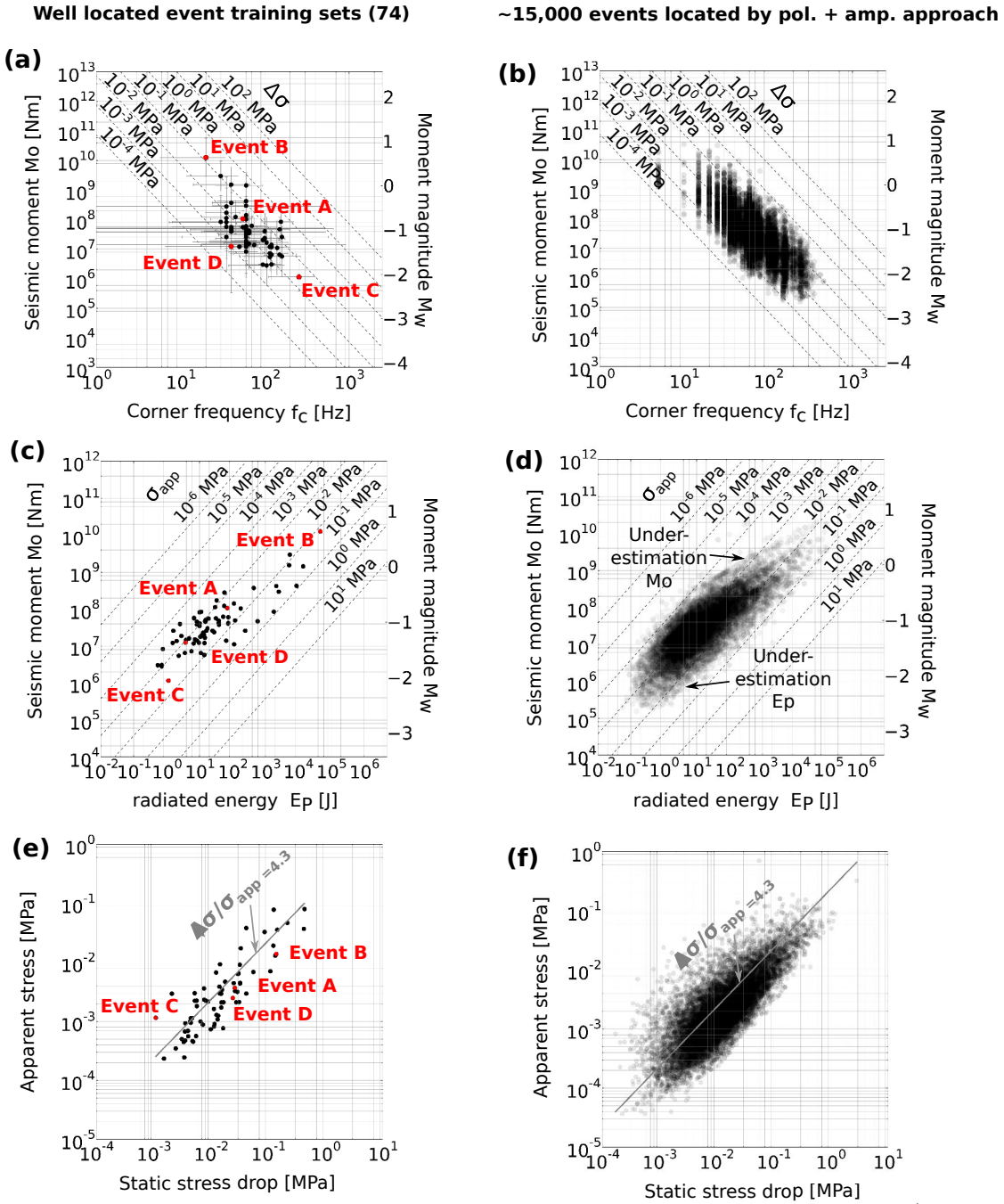

Figure 3.27: Results of source parameter estimation for the 74 well located training set events (Section 2.1 and 2.3.2) (a),(c),(e), and the complete 2008 data set ($\sim 15,000$ events) (b),(d),(f). (a) For better visualization, uncertainties for M_0, f_c (gray error bars) are only shown for the training set events. More source parameters for the 74 events are listed in Table B.5.

A a good source parameter determination result is represented by Event A in Figure 3.26. Also corner frequencies for very small events ($M_w \sim -2$), with > 200 Hz, were accurately

determined when events are close to the station, as represented by Event C (Fig. 3.26). In contrast, for events of very low signal-to-noise ratios, as represented by Event D (Fig. 3.26), errors for M_W can be one order of magnitude, and errors for f_c can be larger than 80% (Fig. 3.26 and 3.28). For larger events with $M_W \gtrsim 0$, as Event B, M_W and f_c determination is clearly borderline as a result of limited spectral resolution, instrumental damping toward lower frequencies and amplification of low frequency noise during instrumental correction (Fig. 3.26). As shown by the results for Event B, instrumental low frequency damping by geophones can generally lead to underestimations of M_W for larger events (e.g. Viegas et al., 2012) (Fig. 3.26). The limited spectral resolution for lower frequencies might be generally improved by choosing larger analyze windows ($\geq$ 0.2 s), what is however impeded by the limited triggered event file length, short S-P travel time differences, and short inter-event times in swarming sequences.

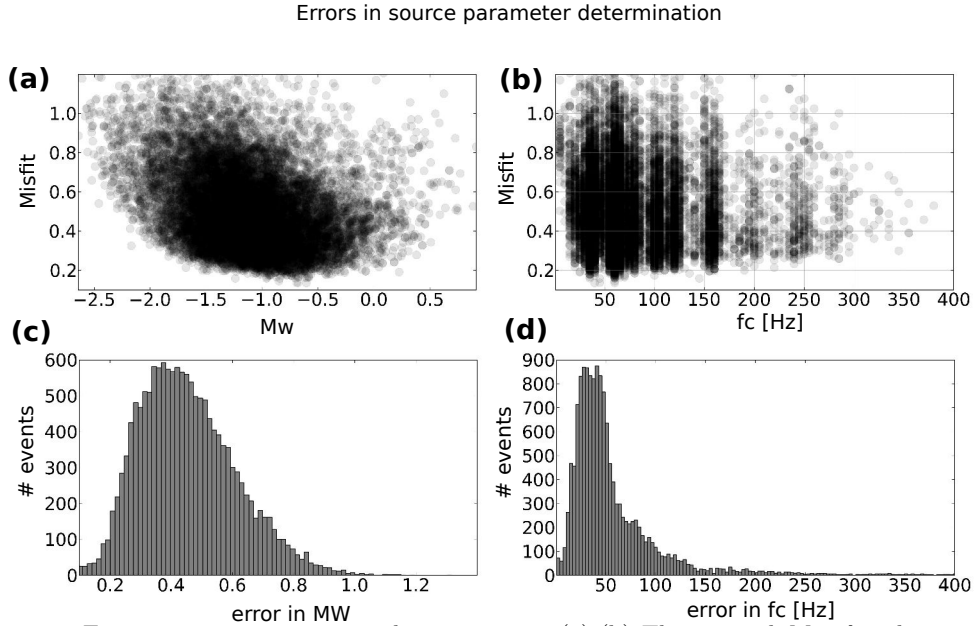

Figure 3.28: Errors in source parameter determination. (a)-(b) The optimal $Misift$ values as a function of the determined (a) seismic moment magnitude, and (b) corner frequency for the $\sim 15,000$ events. (c)-(d) Histograms of uncertainties in (c) M_W and (d) f_c as estimated from Equation (3.11) (see text).

The accuracy of radiated seismic energy E_P estimations is generally better for larger events with lower corner frequencies $\lesssim$ 40 Hz, since the used geophones provide a clear spectral response up to 400 Hz. Approximatively 90% of radiated seismic energy is released by waves of frequencies with up to ten times higher than the corner frequency (Ide and Beroza, 2001). In addition, attenuation related path and site effects significantly increase for higher frequencies, which cannot be completely explained and corrected by the here used attenuation parameters.

Despite these significant uncertainties, the results of the used automatic approach are consistent with the results of Mercerat et al. (2010) and seems to be a good first order approximation of source size (Fig. 3.27). No significant difference can be observed for the results of the well located training set events and the 15,000 events of uncertain source depth. Estimates for M_W are consistent with other studies in salt solution environments where M_w generally ranged around $-2-0.5$ (Godano et al., 2012, Trifu and Shumila, 2010). In addition, a clear increase of M_0 with decreasing f_c can be observed as generally predicted by the used ω^{-2} model (Aki, 1967) and usually observed for natural earthquakes (Fig. 3.27a-b). Moreover, the seismic moment scales clearly proportionally with radiated energy, with exception of the slight increase of radiated energy for larger moments, which result from the underestimation of the seismic moment for larger events and the underestimation of seismic energy for smaller events as discussed above (Fig. 3.27c-d). As a result, the ratio of apparent stress and stress drop is constant (Fig. 3.27e-f) and fits well with the theoretical estimation of Brune's model (Singh and Ordaz, 1994)

$$\Delta\sigma/\sigma_{app} = 4.3. \tag{3.16}$$

This theoretical estimation is based on the principal of self-similar scaling as originally observed for natural earthquakes (Aki, 1967). Self-similarity means that the spectral shape, an thus the rupture process for small and larger events is similar. Accordingly, a large event is similar to a small event scaled upward by a larger factor. As the result, it can be concluded that microseismicity at Cerville probably obeys self-similar scaling, what is actually quite reasonable, since the source mechanism was shown to be widely similar for all events, independent of being isolated or tremor-like character. Moreover, it is again confirmed that the ω^{-2}-model seems to be an appropriate choice to estimate source parameters for this data.

This result generally supports the widely discussed idea that seismic sources can be self-similarly scaled independent of the considered magnitude (e.g. Choy and Boatwright, 1995, Ide and Beroza, 2001, Ide et al., 2003, Kwiatek et al., 2011, McGarr, 1999, Plenkers et al., 2010, Prieto et al., 2004) and contradicts to studies reporting an dependency of stress drop and apparent stress with earthquake size (e.g. Abercrombie, 1995, Izutani and Kanamori, 2001, Kanamori et al., 1993, Mayeda et al., 2005, Mayeda and Walter, 1996, Mori et al., 2003, Prejean and Ellsworth, 2001, Richardson and Jordan, 2002, Singh and Ordaz, 1994, Walter et al., 2006). Major differences of the Cerville data compared to natural earthquakes

are the very low stress drops and apparent stresses with a mean for the 15,000 events of $\Delta\sigma = 0.027$ MPa and $\sigma_{app} = 0.004$ MPa, respectively. Stress drops for natural earthquakes, as well as very small sized events ($M_W \geq -4$) observed in deep mines, usually lie in the range $\Delta\sigma = 1 - 10$ MPa and $\sigma_{app} = 0.1 - 1$ MPa (e.g. Choy and Boatwright, 1995, Ide and Beroza, 2001, Kwiatek et al., 2011). Neither the estimated uncertainties for M_W and f_c, nor different standard source models (e.g. Madariaga, 1976) can explain these differences of a factor 100. Both major obervations and their meaning, namely the apparent validity of self-similar scaling and comparatively low stress dops, will be discussed in the next Chapter 4 in more detail. Nonetheless, in order to validate the here presented results and to exclude a fundamental influence of the high frequency instruments used for source parameter estimation, further source analysis should be performed by using available broadband data (Jousset et al., 2010, Jousset and Rohmer, 2012) (Fig. 1.4).

Chapter 4

On the origin of swarming (caving processes)

Major contents of this chapter are in preparation for publication: Kinscher et al., Superposing and self-reinforcing caving dynamics incorporated by microseismic swarms recorded at an salt solution mine.

Earthquake swarms are a widely observable phenomena in global seismology, but up today poorly understood. Generally, swarms are characterized as sequences of dense spatio-temporal clusters of numerous small events at rather shallow focal depths, where no clear or few identifiable main shocks occur (e.g. Malone et al., 1975). The most common explanations of this phenomenon is seen in heterogeneous stress fields and/or a weakened crust, where no single well defined fault structures developed, and therefore no higher strains can be sustained (Mogi, 1963). In addition, it could be observed that swarming activity reflect sequences of self-triggering earthquake occurrences associated with interaction of fluids, stress field and fault fabrics (e.g. Fischer et al., 2014). Such self-organizing interacting swarm networks seem to appear especially in conditions, where the Earth's crust is in a critical state (Hainzl et al., 1999a,b, 2000, Main, 1996).

One major factor in the generation of swarms is seen in the migration of fluids and increasing pore pressures that alter the resistance of the rocks and faults. As a result, most commonly, earthquakes swarm examples are documented from volcanic and geothermal settings (e.g. Baer et al., 2008, Benoit and McNutt, 1996, Dreger et al., 2000, Hill, 1977, Lees, 1998, Shelly et al., 2013, Wright et al., 2006, Wyss et al., 1997), but are also observed at intra-continental margins (e.g. Fischer et al., 2014, Hainzl and Ogata, 2005, Ibs-von Seht et al., 2008, Lambotte et al., 2014, Lindenfeld et al., 2012, Špičák and Horálek, 2001)) and other

specific tectonic settings where fluids are involved (e.g. Daniel et al., 2011, Golden et al., 2003, Hainzl et al., 2006, Husen et al., 2007, Quittmeyer et al., 1988, Smith et al., 1968). Also shallow aseismic fault slip, "creeping", was found to play a role in swarm formations in tectonic settings (e.g. Lohman and McGuire, 2007).

The formation of swarms is also well known from microseismic monitoring experiments associated with fluid injections as in geothermal, hydrocarbon and salt field reservoirs (e.g. Bourouis and Bernard, 2007, Gilpin and Lee, 1978, Godano et al., 2012, Horton, 2012, Maxwell and Urbancic, 2001, Phillips et al., 2002, Simpson, 1986, Ward and Björnsson, 1971, Warpinski et al., 2004, Zoback and Harjes, 1997). As similar to microseismic monitoring in mines (Chapter 1), these swarms or clusters are clearly of induced character such that already well established empirical and physical laws have been established, able to explain the seismic rate as a function of water injection and hydraulic rock properties (e.g. Shapiro et al., 2005, 2002). In contrast, the occurrence and origin of microseismic swarms and multiple event occurrences observed in prone-to-collapse scenarios as in rock slope studies (e.g. Lévy et al., 2010, Mertl and Brückl, 2007, Spillmann et al., 2007), as well as in specific salt solution mining settings (Emmaunelle Nayman, pers. comm., Branston, 2003) (Chapter 1) are poorly understood, which apparently represent phenomena not alone explainable by the role of fluids.

In this context, this chapter aims to better constrain and characterize the nature and origin of microseismic swarms observed in the solution mine setting in Cerville-Buissoncourt. This discussion focus on the period and microseismic crisis occurring in March to May, 2008, where microseismic swarms seem to be generally related to caving processes of the evolving cavity structure (Chapter 1). First the general spatio-temporal microseismic distribution is characterized, providing some insights into different cavity evolution stages (Section 4.1). Then, the cumulative-energetic characteristics and scaling of swarming events are presented, which provide important information on their origin (Section 4.2.1.1). The mechanical interaction and the underlying physical dynamics of swarming events are finally constrained by systematic trends found from extensive seismic statistical analyses (Section 4.2), including methods, mainly adapted from the study of Hainzl and Fischer (2002), who analyzed natural earthquake swarm occurrences in West Bohemia/Vogtland (Central Europe) (e.g. Fig. 3.21). The results of these analyses are then summarized and discussed in Section 4.3. All analyses steps are generally based on the results of event detection and location and source characteristics

as presented in the previous Chapters 2 and 3, respectively.

4.1 Spatio-temporal evolution

Figures 4.1 and 4.2 shows the epicenter locations as a function of the chronological event index and time, and demonstrate the presence of clear spatio-temporal clusters and migrations for different time scales during the microseismic crisis in 2008. These migrations and partially abrupt, cyclic spatio-temporal changes occur within seconds, as already shown for swarming example 1-3 (Fig. 2.18, 2.19, 2.20 and 2.21), minutes, hours to days (Fig. 4.1 and 4.2). Comparing the epicenter locations for these different time windows and periods, N-S oriented epicenter location changes and migrations seem to be dominant. The most significant abrupt spatio-temporal change is represented by the final peak in activity of the crisis, happening on the 4 th of April 2008, which is represented by a distinct northward epicenter migration associated with swarming example 3 (Fig. 1.7, 2.21, 4.1 and 4.2).

As already discussed in Section 2.6.4, these distinct spatio-temporal trends in epicenter location seem to mainly represent the governing caving processes, where seismic rates seem to be approximately proportional to the detached rock volume at the cavity roof (Fig. 2.25). Moreover, the driving forces associated with the governing caving processes are assumed to be strongly related to the constitution of the cavity roof relief and the asymmetry of the entire cavity structure. The major seismogenic zone is found in the region of strongest cavity roof relief (Fig. 2.25 and 4.1). Furthermore, distinct spatio-temporal microseismic clusters seem to form over the entire crisis in 2008 preferentially in the zone of highest relief and in the region of highest cavity roof extension to the south (Fig. 4.1). Hence, microseismicity is not arbitrarily distributed, but concentrated and clustered to distinct zones associated with distinct topographic features of the cavity roof.

In the following, I tried to visualize the evolution of caving activity during the crisis in 2008 and its apparent relation to the cavity's geometry. Therefore, I considered the spatial (horizontal plane only) distribution of the cumulative seismic moment as a function of time as shown in Figure 4.3. Approximatively, the relief of the cavity roof can be classified in three major zones distributed from the S-S-E to the N-N-W of the cavity zone (Fig. 4.3a): (i) one zone to the south, which comprise the highest cavity roof extensions, (ii) the transition zone further to the north, which is associated with the strongest relief in the cavity roof and (iii) one zone further to the north constituted by the lowest cavity roof extension. Then a

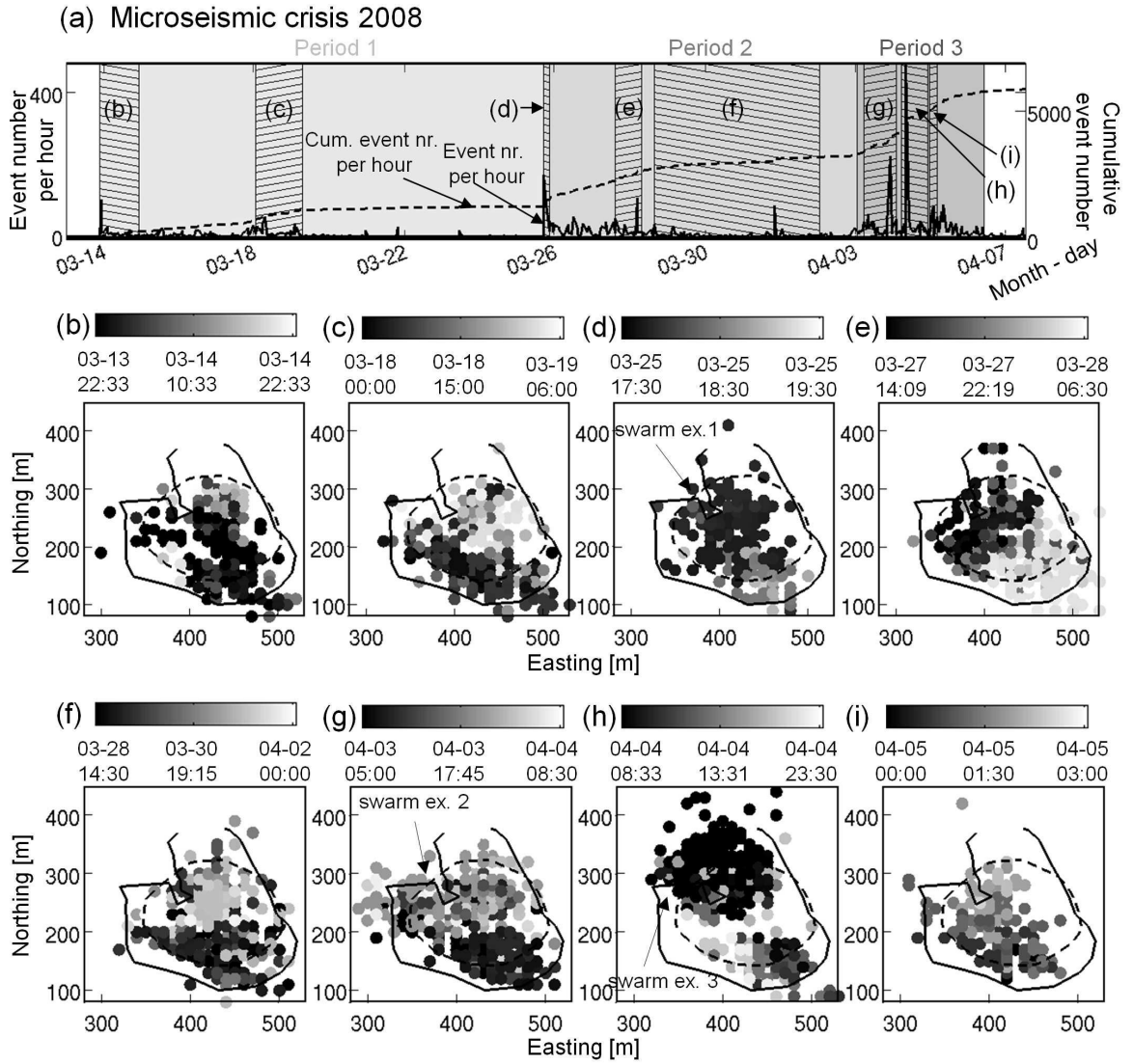

Figure 4.1: Location results of the microseismic crisis in 2008. (a) Seismic activity of the 2008 microseismic crisis, detected and located by the polarization-based and amplitude-based approaches (Chapter 2). The number of seismic events per hour (continuous black line) and the cumulative event number (dashed black line) indicate three distinct periods of seismic activities (gray shaded areas). (b-i) Spatio-temporal epicenter distribution with respect to selected time windows (areas textured with black lines in (a)) for each period of activity.

reference location point R was chosen, which was defined by the mean of the northing and easting coordinate of all events of the microseismic crisis in 2008, which is located in the major seismigenic zone (Fig. 2.25 and 4.3).

Then, the relative horizontal distance r, expressed by the northing N and easting E component, was calculated for each event recorded at time t associated with a specific seismic moment M_0. The cumulative spatial moment corresponding to the northing and easting component is then found by $M_{N,E} = \sum_{t_o}^{t} r_{N,E} \log_{10}(M_0(t))$, where t_0 is the time of the first

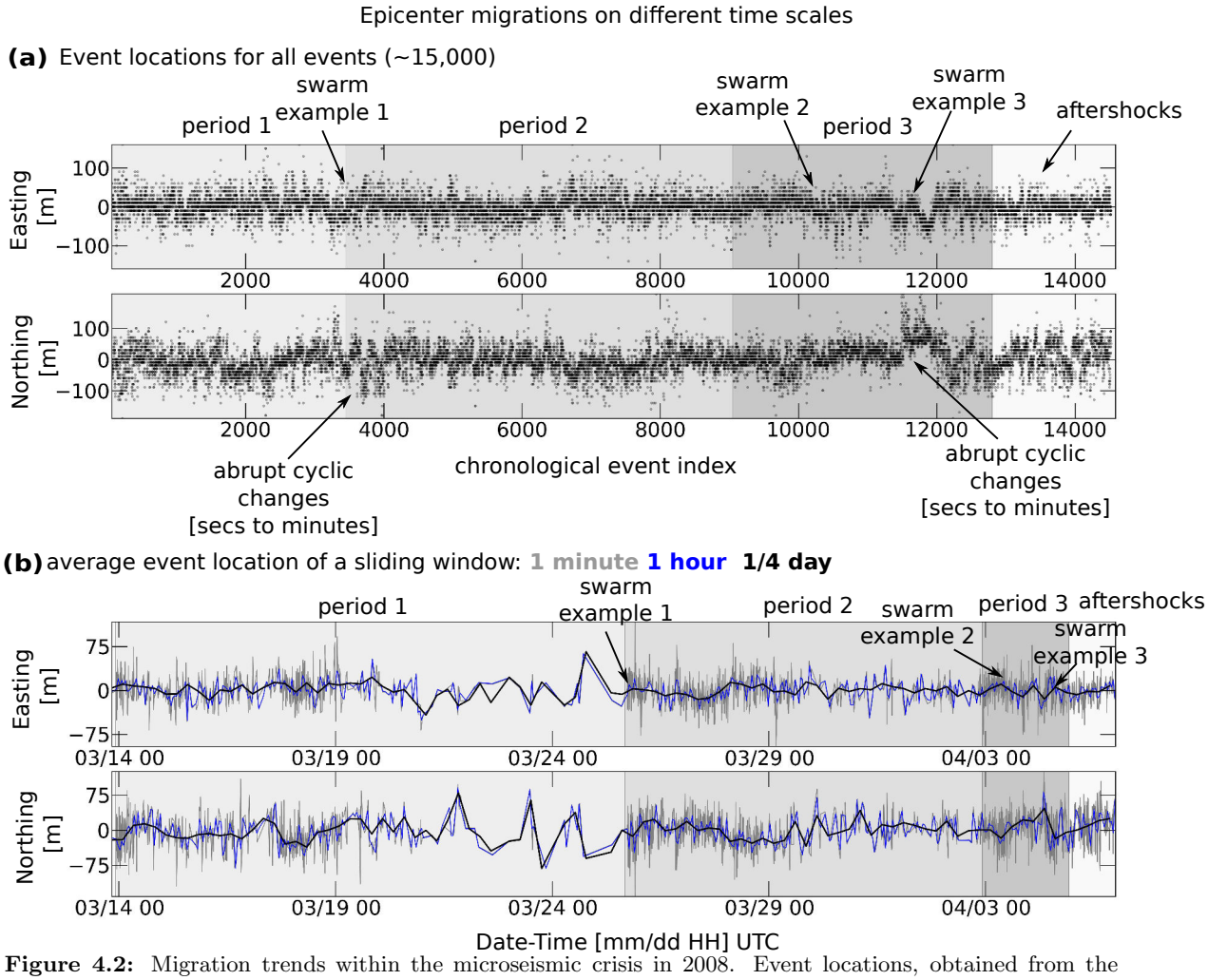

Figure 4.2: Migration trends within the microseismic crisis in 2008. Event locations, obtained from the polarization-based and amplitude-based approache (Chapter 2) are shown by their northing and easting components as a function of the chronological event index (a) and time (b). (b) Migration trends are illustrated for a gliding window of 1 minute (gray line), 1 hour (blue line) and 6 hours (black line) length with 50% overlap, which represent the average of the northing and easting component.

event occurrence in the crisis in 2008. The obtained graphs, as shown in Figure 4.3b, can be interpreted in the following manner. Positive values of $M_{N,E}$ indicate that the cumulative moment release have been strongest to the north and east from the reference point, while negative values indicate a stronger cumulative moment release to the south and west from the reference point, respectively. For the interpretation of these curves it is assumed that the cumulative moment is approximatively proportional to the caving rates, as it was indicated in Figure 2.25.

In this presentation, the curve of the northing cumulative moment is of more interest compared to the easting curve, since it represents approximatively the moment release in the three major classified zones (Fig. 4.3a). Regarding the course of the northing curve, an interesting

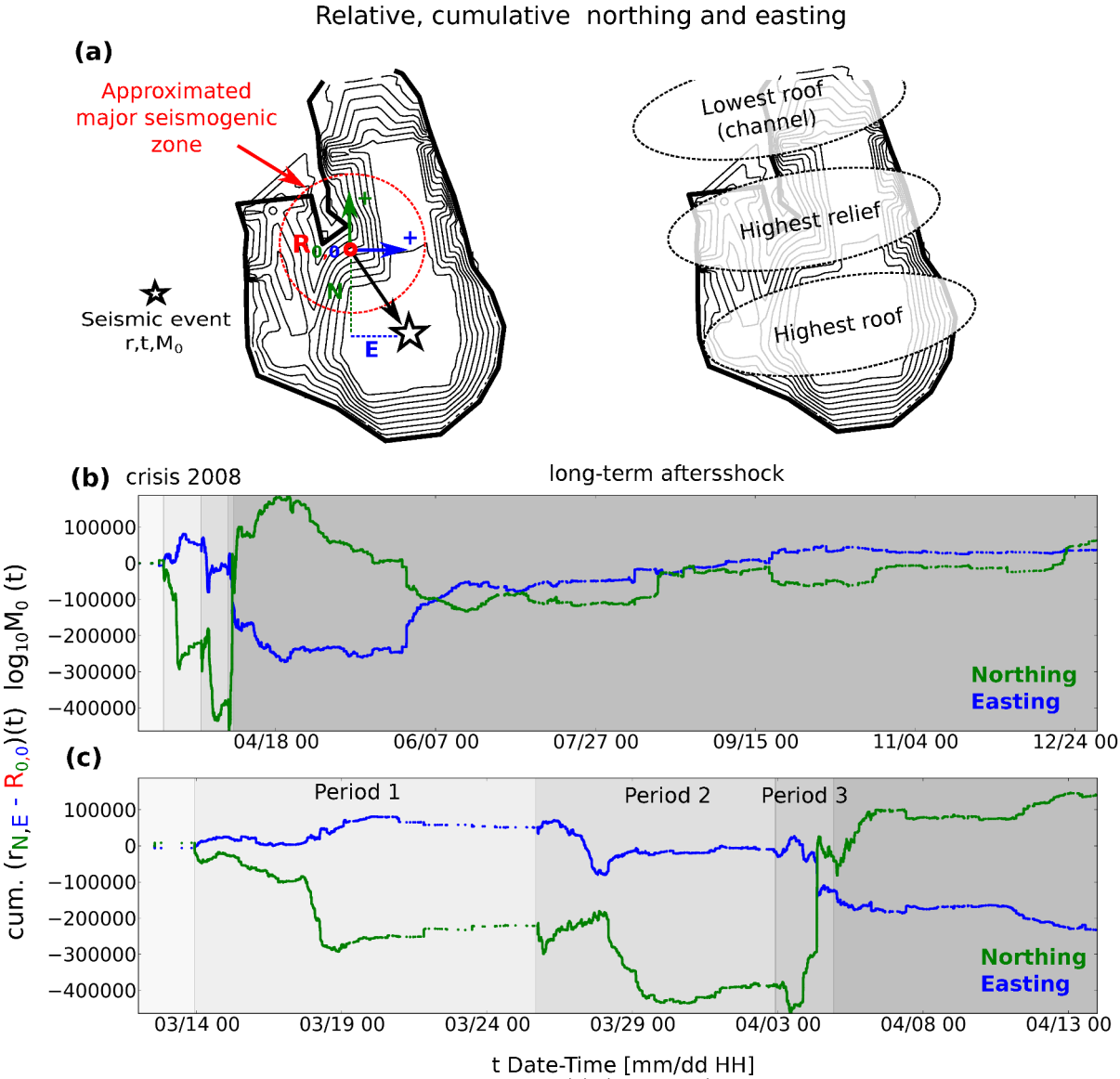

Figure 4.3: Spatial distribution of seismic moment. (a) (left panel) The cavity contour and topographic isolines (Fig. 2.3) (black lines) and the reference point (red point) in the seismogenic zone (red dashed line) and event location (black star) and its epicentral distance expressed by the northing (green vector arrow) and easting component (blue vector arrow). (right panel) Three major topographic zones (black ellipses) of the cavity structure. (b)-(c) Curves of the spatial cumulative moment $M_{N,E}$ for the northing (green line) and easting (blue line) component with respect to the reference point in (a).

behavior can observed, which is summarized and interpreted in the scenario shown in Figure 4.4. The beginnings of the first two periods in 2008 are clearly marked by dominant moment release around the seimogenic zone as indicated by the relatively constant curve course (Fig. 4.3b). This observation indicates that the area of strongest cavity roof relief represent a possible key zone for the initiation of caving processes (Fig. 4.3 and 4.4). Both initial phases for the two first periods are followed by an abrupt increase of the cumulative moment in the highest cavity roof zone to the south, which is succeeded by a slightly increasing, but rather

constant curve course (Fig. 4.3b). These phases can be interpreted as significant cavity roof collapses at the highest levels of the cavity roof to the south (Fig. 4.4).

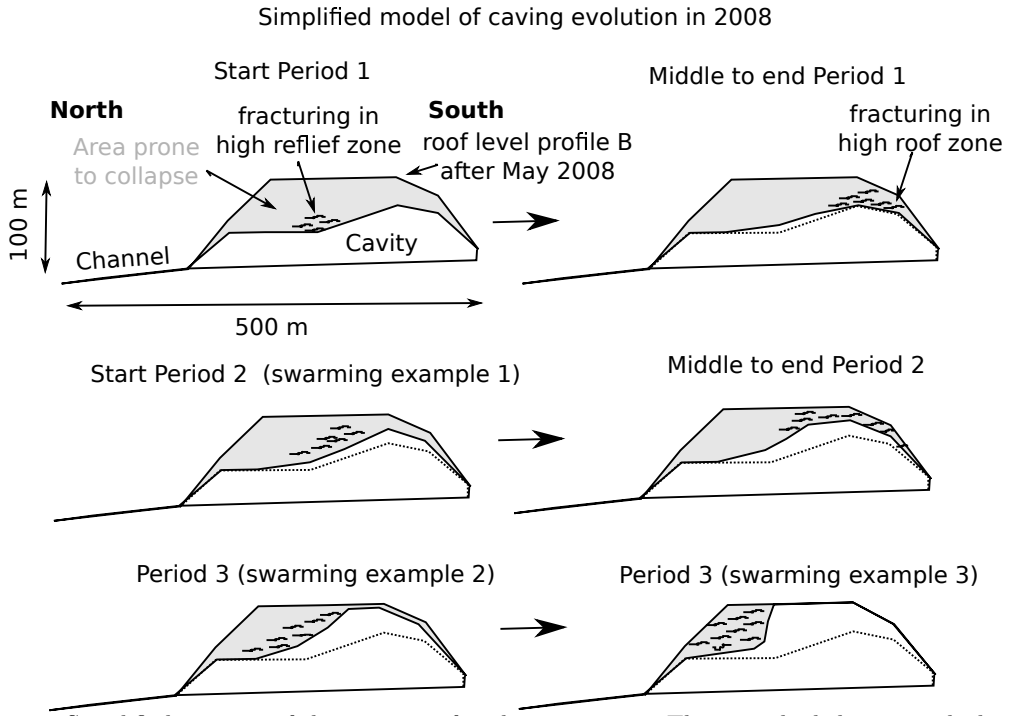

Figure 4.4: Simplified scenario of the cavity roof evolution in 2008. The gray shaded area mark the parts of the cavity roof that collapsed between February and May 2008 (Fig. 1.7 and 2.25) along a N-S cross-section over the center of the cavity structure. Continuous black line marks the current cavity roof extension, while dashed black lines mark the initial state in February 2008.

The end of the second period marks a critical state of stability in the cavity roof constitution, which is related to a strong mass excess in the northern cavity region (Fig. 4.4). This mass disequilibrium probably provoked the final main collapse of the most northern cavity roof zone (Fig. 4.3 and 4.4), which is nicely illustrated by the northward migration trends seen in Figure 4.1 and 4.2, and in the swarming examples 2 and 3 (Fig. 2.20 and 2.21). As shown by the northern component curve (Fig. 4.3), the released moment during this single last collapse seems to be of the same order as the moment release produced by the two preceding roof collapses in the southern cavity zone. Thus, the cavity roof geometry seems to be equilibrated after this major collapse, what increased significantly the stability of the roof as indicated by a decrease in microseismic activity (Fig. 4.1a).

Concluding these observations, it can be confirmed that the governing caving dynamics are significantly controlled by the geometry of the cavity structure and the mechanical constitution of its roof. It seems that the stability of the cavity roof is generally controlled by the equilibrium between its vertical and lateral extension (Fig. 4.4). In other words, if the cavity

exceeds a specific roof height, or vertical dimension, it will grow in its lateral extension. In addition, as shown by the two first periods in 2008, major zones of instability are associated with zones of high relief. These zones might generally represent high stressed zones, where detachments and rock failures are initiated as followed by bulk stress accommodation and redistribution at the entire cavity roof, what is demonstrated by predominantly lateral epicenter migrations across the entire cavity zone (Fig. 2.18-2.21, 4.1 and 4.2). Consequently, lateral stress accommodation processes seems to be dominant, which is consistent with the results of source mechanism analysis, who demonstrate the presence of systematically confined horizontal stresses that are significantly stronger compared to vertical stresses (Fig. 3.20).

4.2 Classification from inter-event time distribution

From the previous Section, it was shown that the microseismic events tend to form distinct spatio-temporal clusters as similar to other seismic swarming phenomena. A more distinct classification of the temporal dynamics associated with the microseismic swarms could be obtained from the quantitative and temporal distribution of the inter-event/waiting times as shown in Figure 4.5 and 4.6. The inter-event-time distribution characterize the temporal occurrence of microseismic events during the microseismic crisis (Fig. 4.5a,b), and thus gives insights into the seismic rate and the degree of correlation of seismicity (e.g. Molchan, 2005, Wu et al., 2013). If the microseismic events occurred randomly in time, wherein the probability of an event occurrence is independent of the time since the previous event, the probability distribution would be an exponential function (Poisson process) (e.g. Molchan, 2005, Van Kampen, 1992) (Fig. 4.5b). In contrast, the distribution of smaller inter-event times ($\lesssim$ 40 s), independent of magnitude, follows a clear power law of inter-event times, $t_w^{-1.9}$ (Fig. 4.5b), as similar to an Omori aftershock law of the form $N(t) = (c + t)^{-p}$, where N is the cumulative event number, t the time after the main shock and c and p are fault-dependent constants (Utsu et al., 1995). This distinct mode of high recurrence times indicates that microseismicity at Cerville, at short time-scales, is clearly correlated. In other words microseismic event occurrences on shorter time scales are not randomly distributed, but dependent on the preceding event occurrence as usually observed in aftershock sequences. Moreover, this power law behavior for smaller inter-event times is remarkably stable over time (Fig. 4.6).

Next to this higher mode of recurrence times, a lower mode of recurrence times for $\gtrsim$ 20 s

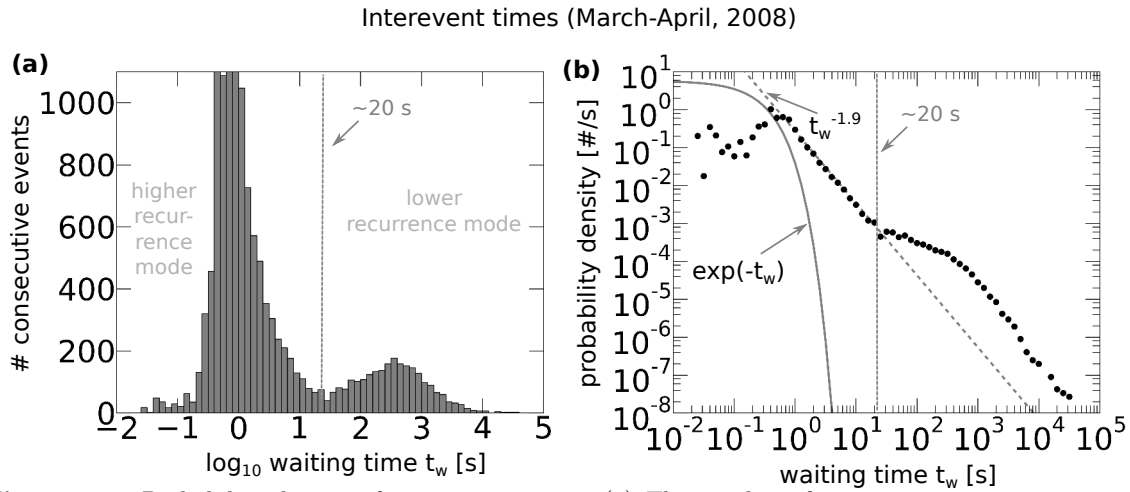

Figure 4.5: Probability density of inter-event times. (a) The number of consecutive event pairs associated with specific inter-event time. (b) Probability density for observing a certain inter-event/waiting time t_w between successive events. Note that both distributions were estimated for the entire event catalogue independent of event magnitude.

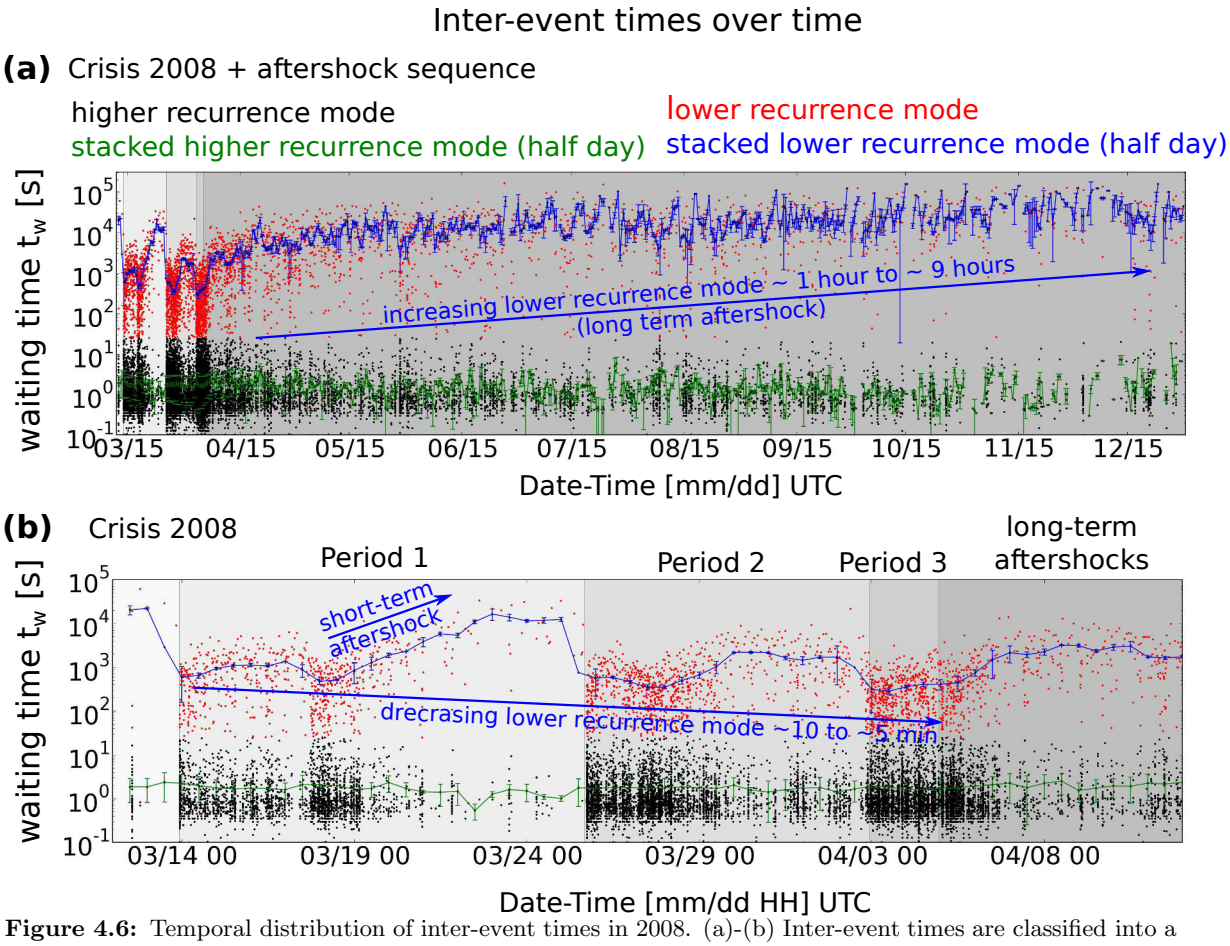

Figure 4.6: Temporal distribution of inter-event times in 2008. (a)-(b) Inter-event times are classified into a higher (black points) and lower (red points) recurrence mode and shown as a function over time. The average of the higher (green line) and the lower (blue line) recurrence mode and the standard deviation (green and blue error bars) are calculated for a half day sized gliding window with 50% overlap. Note the temporal constancy of the higher recurrence mode and temporal changes of the lower recurrence mode.

with dominant periods of around $100 - 1000$ s can be observed (Fig. 4.5a,b and 4.6). This low recurrence mode seems to represent the seismic rate associated with the repetition of the swarm clusters represented by the higher recurrence mode. In other words, the individual events form clusters on short time scales (high recurrence mode) that in its entirety appear on another larger time scale (low recurrence mode), probably related to a more global mechanism or externally driven forces, which are linked to the different evolution stages of the cavity system. Consequently, the low recurrence mode clearly changes over time (Fig. 4.6). During the crisis in 2008, by trend, the average of the low recurrence mode decrease from ~ 10 min to ~ 5 min. This continuous decrease can be interpreted as a period, when the cavity system enters into a more and more critical state of stability probably due to self-reinforcing, triggered collapsing mechanics. Moreover, almost all peaks of microseismic activity within the three major periods in 2008 are followed by a power law-like increase of inter-event times, where the largest and most persistent increase occurs after the major peak in activity, happening on the 4 th of April 2008 (Fig. 4.1 and 4.6). These periods of increasing quiescence can be very likely interpreted as aftershock sequences, and thus probably represent relaxation periods of the cavity system after larger roof collapses.

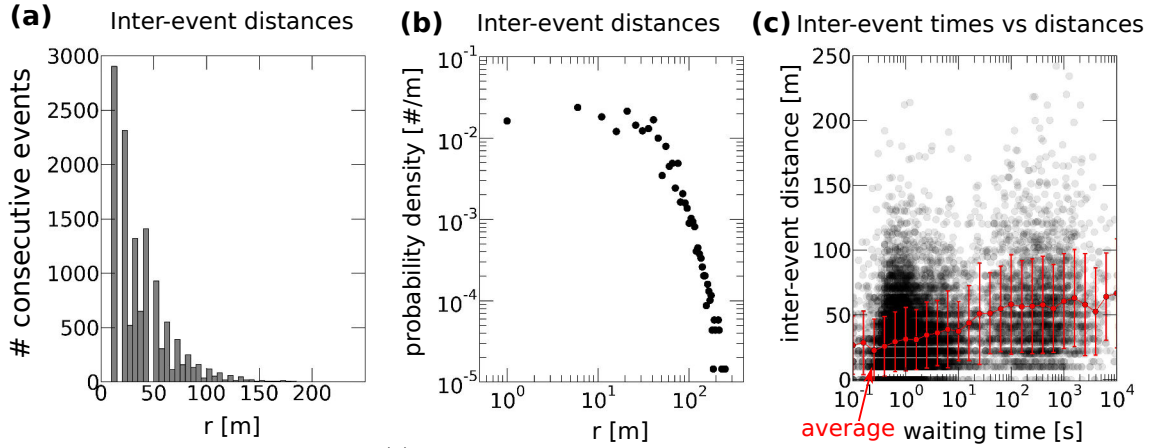

Figure 4.7: Inter-event distances (a) The number of consecutive event pairs as a function of inter-event distances. (b) Probability density of the observed inter-event distances. (c) Inter-event distances shown as a function of inter-event times (Fig. 4.5). The red points and lines and the red error bars indicate the average and the standard deviation, respectively, for inter-event distance calculated for discrete inter-event times using 50% overlap.

In addition, Figure 4.7 shows the distribution of inter-event distance, as well as its relation to the observed inter-event times. Inter-event distance were estimated by the epicenter distance, since source depths are highly uncertain (Section 2.4). It can be observed that inter-event distances become smaller with decreasing inter-event times for the high recurrence mode (Fig. 4.7c). These results indicate that temporal microseismic events clusters are also spatially

strongly clustered. In addition, the slight increase of inter-event distance with increasing inter-event times ($\lesssim$ 10 s), even though not very significant, might indicate that microseismic events are continuously migrating in space as consistent with the observed short-term epicenter migrations (Fig. 2.18-2.21, 4.1 and 4.2). In contrast, inter-event distances for the lower recurrence mode are by trend larger, around 50 m, and thus demonstrate another event interaction mechanism acting on another spatial scale.

Taking these first observations together, it can be concluded that microseismicity at Cerville is characterized by two distinct event recurrence modes. The high recurrence mode, stable over time, demonstrate strong spatial event clustering and swarming on short time scales ($\gtrsim$ 20 s) and is suggested to represent the internal collapsing dynamics at the cavity roof, i.e. its general deformational response with respect to one single event occurrence. The low recurrence mode is assumed to represent the rates of temporal occurrences of the cluster and swarms associated with the high recurrence mode. Interpreting these clusters and swarming events as roof collapses, the low recurrence, thus reflect the more global caving processes and the current "all-over" mechanical state of the entire cavity system at a given time. In the following Sections, both recurrence modes and their origin are analyzed and discussed in more detail (Section 4.2.1 and 4.2.2), considering spatio-temporal and energetic characteristics. Therein, many processing analysis steps and interpretations were adapted from the study of Hainzl and Fischer (2002).

4.2.1 Higher recurrence mode: Internal collapsing dynamics

In this Section it is aimed to characterize and interpret the internal constitution of the dense spatio-temporal clusters characterized by the high recurrence mode. First, these clusters or internal swarming sequences are described in terms of its duration and cumulative energetic constitution (Section 4.2.1.1). Then their internal spatio-temporal and energetic dynamics are constrained by means of an "embedded aftershock technique" proposed by Hainzl and Fischer (2002) (Section 4.2.1.2). Finally, all observations and results are summarized and discussed in Section 4.2.1.3.

4.2.1.1 Temporal energetic constitution

The duration of swarming sequences was estimated from the spectral envelope approach (Section 2.6) and is shown as a function of time during the crisis in 2008 in Figure 4.8.

Durations of swarming sequences are associated with a maximum of around 30 s, which seem to increase during the crisis in 2008 (Fig. 4.8). It can be seen that maximum durations seem to correlate with phases of major roof collapses as indicated by significant increases in the brine level at the exploitation wells (Fig. 1.7, Section 1.3.3.1). This first observation indicates that the formation of longer swarming sequences correspond to cavity roof collapses associated with significant rock falls into the brine filled cavity.

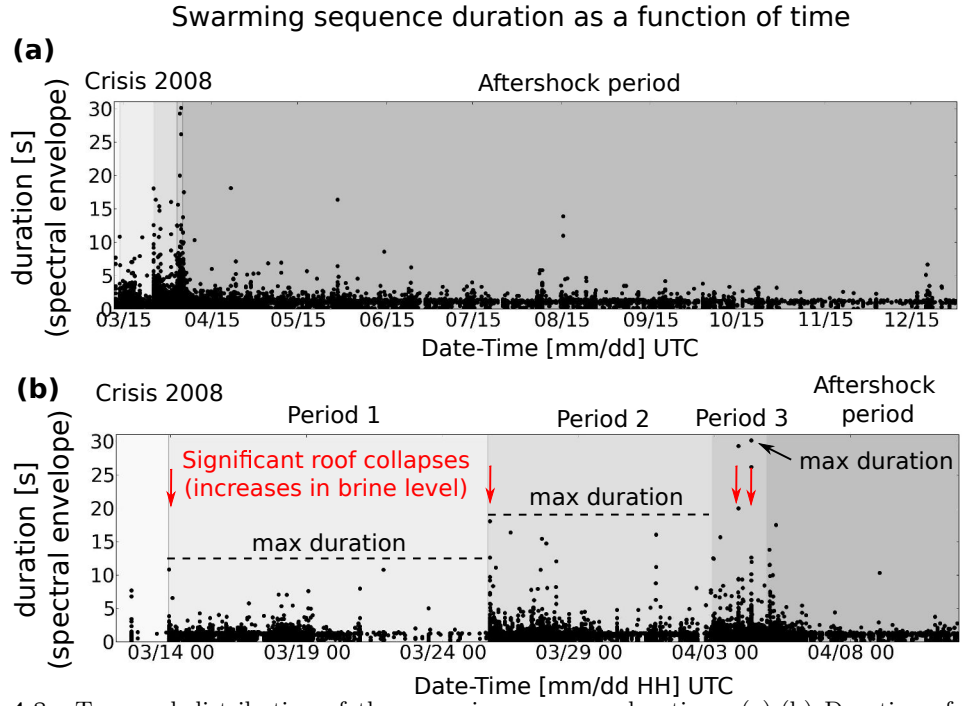

Figure 4.8: Temporal distribution of the swarming sequence duration. (a)-(b) Duration of a swarming sequences estimated by the spectral envelope approach (Section 2.6.1) shown as a function of time.

In addition, Figure 4.9 shows the number of detected events and P wave phases as a function of duration as estimated from the spectral envelope and the polarization-based approach, respectively. From this illustration it is evident that the number of detected events and P wave phases increases with increasing duration. In other words, the longer the duration of a swarming sequence the more individual events are included. In Figure 4.9a, it can be observed that the absolute number of detected events (polarization-based approach) increases with increasing duration by a power law around $\tau^{0.6}$, which means that the event detection rate decreases with increasing length of the swarming sequence. In turn, this trend implies that the event occurrence rate or/and source size exponentially increase with swarming sequence duration. This reversal conclusion is logical, since the capacity of event detection by the polarization-based approach generally depends on the differences in source time origins of two consecutive events, as well as on the length and energy of the event coda of the preceding

event, which depend on source size (Mayeda and Walter, 1996). In addition, it is shown by Figure 4.9b that the number of detected P wave phases, within a detected event, is proportional to its duration. This relationship clearly supports the hypothesis that the decrease in the detection capacity of events is by trend more affected by an increase in the event rate than to an general increase of event source sizes and longer codas.

More fundamental insights to the nature of swarming sequences are obtained by the comparison of swarming sequence duration with seismic moment M_0 (Fig. 4.10). From the shown relationships, it can be clearly seen that the cumulative seismic moment, measured during a swarming sequence, scales with duration by the power law of $\sim \tau^{1.9}$ (Fig. 4.10a). The trend between cumulative seismic moment and duration demonstrate a self-similar scaling behavior for the microseismic swarms (clusters) and is consistent with self-similar scaling observed for individually analyzed microseismic events (Fig. 3.27, Section 3.4) (e.g. Aki and Richards, 2002). Hence, shorter swarming sequences are similarly constituted as longer ones, what indicates similar underlying formation processes. Moreover, the cumulative behavior of a swarming sequence is similar to a single larger event, representing one single rupture processes. In other words, the isolated events included in a swarming sequence clearly interact with each other and superpose in order to release larger moments.

Compared to the moment increase with increasing rupture duration observed for tectonic earthquakes, the moment increase with duration of a swarming sequence at Cerville is smaller, but larger compared to slow earthquakes, which is approximatively τ^3 and τ^1, respectively (e.g. Ide et al., 2007). This observation indicates that the cumulative behavior of swarming sequences at Cerville is comparable to less energetic natural earthquakes, what is in agreement with relatively low stress drops measured for the individual microseismic events (Fig. 3.27, Section 3.4).

Interestingly, next to the cumulative seismic moment $M_{0,cum}$, also the maximum seismic moment $M_{0,max}$ of a swarming sequence seems to scale with duration (Fig. 4.10b). This observation indicates that the longer the duration of a swarming sequence, not only the higher will be the isolate event rate, but also the larger will be the source size of one individual event. In other words, the longer the duration, the bigger will be the rupture zone formed by one individual event (see also Section 4.2.1). On the other hand, the maximum moment increases significantly less than the cumulative moment and scales with swarm duration by $\sim \tau^{1.5}$ (Fig. 4.10b). The relationship between the maximum and the cumulative seismic moment is shown

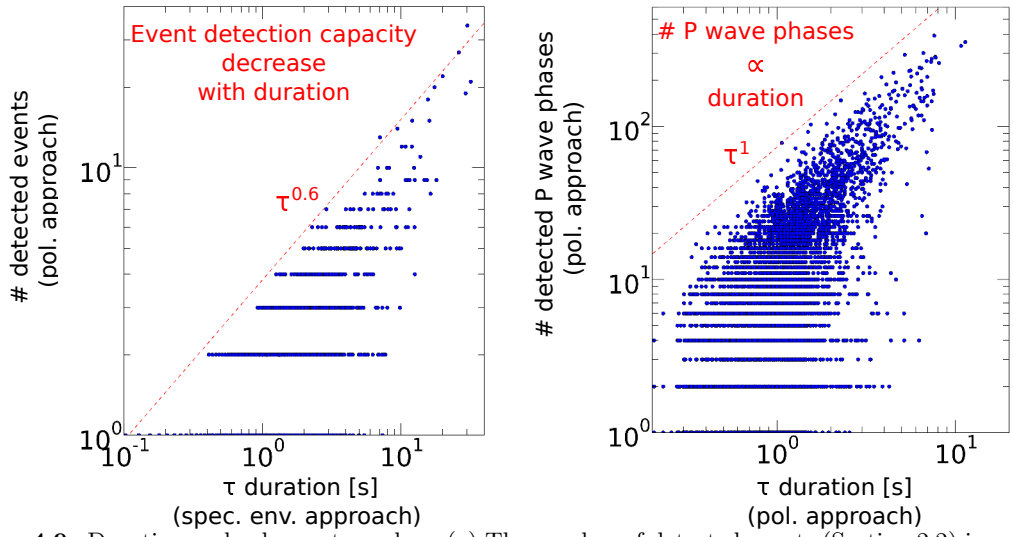

Figure 4.9: Duration and sub-event number. (a) The number of detected events (Section 2.2) in a swarming sequence associated with the duration τ, determined by the spectral envelope approach (Section 2.6.1). (b) The number of detected P wave phases shown as a function of event duration, estimated by the polarization-based approach (Section 2.2).

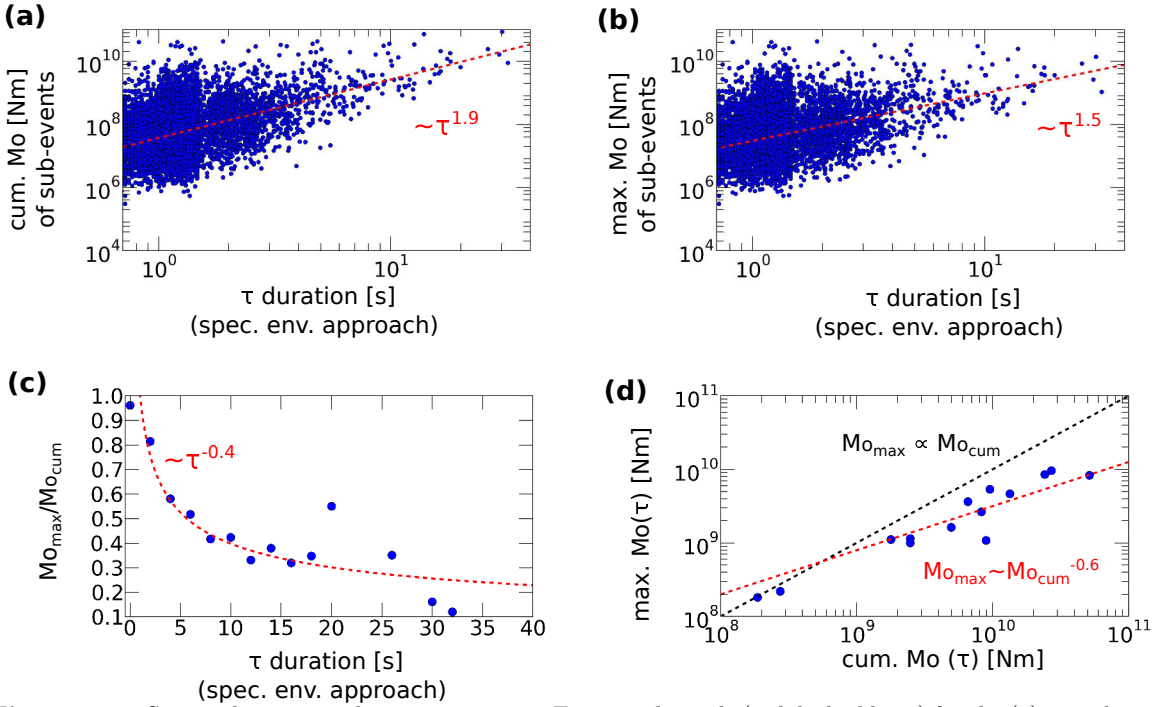

Figure 4.10: Swarm duration and seismic moment. Estimated trends (red dashed lines) for the (a) cumulative and (b) maximum seismic moment (Section 3.4) of swarming sequences (crisis 2008) as a function of sequence duration τ, estimated by the spectral envelope approach (Section 2.6.1). (c) The average of the ratio of the maximum and cumulative moment calculated for discrete durations, using an interval of 1 s and 50% overlap. (d) The average of the cumulative moment as a function of the average of the maximum moment, both taken from (c).

by its ratio in Figure 4.10c as a function of swarm duration. It can be observed that the ratio decrease with increasing swarm duration by a power-law of approximatively $\tau^{0.4}$, while the maximum seismic moment represents only 10% of the entire cumulative moment for the longest swarming sequence (Fig. 4.10c). A similar behavior can be observed from the direct comparison of the average cumulative and maximum moment for distinct swarm durations documenting a relationship of $M_{0,max} \propto M_{0,cum}^{-0.6}$. This observation indicates that the seismic moment and the size of the rupture zone as produced by one individual event is limited.

Taking all together, it can be concluded that short-term spatio-temporal clusters or swarming sequences (high recurrence mode) are formed by superpositions of single events of similar size that together scale up to form larger events (Fig. 4.10). Largest events and maximum cumulative seismic moments correspond to the longest swarming sequences. In addition, the longest swarming sequences ($\gtrsim$ 10 s) coincide with significant roof collapses in the crisis in 2008 (Fig. 4.8). This observation supports the hypothesis that the cumulative moment is approximatively proportional to the caving rates. The origin of the swarming behavior might be related to a limited rupture size capacity of the marly rocks at the cavity roof. The limitation in rupture size and magnitude production as associated with the microseismic events is probably related to low cohesive forces and elastic strength as observed from laboratory experiments (Mercerat, 2007, Mercerat et al., 2010, Souley et al., 2008) and indicated by considerably low stress drops as compared to larger natural earthquakes (Fig. 3.27, Section 3.4). In this respect, also increased pore pressures and fluid inflow at the cavity roof may play an important role, since the cavity is pressurized with brine.

A supplementary result of this analysis is the confirmation that tremor-like events can be interpreted as periods of increases in the microseismic event rate, an thus as a dense superposition of isolated events. Consistently, the number of events in a swarming sequences increase significantly more with its duration compared to the individual event size (Fig. 4.9). In the preceding Chapters, the close link between isolated and tremor-like events was already observed from their similarities in spectral characteristics (Section 1.3.4.1 and 3.2.2), relative locations (Section 2.6.4) and source mechanisms (Chapter 3).

4.2.1.2 Embedded fore- and aftershocks

In order to further characterize the dense spatio-temporal clusters represented by the higher recurrence mode, I used the approach of Hainzl and Fischer (2002) to test for the presence

of embedded fore- and aftershock sequences for immediate, consecutive event occurrences. In this approach, potential trigger events (master shocks) are identified within a gliding window over the entire crisis in 2008, which was defined with a length of two minutes and one minute gliding interval. The potential master shock was then identified as the largest event within the current time window, while events occurring after the master shock are considered as aftershocks, and events occurring before the master shock are referred to foreshocks (Fig. 4.11).

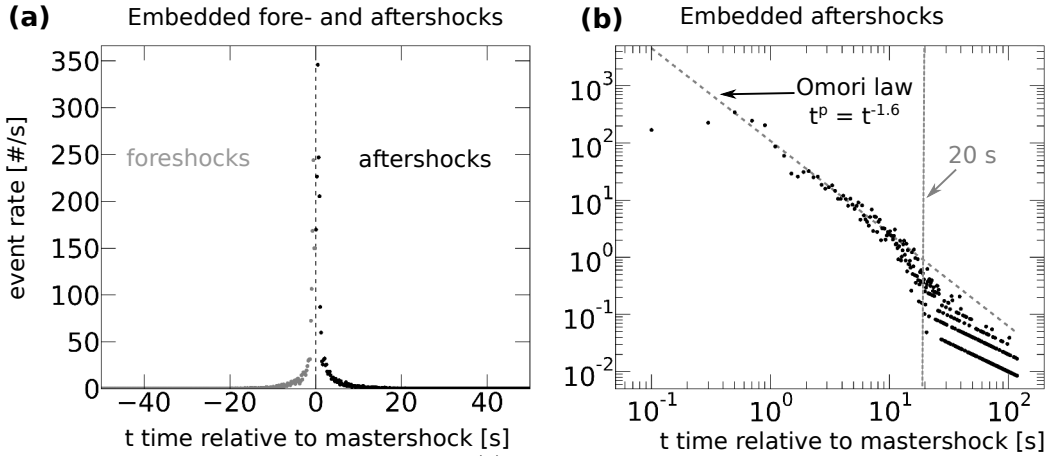

Figure 4.11: Embedded fore- and aftershocks. (a) Rate of embedded fore- and aftershocks The average rate of embedded fore- and aftershocks shown as a function of time relative to the master shocks (see text). (b) The p-value of the Omori law estimated for the embedded aftershocks shown in (a).

The number of identified aftershocks and foreshocks was averaged for 0.2 s time intervals relative to the main shock using an overlap of 50%. The result of this approach is shown in Figure 4.11. The shown fore- and aftershock rate demonstrate typical fore- and aftershock pattern, as usually observed for tectonic main shocks, where the aftershock rate decays by an Omori law relative to the main shock (Fig. 4.11b) and the absolute number of aftershocks significantly exceeds the number of foreshocks (Fig. 4.11a) (Utsu et al., 1995). Thus, spatio-temporal microseismic event clustering observed for short-time scales (high recurrence mode) can be understood as overlapping main shock-aftershock sequences. In contrast, the estimated p-value of the Omori law for of the embedded aftershocks was found with 1.6 (Fig. 4.11b), and is relatively high compared to p values usually found for natural earthquakes and swarms, usually ranging from 0.9 to 1.5 (e.g. Hainzl and Fischer, 2002, Utsu et al., 1995). Accordingly, the effect of the main shock to its environment temporally decays relatively fast, which might be an important constrain for the hidden physical mechanism. In addition, the Omori law is truncated for the embedded aftershock distribution at $\sim$ 20 s relative to the main shock. This observation is consistent with the lower limit found for the low recurrence

mode at $\sim$ 20 s from the inter-event time distribution (Fig. 4.5 and 4.6). Correspondingly, the truncation of the Omori probably results from the occurrence of subsequent swarm clusters or new main shock-aftershock sequences (Fig. 4.11b).

Next to the temporal, the spatial density of the embedded aftershock sequence was investigated by following the approach of Hainzl and Fischer (2002). In this approach, the spatial density $\rho(r)$ is calculated from the number of aftershocks occurring at a distance $r \pm \Delta r/2$ from the master shock as a function of r, which is the epicentral distance, and Δr is the step width defined with 5 m. The number of counted aftershocks is then normalized by the area $2\pi r \Delta r$ for three different magnitude ranges. In this approach, only those embedded aftershock sequence were investigated, where the number of aftershock events was bigger than 20, what yielded a total of 77 analyzed aftershock sequences.

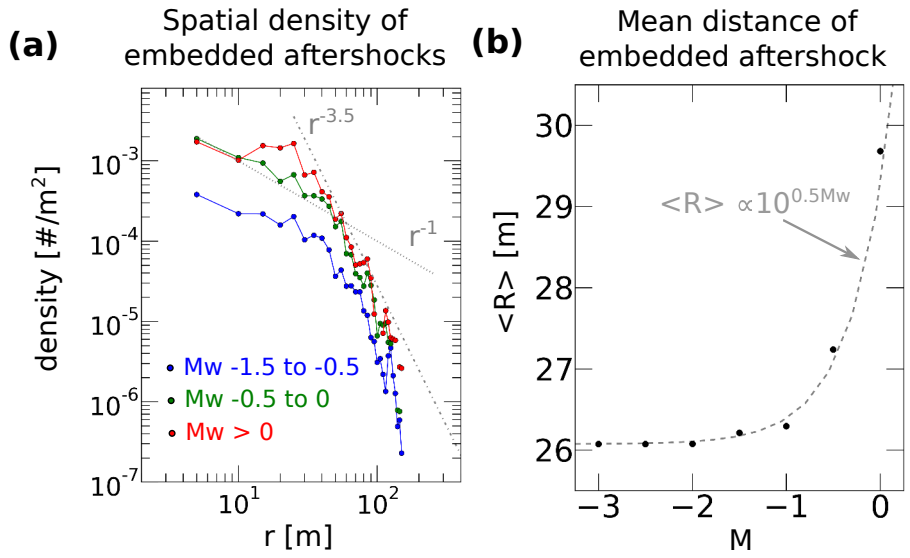

Figure 4.12: Spatial extent of embedded aftershocks. (a) The average spatial density of aftershock activity shown as a function of distance to the master shock for three different magnitude bands of master shocks. (b) The mean distance $\langle R \rangle$ of embedded aftershocks estimated by considering all master shocks associated with a moment magnitude bigger than M.

The average spatial density for the 77 main shock-aftershock sequences is shown in Figure 4.12a for different magnitude ranges of the main shock. As similar to the inter-event distance (Fig. 4.7), the spatial density decrease very rapidly with distance to the main shock, which seem to fit approximatively with a power-law of around $r^{-3.5}$ (Fig. 4.12a). This behavior can be observed for all magnitude ranges and indicates that most of the events in the microseismic crisis in 2008 trigger aftershocks, independent of magnitude. On the other hand, it can be clearly observed that the spatial density of aftershocks clearly increases with magnitude. Moreover, for larger main shock magnitudes ($M_w > 0$), a maximum in the spatial density

appears in the range $10 - 30$ m of epcientral distance to the main shock (red curve in Fig. 4.12a), which is less distinct when considering smaller main shock magnitudes. This distance is consistent with the source radius expected for larger events (Table B.5). Consequently, it can be assumed that the aftershocks are preferentially triggered at the edges of the rupture zone formed by the master shock (e.g. Hainzl and Fischer, 2002, Moradpour et al., 2014). The apparent trend for smaller distances ($\lesssim 30$ m), with r^{-1}, is not stable for the magnitude ranges, and is suggested to reflect the limit in the capacity of event detection and location resolution (location grid with 10 m resolution).

Next to the dependence of the aftershock spatial density with main shock magnitude, I analyzed the relationship between the spatial extent of aftershocks and the main shock magnitude as shown in Figure 4.12b. The spatial extent was calculated by the mean one-dimensional distance of the aftershocks (Hainzl and Fischer, 2002)

$$\langle R \rangle = N^{-1} \int \rho(r) r dr, \tag{4.1}$$

where the constant N is defined by $\int \rho(r) dr$. The mean distances $\langle R \rangle$ were then calculated and plotted for magnitudes M_w larger than M (Fig. 4.12b). The relation of $\langle R \rangle$ with M seems to follow the trend $\langle R \rangle \propto 10^{0.5M}$, which is the proposed relation for the rupture radius and magnitude for larger natural earthquakes (Hainzl and Fischer, 2002, Kanamori and Anderson, 1975, Purcaru and Berckhemer, 1978). This behavior supports the above stated hypothesis that aftershock are preferentially triggered at the edges of the rupture zone formed by the master shock. Moreover, it is demonstrated that both, the spatial density and the spatial extent of embedded aftershocks, increase with increasing main shock magnitude (Fig. 4.12). This observation is very similar to the observed systematic relationship between swarming sequence duration and cumulative seismic moment (Fig. 4.10). Accordingly, the individual events within swarm clusters at short time scales (high recurrence mode) seem to superpose in space and time, while their cumulative behavior is similar to one single larger seismic event occurrence.

This superposition behavior and the involved dynamics were further investigated by considering the average epicentral distances and the average of the differences in magnitude of the embedded fore- and aftershocks relative to the main shock as shown by Figure 4.13. Firstly, it can be clearly seen that epicentral distances decrease significantly for fore- and aftershocks with decreasing time relative to the main shock for $\lesssim 20$ s (Fig. 4.13a). This

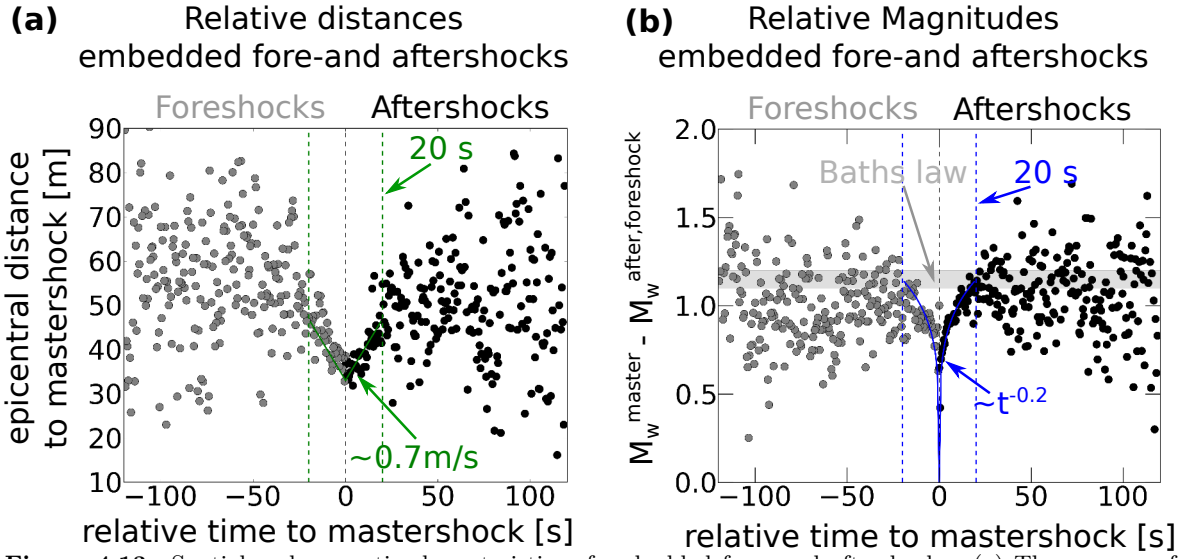

Figure 4.13: Spatial and energetic characteristics of embedded fore- and aftershocks. (a) The average of epicentral distances from the master shock for embedded fore- and aftershocks and (b) the average difference in moment magnitude of embedded fore- and aftershocks relative to the master shock shown as a function of time relative to the master shock considering 0.5 s time intervals with 50% overlap.

result is consistent with the distribution of inter-event times and distances shown in Figure 4.7c, and again confirms the lower limit found for the lower recurrence mode, representing the characteristic relative spacing between dense spatio-temporal clusters (high recurrence mode). The decrease in epicentral distance with decreasing time (< 20 s) relative to the main shock is similar for fore- and aftershocks and can be approximated by a velocity of $\sim 0.7 m/s$ (Fig. 4.13a). This velocity might be a characteristic value for the spatio-temporal epicentral migration trends observed for swarming examples 1-3 (Fig. 2.18-2.21).

In addition, the magnitude difference between the main shock and fore- and aftershocks decrease with decreasing time relative to the main shock (Fig. 4.13b). This means that the magnitude of fore- and aftershocks immediately preceding or following the main shock increases, which can be approximated by a power law of $t^{-0.2}$. This apparent self-reinforcing behavior is also well reflected by continuous temporal increases in the power spectral density, calculated for the major swarming sequences occurrence in 2008 (Fig. 2.18-2.21), as shown by Figure 4.14, which is most distinct for swarming example 2 (Fig. 4.14b). The magnitude increase of fore- and aftershocks close to the main shock is a remarkable characteristic associated with the spatio-temporal cluster formation (high recurrence mode) at Cerville, and is different to earthquake clusters reported from tectonic and global seismological studies. The immediate embedded aftershocks at Cerville are not typical aftershocks, since their magnitude depend on the magnitude of the main shock (Fig. 4.13b), which is usually not observed

for natural earthquakes (e.g. Utsu et al., 1995). The Cerville aftershocks also contradict with the well known Båth law (Båth, 1965) stating that the maximum magnitude of aftershock is 1.1 to 1.2 smaller compared to the main shock.

4.2.1.3 Discussion

Concluding these observations, it can be stated that microseismicity at shorter time scales (high recurrence mode) forms dense clusters in space and time. The characteristic spacing of these clusters in time is approximatively $>$ 20 s for the crisis in 2008. The internal organization of these clusters can be understood as main shock-aftershock sequences in which each individual event triggers itself aftershocks. Simultaneously, the individual events in one cluster seem to superpose systematically in space and time, while their cumulative behavior is similar to one single larger seismic event occurrence. Correspondingly, the spatial extent and duration of one cluster seem to increase with increasing magnitude of the internal main shock (Fig. 4.10b, 4.12).

Moreover, it could be observed that the spatial and energetic extent of these clusters increase with increasing time, associated with propagation velocities in the order of $\sim$ 0.7 s (Fig. 4.13a) and cumulative moment increases with its duration of $\sim \tau^{1.9}$ (Fig. 4.10a), respectively. Moreover, the moment of immediate fore- and aftershock events ($\lesssim$ 20 s) seems to systematically increase towards the main shock with $\sim t^{-0.2}$ (Fig. 4.13b). Accordingly, the potential to produce a larger rupture events (larger moment) is dependent on the number of the preceding events. Consistently, the maximum moment magnitude increase with swarming sequence duration (Fig. 4.10). These observations might indicate that swarming sequences, forming in the order seconds, represent the process of growing, propagating rupture zones. Regarding the results of the source mechanism from Chapter 3, it might be possible that such rupture zones form along systematic conjugate fault networks, composed by thrust fault segments that connect and interact with time and produce major roof collapses (Fig. 4.15). Interestingly, the longest durations of swarming sequences, and thus largest cumulative moments, occurred in the end of the microseismic crisis in 2008 (Fig. 4.8). This observation might indicate that the density of fractures, formed at the cavity roof, increased during the crisis, what increased the potential to produce larger rupture zones by connections along these fractures (Fig. 4.15).

The internal mechanism, controlling small scale fault interaction and superposition and large

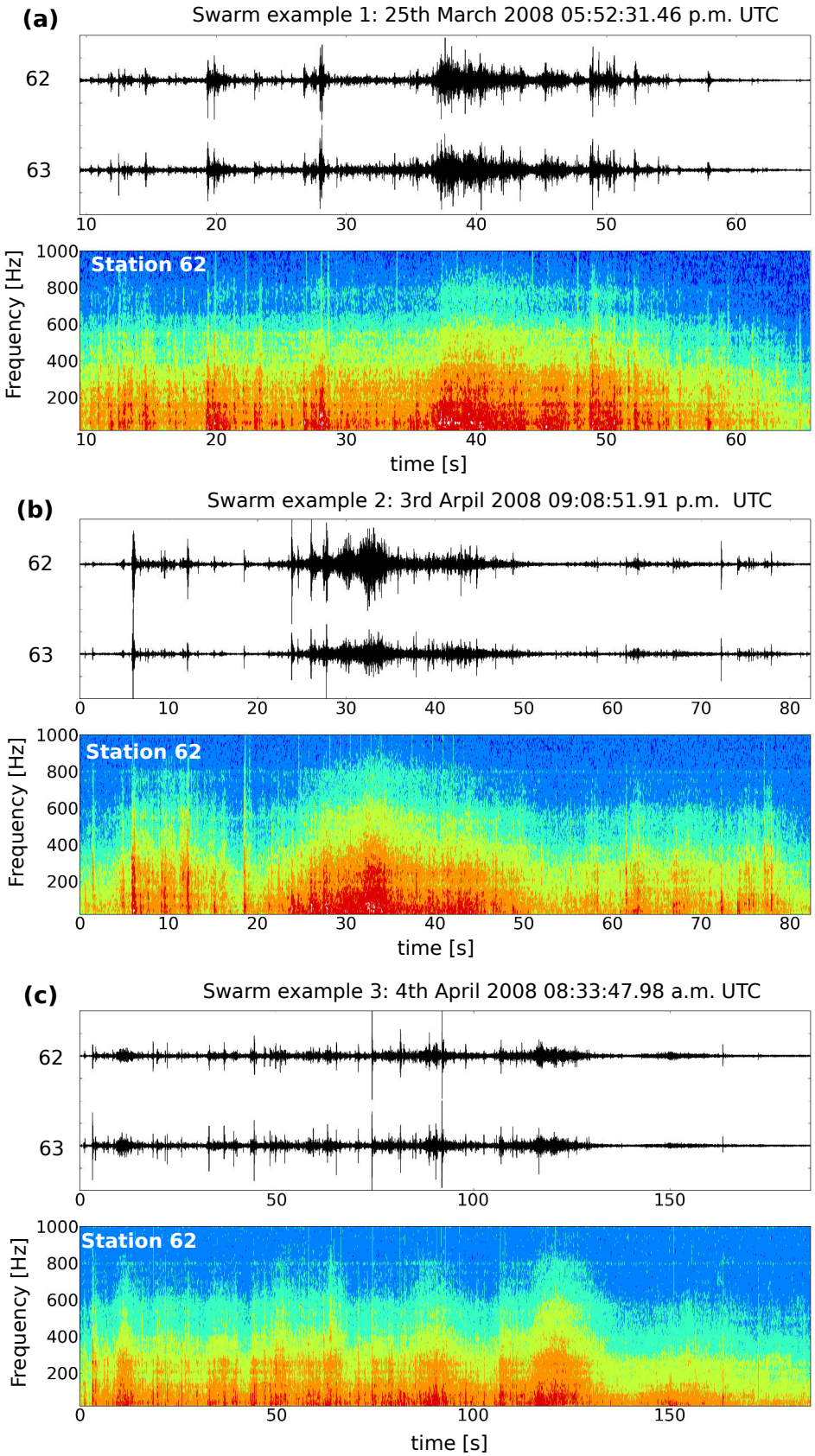

Figure 4.14: Spectrograms of swarming sequences in 2008. (a)-(c) Examples of the three principal swarming sequences of the crisis in 2008 as already shown in Fig. 1.9 and 2.18-2.21. Seismic velocity traces are shown for the vertical components of stations 62 and 63. Spectrograms were calculated using a 0.15 s window length with 90% overlap, while intensities are presented in a normalized dB scale for seven distinct contour levels (colored scale).

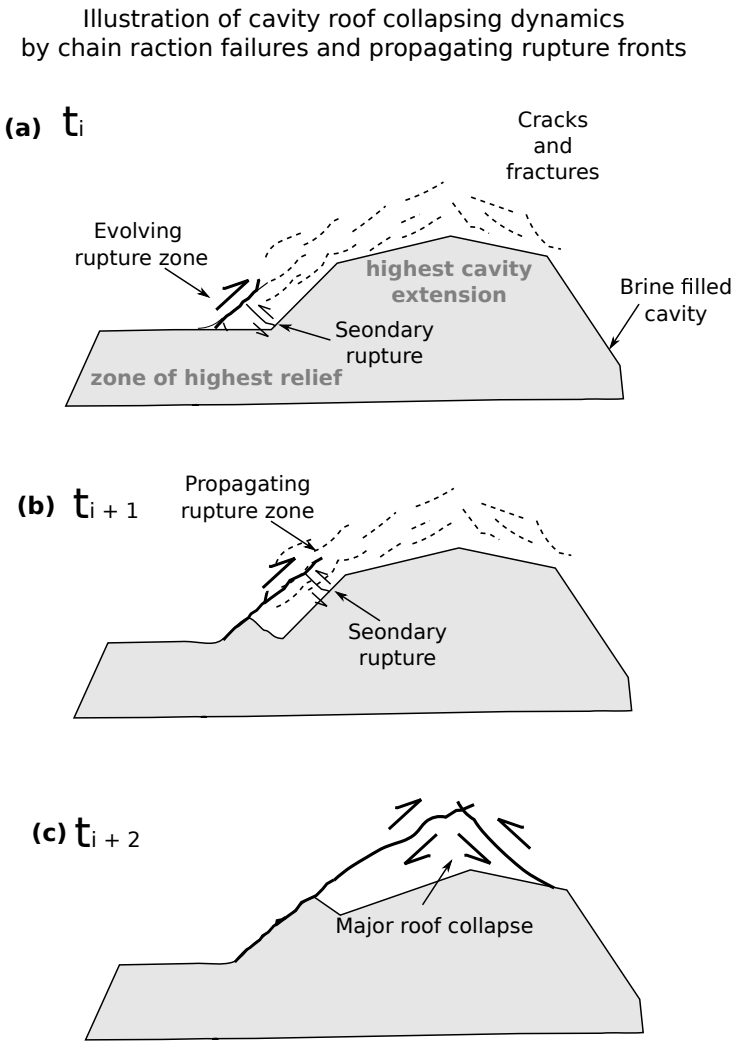

Figure 4.15: Cavity roof collapsing dynamics. Shown is a possible scenario, for three stages (a)-(c) (chronologically shown in time t_i in the order of seconds) constrained by the observations of microseismic swarming sequences that were interpreted as propagating rupture/collapsing zones, organized by networks of interacting dip-slip faults.

scale rupture formation remains speculative. Generally, it seems reasonable that the triggering mechanism is related to static stress transfer, where stresses accumulate at the crack tips, leading to continuous stress accumulations in a propagating rupture front (stick-slip mode) (e.g. Scholz, 2002). The hypothesis is supported by the observations that each event itself is found to trigger aftershocks preferentially at the edge of the rupture zone of the preceding events and that the spatial density of aftershocks increases with magnitude (Fig. 4.12). Moreover, the decrease of the spatial aftershock density relative to the main shock is in the order $\sim r^{-3}$ (Fig. 4.12a), what is consistent with empirical and theoretical observation for static stress transfer, while dynamic stress transfer (shaking) is associated with spatial density decays in the order $\sim r^{-2}$. However, in current research there is still a general debate about the ability to interpret the governing trigger mechanism by means of spatial density estimates of aftershocks, whose interpretation is not straightforward as primarily thought

(e.g. Brodsky, 2006, Felzer and Brodsky, 2006, Hill et al., 1993, Marsan and Lengliné, 2010, Moradpour et al., 2014, Richards-Dinger et al., 2010, Stein, 1999).

According to such a rupture propagation model, stresses are assumed to be concentrated at the crack tips so that the direction of the rupture propagation is determined by the rupture orientation of each single event. Since the source mechanisms of the individual events seem to be generally very similar, mainly NW-SE trending thrust faults (Fig. 3.20, 4.15 and B.1, Section 3.2), one would expected that the rupture propagation direction is equally oriented NW-SE. Unfortunately, the rupture propagation direction and the spatial orientation of the formed rupture zone is difficult to determine for consecutive events. Location errors are generally too high (±50 m) and location resolution too low (10 m grid) (Chapter 2) in order to determine the spatial orientation between two consecutive closely located events (Fig. 4.13). Some rough estimates can be obtained by regarding the orientation of the epicenter migrations for small time scales. As already stated in Section 4.1, migrations seem to be associated with a predominant N-S oriented component (Fig. 4.1 and 4.2). In addition, for all the swarming sequence example, it can be observed that the most energetic events contained in these sequences (Fig. 4.14), tremor-like events, are clearly associated with NW-SE migrations what would agree with the proposed propagating rupture front model (Fig. 2.18-2.21).

Also the inflow of fluids into the evolving rupture zone might play an important role in such a model, which increase the pore pressure in the adjacent, "prone-to-rupture" rocks. However, the found p-value of embedded aftershocks is generally very high with 1.6, indicating a comparatively fast decay of the aftershock rate (Fig. 4.11). In contrast, post-seismic relaxation process associated with fluid flow are rather associated with slower aftershock decays with time (e.g. Freed, 2005). Furthermore, the increase in distance with increasing time relative to the main shocks, as shown in Figure 4.13, seems to be rather linear, what contradicts to classical square-root shaped fluid diffusion laws.

In order to shade more light into this discussion, further investigations need to be done. The distinct spatio-temporal trends should be compared to quantitative predictions of the static stress triggering model using spatio-temporal stochastic prediction models, as e.g. the Epidemic-Type Aftershock Sequence Model (ETAS) (e.g. Zhuang et al., 2012), and seismicity models based on Coulomb stress calculations (e.g. Hainzl et al., 2010). For these simulations, it seems also necessary to further improve the location results, as for example by means of ad-

equate relocation procedures. Also uncertainties in the source mechanisms for the individual seismic events should be better constrained in this respect.

4.2.2 Lower recurrence mode: caving evolution and dynamics

In this Section, the temporal changes of the low recurrence mode (Fig. 4.6) and the associated caving dynamics of the crisis in 2008 are analyzed in more detail. So far it was suggested that the low recurrence mode represent the seismic rate associated with the repetition of the swarm clusters represented by the higher recurrence mode (Fig. 4.5 and 4.6). Since these clusters seems to represent cavity roof collapsing events, at least the longest ones (Fig. 4.8), the low recurrence mode is supposed to provide information on the temporal evolution of these collapses, and thus characterize the state of stability the entire cavity volume. In order to evaluate this hypothesis, the low recurrence mode is compared to in-situ strain measurement at the cavity roof in Section 4.2.2.1. Then the temporal-energetic evolution of the microseismic crisis in 2008 is analyzed in more detail in order to characterize the nature of the governing caving dynamics (Section 4.2.2.2).

4.2.2.1 Comparison to strain in-situ data

The lower recurrence is compared to in-situ strain measurements in form of the multi-point anchor borehole extensometer (Fig. 1.4, 1.5d and 4.16). The extensometer measures the displacement U relative to a reference point at the surface at three anchors installed above (U_1), within (U_2) and below (U_3) the Dolomite layer (Fig. 4.16a). In order to measure the deformation between the geological units of the cavity roof and the overburden, I calculated the differences $U_1 - U_2$ and $U_1 - U_3$ divided by the initial distance of the anchor points (Fig. 4.16b). Regarding the displacements and deformation during the crisis in 2008 over time, it can be observed that the Marl layer at the cavity roof and the overlying Dolomite layer subside more compared to the overburden indicating extensive deformation (Fig. 4.16).

Periods of strongest and most rapid extensive deformation can be found in the beginnings of the three classified periods of the crisis, which correspond to significant roof collapses as indicated from the significant brine level increases in the exploitation wells (Fig. 4.8 and 4.16). As seen by the $U_1 - U_2$ and $U_1 - U_3$ curves in Figure 4.16b-d, the magnitude of these rapid extensive deformation events becomes more important with time and is each time followed by a phase of constant deformation. It is suggested that the rapid extensive

deformation events reflect the opening of fractures during a massive roof collapse, while the following phase marks subsequent closure of these fractures.

On a first order, the lower recurrence mode correlates very well with the extensometer curves during and after the crisis in 2008 (Fig. 4.16). Correspondingly, in periods of roof collapses the lower recurrence mode decreases, indicating an increase in the rate of collapsing events. In the post-collapsing periods, consistently, the lower recurrence mode increases, indicating a current state of relaxation, where the roof collapsing rate decays. This observation furthermore confirms that microseismic monitoring seems to be a very useful tool in order to survey and document the caving dynamics of an evolving cavity system. Nonetheless, in current investigations it is aimed to better understand the detailed relationship between the microseismic rate and in-situ deformation measurements (GPS, tacheometer, extensometer, Fig. 1.4) in order to clarify the question about the representativeness of microseismicity with respect to certain deformation mechanisms. In this context, also seismic broadband observations will be considered.

4.2.2.2 Temporal-energetic distribution

In the following, it is aimed to characterize and discuss the apparent self-reinforcing collapsing mechanics in 2008, which are indicated by the decreasing low recurrence mode, by an increase in the swarm sequence duration and by the extensometer data (Fig. 4.8, 4.1, 4.6 and 4.16). In order to provide more insights into the nature of this phenomenon, the b-value was investigated (Fig. 4.17). The b-value is a common characterization of earthquake populations to characterize the cumulative frequency – magnitude distribution, which is defined by the GR law $\log_{10} N = a - bM$ (Gutenberg and Richter, 1944), where N is the number of earthquakes with magnitudes greater than or equal to M. Assuming a magnitude of completeness Mc with -1, the b-value for the crisis 2008 was estimated with 1.1 (Fig. 4.17a), which is consistent with the tectonic swarm analyzed by Hainzl and Fischer (2002) and with natural earthquakes at plate boundaries (e.g. Scholz, 2002). In contrast, the b-values estimated for the three distinct periods of seismic activity in 2008 show a distinct, chronological decrease in the b-value from $\sim$ 1 to 0.8 (Fig. 4.17b). The decrease in the b-values indicate an increase in the maximum expected magnitude. As proposed by Hainzl and Fischer (2002), the uncertainty of this trends was estimated by determining the 95% confidence interval of the estimated b-values (Aki, 1965, Utsu, 1966) $b = \frac{\log_{10}(exp(1))}{\langle M \rangle - M_c}$ and $\delta b = 1.96\frac{b}{\sqrt{N}}$, where $\langle M \rangle$ is

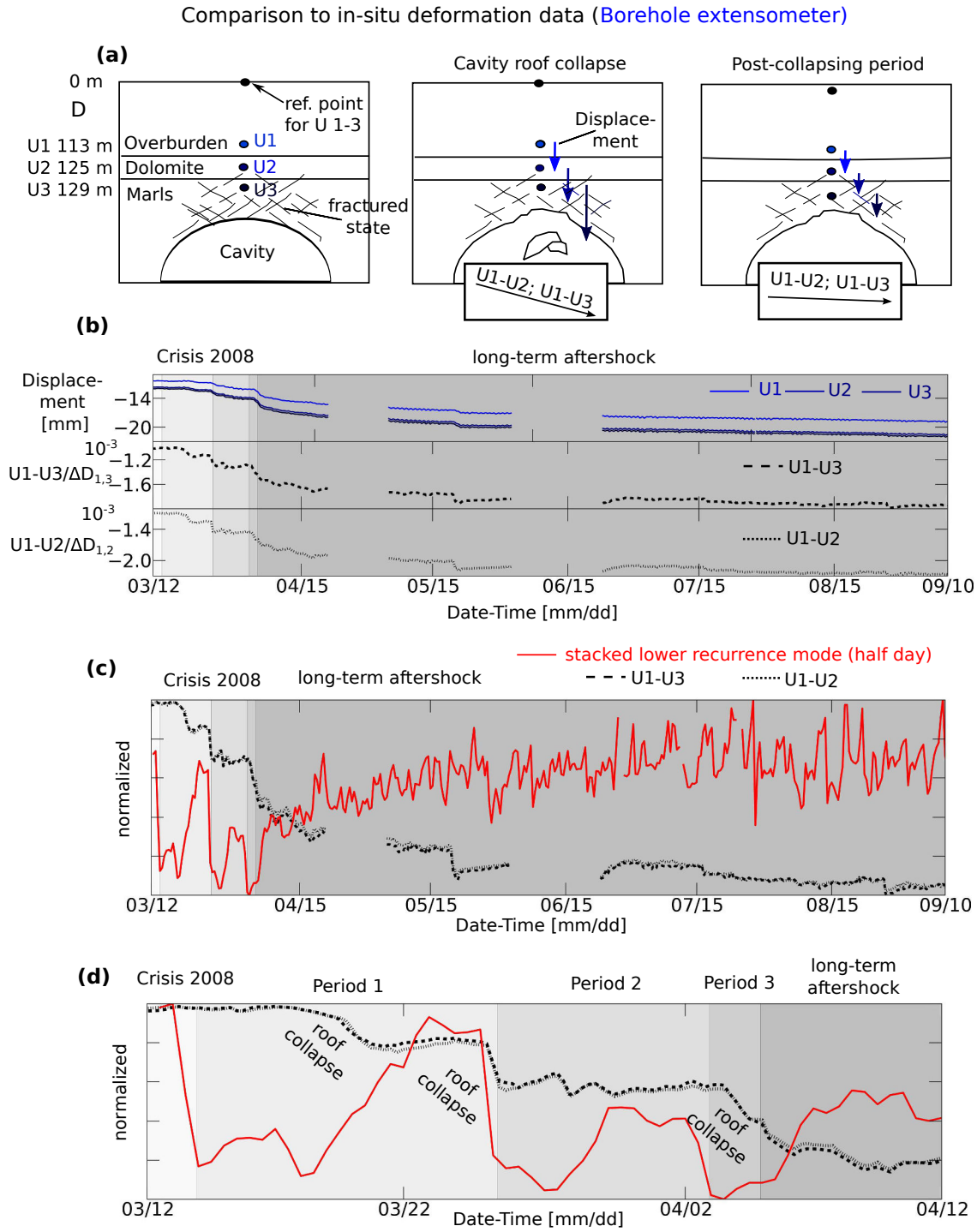

Figure 4.16: Extensometer data and low recurrence mode in 2008. (a) Extensometer data measuring the displacement U relative to a reference point at the surface at three anchor points fixed above (U_1), within (U_2) and below (U_3) the Dolomite layer (Fig. 1.4 and 1.5d). (b) Displacement at each anchor (blue lines) recorded during and after the crisis in 2008, as well as deformation between the overburden and the Dolomite layer ($U_1 - U_2$, black dashed line) and the overburden and the Marl layer below ($U_1 - U_3$, black pointed line). (c)-(d) Comparison of the normalized extensometer data with the normalized and stacked lower recurrence mode (red line) (Fig. 4.6).

the mean of the estimated magnitudes and N the number of seismic events with $M > M_c$ (Fig. 4.17b).

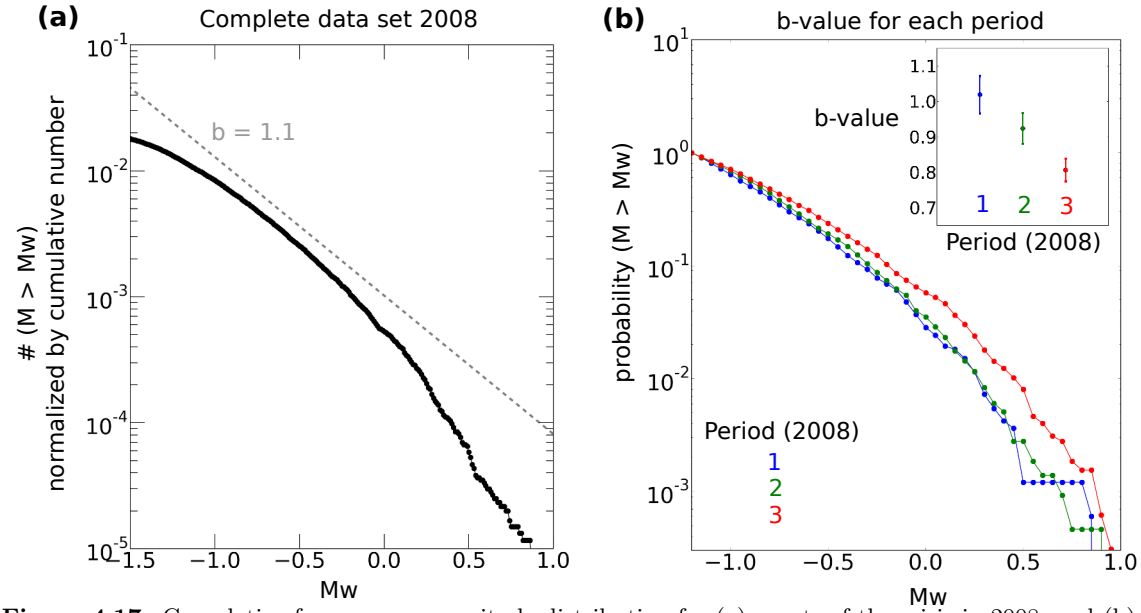

Figure 4.17: Cumulative frequency - magnitude distribution for (a) events of the crisis in 2008, and (b) for the three characteristic periods (e.g. Fig. 4.1), where the b-value continuously decrease (inner panel). b-values were estimated assuming $M_c = -1$ (see text).

Nonetheless, the GR curves have rather rounded shapes, and it seems that larger magnitudes $M_w > 0$ follow a slightly different trend as compared to smaller magnitudes (Fig. 4.17). Consequently, the estimated b-values are related to significant uncertainties, and larger magnitude events are probably associated with different underlying physics as compared to smaller events. This bimodal trend can be explained by two important results found during the analysis of the swarm and cluster formation (higher recurrence mode) in Section 4.2.1. (i) First, there seems to be a limitation in rupture size and magnitude production associated with cavity roof rocks. (ii) Secondly, the maximum moment in swarm sequences is dependent on its duration, and thus is dependent on the number of the preceding events and their magnitudes. Interestingly, the GR curve of the last period of the crisis seems to be truncated at larger magnitudes ($M_w \gtrsim 0.2$) compared to the preceding periods (red curve, Fig. 4.17b). This is consistent with the observation that the swarming sequence durations are longer compared to previous periods (Fig. 4.8), and thus larger maximum moments/rupture zones are produced. The decreasing trend of the b-value and the implied increase in the maximum expected magnitude is also seen from the cumulative distribution of the seismic moment, which is shown as a function of the chronological event index i in Figure 4.18. After Hainzl and Fischer (2002), a time-dependent seismic moment release would be characterized by a linear relationship of

the event index and cumulative moment, as defined by a unique Gutenberg-Richter distribution. However, the cumulative moment release fits better, even though not perfectly, with a power of $i^{1.15}$, documenting an increase in the mean seismic moment with increasing seismic event occurrences.

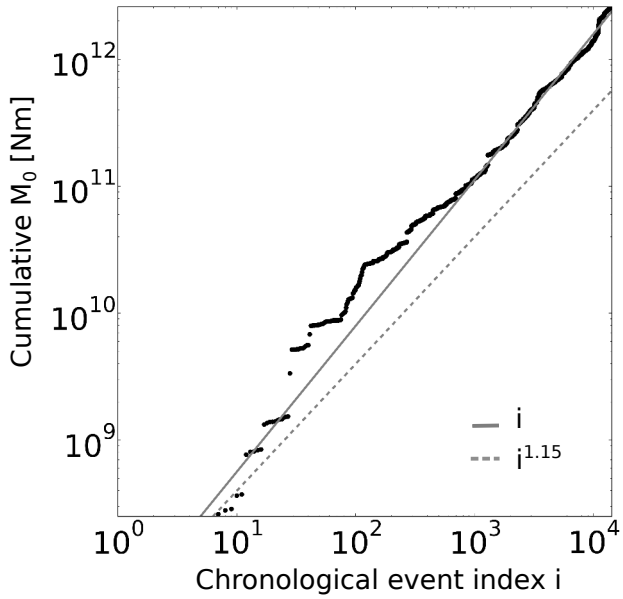

Figure 4.18: The cumulative seismic moment release for all events within the crisis in 2008 shown as a function of the chronologically ordered event index i. The dashed line shows a linear function, while the continuous line shows a power law fit.

The increasing seismic moment release during the microseismic crisis in 2008 confirms that the governing caving processes are related to self-reinforcing dynamics. Thus, each roof collapse in the crises provokes an even bigger subsequent collapse indicating a continuously decreasing stability of the entire cavity system. The increase in size of the collapsing events and moment release might be generally related to an increasing fractured state of the cavity roof allowing for larger rupture zone formations (Fig. 4.15, Section 4.2.1.3). The fact that the caving processes did not end with a total collapse, but reached a new state of stability after the the 4th of April, might be related to the re-equilibration of the cavity's geometry in its vertical and horizontal dimensions as discussed in Section 4.1 (Fig. 4.3).

In order to characterize the post-collapsing periods after larger roof collapses, within and after the crisis, the p-values of the Omori law were calculated for aftershock periods, as shown by Figure 4.19, which were identified from the lower recurrence mode (Fig. 4.6). Interestingly, p-values obtained for aftershock periods within the crisis are smaller, ranging from 1.3 to 1.5, compared to the p-value of 1.7 found for the final long-term aftershock sequence after the crisis (Fig. 4.19). This increase in the p-value means that the decay of the aftershock rate

increased after the final collapse event in April 2008, what indicates that the cavity system became less sensitive to perturbations. Thus, after the final major collapse, the cavity roof experienced stabilization, probably due to a newly reached stable geometry with respect to the externally applied stress field.

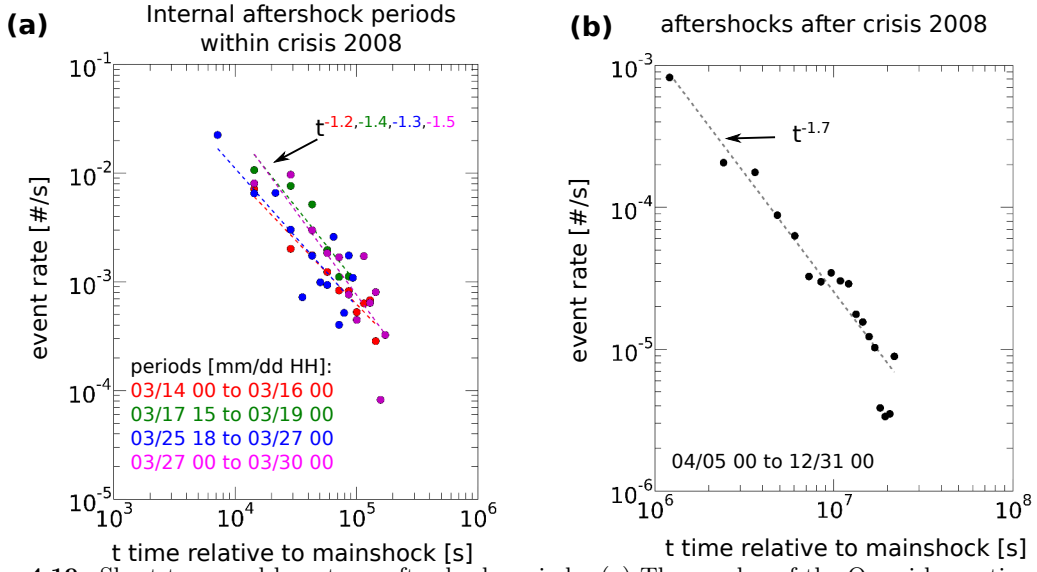

Figure 4.19: Short-term and long-term aftershock periods. (a) The p-value of the Omori law estimated for short-term aftershock sequence within the crisis 2008 as identified from the lower recurrence mode in Fig. 4.6. (b) The p-value of the Omori law estimated for long-term aftershock sequence following the crisis 2008 (e.g. Fig. 4.6).

By current analysis it is aimed to better constrain the observed self-reinforcing caving dynamics by additional statistical analysis. In this analysis, the classification of the lower and higher recurrence mode is used to define event groups/swarming sequences, representing cavity roof collapses, whose internal characteristics are described by their cumulative spatio-temporal and energetic attributes. This simplified catalogue is then used to estimate statistical laws documenting the underlying mechanism of collapse interaction, which might be later evaluated by mechanical modeling and stochastic seismicity prediction models.

4.3 Summary and outlook

Microseismic swarms at Cerville-Buissoncourt are generally linked to caving processes at the cavity roof. However, the characteristics and origin of swarm production was neither understood nor discussed so far. In this context, the characteristics of the microseismic swarms were studied by various statistical approaches, whose results are summarized and discussed in the following.

The first major conclusion inferred from this study is that swarming sequence on short time

scales (in the order of seconds to minutes) and internal microseismic events can be treated and scaled in the same manner as natural earthquakes and widely demonstrate a self-similar scaling behavior (Aki, 1967). The individual microseismic events can be well approximated by a classical DC-model and ω^{-2}-model as usually applied for natural earthquakes (Chapter 3). Stress drops and apparent stress change insignificantly as compared to seismic moment and radiated energy (Fig. 3.27). Swarming sequences are dense event clusters in space and time and are formed by superpositions of individual microseismic events, whose entire duration systematically scales with its cumulative moment (Fig. 4.10). Hence, shorter swarming sequences are probably similarly constituted as longer ones, what indicates a similar underlying formation processes.

On the other hand, compared to tectonic earthquakes, the microseismic events at Cerville are less energetic as demonstrated by significantly lower stress drops (Fig. 3.27). Moreover, it seems that the seismic moment and the size of the rupture zone, produced by one individual event, is limited. This incapacity to sustain larger strains and to release larger stresses seems to be related to the mechanical constitution of the rock strata overlying the cavity (i.e. low strength materials) and is probably the origin of the swarming and superposition behavior. More popular spoken, such a swarming activity would probably also occur along tectonic faults at tectonic plate margins, when significantly accelerating the velocity of the moving tectonic plates. This increase in plate tectonic stress would not lead to a growth of fault and earthquakes size, but would increase the rate of rupturing. Thus, in order to release larger stress in form of cavity roof collapses, networks of smaller scaled, repeated rupturing faults are formed that seem to connect and interact (Fig. 4.15).

The formation of larger collapsing zones by these interacting fault networks, i.e. the cumulative behavior of swarming sequences, is comparable with the rupture process of rather slow natural earthquakes, where the cumulative moment increases with its duration by $\sim \tau^{1.9}$. The internal organization of the rupturing process can be understood as main shock-aftershock sequences in which each individual event triggers itself aftershocks. The spatial extent and duration of a swarming sequence seem to increase with increasing magnitude of the internal main shock. In turn, the potential to produce larger rupture events (larger moment) is dependent on the number of the preceding events, and thus depends on the density and connectivity of the pre-existing fracture network.

The internal mechanism, controlling small scale fault interaction and superposition and large

scale rupture formation, seems to be related to static stress transfer, where stresses accumulate at the crack tips, leading to continuous stress accumulations in a propagating rupture front (stick-slip mode) (e.g. Scholz, 2002). Evidence for this hypothesis comes from the spatial extent and density of aftershocks and its fast rate decay relative to the main shock. However, to prove this theory further investigations need to be done, comparing the obtained results with adapted quantitative seismicity prediction models, as e.g. the Epidemic-Type Aftershock Sequence Model (ETAS) (e.g. Zhuang et al., 2012), and seismicity models based on Coulomb stress calculations (e.g. Hainzl et al., 2010).

Moreover, the spatio-temporal and energetic distribution of swarming sequences, i.e. cavity roof collapsing events, document self-reinforcing caving dynamics in the crisis of 2008. The characteristic spacing and repetition of these swarming sequences in time is approximatively > 20 s, but changes temporally in the range $100 - 1000$ s, as adequately described by a varying lower recurrence mode. Accordingly, it was observed that these long-term seismic rates (lower recurrence mode) increase in periods of intensive roof collapses, as consistent with in-situ strain measurements and observation from brine level increases at the exploitation wells. Moreover, the maximum swarming sequences durations increased during the crisis, indicating that the collapsing events became larger with time. This is consistent with a continuous decrease in the b-value, as well as an exponentially increase of the cumulative seismic moment release. The increase in size of the collapsing events and moment release might be generally related to an increasing fractured state of the cavity roof, allowing for larger rupture zone formations.

In addition, these self-reinforcing caving dynamics seem to be linked to the geometry of the cavity structure and the NNW-SSE trending salt solution exploitation setting. Such a scenario was visualized by the spatio-energetic distribution of seismicity with time in the crisis in 2008, assuming that the seismic rate is approximatively proportional to the rate of detached rock volume. The results of this analysis demonstrated that an increase in the vertical extension of the cavity structure, at some point, will lead to a lateral growth in order to rebuild the natural equilibrium associated with the most stabilizing geometry. This behavior is similar to observations from mining and tunnel construction mechanics, where an excavated zone, exposed to an externally applied stress field, has potentially a most stable state associated with a specific geometry depending on the properties of the surrounding rocks (e.g. strength, heterogeneities).

All these observations and results demonstrate that microseismic monitoring can be a powerful tool in order to validate the degree of stability and the caving rates of a cavity system, and therefore might be used in future as a useful routine in salt solution exploitation mines. Further investigations are currently performed to improve the understanding of the governing caving dynamics and the underlying mechanisms. In this context, the relationship between the microseismic rate and in-situ deformation measurements, as well as seismic broadband observations, will be examined in more detail to clarify the question about the representativeness of microseismicity with respect to certain deformation mechanisms. Moreover, additional statistical analysis is performed to better constrain the spatio-temporal and energetic distribution of important cavity roof collapsing events and the underlying mechanism of collapse interaction.

Chapter 5

Microseismic evolution (from caving to collapse)

This chapter aims to discuss eventual changes of the microseismic signature associated with the collapsing period of the cavity in February 2009 compared to the period of 2008. Such a comparison helps to evaluate previous results and interpretations and the hazard assessment potential of microseismic monitoring in the collapsing period (Fig. 1.8 and Section 1.3.3.2). In this context, I applied the methods, developed for the period in 2008, to the collapsing period and documented the principal similarities and differences between both periods (Section 5.1). This analysis focused on the period before and during the Dolomite failure in order to detect eventual changes or precursor phenomena in the microseismic regime during the pre-collapsing phase of the cavity system. These results are then summarized and discussed in the light of previous studies describing the characteristics and dynamics of the cavity collapsing scenario (Section 5.2).

5.1 Principal observations

In order to discuss the evolution of the collapsing period in 2009, I classified the collapsing stages in four major periods (Fig. 1.8 and 5.1): (i) the first pumping stage associated with the initialisation of brine pumping on the 10th February 2009, (ii) the second pumping stage, where pumping was restarted the 11th February around 4:00 a.m. UTC after the first pumping stage was stopped on the 10th February around 12:00 a.m. UTC, (iii) the third pumping stage, which starts with the stop of the second pumping stage associated with a significant increase in the brine level (iv) and a last period associated with the failure of the Dolomite layer. The failure of the Dolomite layer is marked by the breakdown of geophysical instruments installed in this layer and by a subsequent significant increase in the subsidence rate of the overburden.

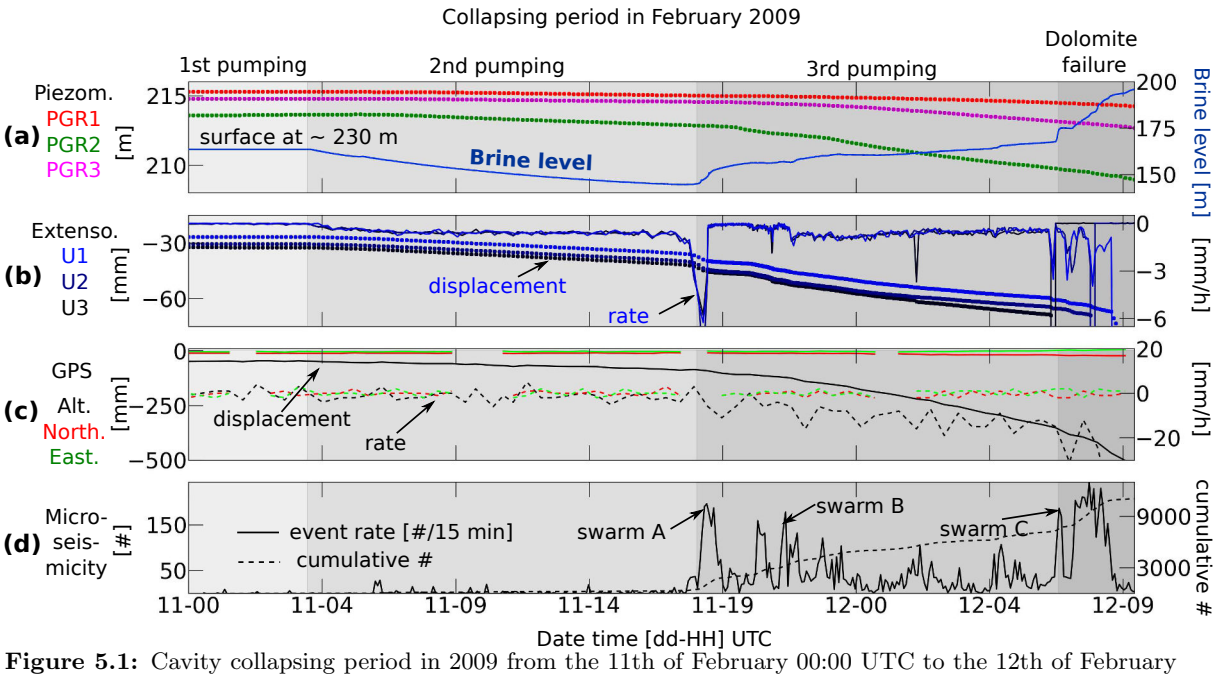

Figure 5.1: Cavity collapsing period in 2009 from the 11th of February 00:00 UTC to the 12th of February 10:00 UTC. Shown are the (a) brine level measured at the exploitation wells and piezometric data (Fig. 1.4), (b) extensometer data measuring the displacement U relative to a reference point at the surface at three anchor points fixed above (U_1), within (U_2) and below (U_3) the Dolomite layer (Fig. 1.4 and 1.5d) given in displacement (blue points) and displacement rate (blue lines), (c) the GPS data (Fig. 1.4) and (d) the microseismic event catalogue obtained by using the polarization-based approach for event detection (Section 2.6).

As introduced in Section 1.3.3.2 and Figure 1.8, during the first two pumping stages, only some few microseismic events and hydroacoustic activity and only small changes in the subsiding rates of the GPS and extensometers ($\sim 2-4$ mm/hour) have been observed (e.g. Cao, 2011, Contrucci et al., 2011, Daupley et al., 2013, Lebert et al., 2011) (Fig. 5.1). The beginning of the third pumping stage was initiated by a significant deformation at the strata overlying the cavity roof, occurring the 11th of February at $\sim$ 18:30 UTC. In addition, the brine level rapidly increased despite to continuous pumping, indicating the generation of significant cavity roof falls (e.g. Contrucci et al., 2011) (Fig. 5.1a). The subsiding rate of the overlying roof strata, including the Dolomite layer, had a maximum of $\sim$ 6 mm/hour (Fig. 5.1b). This collapsing period was accompanied by a significant increase in microseismic and hydroacoustic activity (e.g. Cao, 2011, Contrucci et al., 2011, Daupley et al., 2013, Lebert et al., 2011) (Fig. 5.1d).

In the following period, the displacement rate returned almost to its initial rate and also the microseismic activity relatively decreased, meanwhile the subsidence rate, measured by the GPS at the surface, started to increase (Fig. 5.1c). In addition, this period is associated with a decrease in the hydroacoustic pressure of the aquifer or ground water conduit as

observed from piezometric measurements (Fig. 5.1a). The pressure release is most significant at piezometer PGR2, whose location agrees in latitude with the center of the cavity zone (Fig. 1.4 and 5.1a). This observation might indicate that the overburden and the aquifer over the cavity structure entered into a advanced fractured state leading to a penetration of ground water to more important depth.

The period of the Dolomite failure, similarly to the third pumping stage, was initiated by an abrupt change in the subsiding rate as documented by the extensometer data (Fig. 5.1b), as well as by a significant increase in microseismic activity (Fig. 5.1d). The Dolomite did not ruptured and collapsed at once, but failed successively, in a period lasting around two hours, as seen by the successive breakdown of the extensometer stations and long lasting microseismic activity.

5.1.1 Presence of microseismic swarms

Generally, the temporal and spectral signatures of the recorded microseismic events in the collapsing period in 2009 do not differ to the microseismic data recorded in 2008. As a result, periods of strong microseismic activity (Fig. 5.1) are also associated with dense microseismic swarms with similar spectral characteristics (Fig. 4.14 and 5.2). Hence, from a first simple signal inspection, it seems that swarms in 2009 are generally formed by very similar dynamics as discussed for swarms observed in 2008 (Chapter 4).

The similarity of swarm examples of 2008 and 2009 is furthermore indicated by similar spatio-temporal epicenter migration trends (Fig. 2.18-2.21 and 5.3). Event detection and locations were obtained by using the polarization- and amplitude-based location approach in the same manner as done for swarm sequences in 2008 (Section 2.5). Since no re-calibration procedure was performed for the amplitude-based approach, but attenuation might have been changed (see the following Section), absolute location errors might be generally larger as compared to the ones found for swarms in 2008. However, relative temporal locations changes between the individual events should not be significantly affected.

Some difference in the signature between the swarms in 2008 and 2009 seem to appear when comparing the normalized traces (maximum normalization) for the vertical component of station 63 (Fig. 4.14 and 5.2). Swarms in 2009, especially swarm B and C (Fig. 5.2), show significantly more energetic event peaks over the entire swarming sequence as compared to previously recorded swarming sequences where internal seismic event size seems to be more

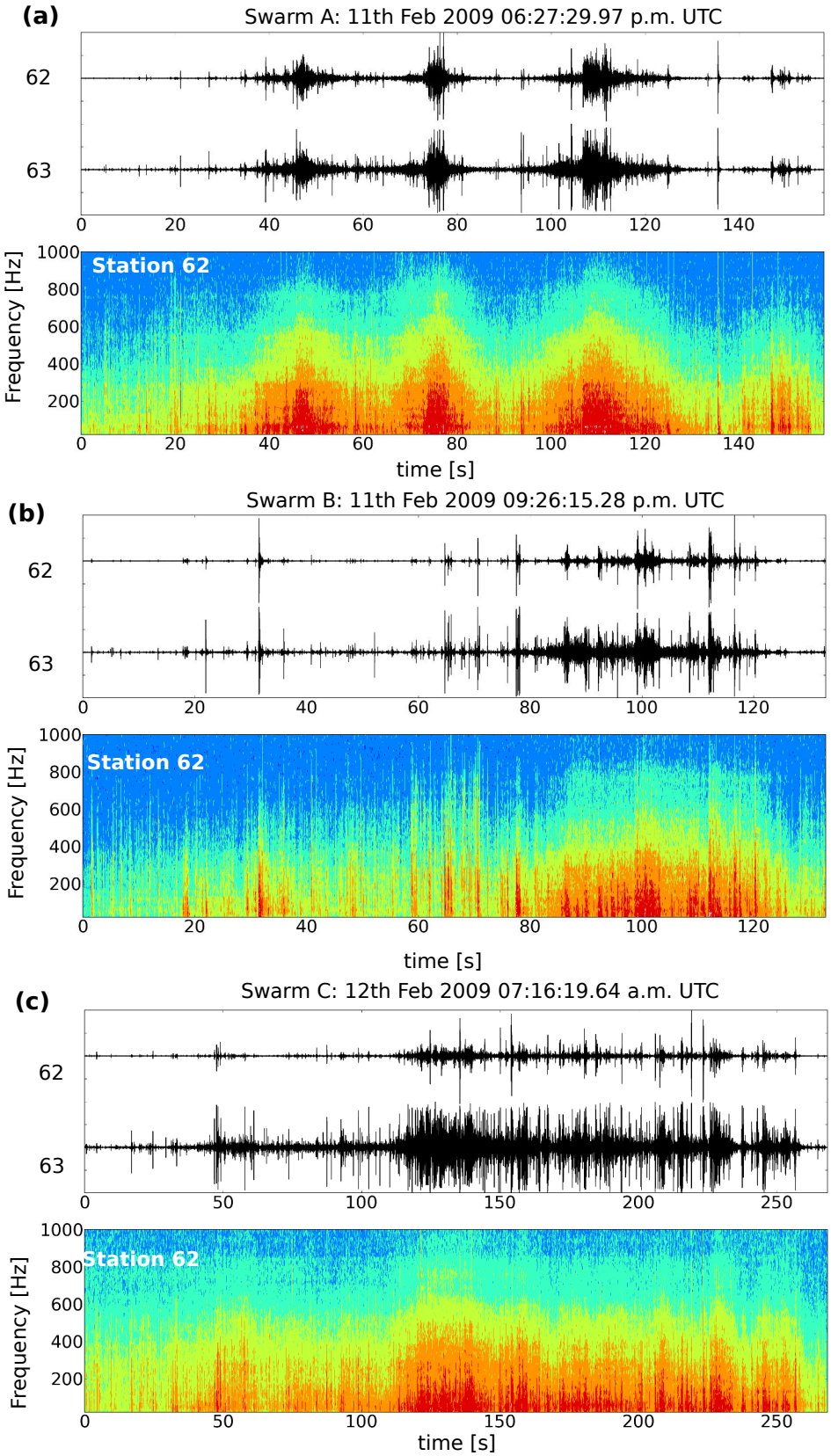

Figure 5.2: pectrograms of swarming sequences in 2009. (a)-(c) Examples of three principal swarming sequences recorded during the peaks of microseismic activity during the collapsing period in 2009 (Fig. 5.1d). Seismic velocity traces are shown for the vertical components of stations 62 and 63. Spectrograms were calculated using a 0.15 s window length with 90% overlap, while intensities are presented in a normalized dB scale for seven distinct contour levels (colored scale)

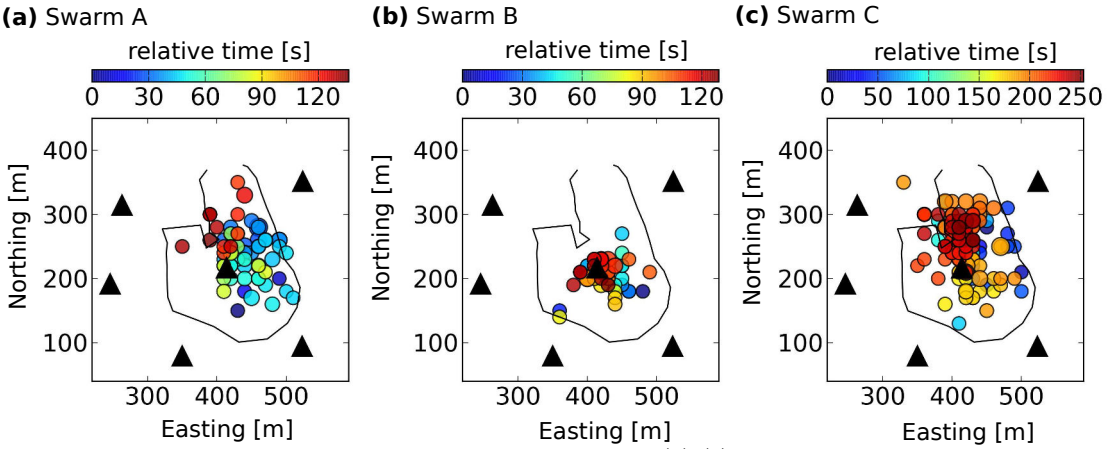

Figure 5.3: Epicenter location of swarming sequences in 2009. (a)-(c) Epicenter locations, obtained from the polarization- and amplitude-based approach (Section 2.6), as a function of time (color bar) shown for three major swarming sequence A-C recorded in February 2009 (Fig. 5.2)

dynamic and variable. This behavior is related to the instrumental saturation, where event peaks are often clipped so that the actual dynamic range between the different event peaks is not visible anymore. Clipping or instrumental saturation could be also observed for some large microseismic events close to station 63 recorded in 2008, as for instance event A in Figure 3.25 and 3.28), which have magnitudes of close to one. These observations indicate that swarms observed in 2009, temporally onwards from swarm A, are very close to station 63 or/and contain generally large internal events associated with magnitudes close to one.

5.1.2 Spatio-energetic distribution and attenuation changes

The location results of the collapsing period in 2009 are summarized in Figure 5.4. For detection and location, I used the same procedure as applied for the data of 2008 (Section 2.6). In Figure 5.4a, the spatio-energetic distribution was calculated for $\sim$ 5700 events, detected during the third pumping stage and the Dolomite failure period. From the comparison to the results of the period in 2008 (Fig. 2.25), no significant differences in the spatio-energetic distribution can be observed. Correspondingly, the period in 2009 is characterized by the same major seismogenic zone located in the transition zone, lying between the highest cavity roof extension to the E-S-E and the lower cavity roof extension to the W-N-W. In addition, the spatio-energetic distribution clearly reshapes the later collapsing zone at the surface (Fig. 2.25).

Epicenter location and migration trends are very similar to the period in 2008 (Fig. 2.25 and 5.4). In contrast, measured incidence angles at station 62 become commonly larger, more horizontal, in 2009 compared to 2008 (Fig. 5.4). The increase in incidence angles in

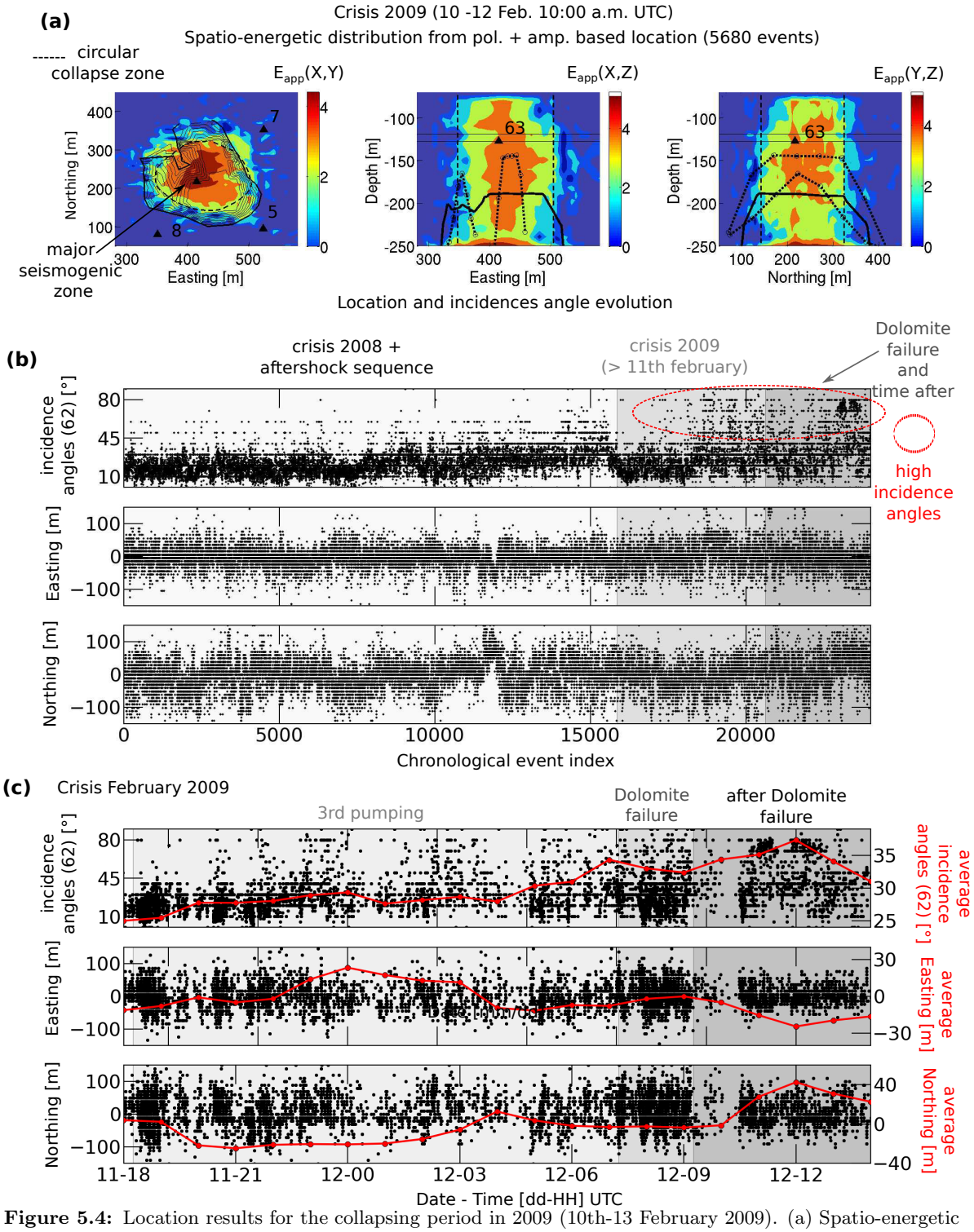

Figure 5.4: Location results for the collapsing period in 2009 (10th-13 February 2009). (a) Spatio-energetic distribution of microseismicity obtained from the polarization- and amplitude-based approach (Section 2.6), calculated in the same manner as done for the period in 2008 (Fig. 2.25 and Section 2.6.3). (b) (upper panel) Incidence polarization angles observed from station 62 and nothing (lower panel) and easting (middle panel) relative to the mean location for all microseismic events detected in the period from 3rd of March 2008 to the 13th February 2009 as a function of chronological event index. (c) (upper panel) Incidence polarization observed from station 62 and nothing (lower panel) and easting (middle panel), shown as a function of time for the collapsing period in 2009 until the Dolomite failure period.

2009 clearly documents an increase in average source depth. Very large incidence angles with $\gtrsim 80°$ indicate microseismic event occurrences in the overburden above the Dolomite layer. Assuming a maximum expected epicentral distance of 200 m to station 62 and an incidence angle of 80°, source depth will be approximatively 35 m below station 62, what is in the overburden above the Dolomite layer.

More insights into the evolution of source depth are given from the peak-to-peak amplitude ratios of the Z components of stations 62 and 63 (A_{62}/A_{63}) for microseismic events located directly below both stations (Fig. 5.5). As stated in Section 2.3.2, for microseismic events located below both stations, the Z components of stations 62 and 63 generally contain predominantly P wave energy and similar wave forms. Moreover, refraction related multiple P-SV conversions and wave superpositions observed in the Z component at station 63 can be excluded in this case (Fig. 1.14). Hence, assuming consistent P wave constitution at both stations and considering Equation (2.11), it can be assumed that event locations close to station 63 (i.e. shallow source depths) are indicated by smaller A_{62}/A_{63} ratios than deeper located events. These changes in the amplitude ratio principally result from difference in geometric spreading observed at both stations.

The amplitude ratios shown in Figure 5.5 were calculated for the vertical components, for a low and high frequency band (i) $30-90$ Hz (red points) and (ii) $100-300$ Hz (blue points), respectively, considering a total set of ~ 530 events occurring in 2008 and 2009, which are all associated with vertical incidence angles of 0° measured at station 62. In the period of 2008, the A_{62}/A_{63} ratios seem to decrease almost continuously for both frequency bands reflecting the growth of the cavity roof and the implied decrease in source depth (Fig. 1.7 and 5.5). In the period of 2009, the ratios for both frequency bands show an abrupt decrease, where ratios for the higher frequency band decrease significantly more compared to the low frequency band (Fig. 5.5a,c). This tendency is further illustrated when considering the ratio of the amplitude ratio for the low and high frequency bands $\frac{(A_{62}/A_{63})_{30-90\text{ Hz}}}{(A_{62}/A_{63})_{100-300\text{ Hz}}}$ (black crosses in Figure 5.5), which significantly increase in the period of 2009. The general decrease of both ratios, namely the low and high frequency band, generally indicate a further decrease in source depth (Fig. 5.5). However, the departure of amplitude ratios for the low and high frequency bands clearly documents the presence of changing attenuation characteristics of the sedimentary layer located between station 62 and 63.

These attenuation changes were studied in more detail by using the cross-correlation and

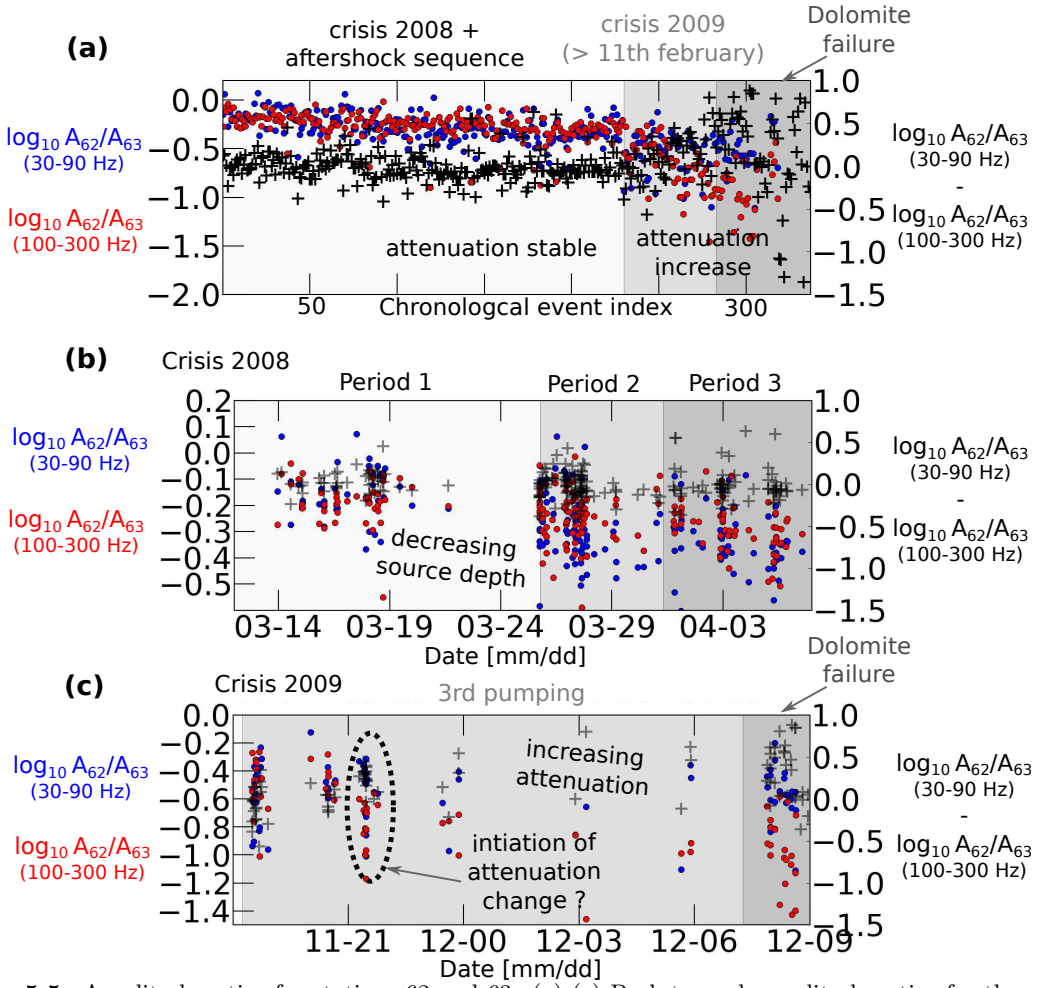

Figure 5.5: Amplitude ratios for stations 62 and 63. (a)-(c) Peak-to-peak amplitude ratios for the vertical component of stations 62 and 63 for events associated with an incidence angle of 0° at station 62, shown for: (a) the period from 3rd of March 2008 to the 13th February 2009 as a function of chronological event index, (b) for crisis in 2008 and (c) the collapsing period in 2009.

spectral ratio approach, introduced in Section 2.3.2, in order to directly measure the temporal changes in P and S wave velocities and Q-factors of the sedimentary layers located between stations 61, 62 and 63. The inferred velocities and Q-factor are presented in Figure 5.6, and document a consistent allover decrease in the period of 2009. Seismic velocities, independent of P or S waves decrease by approximatively 7%, while Q factors decrease by around 75%. It must be noted that the decrease of Q-factors is somewhat overestimated, because constant velocities of the period in 2008 were used for calculation (Table. 2.2) so that the actual velocity changes were not taken into account.

Taking these results together, it can be concluded that microseismicity associated with the third pumping stage period and Dolomite failure period in 2009 is generally characterized by similar spatio-temporal distribution as compared to the period in 2008. This observation

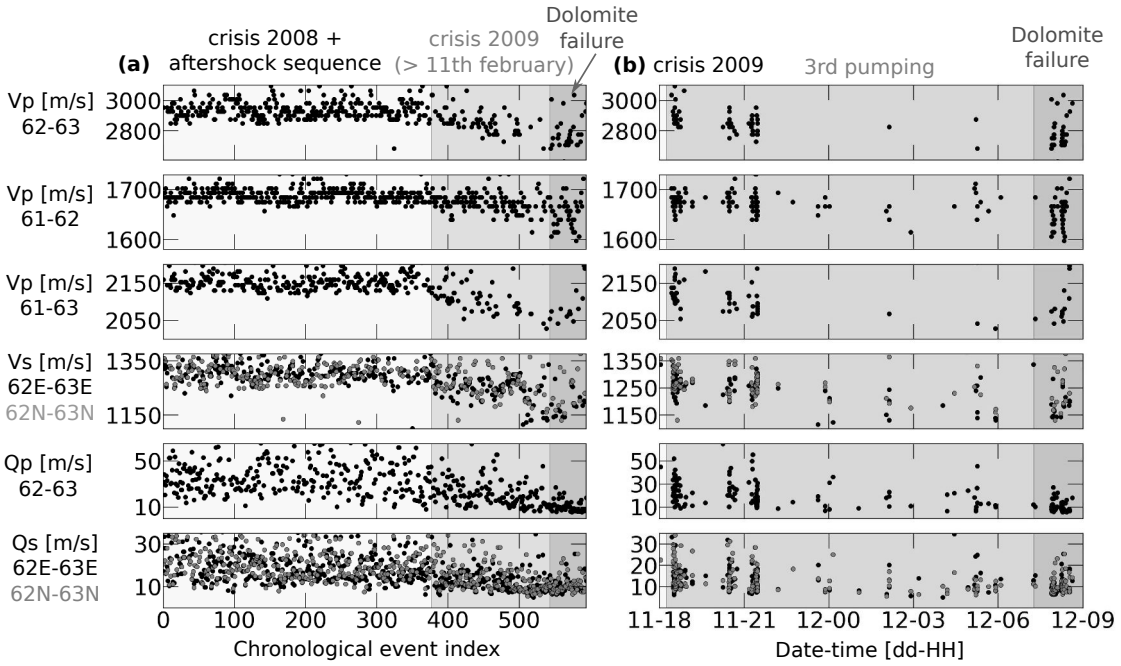

Figure 5.6: Velocity and Q factor evolution. (a)-(b) Velocities and Q-factors are estimated for events associated with an incidence angle of 0° at station 62 and by using the cross-correlation and spectral ratio approach described in Section 2.3.2.2 and shown for (a) the period from 3rd of March 2008 to the 13th February 2009 as a function of chronological event index and (b) for the collapsing period in 2009.

indicates that cavity roof collapses and caving processes follow similar dynamics in 2008 and 2009. In contrast, microseismic activity in the period of 2009 clearly involved significant rupture and fracture processes in the overburden above the Dolomite layer. This observation is consistent with the observed decrease of the hydrostatic pressure in the aquifer located at around 30 m depth (Fig. 5.1a). Accordingly, ground water drainage probably occurred along the newly formed fractures in the overburden. In turn, the observed attenuation changes in the overburden (Fig. 5.6) possibly results from both, the increased density of fractures and heterogeneities as well as ground water inflow and increasing water saturation of the pore spaces.

Furthermore, the documented changes in the attenuation characteristics as well as similar results in event locations for 2008 and 2009 indicate that the location approach based on amplitudes is not significantly affected or biased by these attenuation changes. The robustness of the amplitude-based approach with respect to observed attenuation changes was moreover confirmed by comparing the epicenter locations obtained from the polarization-based approach with the ones obtained from the amplitude-based approach. By this comparison, it was found that the average deviation between the estimated epicenter locations for both approaches remain generally constant over time.

5.1.3 Temporal-energetic distribution

A useful temporal characterization of the microseismic rate was presented based on inter-event times in Chapter 4. By this method, two distinct recurrence modes could be identified: (i) a higher recurrence mode, stable over time, who demonstrates strong spatial event clustering and swarming on short time scales ($\gtrsim$ 20 s) associated with roof collapsing events and (ii) a lower recurrence mode, who characterize the temporal occurrences and repetitions of these swarms and cluster over times (Fig. 4.5 and 4.6).

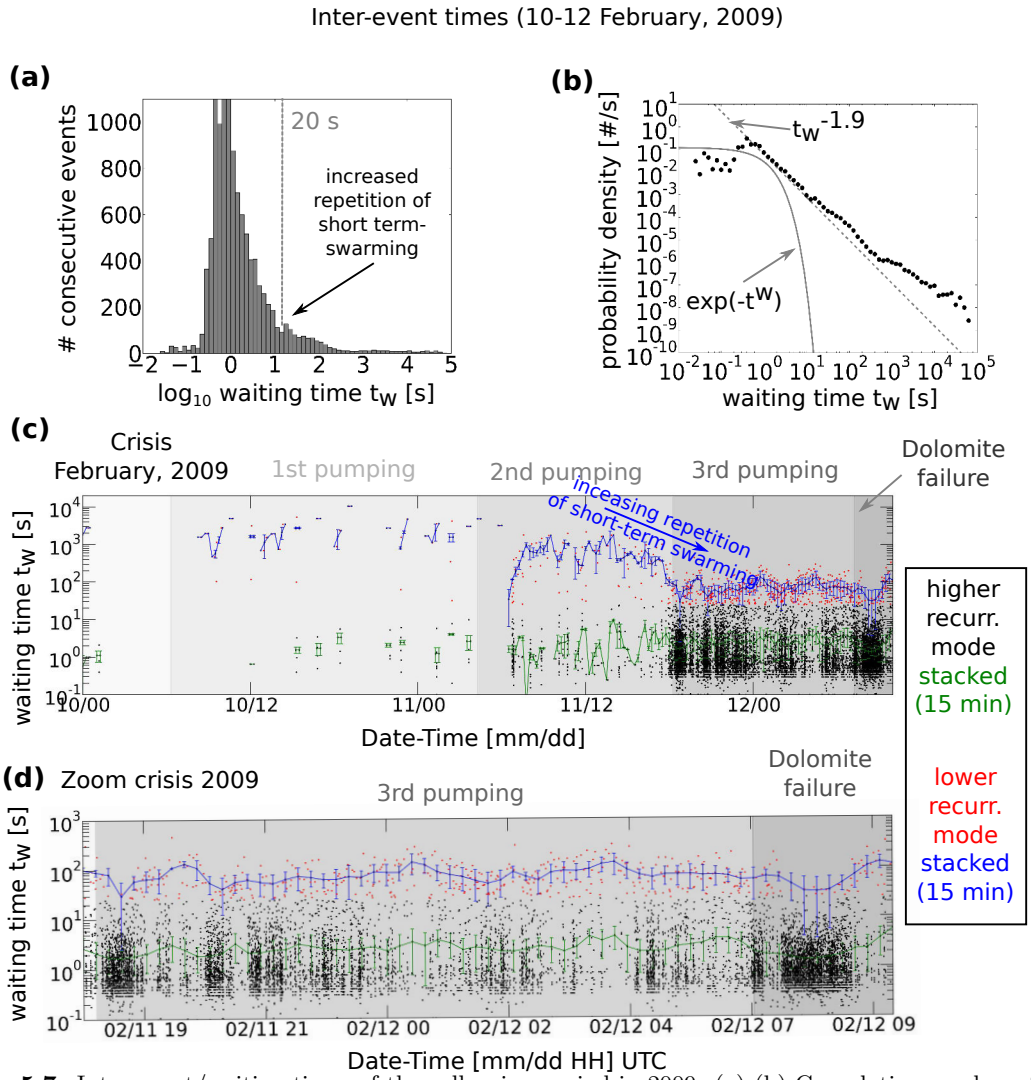

Figure 5.7: Inter-event/waiting times of the collapsing period in 2009. (a)-(b) Cumulative number of inter-event times (see also caption Fig. 4.5) and (c)-(d) inter-event times shown as a function of time (see also caption Fig. 4.6).

In the same manner as for 2008, I calculated the inter-event times for the period in 2009 as shown by Figure 5.7. From the obtained temporal distribution of inter-event times, it can be clearly observed that the low recurrence mode significantly decrease towards the third

pumping period (Fig. 5.7b). This observation indicates that the temporal repetition rate of swarming sequences, i.e. roof collapsing events, is significantly higher in 2009 with dominant recurrence times of $\lesssim 100$ s (Fig. 5.7). In 2008, the dominant recurrence times lied around $100 - 1000$ s (Fig. 4.5, 4.6). As a result, the low recurrence is not very well distinguishable from the higher recurrence mode (Fig. 5.7), since swarming sequences appear close to each other in time at different regions in the cavity structure and partially probably overlap. Consequently, the caving dynamics in the crisis in 2009 seem to be significantly accelerated compared to 2008. In other words, the entire cavity system seems to be entered into a prone-to-collapse state, where the system is continuously resonating and evolving until its total collapse is reached.

In addition, it can be shown that the governing collapsing dynamics are of self-reinforcing nature as very similar to the ones observed in 2008. Consistently, no apparent difference between the period in 2008 and 2009 can be observed when regarding the frequency-magnitude distribution, which seems to follow a very similar GR law characterized with a b-value of around 1.1 (Fig. 5.8). Thus, the underlying physical collapsing dynamics seem to be generally similar for both crisis. Furthermore, the b-values calculated for the third pumping stage and the period of Dolomite failure decrease, which is consistent with the results of Cao (2011) and Contrucci et al. (2011). Interestingly, the b-value associated with the Dolomite failure period is estimated with 0.5, which is similar to b-values estimated for periods preceding larger tectonic earthquakes, indicating a critical phase before main rupture (e.g. Main et al., 1989). Next to this significant decrease in the b-values, also an exponential increase in the cumulative seismic moment as a function of the chronological event index is observed, described by a power law of $\sim i^{1.25}$ (Fig. 5.9). This functional relationship indicates that the mean seismic moment release is approximatively $\langle M_0 \rangle \propto i^{1/4}$, what is clearly stronger as compared to the crisis in 2008 (Fig. 4.18).

Concluding these results, the governing caving dynamics seems to be of similar nature for 2008 and 2009, while the collapsing processes in 2009 seem to be accelerated compared to 2008. This hypothesis is supported by the observation that the constitution of swarming sequence seem to be similar. Correspondingly, the swarming sequences showed similar spectral characteristics, similar epicenter migrations trends and the same temporal clustering characteristics associated with a power law of short-term inter-event times of $t_w^{-1.9}$. In addition, the estimated GR law is similar compared to 2008. However, this issue needs to be tested in

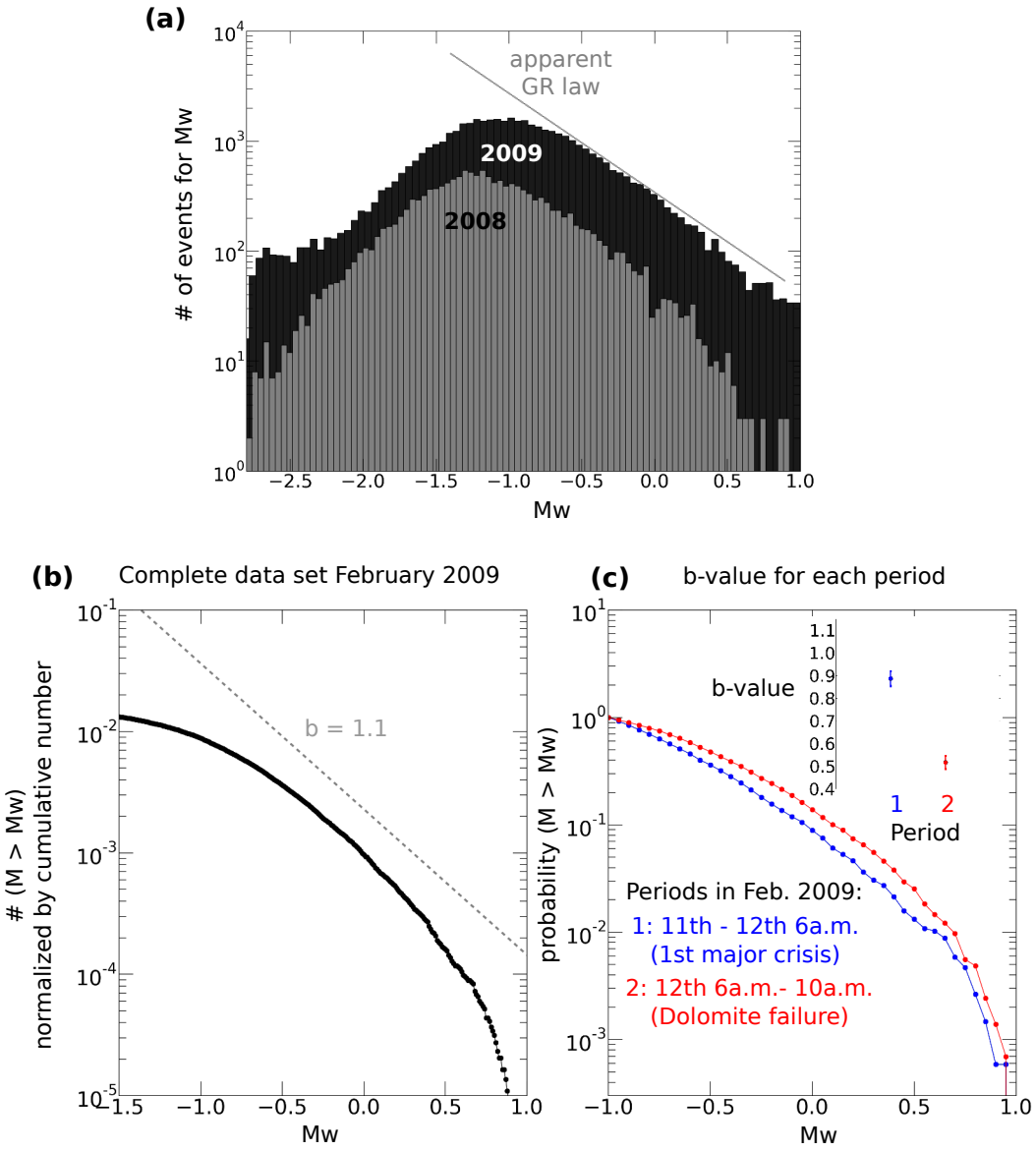

Figure 5.8: Frequency-Magnitude distribution of the collapsing period in 2009. (a) Cumulative number of moment magnitudes shown for the crisis in 2008 (March-April) and 2009 (10th-13 February 2009). (b) b-value for all events and (c) b-values calculated for the third pumping stage and the Dolomite failure period (see also caption of Fig. 4.17).

future research. It need to be clarified if the collapsing processes in 2009 can be interpreted as a simple acceleration of the caving processes observed in 2008 or whether there is an intrinsic difference in the caving dynamics. For example, it need to be ruled out if the increased production of larger magnitude events ($M_w \gtrsim 0$) in 2009 (Fig. 5.8a) can be explained by an acceleration of the dynamics in 2008 or if the collapsing dynamics became more energetic in 2009.

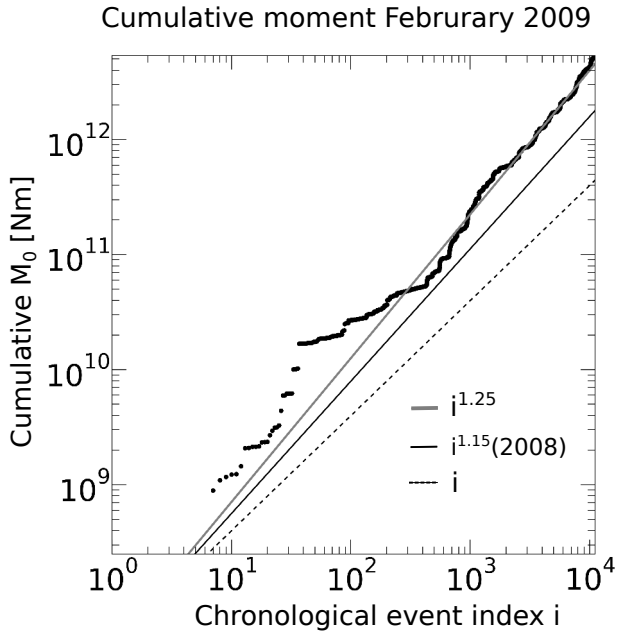

Figure 5.9: Cumulative seismic moment of the collapsing period in 2009 shown as a function of chronological event index (see also caption of Fig. 4.18).

5.1.4 Source mechanism

Next to similarities in the spatio-temporal energetic behavior of the crisis in 2008 and 2009, also source mechanisms seem to be similar. The most dominant source mechanisms of the crisis in 2009 are shown by the SV-P and SV-SH amplitude ratios for station 5 and 62 in Figures 5.10, 5.11 and 5.12. The observed and synthetic amplitude ratios were estimated by the same procedure as applied for the events in 2008 (Fig. 3.10, Section 3.2.3). The amplitude ratios are shown for the entire data set of 2009, the third pumping period and the Dolomite failure period, including all events for which polarization angles were available (Fig. 5.10, 5.11 and 5.12).

For all the three presented data sets and periods, an almost consistent distribution of the amplitude ratios can be observed, indicating a stability of a predominant mechanisms associated with a *ds* faulting mode (Fig. 3.10, 5.10, 5.11 and 5.12). Moreover, the amplitude distribution for station 62 resolves even better the underlying source mechanism, since more observations from higher incidence angles were available (Fig. 5.4). As a result, the presented fit between the observed and synthetic ratios could be even improved by considering a smaller dip of 35° for the modeled "trial" mechanism (Fig. 5.10, 5.11 and 5.12) as for the period in 2008 (45°) (Fig. 3.6). This change in dip, and thus slight deviation from an ideal *ds* mechanism, is consistent with *solution 2* of the inversion approach 1 in Section 3.2.4.1, which was obtained from classical source inversion. In addition, as already discussed in Fig-

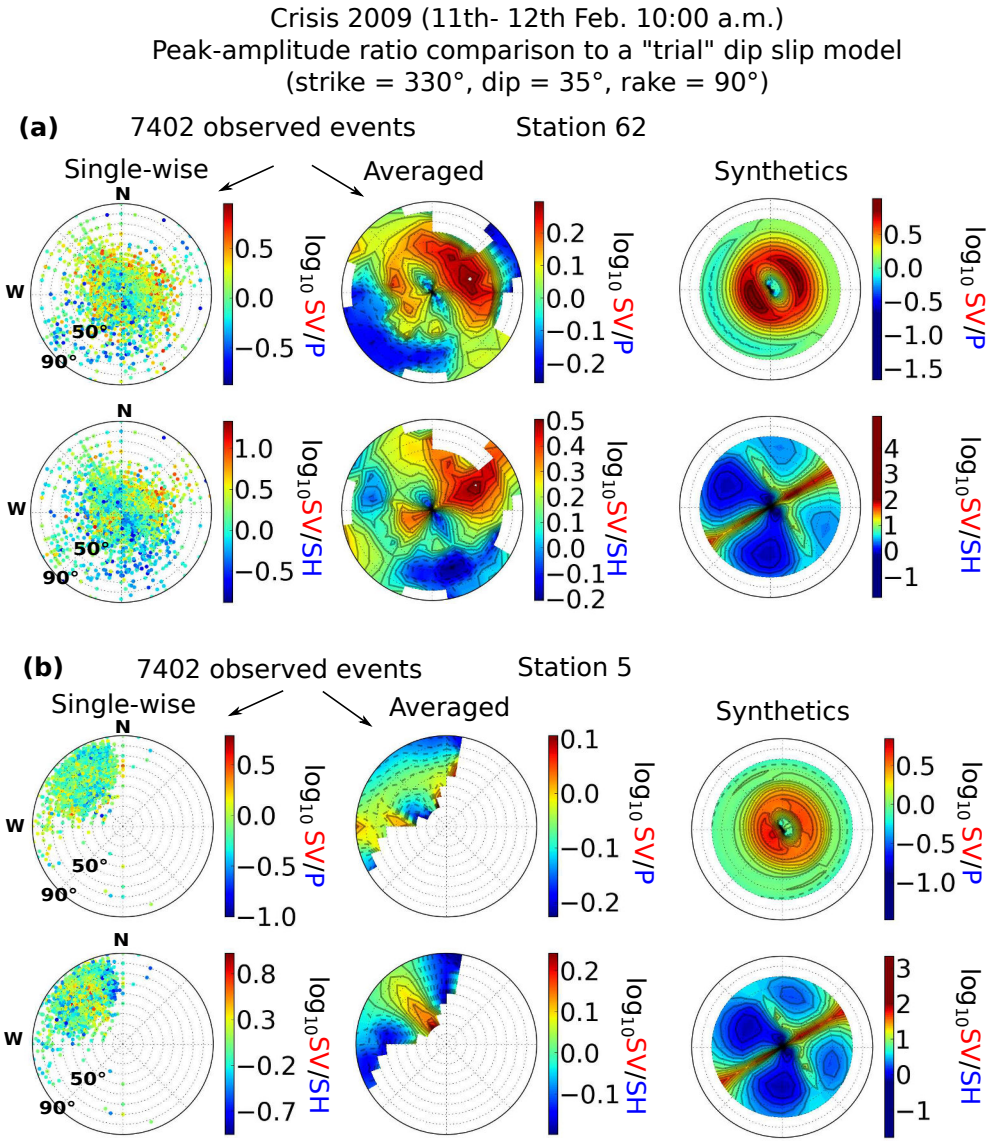

Figure 5.10: Observed and synthetic amplitude ratios for P, SV and SH waves of the collapsing period in 2009 (10th-13 February 2009). For further description of the calculation procedure see Figure 3.10 and Section 3.2.3.

ure 3.22 and Section 3.3, also the P wave detection capacity seems to be strongly controlled by the stability in mechanism and radiation pattern. This dependency can be clearly seen from the distribution of available and non-available backazimuth and incidence angles in the stereo-plots, especially well observable in Figure 5.11.

The average of SV-P and SV-SH amplitude ratios (middle stereo-plots) during the Dolomite failure period are in good agreement with the proposed "trial" *ds* mechanism (leftmost stereo-plots), however the amplitude ratios considered for each individual event (rightmost stereo-plots) seem to be more scattered (Fig. 5.12), compared to the preceding period (Fig. 5.11)

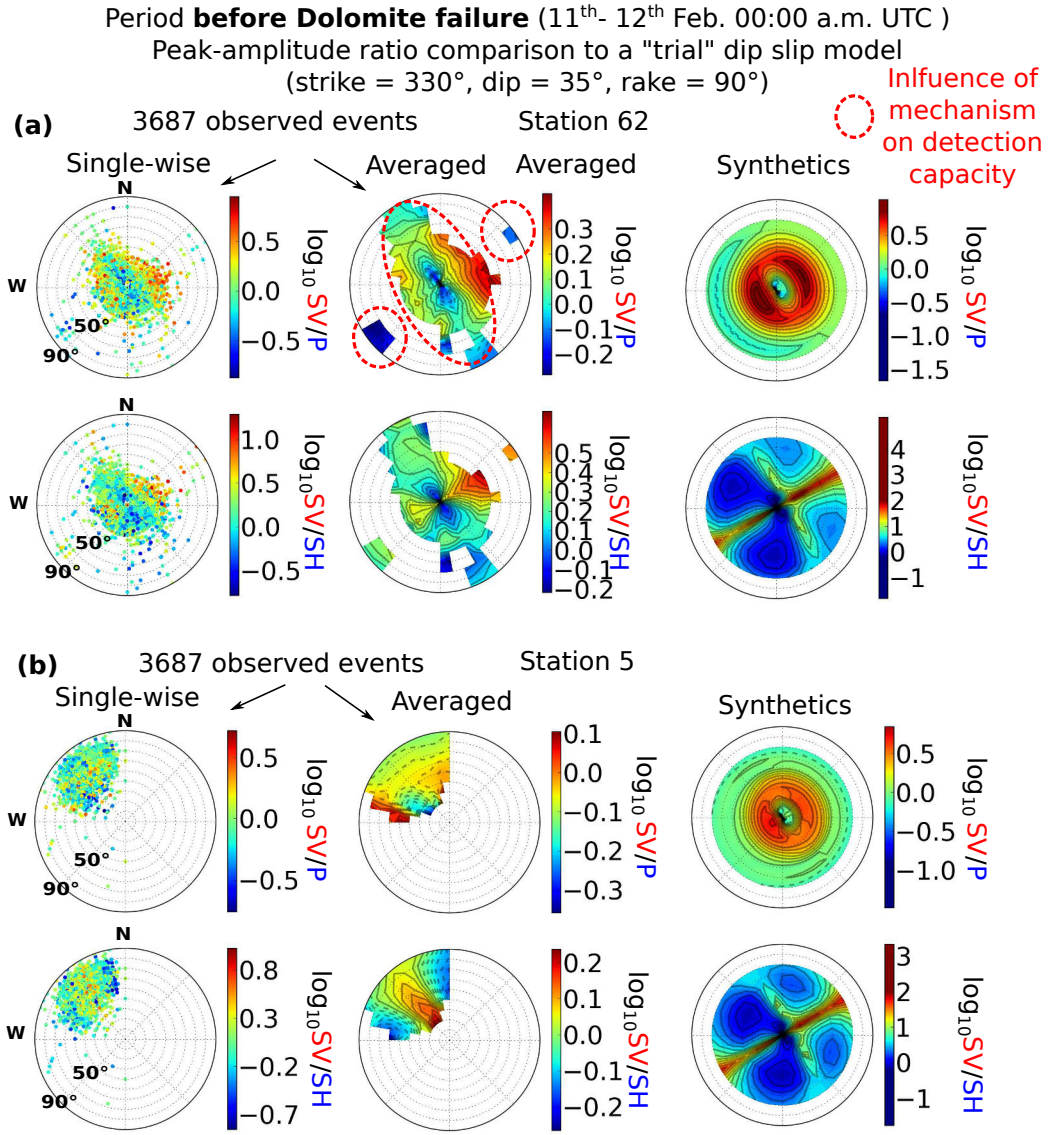

Figure 5.11: Observed and synthetic amplitude ratios for P, SV and SH waves of the third pumping stage 11th February 06:00 p.m. UTC to 12th February 2009 07:00 a.m. UTC. For further description of the calculation procedure see Figure 3.10 and Section 3.2.3.

and the for the crisis in 2008 (Fig. 3.10). This more scattered amplitude ratio distribution might be explained by increasing instability and movements of the installed stations and inaccuracies in the polarization angles, since the overburden becomes unstable during this period as a result of an increased fracture density and an increasing subsidence rate. However, also changes in the fault orientations, strike, of the predominant *ds* faulting mode cannot be completely excluded in this case. On the other hand, the predominance of a *ds* mechanisms is demonstrated by the distribution of T/ZR amplitude ratios for the Dolomite failure period (Fig. 5.13). Regarding the T/ZR ratio distribution, there is no event associated with an abnormally high or low amplitude ratio that deviate significantly from the general *ds* DC

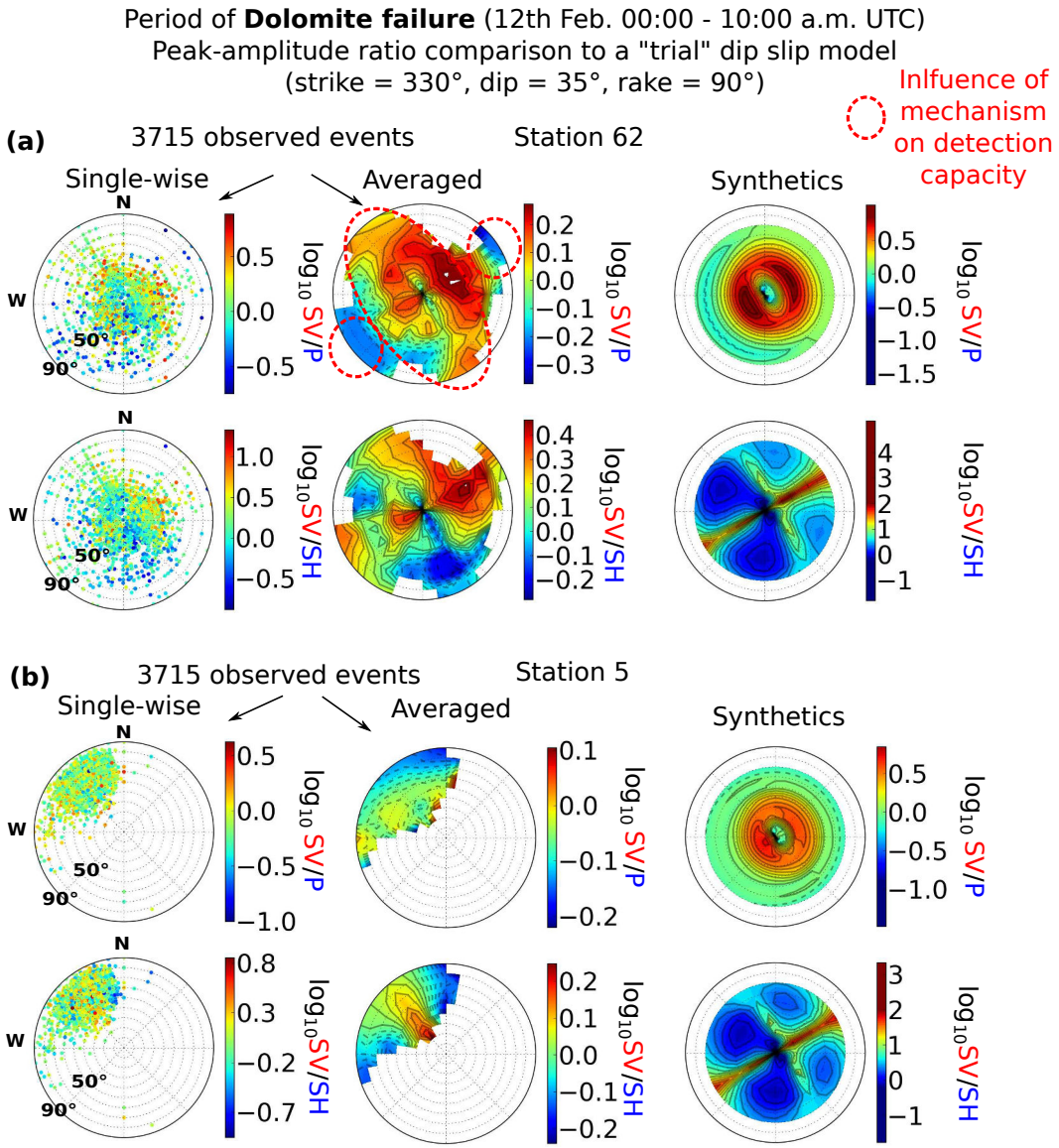

Figure 5.12: Observed and synthetic amplitude ratios for P, SV and SH waves of the Dolomite failure period 12th February 2009 07:00-10:00 a.m. UTC. For further description of the calculation procedure see Figure 3.10 and Section 3.2.3.

solution tendency.

Regarding this consistency in source mechanisms, as well as the results from spatio-temporal energetic analysis, it can be concluded that the deformation and collapsing behavior of the Dolomite layer is generally very similar compared to the behavior observed in the underlying Marls as mainly analyzed for the period in 2008 (Chapter 4). This consistency in the deformation behavior of both geological units is somewhat surprising, since both rock types are associated with very different elastic strength. The Dolomite layer is supposed to follow a typical elastobrittle deformation behavior as indicated by a high Young's modulus around

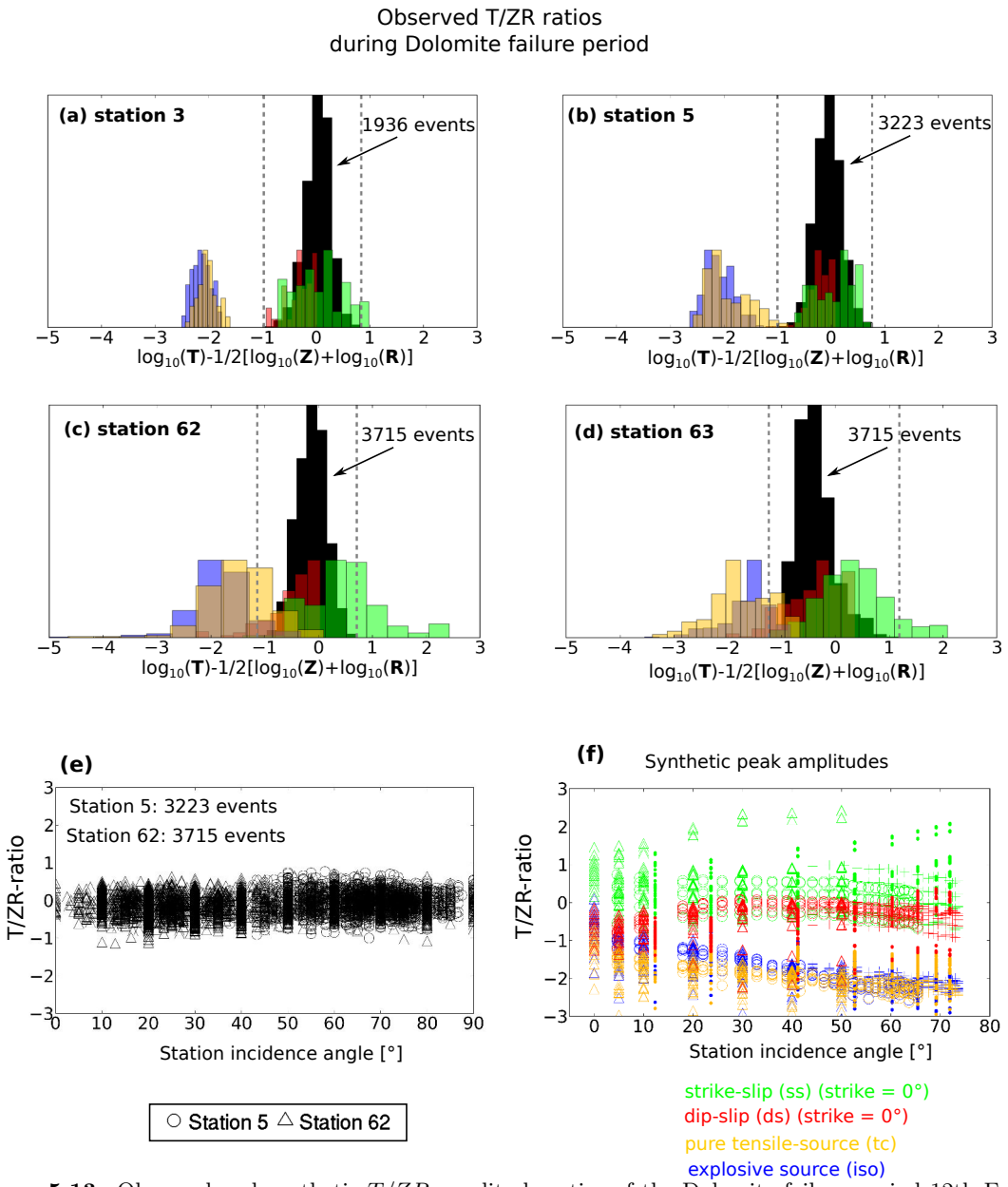

Figure 5.13: Observed and synthetic T/ZR amplitude ratios of the Dolomite failure period 12th February 2009 07:00-10:00 a.m. UTC. For further description of the calculation procedure see Figure 3.7 and 3.9.

80 GPa, whose high strength keeps the overburden stable and favors the creation of large salt caverns in the study region (e.g. Mercerat, 2007, Nothnagel, 2003). In contrast, the underlying Marls are characterized by a clearly smaller Young's modulus of around 15 GPa ,and therefore are supposed to show a more plastic or ductile deformation behavior.

A difference in the deformation behavior of both geological units is reflected in the temporal distribution of the apparent stress as shown in Figure 5.14. Correspondingly, the apparent stress seems somewhat more elevated in the third pumping stage and in the Dolomite failure

period as compared to the period in 2008. Such changes in apparent stress are diagnostic in mines to indicate seismic rupturing associated with different geologies or rock units (e.g. Mendecki, 1996). Hence, in this case it seems possible that the increase in apparent stress represents the increasing deformation around the stiff Dolomite layer, producing more energetic seismic events.

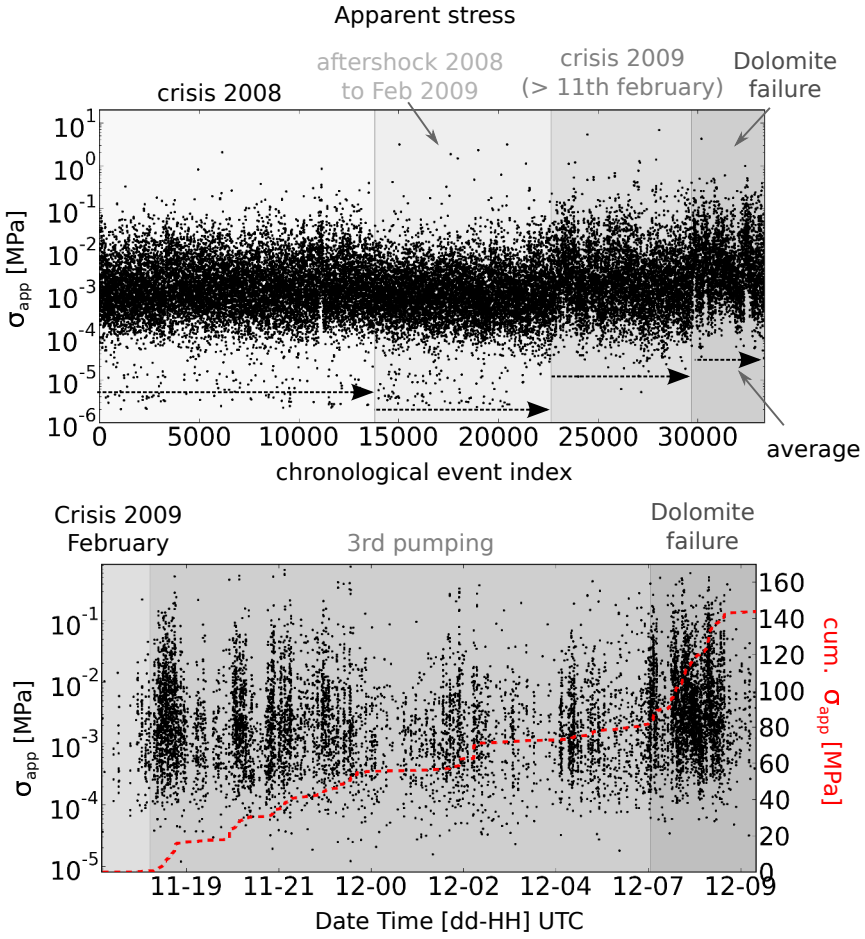

Figure 5.14: Apparent stress evolution. Apparent stress, calculated by the method described in Section 3.4, shown as a function of (a) the chronological event index and (b) time for the third pumping stage and Dolomite failure period in 2009.

On the other hand, the predominant mode of shearing contradicts with previous mechanical models. In a mechanical simulation based on classical beam theory, it was shown that the deformation and collapse of the Dolomite should be associated with a predominant mode of traction in the center of the cavity structure (Mercerat, 2007). Apart from the coherence that microseismicity is concentrated to the center of the cavity (Fig. 5.4a), no dominant mode of traction or tensile faulting could be observed from the recorded microseismicity. In contrast, the here presented results document a dominant *ds* shearing mode (Fig. 5.12).

One possibility to explain the observed discrepancy between model and microseismic observations might be the presence of systematic pre-existing structures in the entire overburden and

cavity roof as it was discussed in Figure 3.21 and Section 3.2.5. This hypothesis would also explain the fact that the orientation of S_H remains stable during the entire collapsing period. If the cavity roof rocks and the Dolomite layer were isotropic, the local S_H orientation was supposed to change depending on the induced stress changes by the evolving and collapsing cavity structure. These changes in the local stress field are not observed, when shearing occurs along similarly oriented pre-existing structures. Moreover, the hypothesis of pre-existing structure is also in agreement with the observed caving dynamics from spatio-temporal energetic analysis, which seems to be similar for the period in 2008 and 2009. As discussed in Chapter 4 and Figure 4.15, the existence of pre-existing structures and their reactivation by consistent *ds* faulting might allow to form dynamically interacting fault networks that successively release larger stresses. Such a scenario is generally consistent with the fact that the rupture and collapse of the Dolomite layer did not occur in one single instant, but rather gradually in a period of around two hours.

5.2 Summary and interpretation

The observations and results presented in the previous Section are summarized in a schematic sketch shown by Figure 5.15. As a consequence of strong caving processes associated with the microseismic crisis in 2008 (Chapter 4), the cavity roof has developed in its vertical dimension close to the overlying Dolomite layer (Fig. 5.15a). After the crisis in 2008, the entire cavity system entered into an apparent state of relaxation which is characterized by a long-term aftershock period and slight subsidence of the overburden (Chapter 4).

In February 2009, this apparent state of equilibrium was continuously perturbed by the initiation of brine pumping stages 1 and 2 (Fig. 5.15b), leading to minor roof collapses. The first period of the final cavity collapse is then marked by an abrupt increase in microseismic activity recorded on the 11th February around $\sim$ 18:00 UTC (Fig. 5.1 and 5.15c). This period is characterized by significant strains accumulated in the Dolomite layer as documented by the abrupt increase in the extensometer displacement rate (Fig. 5.1b). Consequently, the Dolomite layer loosed significantly of its elastic strength, while this lost was probably most dominant in the center of the cavity structure (Fig. 5.15c,f) as indicated by the spatio-energetic microseismic event distribution (Fig. 5.4a). Due to these stronger deformations in the Dolomite layer, fractures propagated into the shallower overburden (Fig. 5.15c), as documented by (i) shallower source depths (Fig. 5.4), (ii) increasing attenuation (Fig. 5.6)

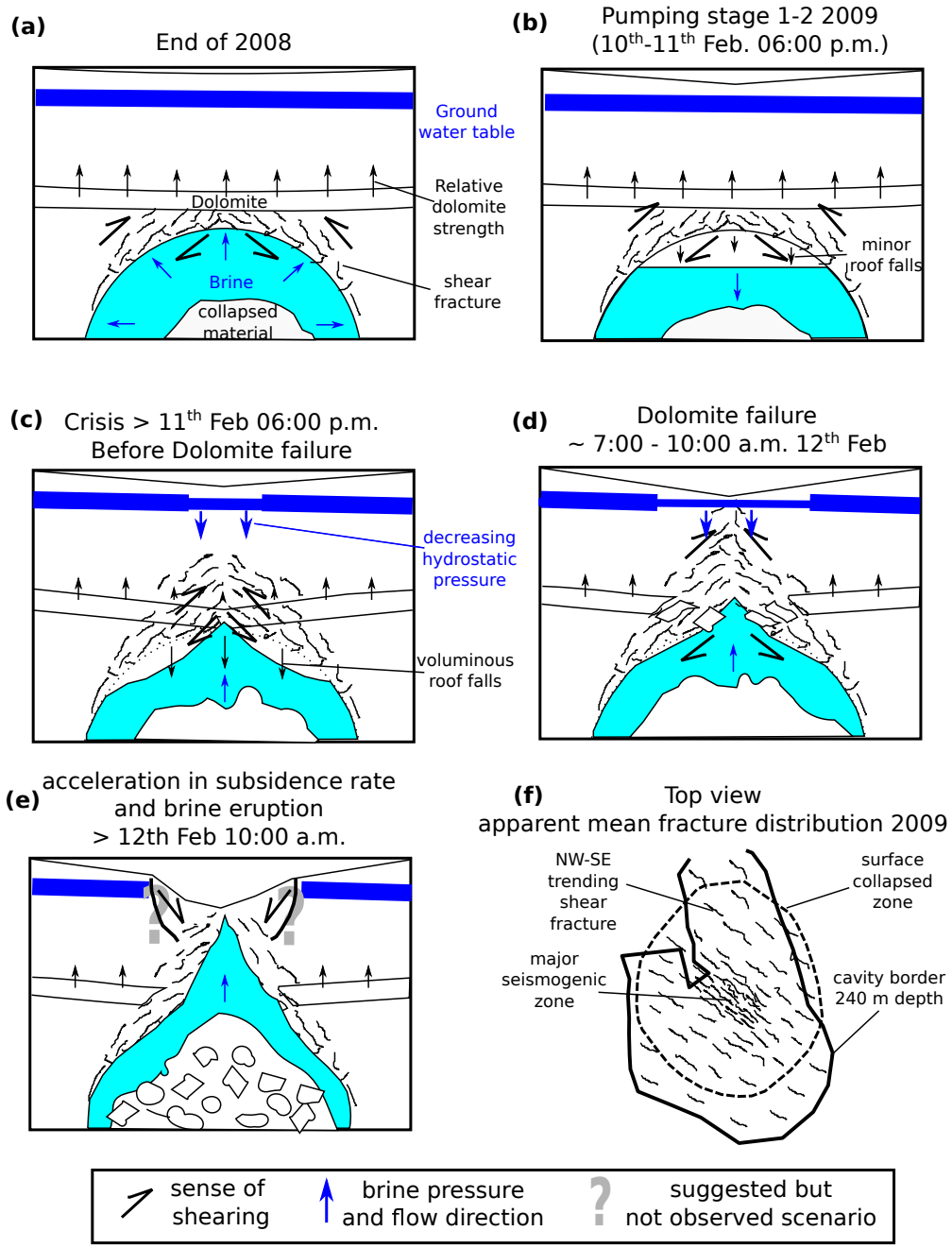

Figure 5.15: Schematic illustration summarizing and interpreting the results and observations of the cavity collapse evolution in 2009.

and (iii) a decrease of the hydroacoustic pressure of the ground water aquifer (Fig. 5.1a). This observation contradicts with previous hypotheses assuming that the overburden collapsed along distinct ring faults that reached down to the Dolomite layer leading to a slip of a cylinder like structure (Lebert et al., 2011) (Fig. 1.8).

Moreover, the involved caving processes and fracture propagation seems to be generally of very similar nature as the ones observed in the period in 2008 (Chapter 4), what is indicated

by (i) the presence of similar microseismic swarm events (Fig. 5.2), (ii) similar epicenter locations and migrations (Fig. 5.3) and (iii) a similar predominating *ds* source mechanism (Fig. 5.10, 5.11 and 5.12). As similar to 2008, these caving processes are associated with self-reinforcing dynamics, what is demonstrated by (i) a decrease of the b-value (Fig. 5.8) and (ii) an increase of the mean seismic moment (Fig. 5.9). In contrast to 2008, these dynamics seem to be more accelerated as indicated by (i) the significant decrease of the low recurrence mode and more frequent repetition of short-term swarming sequences (Fig. 5.7) and (ii) a faster increase in the cumulative moment release (Fig. 5.9). It remains still unclear if the dynamics in 2009 are more energetic, and thus involve different, more efficient collapsing mechanics, what need to be tested by future research.

The trigger of this first collapsing period remains rather speculative from the results of this study. On the other hand, Jousset and Rohmer (2012) found evidence that the increase of the microseismic activity correlates perfectly in time with the passage of low-frequency seismic waves, including body, Love but mainly Rayleigh surface waves produced by a M $\sim$ 7.2 earthquake at 17:34:50 UTC at Kepulauan Talaud, Indonesia, $\sim$ 11800 km distant from the cavern. In their study, the authors stated that the maximum dynamic stress magnitude associated with wave passage is of the same order necessary to bring the Dolomite layer to failure. In addition, stress oscillations as produced by the passage of seismic wave are most efficient with respect to Rayleigh waves, whose dominant periods agreed with the natural fundamental frequency of the cavern system found at about 10–20 s.

In order to evaluate this possible triggering mechanism, I compared the documented microseismic activity increases as documented by Jousset and Rohmer (2012), based on broadband observations, with the high frequency geophone microseismicity, without finding any significant differences. Microseismic event locations that coincide with the instant of the Rayleigh wave passage, like swarm example A (Fig. 5.2a), occurred predominantly in the north-eastern cavity zone, which agrees with the cavity region that got primarily hit by the arriving wave trains (Fig. 5.4c and 5.3a) (Jousset and Rohmer, 2012).

The probably most important period of the cavity collapse is represented by the subsequent failure of the Dolomite layer on the 12th Feburary starting around 07:00 UTC (Fig. 5.15d), which led to an immediate acceleration of the subsidence rate of the overburden and final collapse on the 13th of February (Fig. 1.8 and 5.15e). As already discussed in the previous Section, its failure occurred not at once, but successively within two hours as demonstrated by

the breakdown of installed extensometer stations (Fig. 5.1b). This failure period is generally associated with a similar collapsing mechanisms as observed for the previous caving periods as documented by (i) similar spatio-temporal epicenter migrations (Fig. 5.3c) and (ii) a similar *ds* source mechanism (Fig. 5.12 and 5.13). On the other hand, microseismicity in this period is clearly more energetic as compared to previous periods as indicated by (i) a very small b-value of ~ 0.5 (Fig. 5.8) and (ii) increased apparent stress (Fig. 5.14). A possible energetic amplification of the caving dynamics in this period need to be further examined by future research.

Chapter 6

General conclusion and outlook

Ground failures, caving processes and collapses of large natural or man-made underground cavities can produce significant socio-economic damages and represent a serious risk envisaged by the mine managements and municipalities. In order to improve our understanding of the mechanisms governing such a geohazard and to test the potential of geophysical methods to prevent them, the development and collapse of a salt solution mining cavity was monitored at Cerville-Buissoncourt in the Lorraine basin in northeastern France. During the experiment, a huge microseismic data set ($\sim 50,000$ event files) was recorded by a local microseismic network, which provides a unique opportunity to study in detail the microseismic response of a growing and collapsing underground cavity. However, $\sim 80\%$ of the data set comprised unusual swarming sequences with complex clusters of superimposed microseismic events, which could not be processed through standard automatic detection, location and source analysis routines. This thesis presented innovative methods able to treat this specific microseismic data set, whose developments were inspired by contributions from different fields of current seismological research including tectonic, volcanic and mining investigations. The results obtained by these methods provide new insights into the principal characteristics of caving and collapsing related microseismicity, implying new perspectives for hazard assessment of excavated underground formations.

The recorded microseismic data set represents two major microseismic crisis, (i) one recorded in March to April 2008, related to a period of significant cavity development (without a subsequent surface collapse), and (ii) one in February 2009, associated with the cavity collapsing period induced by brine pumping. The major work of this thesis focused on the interpretation and understanding of the microseismic data recorded in the period in 2008. In this period, caving processes are relatively well constrained by other geophysical parameters, what simplified the development of appropriate methods (summarized in Section 6.1) and the interpretation of microseismicity (summarized in Section 6.2). Since the cavity evolution in the period of 2008 was not provoked by any changes in the solution mining activity, the

governing caving processes and its microseismic signature are supposed to characterize the initial mechanical state of the cavity system under constant "natural" conditions without any changes in the solution mining activity. In the collapsing period 2009, these conditions are supposed to change, when the system was brought to collapse by active brine pumping operations. In order to identify potential changes in the microseismic signature or precursor phenomena indicating the collapsing state of the cavity system, the principal analysis and interpretation steps, as performed for the period in 2008, were repeated for the collapsing period.

6.1 Analysis of microseismicity

Initial analysis, based on body wave phase-based routine detection and location tools, has shown that only a minor portion of the whole microseismic dataset, approximatively $\sim 20\%$, could be successfully treated using these analysis tools. The major reason for this shortcoming was found in the dominance of unusual microseismic swarming sequences, where microseismic events superimpose to dense and complex event clusters, were P wave onsets are often covered by the coda of the preceding events. More detailed analysis from this study has shown that also most of the isolated event occurrences show frequently complicated superposition signatures including precursor, doublets, and multiplets phenomena, as well as complex "cigar-shaped" events with emergent P wave onsets. In addition, the high-frequency microseismic events are affected by strong attenuation and propagation effects associated with refraction along the stiff high-speed Dolomite layer that significantly modify the constitution of the body wave field. The observed signal characteristics and propagation effects make consistent P and S wave picking generally a very challenging task. Moreover, hypocenter distances at the study site are generally very short, and thus body wave travel times are very small, what together with the found uncertainties in phase picking render precise hypocenter location to an almost impossible undertaking.

As a major contribution of this thesis, a semi-automatic detection and location design was developed, able to resolve the spatio-temporal characteristics of these complex microseismic signatures and numerous swarms in a first order. This design is constituted by three principal methods: (i) a spectral envelope detection approach, (ii) a polarization-based detection and location approach and (iii) an amplitude-based based location approach. The spectral envelope approach allows for event detection of different frequency bands using the maxi-

mum spectral amplitude, meanwhile specific seismic phases could not be identified by this method. The method was used as a pre-detection step to guarantee event detection in agreement with the network detection capability and is additionally an useful tool to estimate short-term swarming sequence durations. The polarization-based approach provides P wave phase detection for three component stations in dense microseismic swarm clusters and was used for individual event identification. In addition, the simultaneously obtained polarization angles provide important information on hypocenter location, which was formulated in a probabilistic manner. Further information on hypocenter location is given by the probabilistic amplitude-based approach, which was developed by a detailed study of the attenuation characteristics describing the amplitude decay with distance. Thanks to the probabilistic formulations, both location methods, i.e. the polarization- and amplitude-based approach, can be combined to provide robust information on epicenter source location. On the other hand, source depth estimations were associated with significant uncertainties and could be only reliably constrained in some specific cases.

Based on the detection and location results, also source characteristics could be studied. Source analysis at Cerville is generally difficult due to the presence of event concatenation in swarms, the general high frequency geophone recordings and a limited network station coverage. In order to overcome these shortcomings, the source mechanism was investigate in a step-by-step procedure including various statistical analysis, modeling of observed and synthetic wave forms and amplitude spectra of some well located events, as well as modeling of peak-to-peak amplitude ratios for the majority of the detected events. Within this study, it was possible to assess the common source mechanisms of many swarming events at once, using the observation from only one single three component station. For the theoretical seismic source representation, generally classical seismic source models based on the seismic moment tensor concept were used, while the response of the elastic medium was calculated assuming a 1-D velocity structure. Moreover, several standard seismic source parameters were obtained by using a classical source spectrum scaling approach, which was based on the fit between theoretic and observed source spectral curves.

Thanks to these developed methods, a well constrained seismic catalogue was obtained, whose results and interpretation are summarized in the following Section. In order to further improve the here developed methods and results, the following points should be envisaged by future research. The polarization-based approach turned out to be a very useful tool during

all analysis steps. This approach represents the basis for event detection, whose polarization angles provided important information on source location and were the essential basis for adequate source analysis. To even further improve this approach, it would be desirable to use the identified signal polarization in order to detect S waves, next to P waves. Such an extension of the method would allow to approximate the hypocenter source location in a first order, by using only one single station in an automatic manner as similar to a radio antenna. In addition, as shown by this study, detection based on P wave phases only, can significantly depend on the predominant source radiation pattern. Hence, an inclusion of more seismic phase detections (S waves) would significantly improve the general detection capability. In turn, as equally demonstrated by this result, calculations with respect to the network performance should always take into account the potential source radiation pattern.

The amplitude-based location approach was found to be a very convenient method, independent of seismic phase picking, and thus very useful for location of complex seismic signals, where no distinct seismic phases could be identified. If the attenuation characteristics of the study region are calibrated, this method seems to be relatively robust tool, also with respect to smaller attenuation changes. However, as seen from this study, source radiation pattern have an significant influence on the location results. Consequently, potential source radiation pattern should be taken into account during the method calibration, what might be accomplished using a probabilistic formulation. On the other hand, the sensitivity of this approach to source radiation pattern could represent a great potential for the development of future location approaches that might provide information of source locations and mechanism at once, especially in cases of dense station distributions or consistent microseismic clusters.

In order to further improve the obtained location results also several re-location techniques might be tested in future. As already shown by this study spectral characteristics of the seismic events are generally very similar for similar event locations due to stability in the source mechanism. Consequently, the first order approximations of source locations from this study and the semblance of spectral characteristics might be implemented in an e.g. double difference based relocation procedure to render more precise hypocenter event locations.

6.2 Characterization and interpretation of microseismicity

After a detailed characterization and interpretation of the microseismicity in 2008 I came up with the following principal conclusions. As a first major conclusion, it seems evident

that microseismicity does mainly represent fracturing processes at the cavity roof. This conclusion is consistently indicated from an apparent proportional relationship between the spatio-energetic microseismic distribution and detached rock volumes at the cavity roof, constrained from other geophysical measurements. Microseismic events represent mainly shear fractures with characteristic dimensions in the order of several ones to tens of meters associated with moment magnitudes M_w ranging from around -3 to 1. A particular observation is the remarkable stability of source mechanisms for most microseismic events, representing a predominant thrust fault regime with faults similarly oriented NW-SE, dipping around $35 - 55°$.

In addition, the analysis of source mechanism and source parameters generally indicated that the observed microseismic events can be apparently treated and scaled in the same manner as natural tectonic earthquakes and demonstrate a self-similar scaling behavior. Consequently, theoretic source model developed from classical global seismology, e.g. the classical DC-model and the ω^{-2}-model, seems to be generally applicable and valid with respect to microseismicity related to cavity roof evolution processes. Self-similar scaling behavior is generally demonstrated by the observation that stress drops and apparent stress change insignificantly as compared to seismic moment and radiated energy.

Short-term swarming sequences (in the order of seconds to minutes) can be described as dense event clusters, migrating in space and time. These sequences are formed by superpositions of individual microseismic events, whose entire duration systematically scales with its cumulative moment. The origin of this behavior, to form swarms, is suggested in an incapacity to sustain larger strains and to release larger stresses associated with the mechanical constitution of the rock strata overlying the cavity (i.e. low strength materials). Consistently, the individual microseismic events have a distinct limit in magnitude production ($M_w \lesssim 1$) and result from rather low stress drops, compared to crustal tectonic earthquake. Thus, in order to release larger stresses in form of cavity roof collapses, networks of smaller scaled, repeated rupturing faults are formed that seem to connect and interact.

The formation of larger collapsing zones by these interacting fault networks is comparable with the rupture process of rather slow natural earthquakes. The internal organization of these interacting rupturing processes can be understood as main shock-aftershock sequences in which each individual event triggers itself aftershocks. The potential to produce larger rupture events (larger moment) seem to be dependent on the number of the preceding events,

and thus depends on the density and connectivity of the produced and pre-existing fracture network. However, it is still not very well understood if there are intrinsic differences in the formation processes of shorter and larger swarming sequences, i.e. collapsing events. Also the nature of the internal triggering mechanism remains speculative, but seems to be associated with static stress transfer, where stresses accumulate at crack tips, leading to continuous stress accumulations in a propagating rupture front (stick-slip mode). In order to prove this theory, further investigations need to be done, comparing the obtained results with adapted quantitative seismicity prediction models, as e.g. the ETAS model, and seismicity models based on Coulomb stress calculations.

The spatio-temporal and energetic distribution of swarming sequences, i.e. cavity roof collapsing events, document self-reinforcing caving dynamics in the crisis of 2008. The characteristic spacing and repetition of these swarming sequences in time is approximatively > 20 s, but changes temporally in the range $100 - 1000$ s, as adequately described by a varying lower recurrence mode. Accordingly, it was observed that these long-term seismic rates (lower recurrence mode) increase in the period of 2008, as consistent with in-situ strain measurements and observation from brine level increases at the exploitation wells. Moreover, the maximum swarming sequence durations increased during the crisis, indicating that the collapsing events became larger with time. This is consistent with a continuous decrease in the b-value, as well as an exponentially increase of the cumulative seismic moment release. The increase in size of the collapsing events and moment release might be generally related to an increasing fractured state of the cavity roof, allowing for larger rupture zone formations. The fact that the caving process did not end with a total cavity collapse, but ceased, seem to be related to a re-equilibration of the cavity's geometry, who reached a new relative stable state with respect to the externally applied stress field.

Generally, the microseismic signature during the subsequent collapsing period in 2009 does not seem to differ significantly compared to the period in 2008. Correspondingly, a similar constitution of swarming sequences and self-reinforcing dynamics have been observed. On the other hand, the caving dynamics 2009 seems to be accelerated, what is indicated by more frequent repetition of short-term swarming sequences. It remains still unclear if the dynamics in 2009 are more energetic, and thus involve different, more efficient collapsing mechanics. Comparatively larger events with magnitudes $M_W \geq 0$ have been observed in 2009, which were associated with higher apparent stresses. In order shade more light into this discussion

and to better constrain the underlying mechanism of the observed self-reinforcing collapsing dynamics, current investigations aim to create a simplified catalogue representing the cumulative spatio-temporal and energetic attributes of swarming sequences, i.e. collapsing events, whose statistical behavior might be later evaluated by mechanical modeling and stochastic seismicity prediction models.

The period of the Dolomite failure in 2009 is associated with spatially very concentrated cavity roof propagation into the overburden focusing on the center of the later collapsing circular zone at the surface. This observation contradicts with previous hypotheses assuming that the overburden collapsed along distinct ring faults that reached down to the Dolomite layer leading to a slip of a cylinder like structure. The probably most surprising observation during this collapsing period is without any doubt the general stability in source mechanism, documenting predominant thrust faulting with an NW-SE orientation. This observation contradicts geomechanical models predicting a dominant mode of traction failure in the center of the Dolomite layer. Moreover, the predominating source mechanisms indicate a very stable orientation of the maximum horizontal stress during the caving as well as the collapsing state. It is generally suggested that systematically arranged pre-existing structures play a major role in this context, what could not be proved from this study and need to be further analyzed by comparison with results from future geological and mechanical modeling approaches.

6.3 Implications for hazard assessment and outlook

Regarding these results it is by far too early to make a rigorous assessment with respect to the potential of microseismic monitoring of dangerous underground cavities. On the other hand, the performed analysis and interpretation of microseismicity at Cerville-Buissoncourt has generally shown that microseismic monitoring seems to be an appropriate tool in order to survey the evolution of a hazardous underground cavity. Accordingly, many mechanical and dynamical characteristics of the governing deformation processes at the cavity roof, as well as its general state of stability could be successfully suggested from distinct trends observable in the microseismic data. These results and encouraging trends indicate that caving and collapsing processes proceed not completely chaotically, but are associated with systematical and distinct dynamics observable from microseismic recordings. Hence, it might be possible that evolving underground cavity systems have individual, but systematic microseismic signatures, as principally dependent on the geological context. When these signatures are

manifested by specific empirical laws it seems possible to the survey cavity evolution and indicate periods of collapsing hazard.

For the case of Cerville many of such empirical laws could be observed and interpreted with respect to the current cavity evolution stage, as for example done by analyzing the average event locations, as well as based on simple microseismic attributes as inter-event time distributions. The governing physical processes associated with caving dynamics at Cerville were observed to be approximatively the same for periods of significant cavity evolution, without and with subsequent surface collapse. The collapsing mechanisms seem to differ rather in the collapsing rate than in its energetic constitution. This observation implies that once the microseismic signature is calibrated with respect to the governing dynamics, as manifested by empirical relationships, an increase in the hazard will be directly reflected by an acceleration of these dynamics.

In order to prove this hypotheses, it need to be ruled out if the collapsing processes in 2009 are energetically similar to 2008 or if these processes can be explained by an acceleration of the caving dynamics observed in 2008. In addition, it need to be investigated if similar distinct caving dynamics can be observed at other experimental sites from microseismic observations. A major factor in this context is probably the detection capacity of the microseismic network. As seen by the results of this study, next to attenuation and seismic event sizes also the source mechanism significantly controls the detection rate depending on the respective chosen network geometry. At Cerville, microseismic monitoring conditions were close to ideal, what is not always given in other monitoring contexts as e.g. in larger post-mining districts.

Moreover, further investigations should focus on the apparent proportional relation between released microseismicity and actually detached rock volumes at the cavity. By means of mechanical simulations, taking into account the mechanical properties of the cavity roof rocks, it might be possible to establish empirical laws between the theoretical and observed released microseismic energy and the volume of roof collapses. Such an established empirical law might allow to assess directly the cavity roof geometry based on the microseismic spatio-energetic distribution. Furthermore, detailed research need to be undertaken to examine the relationship of microseismic emissions and observed in-situ deformation measurements (GPS, extensometer, tacheometer), as well as seismic braodband observations. In this study, it was so far shown that the microseismic response is strongly related to periods of cavity roof collapses and the evolution of the cavity roof. However, the relationship of microseismic

emissions and slow and continuous deformation processes, like the subsidence of the overburden, as well as periods increasing deflection of the Dolomite layer was not considered so far. Current investigations focus on this aspect, which is crucial to assess the hazard of the collapsing cavity system.

Chapter 7

Conclusion et perspectives générales

Les cavités souterraines d'origine naturelle ou anthropique, comme les mines actives ou abandonnées, peuvent provoquer des affaissements importants et des effondrements pouvant avoir des conséquences catastrophiques au niveau humain comme économique. Pour améliorer notre compréhension des mécanismes qui régissent ces risques géologiques, l'effondrement provoqué d'une cavité saline, créée par dissolution, a été instrumentée par différentes méthodes géophysiques afin d'en tester l'efficacité. Cette expérimentation a été menée dans le cadre du « Groupement d'Intérêt Scientifique sur l'impact et la Sécurité des Ouvrages Souterrains » (GISOS) sur le site de Cerville- Buissoncourt (Lorraine, France), exploité par SOLVAY. La création de cavités de grandes dimensions sur le site est supposée possible grâce à la présence d'un banc raide (banc de Dolomite) qui jouerait le rôle d'une poutre soutenant le recouvrement et retardant ainsi son effondrement. Pendant l'expérience, un vaste ensemble de données microsismiques ($\sim$ 50.000 fichiers d'événements) a été enregistré par le réseau haute fréquence installé par l'INERIS. Cela constitue une occasion unique d'étudier en détail la réponse microsismique du développement d'une cavité souterraine jusqu'à son effondrement. Toutefois, la majeure partie ($\sim$ 80%) de ces événements microsismiques sont non-isolés, de type rafale, c'est-à-dire constitués par des superpositions complexes de groupes d'événements. Le traitement de ces signaux particuliers n'est pas possible par des approches conventionnelles de détection, localisation (basé sur les temps d'arrivée des ondes de volume) et d'analyse à la source. D'autres difficultés sont apparues dans le traitement des données, à cause de la résolution limitée du réseau à courtes distances hypocentrales et des effets de propagation et de champ proche. Cette thèse présente une analyse et une interprétation détaillée de cette base de données microsismiques grâce à l'adaptation de méthodologies de traitement originales, issues des études d'essaims sismiques d'origine tectonique, volcanique et minière.

L'ensemble des données microsismiques enregistré représente deux crises principales, (i) une crise enregistrée entre mars et avril 2008, liée à une période d'une remontée significative du

toit de la cavité, et (ii) une crise en février 2009, qui correspond à l'effondrement final de la cavité induite par le pompage de la saumure. Le travail principal de cette thèse s'est concentré sur l'interprétation et la compréhension des données microsismiques enregistrées pendant ces deux périodes. La première crise a été étudiée en détail car les processus sont relativement bien contraints par d'autres paramètres géophysiques, ce qui a simplifié la calibration des méthodes de traitement et l'interprétation de la microsismicité.

7.1 Analyse de la microsismicité

Une méthode de détection et de localisation automatique a été développée, pour résoudre les caractéristiques spatio-temporelles des essaims microsismiques au premier ordre. Cette méthode automatique, formulée de manière probabiliste, est constituée par trois approches principales :

(i) une approche de détection utilisant l'enveloppe spectrale du signal,

(ii) une approche de détection et de localisation basée sur la polarisation des ondes,

(iii) une approche de localisation basée sur les rapports d'amplitude des signaux.

La première approche, basée sur l'amplitude spectrale, permet la détection des événements dans différentes bandes de fréquence en utilisant l'amplitude spectrale maximale, sans identification des phases sismiques spécifiques. Cette approche a été utilisée comme une étape de pré-détection pour garantir la détection d'événements en accord avec les capacités de détection du réseau. Cet outil a été également particulièrement utile pour estimer la durée de récurrence de séquences d'essaim sismique. L'approche basée sur la polarisation a permis la détection des ondes P sur les stations trois composantes et l'identification d'événements isolés dans les séquences de rafale. En outre, les angles de polarisation obtenus simultanément donnent des informations importantes sur la localisation de ces événements. Puis la localisation des événements microsismiques a été complétée en combinant les informations des angles de polarisation ainsi que la décroissance de l'amplitude du signal avec la distance. L'approche de localisation basée sur les rapports d'amplitude a été élaborée grâce à l'analyse d'un jeu de donnée de référence qui a permis la calibration de l'atténuation élastique et anélastique du site. Grâce à la combinaison probabiliste des approches de polarisation et d'amplitude, la localisation de l'épicentre est très bien contrainte. D'autre part, l'estimation de la profondeur présente des incertitudes importantes qui peuvent être contraintes de manière fiable

seulement dans certains cas spécifiques.

Sur la base des résultats de détection et localisation, les mécanismes et les paramètres à la source ont pu être analysés. L'analyse de la source des événements microsismiques de Cerville est compliquée à cause de la superposition d'événements dans les essaims, de l'utilisation de géophones haute fréquence et d'une couverture limitée en azimuts du réseau. Afin de surmonter ces difficultés d'analyse, les mécanismes à la source ont été étudiés étape par étape grâce à diverses analyses statistiques, à la modélisation des formes d'onde et aux spectres d'amplitudes observés et synthétiques pour l'ensemble des événements bien localisés et isolés, ainsi que la modélisation des rapports d'amplitude crête-à-crête pour la majorité des événements détectés. D'autre part dans cette étude, il a été possible de contraindre le mécanisme à la source commun d'essaims microsismiques en utilisant un seul capteur trois composantes. Les calculs des sismogrammes synthétiques ont été réalisés sur la base de modèles classiques de la source sismique et du tenseur des moments, tandis que la réponse élastique du milieu a été calculée en 1-D. De plus, les paramètres à la source sismique ont été obtenus en utilisant un modèle de spectre de la source sismique classique, et un réajustement des courbes spectrales théoriques et observés. Grace aux méthodes développées, un catalogue sismique « complet » a pu être obtenu, dont l'interprétation est résumée dans les sections suivantes.

Pour améliorer les méthodes et les résultats développés ici, nous proposons plusieurs pistes de recherche. L'approche basée sur la polarisation s'est avérée être un outil très utile à toutes les étapes d'analyse. Cette approche représente la base de la détection d'événements, dont les angles de polarisation donnent des informations importantes pour la localisation de la source et qui sont essentielles pour son analyse. Pour améliorer cette approche, il serait nécessaire de détecter également les ondes S en fonction de la polarisation du signal. Une telle extension de la méthode permettrait de déterminer l'hypocentre de la source au premier ordre, en utilisant une unique station de manière automatique semblable à une antenne sismique. En outre, comme montré dans cette thèse, la détection basée uniquement sur les phases des ondes P peut fortement dépendre du diagramme de rayonnement de la source sismique. Ainsi, l'ajout de la détection des phases S améliorerait considérablement la capacité de détection générale. À son tour, comme en témoigne ce résultat, les calculs par rapport à la performance de détection d'un réseau sismique devraient toujours tenir compte du diagramme de rayonnement de la source sismique.

L'approche de localisation basée sur les amplitudes s'est révélée être une méthode robuste, ne nécessitant pas le pointé des phases sismiques, et donc très utile pour la localisation de signaux sismiques complexes. Si les caractéristiques d'atténuation du milieu sont bien calibrées, cette méthode est un outil de localisation puissant, même lorsque les variations d'atténuation sont faibles. Cependant, le diagramme de rayonnement de la source a une influence significative sur les résultats de localisation. Par conséquent, ce diagramme de rayonnement devrait être pris en compte au cours du procédé de calibration, ce qui pourrait être réalisé en utilisant une formulation probabiliste. D'autre part, la sensibilité de cette approche au diagramme de rayonnement de la source pourrait apporter un potentiel pour le développement d'approches futures de localisation qui pourraient fournir à la fois des informations de localisation et de mécanisme, dans le cas de formation d'essaims microsismiques.

7.2 Caractérisation et interprétation de la microsismicité

La caractérisation et l'interprétation détaillée de la microsismicité de la crise de 2008 a permis d'arriver aux conclusions suivantes. La première conclusion majeure est que cette microsismicité représente principalement les processus de fracturation du toit de la cavité. Cela est montré par un rapport proportionnel entre la distribution spatio-énergétique de la microsismicité et la quantité de volume de roche détaché au niveau du toit de la cavité, contraint par mesures sonar. En outre, les événements microsismiques représentent principalement des fractures de cisaillement avec des dimensions caractéristiques de l'ordre de un à une dizaine de mètres, associés avec une magnitude de moment Mw variant de ~ -3 à ~ 1. Notons que l'on observe une remarquable stabilité des mécanismes à la source de la plupart des événements microsismiques, qui présentent un régime prédominant en faille inverse orientées NO-SE, avec un pendage de $35 - 55°$.

L'analyse des paramètres à la source indiquent que les événements microsismiques suivent une loi d'échelle comme les séismes naturels tectoniques, qui montrent un comportement de source auto-similaire. Ce comportement auto-similaire est montré par les variations de chute de contrainte, et, de plus, la contrainte apparente est très faible en comparaison des variations du moment sismique et de l'énergie rayonnée. Par conséquent, les modèles de source classiques provenant de la sismologie globale, notamment le modèle double-couple (DC) ainsi que le modèle de Brune (ω^2 modèle), semblent être applicable et valable pour la microsismicité liées aux processus d'évolution du toit de la cavité.

La récurrence des séquences d'essaims microsismiques à court terme (de l'ordre de secondes à quelques minutes) peut être décrite comme des clusters denses qui migrent dans l'espace et le temps. Ces séquences sont formées par la superposition d'événements isolés, dont la durée est proportionnelle à leur moment sismique cumulé. L'origine des essaims microsismiques est certainement due à l'incapacité du système à créer des fractures de grandes dimensions capables de libérer des contraintes très importantes. Cela est vraisemblablement lié aux propriétés mécaniques du toit de la cavité (matériaux de faible résistance élastique). Autrement dit, la magnitude maximale des événements microsismiques isolés est limitée et ces événements produisent donc une chute de contrainte faible comparée aux tremblements de terre tectoniques. Ainsi, la libération de contraintes plus importantes et l'apparition d'effondrements significatifs au niveau du toit de la cavité a lieu grâce à la formation de réseaux de failles à petite échelle qui se connectent, interagissent, et se rompent répétitivement.

La formation d'effondrements par ces réseaux de failles est comparable aux processus de rupture des séismes naturels lents. L'organisation interne de ces processus de rupture peut être représentée comme une séquence d'événements « main shock and aftershock » dans laquelle chaque événement individuel déclenche un événement « aftershock » consécutif. La possibilité de produire une rupture à grande échelle (moment sismique important) semble être fonction du nombre d'événement qui le précède, et dépend donc de la densité et de la connectivité du réseau de fractures néoformé et préexistant. Cependant, les différences intrinsèques dans les processus de formation de courtes et de plus grandes séquences d'essaims (l'effondrement) ne sont toujours pas bien comprises. Aussi la nature du mécanisme de déclenchement interne reste spéculative, mais semble être associée au transfert de contrainte statique, c'est-à-dire à l'accumulation de contraintes aux extrémités des fissures, menant à une propagation d'un front de rupture (stick-slip mode). Pour appuyer cette théorie, d'autres analyses doivent être faites, comme la comparaison des résultats obtenus avec des modèles quantitatifs de prédiction de la sismicité, comme par exemple le modèle ETAS, et les modèles de sismicité basés sur des le critère de rupture de Mohr-Coulomb.

La distribution spatio-temporelle et énergétique des essaims microsismiques, c'est-à-dire les effondrements au niveau du toit de la cavité, témoignent d'une propagation dynamique des instabilités (dynamique d'auto-renforcement, effet domino) pendant l'évolution de la cavité durant la crise en 2008. L'intervalle caractéristique et la répétition des essaims dans le temps sont associés au mode de récurrence bas, qui représente des périodes situées principalement

entre 100 et 1000 s, et qui changent au cours du temps. Par conséquent, il a été observé que ce taux de récurrence sismique à long terme (mode de récurrence bas) augmente pendant la période de 2008, en accord avec les mesures de déformation in situ et l'augmentation du niveau de la saumure dans les puits d'exploitation.

En outre, les durées maximales des essaims ont également augmentées pendant la crise de 2008, ce qui indique que les effondrements du toit de la cavité sont devenus plus étendus avec le temps. Cela est compatible avec une diminution continue de la « b-value », ainsi que l'augmentation exponentielle du moment sismique cumulatif. L'augmentation de la taille des effondrements au niveau du toit de la cavité peut être généralement liée à un état de plus en plus fracturé du toit, permettant la formation de zones de ruptures de plus en plus grandes. Le fait que le processus de dégradation du toit de la cavité n'a pas pris fin par son effondrement complet en 2008, mais s'est simplement arrêté à cette époque, semble être liée à un rééquilibrage de la géométrie de la cavité, qui a atteint un nouvel état relativement stable par rapport au champ de contrainte appliqué.

La signature microsismique pendant la période d'effondrement en 2009 ne semble pas différer sensiblement par rapport à la période de 2008. Corrélativement, une structure semblable d'essaims et de dynamique d'auto-renforcement ont été observés. D'autre part, la dynamique des effondrements au niveau du toit de la cavité en 2009 s'est accélérée, comme indiqué par une répétition plus fréquente de l'occurrence d'essaims. Il reste cependant difficile de savoir cette dynamique d'effondrement de 2009 est plus énergétique, comme indiqué par la faible augmentation des contraintes apparentes, qui pourraient être lié à un mécanisme d'effondrement différent ou même plus efficace que celui de 2008. Pour mieux contraindre le mécanisme sous-jacent de cette dynamique d'effondrement, la recherche en cours propose de créer un catalogue simplifié représentant les attributs spatio-temporels et énergétiques cumulatifs des essaims, dont le comportement statistique pourra être évalué par la modélisation mécanique et par des modèles stochastiques de prévision de la sismicité (modèle ETAS).

La période de la rupture de la couche de Dolomie en 2009 est associée à une propagation de la microsismicité dans le recouvrement très concentrée spatialement dans de la zone circulaire de l'effondrement final. Cette observation contredit les hypothèses précédentes qui supposaient que le recouvrement s'est effondré le long de failles annulaires qui se prolongent jusqu'à la couche de dolomite, menant ainsi au glissement du cylindre entier. Par contre, l'observation sans doute la plus surprenante au cours de cette période est la stabilité générale du mécanisme

à la source, représenté par des failles inverses avec une orientation stable NO-SE. Cette observation contredit les modèles mécaniques qui proposent une déformation dominée par un mode en traction dans la couche de Dolomie. Ce phénomène est probablement lié à la présence de fractures préexistantes sur le site. Cependant, cette hypothèse doit encore être vérifiée en utilisant des approches permettant de mesurer in-situ le degré d'anisotropie du recouvrement et par la mise en œuvre de modélisation mécaniques adaptées.

7.3 Implications pour l'évaluation des risques et les perspectives

Les travaux de recherche de cette thèse confirment, que la surveillance microsismique est un outil puissant pour étudier les processus d'instabilité des cavités souterraines, même avec un nombre réduit de capteurs si des outils d'analyse adaptés sont utilisés. En conséquence, de nombreuses caractéristiques mécaniques et dynamiques des processus régissant les processus de déformation au toit de la cavité, ainsi que son état général de stabilité, peuvent être suivis avec une bonne résolution à partir d'observables issues des données microsismiques. Ces résultats encourageants indiquent que les processus associés à l'évolution et l'effondrement d'une cavité souterraine ne sont pas complètement chaotiques, mais sont associées à une dynamique systématique et distincte, observable à partir des enregistrements microsismiques. Par conséquent, il est possible que l'évolution des systèmes de cavités souterraines montre des signatures microsismiques individuelles, mais systématiques, qui dépendent principalement du contexte géologique. Lorsque ces signatures sont caractérisées par des lois empiriques spécifiques, il est alors possible de surveiller l'évolution d'une cavité et d'en estimer l'aléa d'effondrement.

Pour le cas de Cerville, nous avons déterminé plusieurs lois empiriques permettant d'interpréter l'état d'évolution actuelle de la cavité, comme cela a été fait par exemple pour la distribution spatio-énergétique relative ainsi que pour les temps de récurrence des événements. Les processus physiques associés à l'évolution de la cavité durant la crise de 2008 semblent être similaires aux processus caractérisant l'effondrement final de la cavité en 2009. Les mécanismes d'effondrement semblent plutôt s'accélérés, mais n'augmentent pas forcement au niveau énergétique, en comparaison avec les périodes précédentes. Cette observation implique qu'une fois la signature microsismique étalonnée par rapport à la dynamique d'évolution de la cavité par des relations empiriques, une augmentation du risque sera directement visible par

une accélération de cette dynamique. Afin de prouver cette hypothèse, il faut confirmer que les processus se effondrent en 2009 sont énergétiquement similaire à 2008 ou si ces processus peuvent être expliqués par une accélération de la dynamique observés pour la crise en 2008. En outre, d'autres investigations devraient se concentrer sur le rapport apparemment proportionnel entre la microsismicité libérée et le volume de roche effectivement détaché au toit de la cavité. Au moyen de simulations mécaniques, en prenant en compte les propriétés mécaniques de la roche du toit de la cavité, il pourrait être possible d'établir des lois empiriques reliant la valeur théorique et observée de l'énergie microsismique libérée et le volume des effondrements du toit. Une telle loi empirique pourrait permettre d'évaluer directement la géométrie du toit de la cavité basé sur la distribution spatio-énergétique microsismique. Les travaux à venir porteront également sur des investigations détaillées des relations entre émissions microsismiques et mesures de déplacements in-situ (GPS, extensomètres et tachéomètre) incluant les observations sismologiques large bande. Dans cette thèse, il a été démontré que la réponse microsismique est fortement liée à des périodes d'effondrement du toit de la cavité, cependant, la relation entre les émissions microsismiques et les processus de déformation lents et continus, comme celle de la subsidence du recouvrement, ainsi que les périodes de déflection de la couche de Dolomie n'ont pas encore été étudié en détail. Les recherches futures doivent se concentrer sur cet aspect, qui est crucial pour évaluer l'aléa lié à l'instabilité des cavités souterraines.

Bibliography

Abercrombie, R. E. (1995). Earthquake source scaling relationships from- 1 to 5 ml using seismograms recorded at 2.5-km depth. *Journal of Geophysical Research: Solid Earth (1978–2012)*, 100(B12):24015–24036.

Aki, K. (1965). Maximum likelihood estimate of b in the formula log n= a-bm and its confidence limits. *Bull. Earthq. Res. Inst. Univ. Tokyo*, 43:237–239.

Aki, K. (1967). Scaling law of seismic spectrum. *Journal of Geophysical Research*, 72(4):1217–1231.

Aki, K. and Richards, P. (2002). Quantitative Seismology. *University of Science, Sausalito, California*.

Allen, R. (1982). Automatic phase pickers: their present use and future prospects. *Bulletin of the Seismological Society of America*, 72(6B):S225.

Anderson, E. (1905). The dynamics of faulting. *Transactions of the Edinburgh Geological Society*, 8(3):387–402.

Anderson, E. (1951). The dynamics of faulting. *Oliver and Boyd, Edinburgh*, 206:7–21.

André, G. (2003). *Caractérisation des déformations méso-cénozoïques et des circulations de fluides dans l'Est du Bassin de Paris*. PhD thesis, Universite de Lorraine, Nancy.

André, G., Proudhon, B., Rebours, H., and Wileveau, Y. (2006). Paramètres contrôlant la distribution de la fracturation: exemple dans une série marno-calcaire du jurassique supérieur (est du bassin de paris). *Comptes Rendus Geoscience*, 338(12):931–941.

Arkin, Y. and Gilat, A. (2000). Dead sea sinkholes: an everdeveloping hazard. *Environmental Geology*, 39(7):711–722.

Backus, G. and Mulcahy, M. (1976). Moment tensors and other phenomenological descriptions of seismic sources—II. Discontinuous displacements. *Geophysical Journal of the Royal Astronomical Society*, 47(2):301–329.

Baer, G., Hamiel, Y., Shamir, G., and Nof, R. (2008). Evolution of a magma-driven earthquake swarm and triggering of the nearby oldoinyo lengai eruption, as resolved by insar, ground observations and elastic modeling, east african rift, 2007. *Earth and Planetary Science Letters*, 272(1):339–352.

Balland, C., Al Heib, M., and Didier, C. (2009). Monitoring the long term stability and sinkhole of shallow underground cavities using micro-seismic technique - gypsum mine (France). In *AGU Fall Meeting 2009*.

Bardainne, T., Dubos-Sallée, N., Sénéchal, G., Gaillot, P., and Perroud, H. (2008). Analysis of the induced seismicity of the lacq gas field (southwestern france) and model of deformation. *Geophysical Journal International*, 172(3):1151–1162.

Barla, G., Jarre, P., et al. (1991). Subsidence over an abandoned dissolving salt mine. In *The 32nd US Symposium on Rock Mechanics (USRMS)*. American Rock Mechanics Association.

Båth, M. (1965). Lateral inhomogeneities of the upper mantle. *Tectonophysics*, 2(6):483–514.

Battaglia, J. and Aki, K. (2003). Location of seismic events and eruptive fissures on the piton de la fournaise volcano using seismic amplitudes. *Journal of Geophysical Research: Solid Earth (1978–2012)*, 108(B8).

Battaglia, J., Aki, K., and Ferrazzini, V. (2005). Location of tremor sources and estimation of lava output using tremor source amplitude on the piton de la fournaise volcano: 1. location of tremor sources. *Journal of volcanology and geothermal research*, 147(3):268–290.

Ben-Menahem, A., Gibson Jr, R., and Sena, A. (1991). Green's tensor and radiation patterns of point sources in general anisotropic inhomogeneous elastic media. *Geophysical Journal International*, 107(2):297–308.

Benoit, J. and McNutt, S. (1996). Global volcanic earthquake swarm database and preliminary analysis of volcanic earthquake swarm duration. *Annals of Geophysics*, 39(2):page 221.

Bergery, G. and Nayman, E. (2007). Forecasting collapse hazard using real-time microseismic monitoring–case of a solution mining production field. In *69th EAGE Conference & Exhibition*.

Beyreuther, M., Barsch, R., Krischer, L., Megies, T., Behr, Y., and Wassermann, J. (2010). Obspy: A python toolbox for seismology. *Seismological Research Letters*, 81(3):530–533.

Bigarré, P., Bennani, M., Contrucci, I., Klein, E., Baroudi, H., Hadadou, R., Vuidart, I., and Josien, J. (2011). Microseismic monitoring strategy as a key component of post-mining risk management: Review and feedback experience over the past decade. *Harmonising Rock Engineering and the Environment*, page 404.

Boatwright, J. and Fletcher, J. B. (1984). The partition of radiated energy between p and s waves. *Bulletin of the Seismological Society of America*, 74(2):361–376.

Boettcher, M., McGarr, A., and Johnston, M. (2009). Extension of gutenberg-richter distribution to m w–1.3, no lower limit in sight. *Geophys. Res. Lett*, 36:L10307.

Boore, D. M. and Boatwright, J. (1984). Average body-wave radiation coefficients. *Bulletin of the Seismological Society of America*, 74(5):1615–1621.

Bouchon, M. (1981). A simple method to calculate green's functions for elastic layered media. *Bulletin of the Seismological Society of America*, 71(4):959–971.

Bourouis, S. and Bernard, P. (2007). Evidence for coupled seismic and aseismic fault slip during water injection in the geothermal site of soultz (france), and implications for seismogenic transients. *Geophysical Journal International*, 169(2):723–732.

Brady, B. H. (2004). *Rock mechanics: for underground mining*. Springer.

Branston, M. W. (2003). *The application of time-lapse microgravity to investigate and monitor subsidence related to salt dissolution*. PhD thesis, PUniversity of Keele, England.

Brodsky, E. E. (2006). Long-range triggered earthquakes that continue after the wave train passes. *Geophysical research letters*, 33(15).

Brune, J. N. (1970). Tectonic stress and the spectra of seismic shear waves from earthquakes. *Journal of Geophysical Research*, 75(26):4997–5009.

Burridge, R. and Knopoff, L. (1964). Body force equivalents for seismic dislocations. *Bulletin of the Seismological Society of America*, 54(6A):1875–1888.

Campillo, M., Bouchon, M., and Massinon, B. (1984). Theoretical study of the excitation, spectral characteristics, and geometrical attenuation of regional seismic phases. *Bulletin of the Seismological Society of America*, 74(1):79–90.

Cao, N.-T. (2011). Apport de la surveillance microsismique en champ proche pour la détection de mécanismes et signes précurseurs aux instabilités gravitaires. *Ph.D. Thesis, LAEGO Institut National Polytechnique de Lorraine, France (in French).*

Caramanna, G., Ciotoli, G., and Nisio, S. (2008). A review of natural sinkhole phenomena in italian plain areas. *Natural hazards*, 45(2):145–172.

Cesca, S. and Heimann, S. (2013). A practical on moment tensor inversion using the kiwi tools. *Manual of Seismological Observatory Practice, GFZ Potsdam, Germany.*

Choy, G. L. and Boatwright, J. L. (1995). Global patterns of radiated seismic energy and apparent stress. *Journal of Geophysical Research: Solid Earth (1978–2012)*, 100(B9):18205–18228.

Coccia, S., Lizeur, A., Bigarre, P., Contrucci, I., Klein, E., et al. (2013). Accurate 3d location of mine induced seismicity in complex near-field underground conditions. In *Proceedings of the 8th International Symposium on Rockbursts and Seismicity in Mines.*

Collins, D. and Young, R. (2000). Lithological controls on seismicity in granitic rocks. *Bulletin of the Seismological Society of America*, 90(3):709–723.

Contrucci, I., Klein, E., Bigarré, P., Lizeur, A., Lomax, A., and Bennani, M. (2010). Management of post-mining large-scale ground failures: Blast swarms field experiment for calibration of permanent microseismic early-warning systems. *Pure and Applied Geophysics*, 167(1):43–62.

Contrucci, I., Klein, E., Cao, N., Daupley, X., and Bigarré, P. (2011). Multi-parameter monitoring of a solution mining cavern collapse: First insight of precursors. *Comptes Rendus Geoscience*, 343(1):1–10.

Cook, N. (1963). The seismic location of rockbursts. *Proceedings of the Fifth Rock Mechanics Symposium*, pages 463–516.

Cornet, F. H. and Röckel, T. (2012). Vertical stress profiles and the significance of "stress decoupling". *Tectonophysics*, 581:193–205.

Couffm, S. and Bigarré, P. (2003). Permanent real time microseismic monitoring of abandoned mines for public safety. In *Field Measurements in Geomechanics: Proceedings of the 6th International Symposium, Oslo, Norway, 23-26 September 2003*, page 437. CRC Press.

Coutant, O. (1989a). Numerical study of the diffraction of elastic waves by fluid-filled cracks. *Journal of Geophysical Research: Solid Earth (1978–2012)*, 94(B12):17805–17818.

Coutant, O. (1989b). Program of numerical simulation axitra. *Res. Rep. LGIT (in French), Universite Joseph Fourier, Grenoble*.

Dahm, T. (1993). *Relativmethoden zur Bestimmung der Abstrahlcharakteristik von seismischen Quellen*. PhD thesis, Phd thesis, Univ. Karlsruhe.

Dahm, T., Heimann, S., and Bialowons, W. (2011). A seismological study of shallow weak micro-earthquakes in the urban area of hamburg city, germany, and its possible relation to salt dissolution. *Natural hazards*, 58(3):1111–1134.

Dahm, T. and Krueger, F. (1999). Higher-degree moment tensor inversion using far-field broad-band recordings: theory and evaluation of the method with application to the 1994 Bolivia deep earthquake. *Geophysical Journal International*, 137(1):35–50.

Dahm, T., Manthei, G., and Eisenblatter, J. (1999). Automated moment tensor inversion to estimate source mechanisms of hydraulically induced micro-seismicity in salt rock. *Tectonophysics*, 306(1):1–17.

Daniel, G., Prono, E., Renard, F., Thouvenot, F., Hainzl, S., Marsan, D., Helmstetter, A., Traversa, P., Got, J.-L., Jenatton, L., et al. (2011). Changes in effective stress during the 2003–2004 ubaye seismic swarm, france. *Journal of Geophysical Research: Solid Earth (1978–2012)*, 116(B1).

Daupley, X., Cuche, H., Ghoreychi, M., et al. (2005). Typology of strata movement related to old solution mining of salt at sarralbe (lorraine, france). In *Proceedings of the symposium Post mining 2005*.

Daupley, X., Fabriol, R., Contrucci, I., Bernardie, S., Cao, N.-T., Jousset, P., Klein, E., Lebert, F., and Behrooz, B. (2010). Multiparameter monitoring of a salt cavern collapse (cerville-buissoncourt site, france). In *EGU General Assembly Conference Abstracts*, volume 12, page 12404.

Daupley, X., Laouafa, F., and Contrucci, I. (2013). L'effondrement de la cavité saline de cerville-buissoncourt - analyse des mécanismes conduisant à l'effondrement. *Manuel de mécanique des roches. Tome III : Retours d'expériences - Génie minier et pétrolier*, pages 59–69.

Deck, O. (2002). *Etude des conséquences des affaissements miniers sur le bâti. Propositions pour une méthodologie d'évaluation de la vulnérabilité du bâti.* PhD thesis, LAEGO, Institut National Polytechnique de Lorraine, France.

Di Grazia, G., Falsaperla, S., and Langer, H. (2006). Volcanic tremor location during the 2004 mount etna lava effusion. *Geophysical research letters*, 33(4).

Didier, C. (2008). The french experience of post-mining management. In *Symposium Post-Mining 2008. Feb 2008, Nancy, France.*

Didier, C., Josien, J.-P., et al. (2003). Importance of failure mechanisms for management of surface instability risk above abandoned mines. In *Proceedings of the 10th International Congress on Rock Mechanics ISRM 2003*, volume 1, pages 243–248.

Dreger, D. S., Tkalčić, H., and Johnston, M. (2000). Dilational processes accompanying earthquakes in the long valley caldera. *Science*, 288(5463):122–125.

Duplancic, P., Brady, B., et al. (1999). Characterisation of caving mechanisms by analysis of seismicity and rock stress. In *9th ISRM Congress*. International Society for Rock Mechanics.

Eaton, D. W. and Forouhideh, F. (2010). Microseismic moment tensors: The good, the bad and the ugly. *CSEG Recorder*, 35(9):45–49.

Ege, J. R. (1984). Mechanisms of surface subsidence resulting from solution extraction of salt. *Reviews in Engineering Geology*, 6:203–221.

Eisner, L., Gei, D., Hallo, M., Opršal, I., and Ali, M. Y. (2013). The peak frequency of direct waves for microseismic events. *Geophysics*, 78(6):A45–A49.

Eisner, L., Thornton, M., Griffin, J., et al. (2011). Challenges for microseismic monitoring. In *2011 SEG Annual Meeting*. Society of Exploration Geophysicists.

Felzer, K. R. and Brodsky, E. E. (2006). Decay of aftershock density with distance indicates triggering by dynamic stress. *Nature*, 441(7094):735–738.

Feustel, A. J. (1998). Seismic attenuation in underground mines : a comparative evaluation of methods and results. *Tectonophysics*, 289:31–49.

Fidelibus, M. D., Gutiérrez, F., and Spilotro, G. (2011). Human-induced hydrogeological changes and sinkholes in the coastal gypsum karst of lesina marina area (foggia province, italy). *Engineering Geology*, 118(1):1–19.

Fischer, T., Horálek, J., Hrubcová, P., Vavryčuk, V., Bräuer, K., and Kämpf, H. (2014). Intra-continental earthquake swarms in west-bohemia and vogtland: A review. *Tectonophysics*, 611:1–27.

Flinn, E. (1965). Signal analysis using rectilinearity and direction of particle motion. *Proceedings of the IEEE*, 53(12):1874–1876.

Freed, A. M. (2005). Earthquake triggering by static, dynamic, and postseismic stress transfer. *Annu. Rev. Earth Planet. Sci.*, 33:335–367.

Gane, P., Hales, A., and Oliver, H. (1946). A seismic investigation of the witwatersrand earth tremors. *Bulletin of the Seismological Society of America*, 36(2):49–80.

Gay, N. and Ortlepp, W. (1979). Anatomy of a mining-induced fault zone. *Bulletin of the Geological Society of America*, 90(1):47.

Ge, M. (2005). Efficient mine microseismic monitoring. *International journal of coal geology*, 64(1-2):44–56.

Gibowicz, S. (2006). Seismic doublets and multiplets at polish coal and copper mines. *Acta Geophysica*, 54(2):142–157.

Gibowicz, S. (2009). Seismicity induced by mining: Recent research. *Advances in Geophysics*, 51:1–53.

Gibowicz, S. and Kijko, A. (1994). An introduction to mining seismology. *Academic Press San Diego*, 399.

Gilbert, F. (1971). Excitation of the normal modes of the Earth by earthquake sources. *Geophysical Journal of the Royal Astronomical Society*, 22(2):223–226.

Gilpin, B. and Lee, T.-C. (1978). A microearthquake study in the salton sea geothermal area, california. *Bulletin of the Seismological Society of America*, 68(2):441–450.

Glazer, S. and Hepworth (2005). Seismicity induced by cave mining, palabora experience. *Rockbursts and Seismicity in Mines, Perth, Western Australia, 9-11 March. Australian Centre for Geomechanics*, pages 280–289.

Godano, M., Bardainne, T., Regnier, M., and Deschamps, A. (2011). Moment-tensor determination by nonlinear inversion of amplitudes. *Bulletin of the Seismological Society of America*, 101(1):366–378.

Godano, M., Bardainne, T., Regnier, M., Deschamps, A., and Valette, M. (2012). Spatial and temporal evolution of a microseismic swarm induced by water injection in the arkema-vauvert salt field (southern france). *Geophysical Journal International*, 188(1):274–292.

Godano, M., Regnier, M., Deschamps, A., Bardainne, T., and Gaucher, E. (2009). Focal mechanisms from sparse observations by nonlinear inversion of amplitudes: method and tests on synthetic and real data. *Bulletin of the Seismological Society of America*, 99(4):2243–2264.

Golden, C. E., Webb, S. C., and Sohn, R. A. (2003). Hydrothermal microearthquake swarms beneath active vents at middle valley, northern juan de fuca ridge. *Journal of Geophysical Research: Solid Earth (1978–2012)*, 108(B1).

Guarisco, M. (1987). Microseismic monitoring of solution mining cavities. *APCOM 87: Mining. Procdeeding of the Twentieth Internation Symposium on the Application of Computers and Mathematics in the Mineral Industries, Johannesburg, Soth Afrcia*, 1:49–54.

Gunzburger, Y. and Magnenet, V. (2014). Stress inversion and basement-cover stress transmission across weak layers in the paris basin, france. *Tectonophysics*, 617:44–57.

Gutenberg, B. and Richter, C. (1944). Frequency of earthquakes in california. *Bulletin of the Seismological Society of America*, 34(4):185–188.

Gutierrez, F., Cooper, A., and Johnson, K. (2008). Identification, prediction, and mitigation of sinkhole hazards in evaporite karst areas. *Environmental Geology*, 53(5):1007–1022.

Hainzl, S. and Fischer, T. (2002). Indications for a successively triggered rupture growth underlying the 2000 earthquake swarm in vogtland/nw bohemia. *Journal of Geophysical Research: Solid Earth (1978–2012)*, 107(B12):ESE–5.

Hainzl, S., Kraft, T., Wassermann, J., Igel, H., and Schmedes, E. (2006). Evidence for rainfall-triggered earthquake activity. *Geophysical Research Letters*, 33(19).

Hainzl, S. and Ogata, Y. (2005). Detecting fluid signals in seismicity data through statistical earthquake modeling. *Journal of Geophysical Research: Solid Earth (1978–2012)*, 110(B5).

Hainzl, S., Steacy, S., and Marsan, D. (2010). Seismicity models based on coulomb stress calculations. *Community Online Resource for Statistical Seismicity Analysis, doi:10.5078/corssa-32035809. Available at* `http://www.corssa.org`.

Hainzl, S., Zöller, G., and Kurths, J. (1999a). Self-organization of spatio-temporal earthquake clusters. *Nonlinear Processes in Geophysics*, 7(1/2):21–29.

Hainzl, S., Zöller, G., and Kurths, J. (1999b). Similar power laws for foreshock and aftershock sequences in a spring-block model for earthquakes. *Journal of Geophysical Research: Solid Earth (1978–2012)*, 104(B4):7243–7253.

Hainzl, S., Zöller, G., Kurths, J., and Zschau, J. (2000). Seismic quiescence as an indicator for large earthquakes in a system of self-organized criticality. *Geophysical research letters*, 27(5):597–600.

Hanks, T. C. and Wyss, M. (1972). The use of body-wave spectra in the determination of seismic-source parameters. *Bulletin of the Seismological Society of America*, 62(2):561–589.

Hardy, H., Belesky, R. M., Mrugala, M., Kimble, E. J., and Hager, M. E. (1986). A study to monitor microseismic activity to detect sinkholes. *Pennsylvania State University Report, United States*, 1.

Haskell, N. A. (1953). The dispersion of surface waves on multilayered media. *Bull. Seism. Soc. Am.*, 43:17–34.

Hazzard, J. and Young, R. (2002). Moment tensors and micromechanical models. *Tectonophysics*, 356(1-3):181–197.

Heidbach, O., Tingay, M., Barth, A., Reinecker, J., Kurfeß, D., and Müller, B. (2010). Global crustal stress pattern based on the world stress map database release 2008. *Tectonophysics*, 482(1):3–15.

Heimann, S. (2011). *A robust method to estimate kinematic earthquake source parameters*. PhD thesis, Department of Geoscience, University Hamburg, Germany).

Heimann, S., Cesca, S., Kriegerowski, M., and Dahm, T. (2014). Synthetic seismogram web service and python tools. In *EGU General Assembly Conference Abstracts*, volume 16, page 10466.

Hernandez, O. (2008). Recollement des données d'entrée pour le traitement automatique des données microsismiques de cerville sur sytmisauto. *Internal report, INERIS, Nancy, France*.

Hill, D., Reasenberg, P., Michael, A., Arabaz, W., Beroza, G., Brumbaugh, D., Brune, J., Castro, R., Davis, S., Ellsworth, W., et al. (1993). Seismicity remotely triggered by the magnitude 7.3 landers, california, earthquake. *Science*, 260(5114):1617–1623.

Hill, D. P. (1977). A model for earthquake swarms. *Journal of Geophysical Research*, 82(8):1347–1352.

Horner, R. and Hasegawa, H. (1978). The seismotectonics of southern saskatchewan. *Canadian Journal of Earth Sciences*, 15(8):1341–1355.

Horton, S. (2012). Disposal of hydrofracking waste fluid by injection into subsurface aquifers triggers earthquake swarm in central arkansas with potential for damaging earthquake. *Seismological Research Letters*, 83(2):250–260.

Hudyma, M., Frenette, P., and Leslie, I. (2010). Monitoring open stope caving at goldex mine. *Mining Technology*, 119(3):142–150.

Hudyma, M., Potvin, Y., and Allison, D. (2008). Seismic monitoring of the northparkes lift 2 block cave-part i undercutting. *Journal of the South African Institute of mining and metallurgy*, 108(7):405–419.

Hudyma, M. and Potvin, Y. H. (2010). An engineering approach to seismic risk management in hardrock mines. *Rock mechanics and rock engineering*, 43(6):891–906.

Husen, S., Bachmann, C., and Giardini, D. (2007). Locally triggered seismicity in the central swiss alps following the large rainfall event of august 2005. *Geophysical Journal International*, 171(3):1126–1134.

Ibs-von Seht, M., Plenefisch, T., and Klinge, K. (2008). Earthquake swarms in continental rifts—a comparison of selected cases in america, africa and europe. *Tectonophysics*, 452(1):66–77.

Ide, S. and Beroza, G. (2001). Does apparent stress vary with earthquake size? *Geophysical research letters*, 28(17):3349–3352.

Ide, S., Beroza, G. C., Prejean, S. G., and Ellsworth, W. L. (2003). Apparent break in earthquake scaling due to path and site effects on deep borehole recordings. *Journal of Geophysical Research*, 108(B5):2271.

Ide, S., Beroza, G. C., Shelly, D. R., and Uchide, T. (2007). A scaling law for slow earthquakes. *Nature*, 447(7140):76–79.

Izutani, Y. and Kanamori, H. (2001). Scale-dependence of seismic energy-to-moment ratio for strike-slip earthquakes in japan. *Geophysical Research Letters*, 28(20):4007–4010.

Jechumtálová, Z. and Šílenỳ, J. (2005). Amplitude ratios for complete moment tensor retrieval. *Geophysical research letters*, 32(22):22303.

Jechumtálová, Z., Šílenỳ, J., and Trifu, C. (2014). Microearthquake mechanism from wave amplitudes recorded by a close-to-surface seismic array at ocnele mari, romania. *Geophysical Journal International*, 197(3):1608–1626.

Jeffreys, H. (1973). On isotropic tensors. *Mathematical Proceedings of the Cambridge Philosophical Society, Cambridge Univ Press*, 73(01):173–176.

Johnson, K. S. (2005). Subsidence hazards due to evaporite dissolution in the united states. *Environmental geology*, 48(3):395–409.

Jolly, A., Thompson, G., and Norton, G. (2002). Locating pyroclastic flows on soufriere hills volcano, west indies, using amplitude signals from high dynamic range instruments. *Journal of Volcanology and Geothermal Research*, 118:299–317.

Jones, G., Kulessa, B., Doyle, S., Dow, C., and Hubbard, A. (2013). An automated approach to the location of icequakes using seismic waveform amplitudes. *Annals of Glaciology*, 54(64):1–9.

Jost, M. and Herrmann, R. (1989). A student's guide to and review of moment tensors. *Seismological Research Letters*, 60(2):37–57.

Jousset, P., Bazargan-Sabet, B., Lebert, F., Bernardie, S., and Gourry, J.-C. (2010). Geophysical observations at cavity collapse. In *EGU General Assembly Conference Abstracts*, volume 12, page 4993.

Jousset, P. and Rohmer, J. (2012). Evidence for remotely triggered microearthquakes during salt cavern collapse. *Geophysical Journal International*, 191(1):207–223.

Julià, J., Nyblade, A., Durrheim, R., Linzer, L., Gok, R., Dirks, P., and Walter, W. (2009). Source mechanisms of mine-related seismicity, savuka mine, south africa. *Bulletin of the Seismological Society of America*, 99(5):2801.

Julian, B., Miller, A., and Foulger, G. (1998). Non-double-couple earthquakes 1. Theory. *Reviews in Geophysics*, 36(4):525–549.

Jurkevics, A. (1988). Polarization analysis of three-component array data. *Bulletin of the Seismological Society of America*, 78(5):1725–1743.

Kanamori, H. (1977). The energy release in great earthquakes. *Journal of geophysical Research*, 82(20):2981–2987.

Kanamori, H. and Anderson, D. L. (1975). Theoretical basis of some empirical relations in seismology. *Bulletin of the Seismological Society of America*, 65(5):1073–1095.

Kanamori, H., Mori, J., Hauksson, E., Heaton, T. H., Hutton, L. K., and Jones, L. M. (1993). Determination of earthquake energy release and ml using terrascope. *Bulletin of the Seismological Society of America*, 83(2):330–346.

Kawasaki, I. and Tanimoto, T. (1981). Radiation patterns of body waves due to the seismic dislocation occurring in an anisotropic source medium. *Bulletin of the Seismological Society of America*, 71(1):37–50.

Kennett, B. (2001). The seismic wavefield. *Cambridge University Press*.

Kijko, A., Lasocki, S., and Graham, G. (2001). Non-parametric seismic hazard in mines. *Pure and Applied Geophysics*, 158(9):1655–1675.

Klein, E., Contrucci, I., Daupley, X., Hernandez, O., Bigarré, P., Nadim, C., and Cauvin, L. (2008). Experimental monitoring of a solution-mining cavern in salt: Identifying and analyzing early-warning signals prior to collapse. In *SMRI Fall Technical Conference, Galveston (Austin), Texas, USA*, pages 135—146.

Knopoff, L. and Randall, M. (1970). The compensated linear-vector dipole: a possible mechanism for deep earthquakes. *Journal of Geophysical Research*, 75(26):4957–4963.

Kosecki, A., Piwakowski, B., and Driad-Lebeau, L. (2010). High resolution seismic investigations in salt mining context. *Acta Geophysica*, 58(1):15–33.

Kruger, F. and Rossler, D. (2009). Moment tensor inversion in cylindrical medium. *Study internal handout, University Potsdam*.

Kuge, K. and Lay, T. (1994). Data-dependent non-double-couple components of shallow earthquake source mechanisms: effects of waveform inversion instability. *Geophysical Research Letters*, 21(1):9–12.

Kwiatek, G. and Ben-Zion, Y. (2013). Assessment of p and s wave energy radiated from very small shear-tensile seismic events in a deep south african mine. *Journal of Geophysical Research: Solid Earth*, 118(7):3630–3641.

Kwiatek, G., Plenkers, K., Dresen, G., et al. (2011). Source parameters of picoseismicity recorded at mponeng deep gold mine, south africa: Implications for scaling relations. *Bulletin of the Seismological Society of America*, 101(6):2592–2608.

Lambotte, S., Lyon-Caen, H., Bernard, P., Deschamps, A., Patau, G., Nercessian, A., Pacchiani, F., Bourouis, S., Drilleau, M., and Adamova, P. (2014). Reassessment of the rifting process in the western corinth rift from relocated seismicity. *Geophysical Journal International*, 197(3):1822–1844.

Land, L. (2009). Anthropogenic sinkholes in the delaware basin region—west texas and southeastern new mexico. *W Tex Geol Soc Bull*, 48:10–22.

Lay, T. and Wallace, T. (1995). Modern global seismology. *Elsevier, New York*.

Lebert, F., Bernardie, S., Mainsant, G., et al. (2011). Hydroacoustic monitoring of a salt cavity: an analysis of precursory events of the collapse. *Natural Hazards and Earth System Sciences*, 11(9).

Lees, J. M. (1998). Multiplet analysis at coso geothermal. *Bulletin of the Seismological Society of America*, 88(5):1127–1143.

Lenti, L., Martino, S., Paciello, A., Prestininzi, A., and Rivellino, S. (2012). Microseismicity within a karstified rock mass due to cracks and collapses as a tool for risk management. *Natural hazards*, 64(1):359–379.

Lévy, C., Baillet, L., Jongmans, D., Mourot, P., and Hantz, D. (2010). Dynamic response of the chamousset rock column (western alps, france). *Journal of Geophysical Research: Earth Surface (2003–2012)*, 115(F4).

Lindenfeld, M., Rümpker, G., Link, K., Koehn, D., and Batte, A. (2012). Fluid-triggered earthquake swarms in the rwenzori region, east african rift—evidence for rift initiation. *Tectonophysics*, 566:95–104.

Lohman, R. B. and McGuire, J. J. (2007). Earthquake swarms driven by aseismic creep in the salton trough, california. *Journal of Geophysical Research: Solid Earth (1978–2012)*, 112(B4).

Lomax, A. and Curtis, A. (2001). Fast, probabilistic earthquake location in 3d models using oct-tree importance sampling. *Geophysical Research Abstracts*, 3:955.

Madariaga, R. (1976). Dynamics of an expanding circular fault. *Bulletin of the Seismological Society of America*, 66(3):639–666.

Main, I. (1996). Statistical physics, seismogenesis, and seismic hazard. *Reviews of Geophysics*, 34(4):433–462.

Main, I. G., Meredith, P. G., and Jones, C. (1989). A reinterpretation of the precursory seismic b-value anomaly from fracture mechanics. *Geophysical Journal International*, 96(1):131–138.

Maisons, C., Fortier, E., and Valette, M. (1997). Induced microseismicity and procedure for closure of brine production caverns. *Pure and Applied Geophysics*, 3.

Malone, S. D., Rothe, G. H., and Smith, S. W. (1975). Details of microearthquake swarms in the columbia basin, washington. *Bulletin of the Seismological Society of America*, 65(4):855–864.

Malovichko, D., Dyagilev, R., Shulakov, D. Y., Butyrin, P., and Glebov, S. V. (2009). Seismic monitoring of large-scale karst processes in a potash mine. *Controlling seismic hazard and sustainable development of deep mines*, 2:989–1002.

Malovichko, D., Kadebskaya, O., Shulakov, D. Y., and Butyrin, P. (2010). Local seismologic observations of karst processes. *Izvestiya, Physics of the Solid Earth*, 46(1):57–73.

Mancini, F., Stecchi, F., Zanni, M., and Gabbianelli, G. (2009). Monitoring ground subsidence induced by salt mining in the city of tuzla (bosnia and herzegovina). *Environmental geology*, 58(2):381–389.

Marsan, D. and Lengliné, O. (2010). A new estimation of the decay of aftershock density with distance to the mainshock. *Journal of Geophysical Research: Solid Earth (1978–2012)*, 115(B9).

Matsumura, S. (1984). Evaluation of detection capability of microearthquakes for an observational network: the kanto-tokai observational network of the national research center for disaster prevention. *Journal of the Seismological Society of Japan)*, 37:475–489.

Maxwell, S. C. and Urbancic, T. I. (2001). The role of passive microseismic monitoring in the instrumented oil field. *The Leading Edge*, 20(6):636–639.

Mayeda, K., Gök, R., Walter, W. R., and Hofstetter, A. (2005). Evidence for non-constant energy/moment scaling from coda-derived source spectra. *Geophysical research letters*, 32(10).

Mayeda, K. and Walter, W. R. (1996). Moment, energy, stress drop, and source spectra of western united states earthquakes from regional coda envelopes. *Journal of Geophysical Research: Solid Earth (1978–2012)*, 101(B5):11195–11208.

McGarr, A. (1971a). Stable deformation of rock near deep-level tabular excavations. *Journal of Geophysical Research*, 76(29):7088–7106.

McGarr, A. (1971b). Violent deformation of rock near deep-level, tabular excavations—seismic events. *Bulletin of the Seismological Society of America*, 61(5):1453–1466.

McGarr, A. (1992). Moment tensors of ten witwatersrand mine tremors. *Pure and Applied Geophysics*, 139(3):781–800.

McGarr, A. (1999). On relating apparent stress to the stress causing earthquake fault slip. *Journal of Geophysical Research: Solid Earth (1978–2012)*, 104(B2):3003–3011.

McGarr, A., Bicknell, J., Sembera, E., and Green, R. (1989). Analysis of exceptionally large tremors in two gold mining districts of south africa. *Pure and Applied Geophysics*, 129(3):295–307.

McNutt, S. R. (1992). Volcanic tremor. *Encyclopedia of earth system science*, 4:417–425.

Mégnien, C. (1980). Synthèse géologique du bassin de paris: Lexique des noms de formation. *BRGM report, (french)*, 3.

Mendecki, A. (1996). Seismic monitoring in mines. *Springer*.

Mercerat, D. (2007). Sismicite induite et modelisation numerique de l'endommagement dans un contexte salin. *Ph.D. Thesis, LAEGO Institut National Polytechnique de Lorraine, France (in French)*.

Mercerat, E., Driad-Lebeau, L., and Bernard, P. (2010). Induced seismicity monitoring of an underground salt cavern prone to collapse. *Pure and Applied Geophysics*, 167(1):5–25.

Mertl, S. and Brückl, E. (2007). Observation of fracture processes in creeping rock masses by seismic monitoring. In *Proceedings at 11th Congress of the International Society for Rock Mechanics*.

Milev, A. and Spottiswoode, S. (2002). Effect of the rock properties on mining-induced seismicity around the ventersdorp contact reef, witwatersrand basin, south africa. *Pure and Applied Geophysics*, 159(1):165–177.

Miller, A., Foulger, G., and Julian, B. (1998). Non-double-couple earthquakes. 2. Observations. *Reviews in Geophysics*, 36(4):551–568.

Miller, A., Richards, J., and McCann, D. (1988). Microseismic monitoring of the infill trial at castlefields mine, dudley. *Geological Society, London, Engineering Geology Special Publications*, 5(1):319–324.

Miller, A., Richards, J., McCann, D., Browittt, C., and Jackson, P. (1989). Microseismic techniques for monitoring incipient hazardous collapse conditions above abandoned limestone mines. *Quarterly Journal of Engineering Geology and Hydrogeology*, 22(1):1–18.

Mogi, K. (1963). Some discussions on aftershocks, foreshocks and earthquake swarms: the fracture of a semi-infinite body caused by an inner stress origin and its relation to the earthquake phenomena (third paper). *Bulletin of the Earthquake Research Institute*, 41:615–658.

Molchan, G. (2005). Interevent time distribution in seismicity: a theoretical approach. *Pure and Applied Geophysics*, 162(6-7):1135–1150.

Moradpour, J., Hainzl, S., and Davidsen, J. (2014). Nontrivial decay of aftershock density with distance in southern california. *Journal of Geophysical Research: Solid Earth*, 119(7):5518–5535.

Mori, J., Abercrombie, R. E., and Kanamori, H. (2003). Stress drops and radiated energies of aftershocks of the 1994 northridge, california, earthquake. *Journal of Geophysical Research: Solid Earth (1978–2012)*, 108(B11).

Nabalek, J. (1984). *Determination of earthquake source parameters from inversion of body waves*. PhD thesis, Massachusetts Institute of Technology, Columbia University.

Neuberg, J. and Pointer, T. (2000). Effects of volcano topography on seismic broad-band waveforms. *Geophysical Journal International*, 143(1):239–248.

Neunhofer, H. (1997). Uberwachung nichttektonischer erderschutterungen in mittel-/ostdeutschland mit lokalen seismischen stationen. *Zur Geschichte der Geophysik in Deutschland. Jubilaumsschrift, Deutsche Geophysikalische Gesellschaft, (german)*, pages 201–206.

Nothnagel, R. (2003). *Modélisation des instabilités en mécanique des roches: application à l'exploitation de la concession de Drouville*. PhD thesis, Ecole des Mines de Paris, France.

Ogasawara, H., Fujimori, K., Koizumi, N., Hirano, N., Fujiwara, S., Otsuka, S., Nakao, S., Nishigami, K., Taniguchi, K., Iio, Y., et al. (2002a). Microseismicity induced by heavy rainfall around flooded vertical ore veins. *Pure and Applied Geophysics*, 159(1-3):91–109.

Ogasawara, H., Kuwabara, Y., Miwa, T., Fujimori, K., Hirano, N., and Koizumi, M. (2002b). Post-seismic effects of an m 7.2 earthquake and microseismicity in an abandoned, flooded, deep mine. In *The Mechanism of Induced Seismicity*, pages 63–90. Springer.

Ortlepp, W., Armstrong, R., Ryder, J., and O'Connor, D. (2005). Fundamental study of micro-fracturing on the slip surface of mine-induced dynamic brittle shear zones. In *Proceedings of the 6th International Symposium on Rockbursts and Seismicity in Mines Controlling on Seismic Risk ACG*, pages 229–237.

Oye, V., Bungum, H., and Roth, M. (2005). Source parameters and scaling relations for mining-related seismicity within the pyhasalmi ore mine, finland. *Bulletin of the Seismological Society of America*, 95(3):1011.

Papanastassiou, D. and Matsumura, S. (1987). Examination of the nrcdp's (the national research center for disaster prevention) seismic observational network as regards. i. *Report of the National Research Center for Disaster Prevention*, 39:37–65.

Phillips, S., Pearson, D. C., Edwards, C., and Stump, B. W. (1996). The white pine controlled collapse experiment. Technical report, LA-UR-96.

Phillips, W. S., Rutledge, J. T., House, L. S., and Fehler, M. C. (2002). Induced microearthquake patterns in hydrocarbon and geothermal reservoirs: six case studies. pages 345–369.

Pinsky, V., Husen, S., and Lomax, A. (2008). A comparative study of robust algorithms for rapid, automatic earthquake location. In *EGU General Assembly, Geophysical Research Abstracts 10, EGU2008-A-07074*, volume 10.

Piwakowski, B., Driad-Lebeau, L., and Kosecki, A. (2006). High resolution seismic investigations in salt mining context. *EAGE, Near Surface, Helsinki, Finland*.

Plenkers, K., Kwiatek, G., Nakatani, M., Dresen, G., et al. (2010). Observation of seismic events with frequencies f¿ 25 khz at mponeng deep gold mine, south africa. *Seismological Research Letters*, 81(3):467.

Plesinger, A., Hellweg, M., and Seidl, D. (1986). Interactive high-resolution polarization analysis of broad-band seismograms. *Journal of Geophysics*, 59:129–139.

Potvin, Y. and Hudyma, M. (2001). Seismic monitoring in highly mechanized hardrock mines in canada and australia. *Rock Burst and Seismicity in Mines*, pages 267–280.

Prejean, S. G. and Ellsworth, W. L. (2001). Observations of earthquake source parameters at 2 km depth in the long valley caldera, eastern california. *Bulletin of the Seismological Society of America*, 91(2):165–177.

Prieto, G. A., Shearer, P. M., Vernon, F. L., and Kilb, D. (2004). Earthquake source scaling and self-similarity estimation from stacking p and s spectra. *Journal of Geophysical Research: Solid Earth (1978–2012)*, 109(B8).

Purcaru, G. and Berckhemer, H. (1978). A magnitude scale for very large earthquakes. *Tectonophysics*, 49(3):189–198.

Quittmeyer, R., Mrotek, K., Agnew, J., Naumoff, P., and Statton, C. (1988). Recent shallow swarms of seismicity in southeastern new york, northern new jersey and central connecticut. *Seismological Research Letters*, 59(4):197–206.

Raucoules, D., Maisons, C., Carnec, C., Le Mouelic, S., King, C., and Hosford, S. (2003). Monitoring of slow ground deformation by ers radar interferometry on the vauvert salt mine (france): Comparison with ground-based measurement. *Remote sensing of environment*, 88(4):468–478.

Richards, J. and Miller, A. (1988). Roof-fall observations at castlefields mine, dudley. *Geological Society, London, Engineering Geology Special Publications*, 5(1):293–298.

Richards-Dinger, K., Stein, R. S., and Toda, S. (2010). Decay of aftershock density with distance does not indicate triggering by dynamic stress. *Nature*, 467(7315):583–586.

Richardson, E. and Jordan, T. (2002). Seismicity in deep gold mines of south africa: Implications for tectonic earthquakes. *Bulletin of the Seismological Society of America*, 92(5):1766.

Riemer, K. (2005). Interpreting complex waveforms from some mining related seismic events. *Controlling Seismic Risk. Rockbursts and Seismicity in Mines. Nedlands: Australian Centre for Geomechanics*.

Rossler, D. (2006). *Retrieval of earthquake source parameters in Inhomogeneous anisotropic media with application to swarm events in West Bohemia in 2000*. PhD thesis, German Research Centre Potsdam, University Potsdam.

Rydelek, P. and Sacks, I. (1989). Testing the completeness of earthquake catalogues and the hypothesis of self-similarity. *Nature*, 337(6204):251–253.

Scholz, C. (2002). The mechanics of earthquakes and faulting. *Cambridge University Press*.

Sen, A. T., Cesca, S., Bischoff, M., Meier, T., and Dahm, T. (2013). Automated full moment tensor inversion of coal mining-induced seismicity. *Geophysical Journal International*, pages 1267–1281.

Senfaute, G., Abdul-Wahed, M. K., Piguet, J.-P., Josien, J.-P., et al. (2000). Qualification of the microseismic monitoring technique applied to the risk of collapse in iron ore mines. In *International symposium of the international society for rock mechanics (EUROCK 2000)*.

Senfaute, G., Wassermann, J., Homand, F., et al. (2008). Induced micro-seismicity and mechanical response during the experimental flooding of an iron ore mine. In *Post-Mining 2008. Symposium Proceedings*.

Sethian, J. A. (1999). Fast marching methods. *SIAM review*, 41:199–235.

Shapiro, S. A., Rentsch, S., and Rothert, E. (2005). Characterization of hydraulic properties of rocks using probability of fluid-induced microearthquakes. *Geophysics*, 70(2):F27–F33.

Shapiro, S. A., Rothert, E., Rath, V., and Rindschwentner, J. (2002). Characterization of fluid transport properties of reservoirs using induced microseismicity. *Geophysics*, 67(1):212–220.

Shelly, D. R., Hill, D. P., Massin, F., Farrell, J., Smith, R. B., and Taira, T. (2013). A fluid-driven earthquake swarm on the margin of the yellowstone caldera. *Journal of Geophysical Research: Solid Earth*, 118(9):4872–4886.

Šílenỳ, J. (1989). The mechanism of small mining tremors from amplitude inversion. *Pure and Applied Geophysics*, 129(3):309–324.

Sileny, J. (2004). Regional moment tensor uncertainty due to mismodeling of the crust. *Tectonophysics*, 383:133–147.

Šílenỳ, J. and Milev, A. (2008). Source mechanism of mining induced seismic events—resolution of double couple and non double couple models. *Tectonophysics*, 456(1):3–15.

Simpson, D. (1986). Triggered earthquakes. *Annual Review of Earth and Planetary Sciences*, 14:21.

Singh, S. and Ordaz, M. (1994). Seismic energy release in mexican subduction zone earthquakes. *Bulletin of the Seismological Society of America*, 84(5):1533–1550.

Smith, T., Whitham, K., and Piche, W. (1968). A microearthquake swarm in 1965 near mould bay, nwt, canada. *Bulletin of the Seismological Society of America*, 58(6):1991–2011.

Souley, M., Mercerat, D., Driad-Lebeau, L., Bernard, P., et al. (2008). A large scale continuum-discrete numerical modelling: Application to overburden damage of a salt cavern. In *Post-Mining 2008. Symposium Proceedings*.

Špičák, A. and Horálek, J. (2001). Possible role of fluids in the process of earthquake swarm generation in the west bohemia/vogtland seismoactive region. *Tectonophysics*, 336(1):151–161.

Spillmann, T., Maurer, H., Green, A. G., Heincke, B., Willenberg, H., and Husen, S. (2007). Microseismic investigation of an unstable mountain slope in the swiss alps. *Journal of Geophysical Research: Solid Earth (1978–2012)*, 112(B7).

Spottiswoode, S. (1989). Perspectives on seismic and rockburst research in the south african gold mining industry: 1983–1987. *Pure and Applied Geophysics*, 129(3):673–680.

Spottiswoode, S. and McGarr, A. (1975). Source parameters of tremors in a deep-level gold mine. *Bulletin of the Seismological Society of America*, 65(1):93–112.

Spottiswoode, S. and Milev, A. (1998). The use of waveform similarity to define planes of mining-induced seismic events. *Tectonophysics*, 289(1-3):51–60.

Stabile, T., Iannaccone, G., Zollo, A., Lomax, A., Ferulano, M., Vetri, M., and Barzaghi, L. (2013). A comprehensive approach for evaluating network performance in surface and borehole seismic monitoring. *Geophysical Journal International*, 192(2):793–806.

Stein, R. (1999). The role of stress transfer in earthquake occurrence. *Nature*, 402(6762):605–609.

Suffert, J. (2006). Etude d'une cavite saline par methodes sismiques. *BRGM Report.*

Syratt, P. (1990). Seismicity associated with the extraction of stressed remnants in the klerksdorp gold mining district, south africa. In *Rockbursts and Seismicity in Mines; Proc. 3rd International Congress*.

Taisne, B., Brenguier, F., Shapiro, N., and Ferrazzini, V. (2011). Imaging the dynamics of magma propagation using radiated seismic intensity. *Geophysical Research Letters*, 38:L04304.

Takei, Y. and Kumazawa, M. (1994). Why have the single force and torque been excluded from seismic source models? *Geophysical Journal International*, 118(1):20–30.

Tarantola, A. (2005). Inverse problem theory and methods for model parameter estimation. *Society for Industrial and Applied Mathematics, Philadelphia*.

Tarantola, A. and Valette, B. (1982). Inverse problems = quest for information. *Journal of Geophysics*, 20(2):159–170.

Tary, J., Baan, M., and Eaton, D. (2014). Interpretation of resonance frequencies recorded during hydraulic fracturing treatments. *Journal of Geophysical Research: Solid Earth*, 119(2):1295–1315.

Thomson, W. (1950). Transmission of Elastic Waves through a Stratified Solid Medium. *Journal of Applied Physics*, 21:89–93.

Toon, S. and Styles, P. (2004). Microseismic monitoring of abandoned salt mines beneath northwich, cheshire, uk. In *10th European Meeting of Environmental and Engineering Geophysics*.

Trifu, C. and Shumila, V. (2010). Microseismic monitoring of a controlled collapse in field ii at ocnele mari, romania. *Pure and applied geophysics*, 167(1-2):27–42.

Utsu, T. (1966). A statistical significance test of the difference in b-value between two earthquake groups. *Journal of Physics of the Earth*, 14(2):37–40.

Utsu, T., Ogata, Y., and Matsu'ura, R. S. (1995). The centenary of the omori formula for a decay law of aftershock activity. *Journal of Physics of the Earth*, 43(1):1–33.

Van Kampen, N. G. (1992). Stochastic processes in physics and chemistry. *Elsevier*.

Vavryčuk, V. (2001). Inversion for parameters of tensile earthquakes. *Journal of Geophysical Research: Solid Earth (1978–2012)*, 106(B8):16339–16355.

Vavryčuk, V. (2011). Tensile earthquakes: theory, modeling, and inversion. *Journal of Geophysical Research: Solid Earth (1978–2012)*, 116(B12).

Vavryvcuk, V. (2002). Non-double-couple earthquakes of 1997 January in West Bohemia, Czech Republic: evidence of tensile faulting. *Geophysical Journal International*, 149(2):364–373.

Viegas, G., Baig, A., Coulter, W., and Urbancic, T. (2012). Effective monitoring of reservoir-induced seismicity utilizing integrated surface and downhole seismic networks. *First Break*, 30(7):77–81.

Wachs, D., Yechieli, Y., Shtivelman, V., Itamar, A., Baer, G., Goldman, M., Raz, E., Rybekov, M., and Schattner, U. (2000). Formation of sinkholes along the dead sea shore–summary of findings from the first stage of research. *Israel Geological Survey, Jerusalem, Rep*, 41:49.

Walter, W. R. and Brune, J. N. (1993). Spectra of seismic radiation from a tensile crack. *Journal of Geophysical Research: Solid Earth (1978–2012)*, 98(B3):4449–4459.

Walter, W. R., Mayeda, K., Gok, R., and Hofstetter, A. (2006). The scaling of seismic energy with moment: Simple models compared with observations. *Earthquakes: Radiated energy and the physics of faulting*, pages 25–41.

Waltham, T., Bell, F. G., and Culshaw, M. (2005). Sinkholes and subsidence. *Springer*.

Waltham, T., Park, H., Suh, J., Yu, M., Kwon, H., and Bang, K. (2011). Collapses of old mines in korea. *Engineering Geology*, 118(1):29–36.

Wang, R. (1999). A simple orthonormalization method for stable and efficient computation of Green's functions. *Bulletin of the Seismological Society of America*, 89(3):733–741.

Ward, P. L. and Björnsson, S. (1971). Microearthquakes, swarms, and the geothermal areas of iceland. *Journal of Geophysical Research*, 76(17):3953–3982.

Warpinski, N. (2009). Microseismic monitoring: Inside and out. *Journal of Petroleum Technology*, 61(11):80–85.

Warpinski, N., Wolhart, S., Wright, C., et al. (2004). Analysis and prediction of microseismicity induced by hydraulic fracturing. *SPE Journal*, 9(01):24–33.

Whyatt, J. and Varley, F. (2008). Catastrophic failures of underground evaporite mines. In *Proceedings: 27th International Conference on Ground Control in Mining*, pages 29–31.

Wielandt, E. (2001). Basics of the volume-source model and its application in volcano seismology. *Lesson script, Institute of Geophysics, University of Stuttgart. Online at ftp.geophys.uni-stuttgart.de/pub/ew/postscripts.*

Wileveau, Y., Cornet, F., Desroches, J., and Blumling, P. (2007). Complete in situ stress determination in an argillite sedimentary formation. *Physics and Chemistry of the Earth*, 32(8):866–878.

Woessner, J. and Wiemer, S. (2005). Assessing the quality of earthquake catalogues: Estimating the magnitude of completeness and its uncertainty. *Bulletin of the Seismological Society of America*, 95(2):684–698.

Wright, T. J., Ebinger, C., Biggs, J., Ayele, A., Yirgu, G., Keir, D., and Stork, A. (2006). Magma-maintained rift segmentation at continental rupture in the 2005 afar dyking episode. *Nature*, 442(7100):291–294.

Wu, C., Shelly, D. R., Gomberg, J., Peng, Z., and Johnson, P. (2013). Long-term changes of earthquake inter-event times and low-frequency earthquake recurrence in central california. *Earth and Planetary Science Letters*, 368:144–150.

Wuestefeld, A., Al-Harrasi, O., Verdon, J. P., Wookey, J., and Kendall, J. M. (2010). A strategy for automated analysis of passive microseismic data to image seismic anisotropy and fracture characteristics. *Geophysical Prospecting*, 58(5):755–773.

Wuestefeld, A., Kendall, J. M., Verdon, J. P., and van As, A. (2011). In situ monitoring of rock fracturing using shear wave splitting analysis: an example from a mining setting. *Geophysical Journal International*, 187(2):848–860.

Wust-Bloch, G. H. and Joswig, M. (2006). Pre-collapse identification of sinkholes in unconsolidated media at dead sea area by nanoseismic monitoring (graphical jackknife location of weak sources by few, low-snr records). *Geophysical Journal International*, 167(3):1220–1232.

Wyss, M. and Brune, J. N. (1968). Seismic moment, stress, and source dimensions for earthquakes in the california-nevada region. *Journal of Geophysical Research*, 73(14):4681–4694.

Wyss, M., Shimazaki, K., and Wiemer, S. (1997). Mapping active magma chambers by b values beneath the off-ito volcano, japan. *Journal of Geophysical Research: Solid Earth (1978–2012)*, 102(B9):20413–20422.

Yamasato, H. (1997). Quantitative analysis of pyroclastic flows using infrasonic and seismic data at unzen volcano. *Physics of the Earth*, 45:397–416.

Zamfirescu, F., Mocuta, M., Constantinecu, T., Medves, E., and Danchiv, A. (2003). The main causes of a geomechanical accident of brine caverns at field ii of ocnele mari-romania. *RMZ-Materials and Geoenvironment*, 50:431–434.

Zhu, T., Chun, K., and G.F., W. (1991). Geometrical spreading and q of pn waves: An investigative study in eastern canada. *Bulletin of the Seismological Society of America*, 81:882–896.

Zhuang, J., Harte, D., Werner, M. J., Hainzl, S., and Zhou, S. (2012). Basic models of seismicity: Temporal models. *Community Online Resource for Statistical Seismicity Analysis, doi:10.5078/corssa-79905851. Available at* `http://www.corssa.org`.

Zoback, M. D. and Harjes, H.-P. (1997). Injection-induced earthquakes and crustal stress at 9 km depth at the ktb deep drilling site, germany. *Journal of Geophysical Research: Solid Earth (1978–2012)*, 102(B8):18477–18491.

Appendix A

Glossary

Abbreviations

abbreviations	description
BRGM	Bureau de Recherches Géologiques et Minières
CLVD	Compensated linear vector dipole
d	Day
DC	Equivalent body force double-couples
ds	Dip-slip
E	East
EDT	Equal Differential Time likelihood function
ETAS	Epidemic-Type Aftershock Sequence Model
fft	Fast Fourier transformation
GISOS	Groupement d'Intérêt Scientifique sur l'impact et la Sécurité des Ouvrages Souterrains
GPS	Global Positioning System
H	Hour
INERIS	l'Institut National de l'Environnement Industriel et des Risques
ISO	Isotropic moment tensor
iso	Explosion
IPGP	l'Institut de Physique du Globe de Paris
L	Aligned in direction of P wave propagation
$l1$-norm	Manhattan norm
$l2$-norm	Euclidean norm
LP	Long period
KIWI	Kinematic Waveform Inversion
m	Month
M	Minute
Moho	The Mohorovičić discontinuity
MT	Moment tensor
N	North
NGF	Nivellement Général de la France
Q	Aligned in the direction of the SV phase movement
P	compressional wave
Pg	Direct compressional wave
Pn	Refracted compressional wave / head wave
PDF	Probability densities function
R	Radial
RSD	Relative standard deviation
RTK	Real Time Kinematic
S	Shear wave / South
SH	Shear waves polarized in the horizontal plane / horizontal shear mode
SV	Shear wave polarized in the vertical plane / vertical shear mode
STA/LTA	short-time-average through long-time-average trigger
SYTGEM	Systeme de Télésurveillance et analyse de données d'monitoring microsismique et géotechnique
ss	Strike-slip
T	Transversal/Aligned in the direction of the SH phase movement
tc	Tensile crack
UTC	Coordinated Universal Time
W	West
WSM	World Stress Map
y	Year
Z	Vertical

Operators

operator	description
$*$	Convolution symbol
$\langle\rangle$	Arithmetic mean
$\|\|$	Absolute value
log	Natural logarithm (Euler's number)
$\log_{10}$	Decadic logarithm
exp	Natural exponential function (Euler's number)

Symbols

quantity	unit	description
$\#$		number
θ	$^\circ$	Incidence angle
ρ	g/cm^3	Density
ρ_D		Probability density between model and data space
ρ_M		Prior probability density in the model space
σ		Posterior probability density (PDF)
$\Delta\sigma$	Pa	Stress drop
σ_{app}	Pa	Apparent stress
φ	$^\circ$	Backazimuth angle
A		Amplitude
A_0		Amplitude at the source
C		Cross-correlation coefficient
E		apparent radiated energy
E_P	J	Radiated P wave energy
f	Hz	Frequency
M_0	Nm	Scalar seismic moment
M		Earthquake magnitudes
M_L		Local magnitude
M_w		Moment magnitude
M_C		Magnitude of completeness
n		Coefficient of geometrical spreading
$Q_{P,S}$		Quality factor
r	SI-distance	Distance
r_0	SI-length	Source radius
s		Receiver amplification site effect
S_H	Pa	Maximal horizontal stress
S_h	Pa	Minimal horizontal stress
S_v	Pa	Maximal vertical stress
V_P	SI-velocity	P-wave velocity
V_S	SI-velocity	S-wave velocity
V	SI-volume	Source volume

Appendix B

Supplementary Tables and Figures

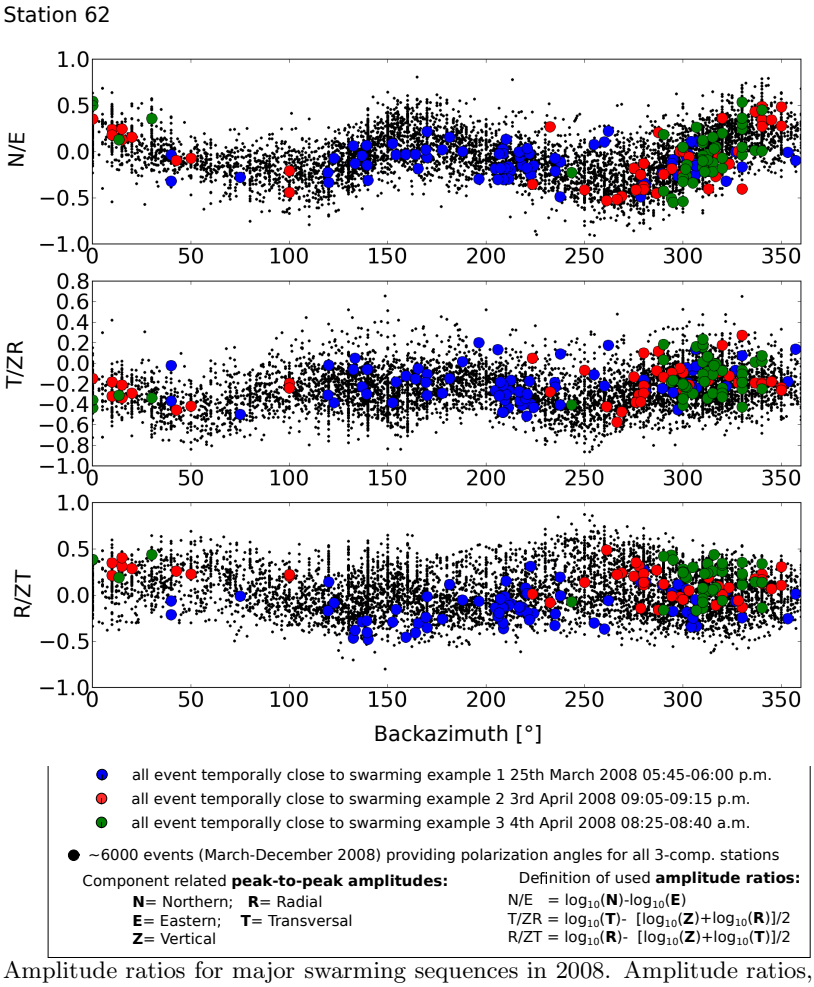

Figure B.1: Amplitude ratios for major swarming sequences in 2008. Amplitude ratios, as used during the inversion approach 3 (Section 3.2.4.3), are shown as a function of backazimuth angle of station 62 for the events temporally close ($\sim$ 10 min) to the major swarming examples 1-3 (colored dots) (Fig. 2.18-2.21) and the $\sim$ 6000 events of the microseismic crisis in 2008 (black dots).

Table B.1: Training set of the 54 located events (Section 2.1). Hypocenter source locations are listed by northing (Y), easting(X) coordinates in meters relative to a reference point X = 892900 m and Y= 116000 m defined by the Lambert 1 Nord (NTF, Paris) coordinate system and depth (Z) in meters relative to the surface. Manually picked P and S wave arrival times (t_p and t_s) are given in seconds relative the triggered event file onset date and time (is the same for all stations).

dat-time	X	Y	Z	$t_{p,1}$	$t_{p,2}$	$t_{p,3}$	$t_{p,5}$	$t_{p,63}$	$t_{p,62}$	$t_{p,61}$	$t_{p,7}$	$t_{p,8}$	$t_{s,3}$	$t_{s,5}$	$t_{s,63}$	$t_{s,62}$	θ_3	θ_5	θ_{63}	θ_{62}	φ_3	φ_5	φ_{63}	φ_{62}
[yymmdd_hhmmssss]	[m]	[m]	[m]	[s]	[s]	[s]	[s]	[s]	[s]	[s]	[s]	[s]	[s]	[s]	[s]	[s]	[°]	[°]	[°]	[°]	[°]	[°]	[°]	[°]
080316_11222906	370	150	−220	0.392	0.3636	0.3650	0.3690	0.3010	0.3150	0.3746	0.4068	0.3714	0.4110	0.4800	0.3390	0.3870	160	60	282	53	212	68	208	30
080317_17470327	400	130	−200	0.4194	0.3768	0.3750	0.3750	0.3350	0.3560	0.3878	0.4164	0.3810	0.4160	0.4600	0.3560	0.4030	153	49	282	51	186	65	188	15
080318_03542811	470	120	−220	0.4326	0.3862	0.3850	0.3670	0.3160	0.3360	0.3746	0.4084	0.3802	0.4380	0.4560	0.3560	0.4120	135	55	290	60	135	65	135	25
080325_21020502	430	120	−210	0.4288	0.3740	0.3800	0.3678	0.3384	0.3592	0.3802	0.4112	0.3780	0.4470	0.4258	0.3518	0.4186	140	55	284	55	168	70	170	22
080326_07474929	360	150	−210	0.394	0.3526	0.3610	0.3600	0.3250	0.3450	0.3632	0.4112	0.3572	0.4440	0.4380	0.3410	0.3890	160	64	271	55	210	45	215	25
080403_07284806	360	160	−220	0.4276	0.3594	0.3840	0.3980	0.3350	0.3660	0.3798	0.3950	0.3740	0.4310	0.4720	0.3560	0.4060	143	59	298	45	215	74	215	20
080403_14202167	370	200	−210	0.4406	0.3726	0.3840	0.4100	0.3380	0.3750	0.3768	0.4094	0.3840	0.4210	0.4900	0.3650	0.4170	138	42	302	30	250	62	250	20
080405_13431225	370	170	−220	0.4204	0.3806	0.3840	0.4030	0.3360	0.3560	0.3934	0.4186	0.3966	0.4300	0.4800	0.3500	0.4130	143	54	285	40	210	73	230	55
080318_11452447	390	210	−180	0.4258	0.3754	0.3680	0.3920	0.3290	0.3500	0.3544	0.3850	0.3938	0.4260	0.4810	0.3440	0.3870	137	55	305	45	245	70	252	42
080327_21575315	380	150	−200	0.4294	0.3710	0.3750	0.3890	0.3340	0.3640	0.3826	0.4134	0.3808	0.4250	0.4720	0.3450	0.4210	178	61	287	45	200	70	203	34
080327_23231661	410	170	−210	0.4296	0.3726	0.3730	0.3810	0.3280	0.3500	0.3724	0.4006	0.3784	0.4350	0.4660	0.3390	0.3960	150	55	297	51	189	76	192	60
080401_03170422	340	190	−230	0.3922	0.3574	0.3520	0.3810	0.3200	0.3400	0.3736	0.4012	0.3724	0.4130	0.4690	0.3370	0.3960	141	62	300	50	238	73	253	39
080402_23311877	340	200	−210	0.3976	0.3514	0.3440	0.4160	0.3200	0.3400	0.3656	0.4278	0.3684	0.4090	0.4850	0.3380	0.3800	148	60	303	36	261	78	254	18
080404_22580698	340	250	−200	0.4078	0.3606	0.3440	0.3930	0.3220	0.3410	0.3706	0.3984	0.3864	0.3970	0.4930	0.3350	0.3840	130	60	307	30	293	70	290	13
080405_08212726	400	210	−190	0.4374	0.3886	0.3810	0.3980	0.3350	0.3610	0.3958	0.4198	0.4024	0.4330	0.4720	0.3420	0.3920	136	60	315	42	236	79	254	44
080504_09590363	370	190	−190	0.4218	0.3798	0.3740	0.4010	0.3380	0.3590	0.3902	0.4168	0.3942	0.4370	0.4910	0.3470	0.4280	139	60	297	53	234	73	233	30
080310_10162058	480	260	−230	0.4406	0.3784	0.3600	0.3660	0.3150	0.3320	0.3658	0.3638	0.3984	0.4330	0.4650	0.3360	0.3860	99	56	337	54	52	74	47	34
080314_10345214	450	290	−190	0.4454	0.3726	0.3870	0.4040	0.3440	0.3560	0.3902	0.3858	0.4172	0.4640	0.5160	0.3660	0.4250	92	57	335	56	36	63	22	16
080315_11060290	450	290	−200	0.4186	0.3718	0.3450	0.3770	0.3100	0.3300	0.3674	0.3548	0.3916	0.3920	0.4690	0.3420	0.3700	90	61	328	55	44	70	23	14
080317_22522921	500	220	−220	0.4516	0.3952	0.3800	0.3750	0.3250	0.3490	0.3836	0.3860	0.4022	0.4250	0.4650	0.3420	0.3910	107	48	337	63	87	75	77	28
080320_01343152	470	300	−210	0.4488	0.3924	0.3620	0.3952	0.3402	0.3628	0.3550	0.3628	0.3986	0.4280	0.4848	0.3648	0.4094	116	50	340	50	30	68	40	5
080327_07033611	450	260	−200	0.4450	0.3900	0.3770	0.3900	0.3190	0.3400	0.3738	0.3828	0.4034	0.4400	0.4830	0.3380	0.3910	106	63	332	43	26	77	39	41
080328_00393962	420	290	−180	0.4390	0.3878	0.3690	0.4050	0.3380	0.3560	0.3830	0.3920	0.4210	0.4260	0.5100	0.3560	0.3930	87	60	324	31	358	68	6	5
080329_12051154	460	290	−210	0.4328	0.3930	0.3550	0.3730	0.3190	0.3380	0.3732	0.3632	0.3926	0.4240	0.4760	0.3510	0.3970	93	57	339	53	44	68	38	10
080405_08493788	370	280	−230	0.3830	0.3408	0.3190	0.3910	0.3120	0.3260	0.3628	0.3514	0.3748	0.3960	0.5000	0.3410	0.3740	103	74	330	30	325	52	330	20
080411_12264951	390	270	−150	0.4326	0.3848	0.3650	0.4100	0.3310	0.3510	0.3866	0.3942	0.4078	0.3970	0.5000	0.3410	0.3900	110	62	331	40	341	66	355	10
080414_14275367	470	260	−160	0.7124	0.6594	0.6440	0.6540	0.5920	0.6120	0.6388	0.6426	0.6722	0.6910	0.7610	0.6060	0.6780	100	45	330	40	51	73	42	7
080414_15212185	480	280	−160	0.4570	0.3972	0.3810	0.3890	0.3390	0.3580	0.3932	0.3808	0.4134	0.4300	0.4860	0.3510	0.3930	99	53	339	41	37	72	44	5
080415_19473377	320	300	−200	0.4112	0.3732	0.3520	0.4010	0.3330	0.3510	0.3796	0.4068	0.3912	0.3920	0.4900	0.3470	0.3920	95	48	324	42	289	76	302	20
080502_01543119	330	280	−230	0.3488	0.3232	0.3020	0.3640	0.2900	0.3090	0.3444	0.3530	0.3538	0.3600	0.4920	0.3250	0.3780	108	75	327	27	308	60	290	28
080314_01311632	490	160	−200	0.4560	0.3860	0.3830	0.3570	0.3280	0.3480	0.3794	0.3916	0.3930	0.4560	0.4360	0.3580	0.4010	127	54	325	45	127	76	133	11
080314_05492504	440	150	−210	0.4300	0.3748	0.3850	0.3684	0.3230	0.3432	0.3786	0.4000	0.3798	0.4530	0.4642	0.3508	0.3996	133	54	310	51	161	70	170	40
080318_05470617	460	140	−190	0.4282	0.3824	0.3880	0.3616	0.3232	0.3466	0.3644	0.3936	0.3812	0.4740	0.4030	0.3474	0.3806	140	53	294	63	154	63	150	21
080318_14571255	480	170	−210	0.4538	0.3862	0.3930	0.3680	0.3290	0.3520	0.3850	0.3936	0.3938	0.4590	0.4610	0.3590	0.4080	135	53	313	68	128	66	120	20
080325_18265881	440	130	−180	0.4328	0.3776	0.3850	0.3662	0.3256	0.3472	0.3818	0.4050	0.3792	0.4520	0.4546	0.3440	0.4016	155	54	280	55	164	68	165	15
080326_20575908	510	150	−180	0.4466	0.3942	0.3920	0.3510	0.3310	0.3410	0.3728	0.3800	0.3824	0.4500	0.4460	0.3540	0.3980	136	46	321	66	123	51	114	6
080403_05524621	520	190	−230	0.4452	0.3878	0.3950	0.3500	0.3160	0.3370	0.3592	0.3670	0.3794	0.4510	0.4410	0.3500	0.3840	105	55	328	71	100	67	95	16
080404_13020368	470	140	−180	0.4366	0.3986	0.3970	0.3834	0.3266	0.3624	0.3580	0.3806	0.3738	0.4310	0.4542	0.3466	0.3966	154	62	305	56	137	75	140	23
080409_04404319	480	150	−180	0.4410	0.3942	0.3940	0.3660	0.3358	0.3542	0.3846	0.3994	0.3920	0.4540	0.4448	0.3506	0.3958	140	59	308	67	133	62	132	5
080520_16321889	460	90	−230	0.4106	0.3516	0.3670	0.3280	0.3360	0.3600	0.3396	0.3570	0.3196	0.4460	0.4210	0.3580	0.4190	142	58	265	66	151	66	151	21
080319_15051184	480	220	−190	0.4586	0.3886	0.4240	0.3960	0.3320	0.3460	0.3796	0.3842	0.3960	0.4790	0.4620	0.3560	0.3870	122	42	336	64	92	70	89	37
080326_01394174	440	190	−200	0.4600	0.3962	0.4500	0.4200	0.3320	0.3930	0.3884	0.4062	0.4002	0.4970	0.4970	0.3560	0.4550	133	50	321	57	135	60	135	28
080327_09212718	440	210	−200	0.4436	0.3948	0.3930	0.3930	0.3390	0.3600	0.3890	0.3996	0.4064	0.4680	0.4730	0.3550	0.4340	117	47	325	54	115	76	100	35
080327_20182797	460	240	−180	0.4674	0.3832	0.3900	0.3880	0.3012	0.3266	0.3682	0.3788	0.4010	0.4270	0.4980	0.3274	0.3792	125	58	322	44	56	68	56	22
080328_00123791	410	200	−200	0.4308	0.3768	0.3690	0.3830	0.3140	0.3470	0.3806	0.4030	0.3952	0.4320	0.4720	0.3330	0.3960	139	58	316	44	200	84	197	45
080329_00222991	460	230	−180	0.4576	0.3988	0.3930	0.3930	0.3320	0.3530	0.3950	0.3978	0.4106	0.4230	0.4670	0.3460	0.4020	114	51	316	47	65	84	77	49
080329_06192049	440	210	−190	0.4548	0.4010	0.3900	0.3970	0.3380	0.3600	0.3954	0.4086	0.4080	0.4260	0.4680	0.3560	0.4200	125	57	317	46	98	84	87	56
080403_10130177	440	150	−190	0.4440	0.3932	0.3950	0.3870	0.3340	0.3560	0.3888	0.4084	0.3998	0.4440	0.4580	0.3450	0.4090	146	55	280	64	160	77	151	62
080404_07232788	360	210	−210	0.4198	0.3748	0.3700	0.3990	0.3380	0.3600	0.3900	0.4128	0.3992	0.4240	0.4840	0.3480	0.4110	138	60	303	42	268	77	270	34
080405_03374333	460	210	−150	0.4500	0.4018	0.3960	0.3850	0.3380	0.3570	0.3894	0.4054	0.4026	0.4550	0.4710	0.3480	0.3910	144	54	339	30	107	72	88	5
080405_03440140	460	170	−150	0.4500	0.4068	0.4020	0.3810	0.3370	0.3560	0.3924	0.4272	0.4030	0.4730	0.4600	0.3480	0.3900	123	50	326	50	123	70	126	7
080405_08053299	410	190	−190	0.4436	0.3924	0.3860	0.3920	0.3370	0.3570	0.3838	0.4150	0.3974	0.4440	0.4730	0.3440	0.3960	148	56	307	39	190	75	187	18
080405_22381203	420	130	−220	0.4364	0.3848	0.3920	0.3820	0.3360	0.3560	0.3926	0.4238	0.3888	0.4490	0.4780	0.3450	0.4280	126	56	267	55	177	70	177	18
080501_05543599	420	130	−180	0.4270	0.3830	0.4100	0.3838	0.3744	0.3952	0.3884	0.4180	0.3888	0.4650	0.4434	0.3812	0.4260	152	59	295	48	179	73	173	28

Table B.2: Training set of 20 located events below station 6 1-3 (Section 2.3.2.2). Depth (Z) is given in meters relative to the surface. Manually picked P and S wave arrival times (t_p and t_s) are given in seconds relative the triggered event file onset date and time (is the same for all stations). Velocities and Q factor estimations for sedimentary layers between station 6 1-3 were estimated by the cross-correlation and spectral ratio methods described in Section 2.3.2.2.

dat-time [yymmdd_hhmmssss]	Z [m]	$t_{p,62}$ [s]	$t_{s,62}$ [s]	$t_s - t_p$ [s]	$V_{p,61-62}$ [m/s]	$V_{p,61-63}$ [m/s]	$V_{p,62-63}$ [m/s]	$V_{s,62-63;N}$ [m/s]	$V_{s,62-63;E}$ [m/s]	$Q_{p,61-62}$	$Q_{p,61-63}$	$Q_{p,62-63}$	$Q_{s,62-63;N}$	$Q_{s,62-63;E}$
080315_01091031	−216	0.3640	0.4420	0.0780	1685	2138	2902	1295	|	6	10	42	18	27
080318_05493013	−204	0.5250	0.5910	0.0660	1694	2190	2982	1343	1300	7	10	30	12	16
080318_09170764	−200	0.3700	0.4290	0.0590	1703	2197	2982	|	1295	6	8	72	12	22
080318_23112620	−165	0.3670	0.4110	0.0440	1694	2131	2876	|	1432	5	8	58	20	26
080325_20504198	−185	3.0070	3.0630	0.0560	1694	2131	2876	1419	1332	5	15	34	24	24
080327_07513579	−195	0.4230	0.4660	0.0430	1713	2131	2851	|	1310	6	13	57	14	15
080327_20400879	−172	0.3650	0.4130	0.0480	1667	2138	2928	1290	1310	7	14	32	21	20
080327_20513983	−167	0.3970	0.4470	0.0500	1676	2145	2928	|	|	7	11	24	15	21
080402_21334282	−167	0.3800	0.4220	0.0420	1694	2131	2876	1270	|	6	11	46	17	|
080403_05293033	−173	0.3700	0.4180	0.0480	1685	2145	2902	|	1310	5	14	50	14	18
080403_10561405	−148	0.3420	0.3820	0.0400	1676	2131	2902	|	1471	5	9	35	18	15
080405_00591230	−188	16.9280	16.9730	0.0450	1722	2182	2955	1295	1371	|	|	51	28	22
080405_06485985	−178	0.3590	0.4220	0.0630	1685	2175	2955	|	|	5	9	|	13	19
080405_20244442	−142	0.6770	0.7130	0.0360	1685	2182	2982	|	1300	6	11	|	15	16
080405_21350054	−142	0.3650	0.4000	0.0350	1694	2190	3009	|	1316	6	11	24	19	18
080407_18433978	−164	0.3640	0.4170	0.0530	1685	2175	3009	|	|	6	8	31	19	15
080409_01134275	−172	2.3350	2.3910	0.0560	1694	2167	2955	|	1295	7	15	54	24	18
080411_08052526	−146	0.3470	0.3840	0.0370	1676	2175	2955	|	1300	5	10	95	|	|
080413_04261694	−159	0.3640	0.4120	0.0480	1685	2205	3009	|	1321	6	12	23	22	14
081019_09060099	−216	0.3700	0.4390	0.0690	1640	2131	2982	1316	|	7	|	58	22	30

Table B.3: P wave travel time difference for different station couples obtained from cross-correlation analysis for the 20 events located below stations 6 1-3 (Section 2.3.2.2, Table B.2). NaN indicates that no travel time difference could be determined because wave forms for the respective event and station couple were not sufficiently similar.

dat-time	Z	Travel time difference P waves [s] for Station couples i-j																												
[yymmdd_hhmmssss]	[m]	$1-2$	$2-3$	$1-61$	$1-62$	$1-63$	$2-3$	$2-61$	$2-62$	$2-63$	$2-8$	$3-61$	$3-62$	$3-63$	$3-7$	$5-61$	$5-62$	$5-63$	$5-7$	$5-8$	$61-62$	$61-63$	$61-7$	$61-8$	$62-63$	$62-7$	$62-8$	$63-7$	$63-8$
080315_01091031	−216	NaN	NaN	NaN	NaN	NaN	0.01	-0.00	0.03	0.06	NaN	NaN	0.02	0.04	NaN	NaN	0.04	0.06	NaN	NaN	0.04	0.06	NaN	-0.01	0.02	NaN	-0.05	NaN	-0.07
080318_05493013	−204	NaN	NaN	NaN	NaN	NaN	NaN	NaN	NaN	NaN	NaN	NaN	NaN	0.05	NaN	-0.00	0.03	0.05	NaN	NaN	0.04	0.06	-0.01	NaN	0.02	-0.05	-0.05	-0.07	-0.07
080318_09170764	−200	NaN	NaN	NaN	NaN	NaN	NaN	NaN	NaN	NaN	NaN	NaN	NaN	0.05	NaN	NaN	0.03	NaN	NaN	NaN	0.04	0.06	NaN	-0.01	0.02	NaN	NaN	-0.07	NaN
080318_23112620	−165	NaN	NaN	NaN	0.08	0.10	0.01	-0.00	NaN	0.06	NaN	NaN	0.02	0.04	NaN	NaN	NaN	NaN	NaN	NaN	0.04	0.06	NaN	NaN	0.02	-0.05	-0.05	-0.08	NaN
080325_20504198	−185	0.0428	0.06	0.04	NaN	0.10	NaN	0.00	NaN	NaN	NaN	NaN	NaN	0.05	-0.03	NaN	NaN	NaN	NaN	NaN	-0.01	0.04	0.06	-0.02	NaN	0.02	NaN	NaN	NaN	NaN
080327_07513579	−195	0.043	0.05	NaN	NaN	0.10	0.01	NaN	NaN	NaN	-0.01	NaN	NaN	0.04	NaN	NaN	NaN	NaN	NaN	NaN	-0.01	0.04	0.06	NaN	-0.01	0.02	-0.05	NaN	NaN	NaN
080327_20400879	−172	0.0422	0.06	0.04	NaN	NaN	0.01	NaN	NaN	0.06	-0.02	NaN	0.02	0.04	NaN	NaN	0.04	0.06	NaN	NaN	0.04	0.06	-0.02	-0.02	0.02	NaN	NaN	NaN	NaN
080327_20513983	−167	NaN	NaN	NaN	NaN	NaN	0.01	-0.00	NaN	0.06	NaN	NaN	0.03	0.05	NaN	NaN	0.03	0.06	NaN	NaN	0.04	0.06	NaN	-0.01	0.02	NaN	NaN	NaN	NaN
080402_21334282	−167	0.0428	0.06	NaN	NaN	0.10	NaN	NaN	0.03	NaN	NaN	NaN	0.02	0.04	NaN	NaN	NaN	NaN	NaN	NaN	0.04	0.06	-0.02	-0.01	0.02	NaN	-0.05	-0.08	-0.07
080403_05293033	−173	0.045	NaN	0.05	NaN	0.11	0.01	0.00	0.04	0.06	-0.01	-0.01	NaN	0.05	NaN	NaN	0.03	NaN	NaN	NaN	0.04	0.06	NaN	NaN	0.02	NaN	NaN	NaN	-0.07
080403_10561405	−148	0.0442	NaN	NaN	0.08	NaN	0.01	NaN	NaN	NaN	NaN	NaN	0.03	0.05	-0.03	NaN	NaN	0.06	NaN	NaN	0.04	0.06	NaN	NaN	0.02	-0.05	NaN	-0.08	NaN
080405_00591230	−188	0.0432	0.06	NaN	0.08	NaN	NaN	0.00	NaN	0.06	-0.02	NaN	NaN	0.05	NaN	NaN	NaN	NaN	NaN	NaN	0.04	0.06	NaN	NaN	0.02	-0.05	NaN	NaN	NaN
080405_06485985	−178	NaN	0.05	0.05	NaN	NaN	NaN	0.01	0.04	0.07	-0.01	NaN	NaN	NaN	NaN	0.00	0.04	0.06	NaN	-0.02	0.04	0.06	-0.02	NaN	0.02	NaN	NaN	NaN	NaN
080405_20244442	−142	NaN	NaN	0.05	NaN	NaN	NaN	NaN	NaN	0.07	-0.01	NaN	NaN	NaN	-0.02	NaN	0.04	0.06	NaN	NaN	0.04	0.06	-0.02	NaN	0.02	-0.05	NaN	-0.07	NaN
080405_21350054	−142	0.0448	NaN	NaN	NaN	NaN	0.01	NaN	NaN	NaN	-0.02	NaN	NaN	NaN	NaN	NaN	0.04	NaN	-0.01	NaN	0.04	0.06	NaN	NaN	0.02	NaN	NaN	NaN	NaN
080407_18433978	−164	NaN	0.06	0.05	0.09	NaN	NaN	0.01	0.04	0.06	-0.01	-0.01	NaN	0.05	NaN	NaN	NaN	NaN	NaN	-0.02	0.04	0.06	NaN	NaN	0.02	NaN	NaN	NaN	NaN
080409_01134275	−172	NaN	0.06	0.05	NaN	0.11	NaN	0.01	NaN	0.06	NaN	-0.01	NaN	0.05	-0.02	NaN	NaN	0.06	-0.01	-0.02	0.04	0.06	NaN	-0.02	0.02	NaN	NaN	-0.08	-0.08
080411_08052526	−146	NaN	NaN	NaN	NaN	NaN	NaN	NaN	NaN	NaN	-0.01	NaN	NaN	NaN	NaN	NaN	NaN	NaN	NaN	-0.02	0.04	0.06	NaN	NaN	0.02	NaN	NaN	NaN	NaN
080413_04261694	−159	0.0444	NaN	0.06	0.10	NaN	0.01	NaN	NaN	0.07	NaN	NaN	NaN	NaN	NaN	NaN	0.04	0.06	-0.01	NaN	0.04	0.06	-0.01	NaN	0.02	NaN	NaN	-0.07	NaN
081019_09060099	−216	0.0404	NaN	NaN	0.07	NaN	NaN	NaN	0.03	0.05	NaN	NaN	0.02	0.04	NaN	NaN	NaN	NaN	-0.02	NaN	0.04	0.06	NaN	-0.01	0.02	NaN	-0.04	NaN	-0.07

Table B.4: 90 events used for inversion approach 2 (Section 3.2.4.2). Listed are P wave arrival times (t_p) picked at station 62, given in seconds relative the triggered event file onset date and time, hypocenter source locations re-calculated by assuming a fixed source depth 150 m and using the backazimuth φ and incidence θ angle of station 62 given by northing ($Y_{\varphi,\theta}$), easting($X_{\varphi,\theta}$) coordinates in meters (reference point X = 892900 m and Y= 116000 m defined by the Lambert 1 Nord (NTF, Paris)).

[yymmdd_hhmmssss]	t_p [s]	$X_{\varphi,\theta}$ [m]	$Y_{\varphi,\theta}$ [m]	φ [°]	θ [°]
080315_01091031	0.364	409.0	212.0	225.0	3.0
080327_20400879	0.365	415.0	213.0	166.0	2.0
080403_05293033	0.37	413.0	213.0	194.0	2.0
080403_10561405	0.342	412.0	214.0	214.0	2.0
080405_00591230	16.928	420.0	235.0	18.0	9.0
080405_06485985	0.359	416.0	217.0	90.0	1.0
080405_20244442	0.677	418.0	219.0	63.0	3.0
080405_21350054	0.365	423.0	217.0	90.0	6.0
080407_18433978	0.364	416.0	219.0	45.0	2.0
080413_04261694	0.364	416.0	219.0	45.0	2.0
081019_09060099	0.37	400.0	200.0	219.0	8.0
080315_03093988	0.353	390.0	220.0	278.0	17.0
080315_09430488	0.362	450.0	160.0	124.0	11.0
080315_11174269	0.357	420.0	160.0	193.0	23.0
080315_12513340	0.361	440.0	200.0	123.0	20.0
080315_13035461	0.358	430.0	210.0	113.0	19.0
080315_20293759	0.363	420.0	280.0	28.0	18.0
080315_21413126	0.366	380.0	200.0	194.0	10.0
080316_01162822	0.362	370.0	180.0	221.0	11.0
080316_02380876	0.348	440.0	210.0	125.0	18.0
080316_10125533	0.358	460.0	160.0	140.0	20.0
080317_02000855	0.356	430.0	270.0	58.0	8.0
080317_15544842	0.364	430.0	220.0	98.0	18.0
080317_22522921	0.352	410.0	270.0	107.0	13.0
080318_03542811	0.361	440.0	180.0	157.0	20.0
080318_15564087	0.359	440.0	180.0	110.0	20.0
080318_16385783	0.365	480.0	230.0	114.0	9.0
080318_17262603	0.364	460.0	220.0	120.0	10.0
080319_00015990	0.361	430.0	220.0	94.0	9.0
080319_02211090	0.352	460.0	260.0	60.0	15.0
080319_06113196	0.36	420.0	240.0	334.0	18.0
080319_13002754	0.366	410.0	220.0	293.0	21.0
080319_13475310	0.366	440.0	280.0	357.0	20.0
080325_17412640	0.344	380.0	180.0	225.0	25.0
080325_18124769	0.36	410.0	250.0	320.0	20.0
080325_19452369	0.363	410.0	230.0	327.0	13.0
080326_01394174	0.364	460.0	170.0	152.0	13.0
080326_08413275	0.381	420.0	270.0	275.0	9.0
080326_08414247	0.357	410.0	240.0	322.0	13.0
080326_18422396	0.364	450.0	260.0	330.0	17.0
080326_23080991	0.356	380.0	220.0	283.0	20.0
080327_11571349	0.366	390.0	210.0	203.0	8.0
080327_12262790	0.369	380.0	190.0	242.0	15.0
080327_12560173	0.36	390.0	240.0	288.0	12.0
080327_13462964	0.365	440.0	270.0	360.0	16.0
080327_17370077	0.363	360.0	180.0	255.0	10.0
080327_19124393	0.366	450.0	260.0	340.0	20.0
080327_20400879	0.363	390.0	230.0	214.0	6.0
080327_21401665	0.365	440.0	260.0	57.0	13.0
080327_22060433	0.352	420.0	250.0	350.0	20.0
080328_06183955	0.359	430.0	210.0	115.0	20.0
080328_11364599	0.359	400.0	210.0	214.0	14.0
080328_12043857	0.364	360.0	200.0	245.0	15.0
080328_14135847	0.363	450.0	160.0	160.0	25.0
080328_15273755	0.337	380.0	210.0	230.0	20.0
080328_18014199	0.364	480.0	220.0	118.0	10.0
080328_22360535	0.367	390.0	170.0	230.0	23.0
080329_10325530	0.367	440.0	210.0	93.0	18.0
080330_03412722	0.362	450.0	200.0	106.0	8.0
080330_14124350	0.351	380.0	180.0	227.0	10.0
080402_06212623	0.361	440.0	260.0	10.0	23.0
080402_07262991	0.358	420.0	260.0	120.0	23.0
080402_21053768	0.359	410.0	160.0	168.0	12.0
080402_22413943	0.363	390.0	200.0	223.0	10.0
080403_00271533	0.361	400.0	210.0	226.0	9.0
080403_04430869	0.363	460.0	260.0	103.0	10.0

Table B.4: (continued)

[yymmdd_hhmmssss]	t_p [s]	$X_{\varphi,\theta}$ [m]	$Y_{\varphi,\theta}$ [m]	φ [°]	θ [°]
080403_04442935	0.363	430.0	250.0	70.0	23.0
080403_10253804	0.595	420.0	260.0	5.0	15.0
080403_11060358	0.369	410.0	270.0	50.0	25.0
080403_16350381	0.358	430.0	250.0	60.0	18.0
080403_19513105	0.365	470.0	200.0	138.0	20.0
080403_22454222	0.363	450.0	270.0	350.0	20.0
080404_03040143	0.405	430.0	260.0	34.0	20.0
080404_03291183	0.368	420.0	210.0	100.0	7.0
080404_07232788	0.362	410.0	220.0	279.0	18.0
080404_15302850	0.374	430.0	270.0	52.0	24.0
080404_18370396	0.37	440.0	190.0	170.0	24.0
080405_01303693	0.358	390.0	220.0	293.0	22.0
080405_03520181	0.368	440.0	170.0	117.0	22.0
080405_06310836	0.369	400.0	190.0	214.0	10.0
080405_06485985	0.358	410.0	220.0	206.0	3.0
080405_09301417	0.364	420.0	240.0	20.0	0.0
080405_10261432	0.361	390.0	160.0	210.0	9.0
080405_10275898	0.368	380.0	190.0	227.0	20.0
080405_12473599	0.358	440.0	280.0	12.0	22.0
080405_14155441	0.359	370.0	230.0	293.0	10.0
080405_19502173	0.362	450.0	200.0	156.0	20.0
080405_22024950	0.358	440.0	230.0	95.0	10.0
080406_02255676	0.358	390.0	230.0	297.0	20.0
080406_14522852	0.363	380.0	240.0	288.0	18.0
080406_16365071	0.358	440.0	280.0	360.0	25.0

Table B.5: Source parameters for well located events (Fig. 3.26 and 3.27). (table on this page) Source parameters for the 54 events training set (Table B.1). Source paremeters were determined as described in Section 3.4.

File start [yymmdd_hhmmssss]	M_w	M_0 [Nm]	fc [Hz]	E_P [J]	r_0 [m]	$\Delta\sigma$ [MPa]	σ_{app} [MPa]
080316_11222906	-0.82 ± 0.18	$8.23e+07 \pm 1.31e+10$	35 ± 27	$6.16e+00$	19	$4.81e-03$	$2.82e-04$
080317_17470327	-1.05 ± 0.71	$3.78e+07 \pm 4.48e+09$	65 ± 460	$1.11e+01$	10	$1.41e-02$	$1.11e-03$
080318_03542811	-1.02 ± 0.59	$4.19e+07 \pm 6.11e+09$	65 ± 38	$1.91e+01$	10	$1.57e-02$	$1.72e-03$
080325_21020502	-1.16 ± 1.00	$2.59e+07 \pm 2.41e+09$	60 ± 8	$7.79e+00$	11	$7.64e-03$	$1.13e-03$
080326_07474929	0.02 ± 0.42	$1.54e+09 \pm 4.04e+09$	40 ± 25	$3.37e+03$	17	$1.34e-01$	$8.27e-03$
080403_07284806	-0.91 ± 0.76	$6.05e+07 \pm 2.35e+09$	60 ± 7	$3.43e+01$	11	$1.78e-02$	$2.14e-03$
080403_14202167	-1.28 ± 0.70	$1.68e+07 \pm 1.04e+10$	105 ± 83	$9.31e+00$	6	$2.66e-02$	$2.09e-03$
080405_13431225	-0.76 ± 0.43	$1.04e+08 \pm 4.28e+09$	60 ± 37	$1.39e+02$	11	$3.06e-02$	$5.03e-03$
080318_11452447	-1.52 ± 1.12	$7.31e+06 \pm 5.77e+09$	115 ± 72	$3.35e+00$	5	$1.52e-02$	$1.73e-03$
080327_21575315	-1.59 ± 1.14	$5.74e+06 \pm 6.74e+09$	160 ± 105	$4.30e+00$	4	$3.21e-02$	$2.82e-03$
080327_23231661	-1.33 ± 1.09	$1.41e+07 \pm 3.26e+09$	120 ± 796	$3.41e+01$	5	$3.33e-02$	$9.10e-03$
080401_03170422	-1.24 ± 0.80	$1.92e+07 \pm 6.64e+09$	60 ± 38	$3.74e+00$	11	$5.66e-03$	$7.33e-04$
080402_23311877	-1.37 ± 0.75	$1.23e+07 \pm 1.22e+10$	50 ± 31	$5.17e+00$	13	$2.09e-03$	$1.59e-03$
080404_22580698	-1.16 ± 0.36	$2.60e+07 \pm 2.21e+10$	35 ± 28	$9.28e-01$	19	$1.52e-03$	$1.35e-04$
080405_08212726	-1.04 ± 0.66	$3.86e+07 \pm 5.17e+09$	60 ± 40	$5.44e+00$	11	$1.14e-02$	$5.32e-04$
080504_09590363	-1.16 ± 0.92	$2.60e+07 \pm 3.19e+09$	160 ± 409	$2.12e+02$	4	$1.45e-01$	$3.07e-02$
080310_10162058	-1.33 ± 0.72	$1.41e+07 \pm 1.18e+10$	75 ± 574	$5.49e+00$	9	$8.10e-03$	$1.47e-03$
080314_10345214	-0.45 ± 0.01	$2.95e+08 \pm 6.60e+09$	60 ± 36	$2.44e+03$	11	$8.70e-02$	$3.12e-02$
080315_11060290	-1.37 ± 0.32	$1.25e+07 \pm 5.29e+10$	40 ± 33	$2.81e+00$	17	$1.09e-03$	$8.48e-04$
080317_22522921	-0.99 ± 0.42	$4.56e+07 \pm 1.01e+10$	60 ± 45	$7.19e+00$	11	$1.34e-02$	$5.93e-04$
080320_01343152	-0.93 ± 0.28	$5.65e+07 \pm 1.33e+10$	40 ± 32	$2.90e+00$	17	$4.93e-03$	$1.93e-04$
080327_07033611	-1.07 ± 0.78	$3.51e+07 \pm 3.85e+09$	65 ± 38	$5.90e+00$	10	$1.32e-02$	$6.34e-04$
080328_00393962	-0.82 ± 0.22	$8.44e+07 \pm 1.10e+10$	30 ± 22	$7.52e+00$	22	$3.11e-03$	$3.36e-04$
080329_12051154	-0.96 ± 0.63	$5.13e+07 \pm 4.29e+09$	40 ± 469	$5.99e+00$	17	$4.48e-03$	$4.39e-04$
080405_08493788	-1.40 ± 0.78	$1.11e+07 \pm 1.20e+10$	140 ± 275	$9.11e+01$	4	$4.16e-02$	$3.09e-02$
080411_12264951	-1.61 ± 1.34	$5.47e+06 \pm 3.50e+09$	115 ± 56	$1.51e+00$	5	$1.14e-02$	$1.04e-03$
080414_14275367	-0.39 ± 0.16	$3.73e+08 \pm 2.76e+09$	40 ± 16	$4.32e+02$	17	$3.26e-02$	$4.36e-03$
080414_15212185	-0.90 ± 0.68	$6.22e+07 \pm 3.00e+09$	70 ± 28	$3.52e+01$	9	$2.91e-02$	$2.13e-03$
080415_19473377	-0.93 ± 0.21	$5.77e+07 \pm 1.65e+10$	35 ± 105	$3.46e+00$	19	$3.38e-03$	$2.26e-04$
080502_01543119	-1.16 ± 0.25	$2.61e+07 \pm 3.25e+10$	60 ± 49	$5.66e+00$	11	$7.69e-03$	$8.17e-04$
080314_01311632	-0.71 ± 0.33	$1.23e+08 \pm 5.11e+09$	45 ± 27	$4.53e+01$	15	$1.53e-02$	$1.39e-03$
080314_05492504	-1.02 ± 0.73	$4.10e+07 \pm 3.91e+09$	40 ± 21	$3.42e+00$	17	$3.58e-03$	$3.14e-04$
080318_05470617	-1.38 ± 0.94	$1.21e+07 \pm 6.46e+09$	115 ± 77	$5.59e+00$	5	$2.51e-02$	$1.74e-03$
080318_14571255	-0.99 ± 0.46	$4.56e+07 \pm 8.76e+09$	40 ± 26	$4.21e+00$	17	$3.98e-03$	$3.49e-04$
080325_18265881	-1.04 ± 0.59	$3.95e+07 \pm 6.50e+09$	60 ± 42	$6.47e+00$	11	$1.16e-02$	$6.18e-04$
080326_20575908	-0.97 ± 0.54	$4.92e+07 \pm 6.27e+09$	60 ± 594	$1.03e+02$	11	$1.45e-02$	$7.86e-03$
080403_05524621	-0.73 ± 0.05	$1.13e+08 \pm 1.45e+10$	35 ± 27	$1.60e+01$	19	$6.61e-03$	$5.32e-04$
080404_13020368	-1.31 ± 0.74	$1.52e+07 \pm 1.00e+10$	65 ± 44	$3.43e+00$	10	$5.70e-03$	$8.50e-04$
080409_04404319	-0.93 ± 0.55	$5.67e+07 \pm 5.28e+09$	60 ± 33	$2.12e+01$	11	$1.67e-02$	$1.41e-03$
080520_16321889	-0.47 ± 0.19	$2.81e+08 \pm 1.36e+10$	35 ± 455	$3.07e+01$	19	$1.64e-02$	$4.11e-04$
080319_15051184	-1.27 ± 0.56	$1.77e+07 \pm 1.63e+10$	60 ± 46	$1.04e+01$	11	$5.21e-03$	$2.21e-03$
080326_01394174	-0.35 ± 0.04	$4.21e+08 \pm 3.68e+09$	60 ± 32	$2.09e+03$	11	$1.24e-01$	$1.87e-02$
080327_09212718	-0.98 ± 0.71	$4.71e+07 \pm 3.61e+09$	150 ± 46	$5.96e+02$	4	$2.17e-01$	$4.77e-02$
080327_20182797	-1.39 ± 1.06	$1.18e+07 \pm 4.29e+09$	120 ± 78	$3.78e+00$	5	$2.78e-02$	$1.21e-03$
080328_00123791	-1.32 ± 0.81	$1.48e+07 \pm 8.05e+09$	60 ± 42	$2.65e+00$	11	$4.37e-03$	$6.74e-04$
080329_00222991	-1.80 ± 1.33	$2.83e+06 \pm 7.10e+09$	105 ± 67	$4.25e-01$	6	$4.47e-03$	$5.67e-04$
080329_06192049	-1.18 ± 0.92	$2.38e+07 \pm 3.48e+09$	100 ± 44	$1.93e+01$	6	$3.25e-02$	$3.05e-03$
080403_10130177	-1.56 ± 0.99	$6.51e+06 \pm 1.01e+10$	120 ± 93	$1.92e+00$	5	$1.54e-02$	$1.11e-03$
080404_07232788	-1.02 ± 0.99	$4.20e+07 \pm 1.54e+09$	60 ± 24	$3.61e+01$	11	$1.24e-02$	$3.24e-03$
080405_03374333	-2.06 ± 1.74	$1.16e+06 \pm 4.29e+09$	255 ± 144	$7.04e-01$	2	$2.62e-02$	$2.29e-03$
080405_03440140	-1.04 ± 0.76	$3.95e+07 \pm 3.65e+09$	40 ± 22	$1.92e+00$	17	$3.45e-03$	$1.83e-04$
080405_08053299	-0.75 ± 0.57	$1.07e+08 \pm 2.51e+09$	55 ± 15	$5.53e+01$	12	$2.43e-02$	$1.95e-03$
080405_22381203	-0.97 ± 0.57	$4.90e+07 \pm 5.56e+09$	60 ± 33	$1.73e+01$	11	$1.44e-02$	$1.33e-03$
080501_05543599	-0.94 ± 0.67	$5.56e+07 \pm 3.52e+09$	55 ± 25	$1.09e+01$	12	$1.26e-02$	$7.41e-04$

Table B.5: (continued) (table on this page) source parameters for the 20 events training set (Table B.2).

File start [yymmdd_hhmmssss]	M_w	M_0 [Nm]	fc [Hz]	E_P [J]	r_0 [m]	$\Delta\sigma$ [MPa]	σ_{app} [MPa]
080315_01091031	-1.03 ± 0.64	$4.07e+07 \pm 5.41e+09$	100 ± 66	$5.02e+01$	6	$5.55e-02$	$4.65e-03$
080318_05493013	-0.35 ± 0.05	$4.27e+08 \pm 3.52e+09$	60 ± 24	$8.85e+03$	11	$1.26e-01$	$7.81e-02$
080318_09170764	-1.27 ± 0.85	$1.79e+07 \pm 5.98e+09$	60 ± 35	$6.83e+00$	11	$5.27e-03$	$1.44e-03$
080318_23112620	-1.30 ± 1.05	$1.61e+07 \pm 3.34e+09$	60 ± 27	$4.12e+00$	11	$4.73e-03$	$9.66e-04$
080325_20504198	-0.81 ± 0.48	$8.52e+07 \pm 4.31e+09$	155 ± 65	$2.34e+03$	4	$4.33e-01$	$1.04e-01$
080327_07513579	0.22 ± 0.55	$2.98e+09 \pm 1.56e+09$	30 ± 18	$5.70e+03$	22	$1.10e-01$	$7.22e-03$
080327_20400879	-1.22 ± 0.94	$2.07e+07 \pm 3.75e+09$	95 ± 50	$1.12e+01$	7	$2.42e-02$	$2.04e-03$
080327_20513983	-1.19 ± 0.81	$2.30e+07 \pm 5.33e+09$	100 ± 73	$9.12e+00$	6	$3.13e-02$	$1.50e-03$
080402_21334282	-0.61 ± 0.40	$1.71e+08 \pm 2.72e+09$	35 ± 15	$3.06e+01$	19	$1.00e-02$	$6.75e-04$
080403_05293033	-1.56 ± 1.23	$6.52e+06 \pm 4.38e+09$	150 ± 87	$9.68e+00$	4	$3.00e-02$	$5.60e-03$
080403_10561405	-1.78 ± 1.50	$3.01e+06 \pm 3.74e+09$	95 ± 36	$2.94e-01$	7	$3.52e-03$	$3.68e-04$
080405_00591230	0.64 ± 1.07	$1.27e+10 \pm 6.42e+09$	20 ± 14	$4.89e+04$	34	$1.39e-01$	$1.45e-02$
080405_06485985	-1.11 ± 0.78	$3.03e+07 \pm 4.40e+09$	60 ± 31	$1.10e+01$	11	$8.93e-03$	$1.37e-03$
080405_20244442	-1.34 ± 1.16	$1.37e+07 \pm 2.68e+09$	60 ± 12	$1.89e+00$	11	$4.04e-03$	$5.19e-04$
080405_21350054	-1.77 ± 1.58	$3.08e+06 \pm 2.75e+09$	120 ± 36	$5.52e-01$	5	$7.26e-03$	$6.75e-04$
080407_18433978	-1.25 ± 1.07	$1.88e+07 \pm 2.60e+09$	60 ± 19	$2.30e+00$	11	$5.55e-03$	$4.61e-04$
080409_01134275	-0.67 ± 0.45	$1.42e+08 \pm 2.80e+09$	60 ± 25	$1.11e+02$	11	$4.17e-02$	$2.95e-03$
080411_08052526	-1.49 ± 1.26	$8.30e+06 \pm 3.12e+09$	60 ± 22	$4.51e-01$	11	$2.45e-03$	$2.05e-04$
080413_04261694	-1.38 ± 1.19	$1.22e+07 \pm 2.65e+09$	60 ± 12	$1.12e+00$	11	$3.58e-03$	$3.48e-04$
081019_09060099	0.00 ± 0.30	$1.44e+09 \pm 2.48e+09$	60 ± 34	$1.43e+04$	11	$4.23e-01$	$3.76e-02$

Appendix C

Theoretical seismic source theory

Based on linear filter theory, the observed displacement wave form $u(t)$ (seismogram) can be described as a convolution ($*$) of the source signal $s(t)$, the Earth's elastic response (path) $g(t)$ and the instrumental response $i(t)$ neglecting contributions of noise $n(t)$ (e.g. Lay and Wallace, 1995)

$$u(t) = s(t) * g(t) * i(t). \tag{C.1}$$

This seismogram representation is fundamental in interpretation of seismic data and for the analysis of source characteristics, but is based on major theoretical assumptions. In the following the major assumptions for source and medium representation are summarized, including the (i) the most important assumptions resulting from the elasto-dynamic point of view (Section C.1), (ii) the source representation by the moment tensor (Section C.1 and C.2) and (iii) the far-field approximation (Section C.3) (being the fundamental assumption for Equation C.1). In Section D, the basics of synthetic seismogram calculation are briefly summarized, while Section D.3 introduces the software packages used to calculate synthetic seismograms and to create a Green's function database.

C.1 Equivalent body forces

As a rough physical approximation the seismic source is regarded as a limited volume V within the earth that is affected by impulsive, non-linear, an-elastic displacements. Mathematically, earthquake processes are described simply by elasto-dynamics. Hence, it is enough to complement the equation of motion for an continuous elastic medium by additional external body forces f_i, which are non-zero within V:

$$\rho \ddot{u}_i = \tau_{ij,j} + f_i. \tag{C.2}$$

Here, ρ comprises the density, $\ddot{u}$ the second time derivative of the surface displacement and $\tau_{ij,j}$ the derivative of the stress tensor τ_{ij} regarding the j-th component (note that in Equation

(C.2) and following equations the Einstein summation convention is used). Self-gravitational effects are ignored here. From Equation (C.2), it was shown by Backus and Mulcahy (1976) that body forces arise due to the difference between the assumed model stress field τ and the actual physical stress σ which they called the *stress glut*

$$f_i^e = \sigma_{ij,j} - \tau_{ij,j}. \tag{C.3}$$

These body forces f_i^e are called *equivalent body forces* as they produce equivalent displacement as the actual governing physical source forces imitated by the *stress glut*. Hence, they are proven to be capable for representing any arbitrary indigenous seismic source under the assumption of a certain surface force distribution. This rather general formalism already embodies a fundamental problem concerning the general analysis of seismic sources and is still in the scope of current research. If the *equivalent body forces* should purely represent actual forces governing the seismic source, then the *stress glut* must be equal to the rearrangement of stress contributed only by the source process itself.
Generally, this implies two fundamental assumptions (Kennett, 2001):

1. The spatial variation of the elastic parameters must be known.

2. The character of constitutive stress-strain relation must be known.

Whenever these assumptions prove to be not valid, deviations will occur between the model stress field τ and the actual physical stress field σ giving rise to additional *equivalent body forces*. Assumption 1 can be relatively well approached by expressing the source separated from the elastic response of the surrounding media through the application of the *theorem of reciprocity*. Thus, a solution of Equation (C.2) can be found that comprises a linear relationship of an internal body force density f_j^e at point x_0 and time τ producing the displacements u_i at point $\boldsymbol{x}$ and time t with respect to the earth elastic response within $t-\tau$ defined by the Green's Tensor G_{ij} (for an unidirectional unit δ-Dirac impulse) that satisfies Equation (C.2) and (Aki and Richards, 2002)

$$u_i(\boldsymbol{x},t) = \int_{-\infty}^{\infty} d\tau \int\int\int_V G_{ij}(\boldsymbol{x}, t-\tau, \boldsymbol{x_0}, 0) f_j^e(\boldsymbol{x_0}, \tau) dx_0^3. \tag{C.4}$$

By so called *multipole expansion*, implicating a Taylor expansion of G_{ij} around the source position x_0, and neglecting terms of higher order and of order zero, one can define the second order moment tensor M_{jk} using Equation (C.4), that then reads (Gilbert, 1971)

$$u_i(\boldsymbol{x},t) = \int_{-\infty}^{\infty} M_{jk}(\tau) G_{ij,k}(\boldsymbol{x}, t-\tau, 0, 0) d\tau. \tag{C.5}$$

Ignoring higher terms at this stage of source representation implies the approximation of the extended source by an *effective point source* (Aki and Richards, 2002). Not considered zero-order terms comprise net forces that are associated with volume strain like mass advection and gravity effects (Julian et al., 1998). Furthermore, by assuming no net torque due to the source, the moment tensor is symmetric (Gilbert, 1971). By considering a discontinuity in displacement along a fault area Σ including two adjacent fault surfaces Σ^+, Σ^- that are integratively bounded by the surface S in V, Equation (C.4) can be replaced by (Aki and Richards, 2002)

$$u_i(\boldsymbol{x},t) = \int_{-\infty}^{\infty} d\tau \int\int_{\Sigma} c_{jkpq} \boldsymbol{s}(\boldsymbol{x_0},\tau) \boldsymbol{n} \frac{\partial}{\partial x_{0k}} G_{ij}(\boldsymbol{x}, t-\tau; \boldsymbol{x_0}, 0) d\Sigma. \tag{C.6}$$

This is called the general dislocation model where c_{jkpq} is the elastic tensor and $\boldsymbol{s}$ the slip vector related by the angle δ to the normal vector $\boldsymbol{n}$ of the fault area as shown in Figure C.1. Hence, this source representation is purely kinematical and based on the *theorem of uniqueness*. By this theorem the displacement on Σ is enough to determine displacement everywhere (Aki and Richards, 2002).

From Equation (C.6) the moment tensor density m_{jk} can be defined as (Backus and Mulcahy, 1976)

$$m_{jk}(\boldsymbol{x_0},\tau) = c_{jkpq} \boldsymbol{s}(\boldsymbol{x_0},\tau) \boldsymbol{n}. \tag{C.7}$$

As a result of point source approximation, all contributions from $d\Sigma$ of the whole surface are concentrated at one point and the moment tensor M can be redefined as

$$M_{jk}(\tau) = \int\int_{\Sigma} m_{jk}(\boldsymbol{x_0},\tau) d\Sigma = c_{jkpq} \boldsymbol{s} A_0 \boldsymbol{n} h(\tau), \tag{C.8}$$

where A_0 is the planar fault area, $\boldsymbol{s}$ is the slip vector with components $s_1 ... s_p$ and $\boldsymbol{n}$ the normal vector with components $n_1 ... n_q$. Moreover, all elements of the tensor are assumed to have the same time dependency with respect to the source time function $h(\tau)$, with $h(0) = 0$

and $h(\infty) = 1$.

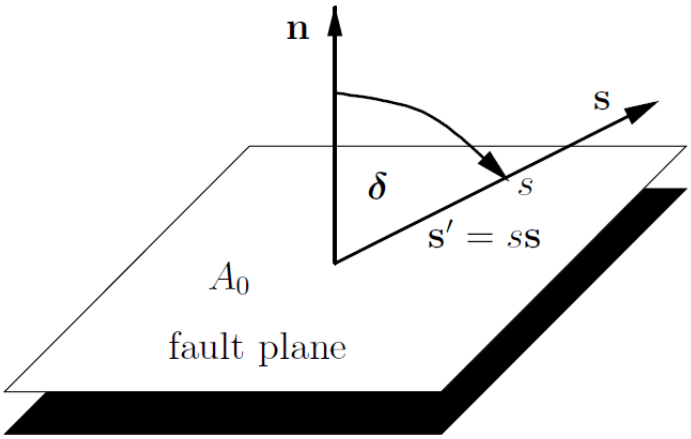

Figure C.1: Geometry of a dislocation source where $\boldsymbol{n}$ is the normal vector to the fault plane A_0 and $\boldsymbol{s}$ the slip vector. If slip inclination given by the angle δ formed by $\boldsymbol{n}$ and $\boldsymbol{s}$ is $\neq 90°$, volumetric changes are included in the dislocation process. Figure is adopted from Rossler (2006).

C.2 Characterization of the moment tensor

In Equation (C.8), the moment tensor represents a dislocation point source in a general anisotropic media described by the superposition of nine elementary force couples (Fig. C.2). In most cases this definition is simplified for isotropic conditions in the source region respectively for c_{jkpq} (Jeffreys, 1973) leading to

$$M_{jk} = \lambda s_p n_p \delta_{jk} A_0 + \mu(s_j n_k + s_k n_j) A_0, \tag{C.9}$$

with Lamé's parameters λ and μ and the Kronecker symbol δ_{jk} (ignoring the uniform time dependency). By defining certain solutions of the eigenvalue problem, the isotropic moment tensor can be decomposed individually with respect to a certain physical source model. An adequate decomposition is the separation into an isotropic (volumetrical) and a deviatoric part

$$M = M^{ISO} + M^{DEV}. \tag{C.10}$$

The isotropical part purely depends on volume changes within the source. When the moment tensor is diagonalized by principal axes transformation, the volume change can be calculated through its trace. After Vavryvcuk (2002) the isotropic part is given in percent by

$$ISO[\%] = \frac{1}{3}\frac{Tr(M)}{m_{max}} 100\%, \tag{C.11}$$

where m are the eigenvalues of M. If $Tr(M) \neq 0$, some volume change occurred that could be associated with an explosion $Tr(M) > 0$ or implosion $Tr(M) < 0$. The deviatoric part M^{DEV} consists of the deviatoric eigenvalues which are $m'_i = m_i - \frac{1}{3}Tr(M)$ with the property $m'_1 + m'_2 + m'_3 = 0$ (Jost and Herrmann, 1989). As used in this study, the following decomposition of the deviatoric part is similar to the moment tensor representation of Knopoff and Randall (1970). After this the deviatoric moment tensor is decomposed into a double couple (DC) and a compensated linear vector dipole (CLVD) $M^{DEV} = M^{DC} + M^{CLVD}$ (Fig. C.3). Hence, by assuming that $|m'_3| \leq |m'_2| \leq |m'_1|$ the complete decomposition of M applies (Lay and Wallace, 1995)

$$\begin{pmatrix} m_1 & 0 & 0 \\ 0 & m_2 & 0 \\ 0 & 0 & m_3 \end{pmatrix} = \frac{1}{3} \overset{ISO}{\begin{pmatrix} Tr(M) & 0 & 0 \\ 0 & Tr(M) & 0 \\ 0 & 0 & Tr(M) \end{pmatrix}} + (1-2\epsilon) \overset{DC}{\begin{pmatrix} 0 & 0 & 0 \\ 0 & -m'_3 & 0 \\ 0 & 0 & m'_3 \end{pmatrix}} + \epsilon \overset{CLVD}{\begin{pmatrix} -m'_3 & 0 & 0 \\ 0 & -m'_3 & 0 \\ 0 & 0 & 2m'_3 \end{pmatrix}}, \quad \text{(C.12)}$$

where $\epsilon = \frac{-m'_2}{m'_3}$. As proved by Burridge and Knopoff (1964), the DC portion comprises the *equivalent body forces* of a shear dislocation as it reproduces the equivalent displacement field. It reflects the observed distant seismic wave-field revealing the famous lobe-shaped radiation pattern. Considering Equation (C.9) for a pure DC source the first term on the right-hand side becomes zero as $\boldsymbol{s} \perp \boldsymbol{n}$. The remaining term constitutes the displacement on the fault that could be also expressed in terms of strike ϕ, dip δ and rake $\overline{\lambda}$ (Jost and Herrmann, 1989) and the well-known scalar seismic moment M_0 (e.g. Aki and Richards, 2002)

$$M_0 = \mu s A, \quad \text{(C.13)}$$

where μ comprises the *shear modulus*. In Equation (C.12) the eigenvalues of the DC term correspond to eigenvectors that are parallel to the principal stress axis. Accordingly, the B-axis (null-axis) is referred to the eigenvalue of zero while the P- and T-axes (pressure and tension) correspond to the negative and positive eigenvalue. In contrast, the physical origin of a CLVD is just speculative. After Equation (C.12) and Figure C.3 the CLVD has one force dipole of strength 2 pointing in direction of the eigenvector, corresponding to the smallest

eigenvalue m_3' and two force dipoles of strength 1 in the remaining eigenvector directions. Originally, this *equivalent body force* system should represent rapid phase transitions in planar zones as a source mechanism for deep located earthquakes (Knopoff and Randall, 1970) what could not be proven until now. Nevertheless, the CLVD is a useful quantitative measure of the non-double couple portion within the deviatoric moment tensor given by (Lay and Wallace, 1995)

$$CLVD[\%] = -\epsilon(200\% - ISO[\%]). \tag{C.14}$$

Hence $\epsilon = \pm 0.5$ represents a pure CLVD while $\epsilon = 0$ is a pure DC with $DC[\%] = 100\% - |ISO| - |CLVD|$. The formation of a Non-DC part is plausible in a lot of possible physical processes as for instance tensile source components induced by fluids in hydrothermal or volcanic active areas, complexity in rupture geometry or rapid phase changes (e.g. Julian et al., 1998). Further testing of such possible physical origins generally includes additional *equivalent body force* terms during *multipole expansion* e.g. higher-order moment tensor approaches (Dahm and Krueger, 1999) or appropriate single force distributions (Takei and Kumazawa, 1994).

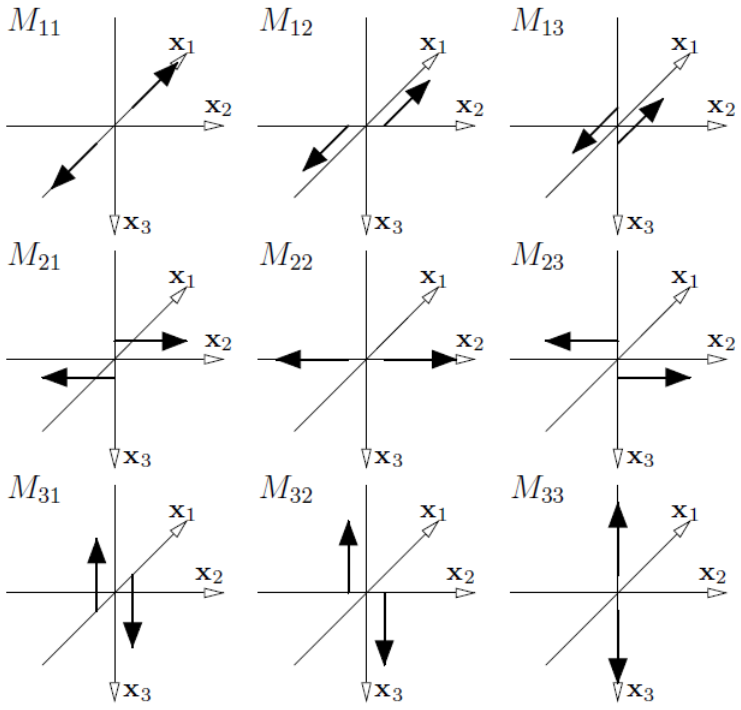

Figure C.2: The nine force-couples composing the moment tensor for a generally oriented displacement discontinuity after Aki and Richards (2002). Hence the components of moment tensor M_{ij} represent forces in x_i directions with moment arms in the x_j directions. Figure was adapted from Rossler (2006).

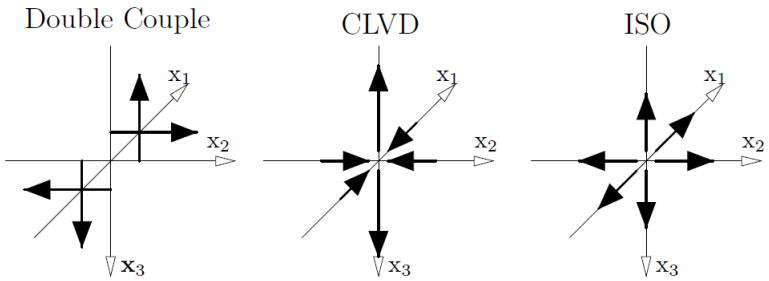

Figure C.3: Component orientations for double-couple (DC), compensated linear vector dipole (CLVD) and isotropic (ISO) portions of the decomposed moment tensor after Knopoff and Randall (1970). Figure was adapted from Rossler (2006).

C.3 Far-field approximation

From Equations (C.5) and (C.8) one can conclude (Dahm, 1993)

$$u_i(\boldsymbol{x},t) = M_{jk}h(t) * G_{ij,k}(\boldsymbol{x},t;\boldsymbol{x_0},0). \tag{C.15}$$

For practical use this temporal convolution integral between the moment tensor and the derivatives of the *Green's tensor* with respect to the source coordinates has to be further simplified. This can be done by a suitable decomposition of the partial derivatives of the *Green's Tensor* to

$$G_{ij,k}(\boldsymbol{x},t-\tau,\boldsymbol{x_0},0) = \frac{\partial G_{ij}}{\partial x_l}\frac{\partial x_l}{\partial x_{0k}} + \frac{\partial G_{ij}}{\partial t}\frac{\partial t}{\partial x_{0k}}. \tag{C.16}$$

This expression can be reduced to the second term on the right-hand side, by neglecting the static displacement in the near-field when observing only the far-field displacement. Due to spherical divergence of waves that are radiated from point sources the second term on the right-hand side of Equation (C.16) decays with distance r from the source as $G_{ij}r^{-1}$ (Aki and Richards, 2002, Dahm, 1993). The first term on the right-hand side of Equation (C.16) decays with higher order of r. Therefore, at large distances $r > \boldsymbol{\lambda}/2\pi$, where $\boldsymbol{\lambda}$ is the considered wavelength (e.g. Wielandt, 2001) amplitudes of the second term will dominate the first term. With the second term of Equation (C.16), Equation (C.15) now reads

$$\begin{aligned} u_i(\boldsymbol{x},t) &= M_{jk}h(t) * \dot{G}_{ij}(\boldsymbol{x},t;\boldsymbol{x_0},0)\boldsymbol{p_k} \\ &= M_{jk}\dot{h}(t) * G_{ij}(\boldsymbol{x},t;\boldsymbol{x_0},0)\boldsymbol{p_k}, \end{aligned} \tag{C.17}$$

where the third-order *Green's Tensor* is replaced by a second-order tensor multiplied by the slowness vector $\boldsymbol{p_k}$ which is $\boldsymbol{p_k} = \frac{\partial t}{\partial x_{0k}}$ (Ben-Menahem et al., 1991). Accordingly, the displacement u produced by the seismic wave-field is proportional to the time derivative

of the source time function $\dot{h}(\tau)$ which is called the *rise time function* of the source. By considering periods of the Green's functions much longer than the source duration τ^{∞} it is possible to represent $G_{ij}(t)$ by Taylor expansion around the source time τ_0 with $0 < \tau_0 < \tau_s$ while ignoring higher order terms (Dahm, 1993, Nabalek, 1984):

$$u_i(\boldsymbol{x}, t) = M^0_{jk} G_{ij}(\boldsymbol{x}, t - \tau_0; \boldsymbol{x_0}, 0)\boldsymbol{p_k}. \tag{C.18}$$

In Equation (C.18), the *equivalent body forces* at the source $M^0_{jk} = M_{jk}\dot{h}(\tau_0)$ and the displacement wave-field $G_{ij}\boldsymbol{p_k}$ are linearly related.

Appendix D

Calculation of synthetic seismograms

The potential to simulate the full theoretical seismic wave-field from a simple 1D, horizontally stratified elastic medium was discovered by the studies of Thomson (1950) and Haskell (1953) and since then has been a very active and progressive field of research.

D.1 Cylindrical symmetric media approximation

Mathematically this is implemented by choosing a cylindrical coordinate system (Fig. D.1) through which one can conveniently reduce the wave equations to a 1-D problem of the elastodynamic equation of motion in the continuum (Eq. C.2). Further, it can be shown that in such cylindrical symmetric media the far-field is composed of just three independent, up- and down-going plane-waves (or modes): P, SV, SH (Ben-Menahem et al., 1991). Hence, the Green's tensor from Equation (C.18) is further simplified to the sum of these propagation modes $G = G^P + G^{SV} + G^{SH}$ comprising now three 3×3 matrices. P modes comprise compressional waves, SV shear waves are polarized in the ρ, z-plane, and SH shear waves are polarized in the ϕ, z-plane (Fig. D.1). For rotation of the Green's Tensor by an angle ϕ five elementary seismograms can be identified where

$$\begin{aligned} I_i^0 &= iwG_{iz}p_z \\ I_i^1 &= iw(G_{i\rho}p_z + G_{iz}p_\rho) \\ I_i^2 &= iwG_{i\rho}p_\rho \\ &\text{with } i = \rho, z \end{aligned} \tag{D.1}$$

represent P and SV respectively for the radial and vertical particle motion, while

$$I_\phi^0 = iwG_{\phi\phi}p_\rho$$
$$I_\phi^1 = iwG_{\phi\phi}p_z \tag{D.2}$$

define SH (transversal particle motion) (Note: in Equations (D.1) and (D.2), i in front of w is the imaginary unit!) $\boldsymbol{p}$ comprises the slowness vector that always lies in the ρ, z-plane. The displacement in Equation (C.18) assembles a convolution of elementary seismograms and (linear independent) elementary sources found by principle axes rotation of the moment tensor M for a given azimuth from the source Φ (Dahm, 1993):

$$\begin{aligned} u_\phi(x,w) &= I_\phi^0\left(\frac{1}{2}(M_{22}-M_{11})sin2\Phi + M_{12}cos2\Phi\right) \\ &\quad + I_\phi^1(M_{23}cos\Phi - M_{13}sin\Phi) \end{aligned} \tag{D.3}$$

$$\begin{aligned} u_z(x,w) &= I_z^2\left(-\frac{1}{2}(M_{22}-M_{11})cos2\Phi + M_{12}sin2\Phi\right) \\ &\quad + I_z^1(M_{13}cos\Phi + M_{23}sin\Phi) \\ &\quad + \frac{1}{3}(I_z^2 - 2I_z^0)\left(\frac{1}{2}(M_{22}+M_{11}) - M_{33}\right) \\ &\quad + \frac{1}{3}(I_z^0 + 2I_z^2)(M_{11}+M_{22}+M_{33}) \end{aligned} \tag{D.4}$$

$$u_\rho(x,w) = \ldots\ . \tag{D.5}$$

Thus, from the cylindrical symmetric medium approach, elementary sources are directly transferred to unique elementary seismograms, determined by the respective azimuth.

To infer the complete synthetic waveform in the time domain and at a desired spatial location relative to the source integration over frequency and wave number (or slowness) is applied. In this process the full response of the planar stacked medium may be described, e.g. by matrices of their reflection and transmission coefficients in the framework of the so called *propagator matrix method* (Haskell, 1953, Thomson, 1950), or by generalized reflection and transmission coefficients for the entire stack as in the *reflectivity method* or discrete wave number method (e.g. Bouchon, 1981, Kennett, 2001). During this study generally both methods were used, implemented by the program QSEIS (version 2006) of Wang (1999) (`http://www.gfz-potsdam.de/en/research/organizational-units/departments/department-2/physic`) and in the code AXITRA Coutant (1989a,b) (`http://www-lgit.obs.ujf-grenoble.fr/~coutant/axitra.ta`) respectively.

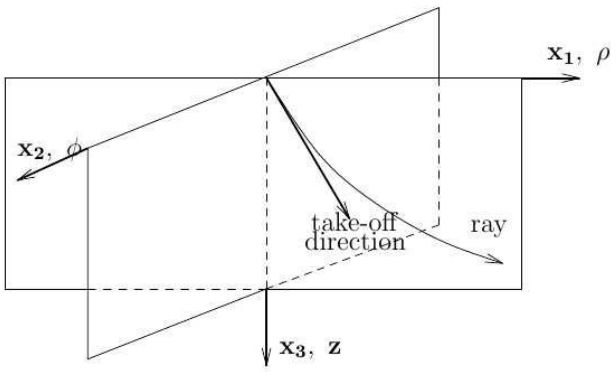

Figure D.1: Coordinate system of a cylindrical symmetric medium (Kruger and Rossler, 2009)

D.2 Readjustment of the velocity model at Cerville-Buissoncourt

This Section documents the readjustment procedure used to improve the velocity model at Cerville-Buissoncourt, whose result is presented in Table 3.1 and which was used for source analysis in Chapter 3. This readjustment generally aimed to define an uppermost soil layer in the overburden responsible for very low P wave velocities observed between station 61 and 62, which are associated with the location of the ground water aquifer (Section 2.3.2). The knowledge of the thickness, depth and velocity of this uppermost layer is generally important to accurately calculate synthetic wave forms for stations 1, 2 and 5 located at depths between station 61 and 62. Moreover, the velocities of the Dolomite layer and the underlying Marls are investigated too (Table D.1). The velocities for these layers were estimated in the laboratory from borehole logs (e.g. Mercerat, 2007) and are generally overestimated due to drilling operations (e.g. Warpinski, 2009). In addition, the velocities obtained by using calibration shots (Table D.1) are maybe not very well constrained, since calibration shots were located at the surface what significantly limits the resolution with depth.

The data basis for the readjustment procedure is represented by the 20 microseismic events located below stations 6 1-3 (Section 2.3.2.2). For these events, the body wave travel time difference for several station couples (Table B.2 and B.3) were identified by using the cross-correlation approach (Eq. 2.12, Section 2.3.2.2) for those cases, where wave forms were similar. The optimal velocity model was obtained by calculating the theoretic travel time differences for P waves tp_{syn} for different velocity models X, and using the fast marching method (e.g. Sethian, 1999) implemented in a Matlab code (provided by the

website `https://sites.google.com/site/patricknraanespro/fast-marching-method`), which were then compared to the observed ones tp_{obs} by using a $l2$-normed misfit function

$$Misfit_X = \frac{\sum_i^n \sum_j^m \sqrt{\left(tp^i_{obs,j} - tp^i_{syn,j}(X)\right)^2}}{\sum_i^n \sum_j^m \sqrt{\left(tp^i_{obs,j}\right)^2}}, \tag{D.6}$$

where i is the considered event and j the considered station couple. The velocity model X was then investigated by a grid-search through the parameter space presented in Table D.2. Grid points, i.e. velocity depth combinations that contradict with the velocity constraints inferred from stations 6 1-3 (Table 2.2 and B.2) were excluded during the grid search. The resulting velocity model (Table 3.1) is generally in well agreement with the other velocity models shown in Table D.1 with exception of the study of Cao (2011), which documents a low velocity above the Dolomite layer and the study of Suffert (2006) documenting significantly higher velocities for the Dolomite layer. Best agreements are found with the study of Hernandez (2008), Mercerat (2007) and Piwakowski et al. (2006).

Table D.1: Comparison to velocity models from previous models

	Depth lower interface [m]	Suffert (2006)	Piwakowski et al. (2006)	Mercerat (2007)	Hernandez (2008)	Cao (2011)	this study
Soil	20	3000	1700	2400 - 3000	3000	3344	1100
Marls and sands	45						2000
Marls and sands	62		3000				
Marls and sands	119					2439	2900
Dolomite	9	6000	5000	5000	5000	4866	4900
Anhydritic marls	∞	3000	4000	4000	4000	4000	4100

Table D.2: Parameter space for grid search on the velocity structure. Varied parameters are marked in red while parameters that kept fixed are marked in black. Note that grid points, i.e. velocity depth combinations, that contradict with the velocity constraints inferred from stations 6 1-3 (Table 2.2 and B.2) were excluded during the grid search.

	Depth [km]	V_p [km/s]	V_p/V_s
Soil	$\{0, 0.1, \ldots, 0.5\}$	$\{1, 1.1, \ldots, 2\}$	2.23
Marls and sands	$\{0.1, 0.2, \ldots, 0.6\}$	$\{1.6, 1.7, \ldots, 2.4\}$	2.23
Marls and sands	$0.06 - 0.118$	2.9	2.23
Dolomite	$0.118 - 0.13$	$\{4.5, 4.6, \ldots, 6.0\}$	1.73
Anhydritic marls and Salt	$0.13 - 0.3$	$\{2.5, 2.6, \ldots, 4.5\}$	2.23

D.3 KIWI Greens function database

The use of synthetic seismograms is without any doubt the most efficient and precise way in order to investigate seismic source parameters. However, in source inversion procedures, calculation of synthetic seismograms can be a very time consuming task, since generally several velocity models and source mechanisms need to be assumed and compared with several

seismic station observations. KIWI Green's function databases are extremely convenient to rapidly calculate synthetic seismograms for different source models and to compare them with the observed data. In these data bases, Green's functions are pre-calculated for arbitrary source-receiver positions based on a specific velocity model using Equation (D.3)-(D.5). Based on this database, synthetic seismograms can then be rapidly calculated by convolution of the source term, defined by the respective source model, with the pre-calculated Green's functions (Eq. D.3-D.5) (Note that in KIWI actually 10 elementary Green's functions are pre-calculated, including near-field terms, what allows for kinematic modeling of extended source models, too).

The KIWI Green's function database was mainly developed by Heimann (2011), Heimann et al. (2014). Supplementary manuals and guides can be found in Cesca and Heimann (2013) and on the webpage `http://kinherd.org/`, where also other very useful software packages for seismic source analysis can be found. One important tool therein, as excessively used in this study, is the Pyrocko tool (`http://emolch.github.io/pyrocko/`), written in the Python programming language which significantly facilitate the practical creation and control of KIWI Green's function data bases and includes also several everyday seismological practice tools as well as ray tracer programs.

In this study, I built Green's function databases for all stations associated with different receiver depth using the velocity model defined in Section D.2. The sampling rate of Green's functions was defined with 500 Hz. Vertical spacing of source depths ranged from 130 to 200 m with a spacing interval of 10 m. Horizontal spacing was defined for the range 1-300 m using a spacing interval of 1 m.